Denudation processes in a tectonically active rift on different time scales: New insights from thermochronology and CRN dating in the Kenya Rift

Dissertation
von

Verónica Torres Acosta

Kumulative Dissertation
zur Erlangung der Würde des akademischen Grades
Doktor Rerum Naturalium
(Dr. rer. Nat)

in der Wissenschaftdisziplin
Geologie

Eingereicht an der
Mathematisch-Naturwissenschaftichen Fakultät
der Universität Potsdam

Potsdam, Juni 2015

Published online at the
Institutional Repository of the University of Potsdam:
URN urn:nbn:de:kobv:517-opus4-84534
http://nbn-resolving.de/urn:nbn:de:kobv:517-opus4-84534

"... We must remember that intelligence is not enough. Intelligence plus character-that is the goal of true education. The complete education gives one not only power of concentration, but worthy objectives upon which to concentrate. The broad education will, therefore, transmit to one not only the accumulated knowledge of the race but also the accumulated experience of social living."

Martin Luther King, Jr., 14th of March, 1947

To my Parents

Declaration of Authorship

I, Veronica Torres Acosta, declare that this thesis titled: "Denudation processes in a tectonically active rift on different time scales: New insights from thermochronology and CRN dating in the Kenya Rift" and the work presented in it are my own. I confirm that:

– This work was done wholly while in candidature for a research degree at Potsdam University.

– Where any part of this thesis has previously been submitted for a degree or any other qualification at this University or any other institution, this has been clearly stated.

– Where I have consulted the published work of others, this is always clearly attributed.

– Where I have quoted from the work of others, the source is always given. With the exception of such quotations, this thesis is entirely my own work.

– I have acknowledged all main sources of help.

– Where the thesis is based on work done by myself jointly with others, I have made clear exactly what was done by others and what I have contributed myself.

Signed: _____

Date: _____

Abstract

Continental rifts are excellent regions where the interplay between extension, the build-up of topography, erosion and sedimentation can be evaluated in the context of landscape evolution. Rift basins also constitute important archives that potentially record the evolution and migration of species and the change of sedimentary conditions as a result of climatic change. Finally, rifts have increasingly become targets of resource exploration, such as hydrocarbons or geothermal systems. The study of extensional processes and the factors that further modify the mainly climate-driven surface process regime helps to identify changes in past and present tectonic and geomorphic processes that are ultimately recorded in rift landscapes.

The Cenozoic East African Rift System (EARS) is an exemplary continental rift system and ideal natural laboratory to observe such interactions. The eastern and western branches of the EARS constitute first-order tectonic and topographic features in East Africa, which exert a profound influence on the evolution of topography, the distribution and amount of rainfall, and thus the efficiency of surface processes. The Kenya Rift is an integral part of the eastern branch of the EARS and is characterized by high-relief rift escarpments bounded by normal faults, gently tilted rift shoulders, and volcanic centers along the rift axis.

Considering the Cenozoic tectonic processes in the Kenya Rift, the tectonically controlled cooling history of rift shoulders, the subsidence history of rift basins, and the sedimentation along and across the rift, may help to elucidate the morphotectonic evolution of this extensional province. While tectonic forcing of surface processes may play a minor role in the low-strain rift on centennial to millennial timescales, it may be hypothesized that erosion and sedimentation processes impacted by climate shifts associated with pronounced changes in the availability in moisture may have left important imprints in the landscape.

In this thesis I combined thermochronological, geomorphic field observations, and morphometry of digital elevation models to reconstruct exhumation processes and erosion rates, as well as the effects of climate on the erosion processes in different sectors of the rift. I present three sets of results: (1) new thermochronological data from the northern and central parts of the rift to quantitatively constrain the Tertiary exhumation and thermal evolution of the Kenya Rift. (2) ^{10}Be-derived catchment-wide mean denudation rates from the northern, central and southern rift that characterize erosional processes on millennial to present-day timescales; and (3) paleo-denudation rates in the northern rift to constrain climatically controlled shifts in paleoenvironmental conditions during the early Holocene (African Humid Period).

Taken together, my studies show that time-temperature histories derived from apatite fission track (AFT) analysis, zircon (U-Th)/He dating, and thermal modeling bracket the onset of rifting in the Kenya Rift between 65-50 Ma and about 15 Ma to the present. These two episodes are marked by rapid exhumation and, uplift of the rift shoulders. Between 45 and 15 Ma the margins of the rift experienced very slow erosion/exhumation, with the accommodation of sediments in the rift basin.

In addition, I determined that present-day denudation rates in sparsely vegetated parts of the Kenya Rift amount to 0.13 mm/yr, whereas denudation rates in humid and more densely

vegetated sectors of the rift flanks reach a maximum of 0.08 mm/yr, despite steeper hillslopes. I inferred that hillslope gradient and vegetation cover control most of the variation in denudation rates across the Kenya Rift today. Importantly, my results support the notion that vegetation cover plays a fundamental role in determining the voracity of erosion of hillslopes through its stabilizing effects on the land surface.

Finally, in a pilot study I highlighted how paleo-denudation rates in climatic threshold areas changed significantly during times of transient hydrologic conditions and involved a sixfold increase in erosion rates during increased humidity. This assessment is based on cosmogenic nuclide (^{10}Be) dating of quartzitic deltaic sands that were deposited in the northern Kenya Rift during a highstand of Lake Suguta, which was associated with the Holocene African Humid Period. Taken together, my new results document the role of climate variability in erosion processes that impact climatic threshold environments, which may provide a template for potential future impacts of climate-driven changes in surface processes in the course of Global Change.

Zusammenfassung

Kontinentale Riftsysteme wie das ostafrikanische Riftsystem (OARS) bieten ideale Voraussetzungen, um die verschiedenen Wechselwirkungen zwischen Extension, Änderungen in der Topographie, Erosion und Sedimentation im Zusammenhang mit Prozessen der Landschaftsentwicklung auf unterschiedlichen Zeitskalen zu untersuchen. Darüber hinaus spielen diese Regionen eine bedeutsame Rolle für die Entwicklung und Verbreitung der Arten und stellen durch eine kontinuierliche Entwicklung von Sedimentationsräumen und die in ihnen gespeicherten Klimasignale wichtige Klimaarchive dar. Rifts sind auSSerdem wichtige Regionen, in denen MaSSnahmen zur Exploration natürlicher Ressourcen zunehmend wichtiger werden. Von Bedeutung ist hier, diese Prozesse und ihre Auslösemechanismen besser zu verstehen und Veränderungen in den tektonischen und geomorphologischen Prozessen der Vergangenheit und der Gegenwart zu identifizieren, deren Raten zu bestimmen und in den Kontext der Landschaftsentwicklung zu setzen.

Das OARS ist eine markante tektonische und topographische Erscheinung in Ostafrika, die einen tiefgreifenden Einfluss auf die Verteilung und Menge von Niederschlägen und damit auf die Effizienz von Oberflächenprozessen hat. Das Kenia-Rift ist ein integraler Bestandteil des östlichen Zweigs des OARS und ist durch ausgeprägte Riftflanken mit Abschiebungen, und flacheren Riftschultern sowie vulkanischen Zentren entlang des Grabens gekennzeichnet.

In Anbetracht der tektonischen Prozesse im Kenia-Rift während der letzten 60 Millionen Jahre, bilden die Bestimmung der Abkühlungsgeschichte der Riftschultern, sowie die Ablagerungsgeschichte im Riftbecken und auf den Riftschultern die Grundlage für die Rekonstruktion der strukturellen Entwicklung des Rifts. Auf kurzen, hundertjährigen bis tausendjährigen Zeitskalen, spielt tektonische Aktivität aufgrund langsamer Deformationsraten eine untergeordnete Rolle bei der Kontrolle von Erosion und Sedimentation. Dem gegenüber stehen klimagesteuerte Prozesse, die die Verfügbarkeit von Feuchtigkeit, die Niederschlagstätigkeit, die Vegetationsbedeckung sowie die Erosionsprozesse kontrollieren.

In dieser Dissertation habe ich thermochronologische Untersuchungen, geomorphologische Geländeergebnisse und morphometrische Analysen an digitalen Geländemodellen kombiniert, um Exhumationsprozesse und Erosionsraten sowie die Wirkung des Klimas auf die känozoische Entwicklung des Kenia-Rifts zu rekonstruieren. Ich präsentiere: (1) neue thermochronologische Daten aus den nördlichen und zentralen Teilen des Kenia-Rifts, um quantitative Angaben zur Exhumationsgeschichte und der thermischen Entwicklung im Känozoikum zu erhalten, die letztlich die Basis für regionale Riftmodelle bilden und die Dynamik der Riftbildung im Inneren eines Kontinents beleuchten; (2) mittlere Denudationsraten (mithilfe des kosmogenen Nuklids ^{10}Be) in Einzugsgebieten des nördlichen, zentralen und südlichen Rifts um Abhängigkeiten der Erosionsprozesse von klimatischen, lithologischen und tektonischen Parametern auf einer Zeitskala von mehreren 10^3 Jahren zu erfassen; (3) Paläo-Denudationsraten im nördlichen Rift, um klimatisch kontrollierte Veränderungen der Umweltbedingungen im Früh-Holozän zu bestimmen.

Meine Studien zeigen, dass Zeit-Temperatur-Pfade von Apatit Spaltspurenanalysen, Zirkon-(U-Th)/He-Datierungen und thermischen Modellierung den Zeitraum der Grabenbildung im

Kenia Rift zwischen 65-50 Ma und von 15 Ma bis zur Gegenwart definieren. Diese beiden Phasen werden durch schnelle Exhumierung der Riftflanken und Anhebung der Riftschultern begleitet. Zwischen 45 und 15 Ma wurden die Riftschultern und -flanken nur sehr langsam erodiert/exhumiert, und Sedimente aus diesen Gebieten im Rift abgelagert, die zum Teil auf die damaligen Riftschultern sedimentiert wurden.

Darüber hinaus ermittelte ich, dass Denudationsraten in spärlich bewachsenen Gebieten heute bis zu 0,13 mm/a erreichen können, während in feuchten und dicht bewachsenen Gebieten ein Maximum von nur 0,08 mm/a erreicht wird, trotz z.T. steilerer Hänge. Die Kombination morphometrischer Untersuchungen und Analysen des kosmogenen Nuklids ^{10}Be zeigt, dass Vegetation und Hangneigung weitgehend die Variabilität von Erosionsraten im heutigen Kenia Rift beeinflussen. Meine Ergebnisse unterstützen mit robusten quantitativen Daten die Hypothese, dass die Vegetationsdecke eine wichtige Rolle bei der Stabilisierung von Hängen spielt.

In einer weiterführenden Pilotstudie konnte ich zeigen, wie Paläo-Denudationsraten zum Verständnis bekannter Perioden der Klimaschwankung und den damit verbundenen Änderungen hydrologischer Bedingungen beitragen können. Diese Beobachtung basiert auf der Analyse kosmogener Nuklide (^{10}Be) an früh-holozänen Deltaablagerungen im nördlichen Kenia Rift, die auf eine Vervierfachung der Erosionsraten in der Anfangsphase eines Wechsels von ariden zu humiden Klimabedingungen hindeuten. Diese Untersuchungen dokumentieren somit die Bedeutung von Klimavariabilität im Erosions- und Sedimentationsregime klimatischer Schwellenregionen und verdeutlichen ein Szenario der Veränderung von Oberflächenprozessen, wie es bei zukünftigen Änderungen des Klimas im Zuge des globalen Wandels erwartet werden kann.

Allgemeine Zusammenfassung

Kontinentale Riftsysteme wie das ostafrikanische Riftsystem (OARS) bieten ideale Voraussetzungen, um die verschiedenen Wechselwirkungen zwischen Extension, Änderungen in der Topographie, Erosion und Sedimentation im Zusammenhang mit Prozessen der Landschaftsentwicklung auf unterschiedlichen Zeitskalen zu untersuchen. Darüber hinaus spielen diese Regionen eine bedeutsame Rolle für die Entwicklung und Verbreitung der Arten und stellen durch eine kontinuierliche Entwicklung von Sedimentationsräumen und die in ihnen gespeicherten Klimasignale wichtige Klimaarchive dar. Rifts sind außerdem wichtige Regionen, in denen Maßnahmen zur Exploration natürlicher Ressourcen zunehmend wichtiger werden. Von Bedeutung ist hier, diese Prozesse und ihre Auslösemechanismen besser zu verstehen und Veränderungen in den tektonischen und geomorphologischen Prozessen der Vergangenheit und der Gegenwart zu identifizieren, deren Raten zu bestimmen und in den Kontext der Landschaftsentwicklung zu setzen.

In dieser Dissertation habe ich thermochronologische Untersuchungen, geomorphologische Geländeergebnisse und morphometrische Analysen an digitalen Geländemodellen kombiniert, um Exhumationsprozesse und Erosionsraten sowie die Wirkung des Klimas auf die känozoische Entwicklung des Kenia-Rifts zu rekonstruieren. Ich präsentiere: (1) neue thermochronologische Daten aus den nördlichen und zentralen Teilen des Kenia-Rifts, um quantitative Angaben zur Exhumationsgeschichte und der thermischen Entwicklung im Känozoikum zu erhalten, die letztlich die Basis für regionale Riftmodelle bilden und die Dynamik der Riftbildung im Inneren eines Kontinents beleuchten; (2) mittlere Denudationsraten (mithilfe des kosmogenen Nuklids ^{10}Be) in Einzugsgebieten des nördlichen, zentralen und südlichen Rifts um Abhängigkeiten der Erosionsprozesse von klimatischen, lithologischen und tektonischen Parametern auf einer Zeitskala von mehreren 10^3 Jahren zu erfassen; (3) Paläo-Denudationsraten im nördlichen Rift, um klimatisch kontrollierte Veränderungen der Umweltbedingungen im Früh-Holozän zu bestimmen.

Mit thermochronologischen Verfahren kann ich den Zeitraum der Grabenbildung im Kenia Rift zwischen 65-50 Ma und von 15 Ma bis zur Gegenwart definieren. Diese beiden Phasen werden durch schnelle Exhumierung der Riftflanken und Anhebung der Riftschultern begleitet. Zwischen 45 und 15 Ma wurden die Riftschultern und -flanken nur sehr langsam erodiert/exhumiert, und Sedimente aus diesen Gebieten im Rift abgelagert, die zum Teil auf die damaligen Riftschultern sedimentiert wurden.

Die Kombination morphometrischer Untersuchungen und Analysen des kosmogenen Nuklids ^{10}Be zeigt, dass Vegetation und Hangneigung weitgehend die Variabilität von Erosionsraten im heutigen Kenia Rift beeinflussen. Meine Ergebnisse unterstützen mit robusten quantitativen Daten die Hypothese, dass die Vegetationsdecke eine wichtige Rolle bei der Stabilisierung von Hängen spielt.

In einer weiterführenden Pilotstudie konnte ich zeigen, wie Paläo-Denudationsraten zum Verständnis bekannter Perioden der Klimaschwankung und den damit verbundenen Änderungen hydrologischer Bedingungen beitragen können. Diese Untersuchungen dokumentieren die Bedeutung von Klimavariabilität im Erosions- und Sedimentationsregime klimati-

scher Schwellenregionen und verdeutlichen ein Szenario der Veränderung von Oberflächenprozessen, wie es bei zukünftigen Änderungen des Klimas im Zuge des globalen Wandels erwartet werden kann.

Aknowledgments

First, I would like to thank my advisor Manfred Strecker for his guidance and support, as this work was financed through the Graduate School GRK1364 "Shaping Earth's Surface in a Variable Environment", funded by a DFG grant awarded to Strecker (grant STR 373-20/1), and by the Potsdam Graduate School (PoGs) for granting travel support for conference participation. Additionally, I thank Taylor Schildgen for her support, and contributions to the different manuscripts presented in this thesis.

I thank all my co-authors and colleagues that shared in many ways their knowledge with me and helped me during lab work, field work and scientific discussions at the different stages of this dissertation. I also thank them for having given me the opportunity to work with them on the articles presented here.

I acknowledge my colleagues, professors, secretaries and administrative staff of the Institute of Earth and Environmental Sciences at the University of Potsdam who contributed in many ways to enrich my time here. I also acknowledge Andreas Bergner for helping with organizing the session at the Colombian Geological Congress in 2013, and the collaboration agreement with Colombia. I am thankful to the professors and members of the Graduate School GRK1364. I particularly thank my lunch and office mates for a wonderful time, for spontaneous coffee-tee-mate-beer-chocolate breaks or even all of the before mentioned together :-). I also thank them for always having been supportive in many ways. Thanks a lot, I will miss you all.

I also thank colleagues and collaborators in different parts of the world. First of all Fin Stuart and his team in Scotland for guidance before, during and after working in his (U-Th)/He lab, and for a really great time in Glasgow. I thank the members of section 3.4 at GFZ Potsdam for their guidance during sample preparation for cosmogenic nuclide dating. I am also very grateful to the people who helped me in Kenya for their logistical support, Eric Odada, Rose Maghas and Olakas' family in Nairobi, and Hilary Limo Chepchieng, Daniela Marigat and many others in the field. I thank especially Jose Maria Jaramillo in Colombia and Matthias Bernet in France for their support.

Thanks to all my friends around the world and to my friends here. Thank you all of you guys for always having been close, supportive, objective, honest and critical with me.

This thesis would not have been possible without the unconditional support and love of my family. I am extremely grateful to my parents Mauricio and Maria Edith, thank you with all my heart. Thanks to my brother Carlos and my sisters Claudia and especially Lili, my best friend.

I finally thank God for keeping my head up.

Contents

List of Figures

List of Tables

Author Contributions & Publications

The results of this study are presented in four different chapters of this thesis. The manuscripts that correspond to chapters 2 and 3 of this thesis have been published or are currently under review in international peer-reviewed journals. Chapter 4 is a manuscript in preparation and chapter 5 corresponds to additional collaborative research during my PhD. The co-authors mentioned below provided guidance and support during the planning phase of the project planning and the writing of the manuscripts.

Chapter 2: Cenozoic extension in the Kenya Rift from low-temperature thermochronology: Links to diachronous spatiotemporal evolution of rifting in East Africa. ***doi:10.1002/2015TC003949. Tectonics, v.34; 2015.*** **Torres Acosta, V., Bande, A., Sobel, E.R., Parra, M., Schildgen, T.F., Stuart, F., Strecker, M.R.** – V.T.A. helped design the study, collected, processed and analyzed samples, did the data interpretation and modeling, and wrote the manuscript; M.R.S. and T.F.S. helped with designing the study, interpreting the data, and writing of the manuscript; A.B. analyzed AFT and helped writing the manuscript. E.R.S. and M.P. helped with data analysis and writing of the manuscript; F.S. managed the laboratory used for processing (U-Th)/He samples and helped writing the manuscript. All co-authors discussed data interpretation.

Chapter 3: The effect of vegetation cover on millennial-scale landscape denudation rates in East Africa. ***doi:10.1130/L402.1. Lithosphere, v.7; no. 4, 2015.*** **Torres Acosta, V. Schildgen, T.F., Clarke, B.A., Scherler, D., Bookhagen, B., Wittmann, H., von Blanckenburg, F., Strecker M.R.** – V.T.A. helped designing the study, processed and analyzed samples, and wrote the manuscript; T.F.S., B.A.C., and M.R.S. helped with designing the study, analyzing data, and writing the manuscript; D.S. helped with data analysis and writing of the manuscript; B.B. provided remotely sensed precipitation data and helped writing the manuscript; H.W. helped with sample processing and writing of the manuscript; F.v.B. manages the laboratory used for cosmogenic radionuclide sample processing at GFZ Potsdam and helped writing the manuscript. All co-authors discussed data interpretation.

Chapter 4: Climate-controlled variability of Holocene erosion rates in the northern Kenya Rift. ***in preparation.*** **Garcin, Y, Torres Acosta, V., Melnick, D., Willenbring, J., Schildgen, T.F., Strecker, M.R.** – Y.G., V.T.A, D.M, M.R.S., collected the samples,help with designing the study, analizing data and writing of the manuscript; T.F.S., helped designing the study, analyzing data, and writing the manuscript; J.W. analyzed sample, helped with data analysis and writing of the manuscript; All co-authors discussed data interpretation.

Chapter 5: Talas-Fergana Fault Cenozoic timing of deformation and its relation to Pamir indentation.***doi:10.1144/SP427.1. The Geological Society, London, Special publications, 427, 2015.*** **Bande, A., Sobel, E.R., Mikolaichuk, A., Torres Acosta, V.** During my dissertation research I also contributed to this study: Talas-Fergana Fault Cenozoic timing of deformation and its relation to

Pamir indentation.*In press,* Geological Evolution of Central Asian Basins and the Tien Shan Range. Special publication, The Geological Society of London, 2015.

Chapter 1

Introduction

1.1 General background and objectives

Continental rifts are an integral part of the Wilson Cycle, reflecting the first steps of continental break-up that can lead to the formation of passive margins and ocean basins (Wilson, 1966; Burke and Whitemann, 1972; Sengör and Burke, 1978; Ebinger, 2005). At first order, the early stages of rift evolution can be considered to fall between two end-member scenarios: passive rifts that are associated with extensional processes driven by plate-boundary forces and characterized by very limited magmatic activity, and magmatically active rifts that result from tensional stresses above a mantle plume (Sengör and Burke, 1978; Ebinger et al., 2002). The largely amagmatic Baikal Rift and the magmatic Kenya Rift are typical examples of these two scenarios (Sengör and Burke, 1978).

The anomalously high mantle temperatures, diapiric upwelling, and extensive magmatism commonly associated with magmatically active rifts can induce marked changes in the density and rheology of the continental lithosphere, particularly at its base (Ribe and Christensen, 1994). The impingement of a plume head on the base of the lithosphere has, for example, been associated with the thermal conversion of lithospheric material to asthenospheric material (Perry et al., 1987). This thinning of the lithosphere and the emplacement of material with a lower density than the surrounding materials will ultimately cause isostatically driven, long-wavelength crustal updoming and thus affect the evolution of the regional topography (e.g., Crough, 1983; Lithgow-Bertelloni and Silver, 1998; Ebinger and Sleep, 1998; Moucha and Forte, 2011). The combination of highly dynamic topography, mantle upwelling, magmatism, and a distinct, long-wavelength negative Bouguer gravity anomaly centered on East Africa, underscore the importance of these relationships in active rift zones (Latin, 1993; Marty et al., 1996; Ebinger et al, 1989; Simiyu and Keller, 1997; Nyblade and Brazier, 2002; Moucha and Forte, 2011). Furthermore, the combination of isostatic uplift and dynamic uplift associated with mantle upwelling can in turn have a far-reaching effect on the patterns of atmospheric circulation, the amount and distribution of rainfall, and the associated devel-

opment of drainage networks (e.g., Sepulchre et al., 2006; Levin, et al. 2009; Wichura et al., 2010, 2015; Ebinger and Scholz, 2012).

Once rifting has been initiated in a magmatically driven system, tectonic subsidence accompanied by magmatism results in the formation of a basin and associated short-wavelength rift-shoulder uplift in the footwall of the evolving rift-bounding faults (Buck, 1988; Buck et al., 1988). As the basin continues to subside it accommodates sediments eroded from the rift-shoulder areas and from volcanic rocks generated either along a volcano-tectonic axis within the rift, or from the rift-shoulder areas. During protracted extension, tectonic compartmentalization of the original rift basins may result in the formation of smaller basins, which can disrupt drainage networks and induce localized perturbations in rainfall patterns and erosion processes (Bergner et al., 2009; Ebinger and Scholz, 2012).

The combined effects that crustal uplift and the development of short-wavelength topographic relief have on climate and hydrology thus exert a fundamental influence on the surface processes operating in evolving rift systems, over a range of spatial and temporal scales. The formation of vegetation cover, the distribution and flux of nutrients, and the evolution of biota are therefore intimately coupled to deep-seated processes that are initiated within the Earth's mantle.

The general principles of rifting are well known from detailed geological and geophysical investigations, but little is known about the efficiency of the erosional processes that operate within rifts and along rift-shoulder areas. A question that arises is whether erosion rates change significantly through time as the topographic relief evolves as a consequence of protracted extensional processes, and how any such changes might relate to different tectonic processes and/or superimposed climate-driven processes. In view of the steep topographic and climatic gradients in rift zones it is therefore possible that topographic characteristics resulting from tectonic processes (such as the steepness of slopes or the overall size and shape of drainage basins) may exert a greater influence on erosion-rate patterns in these environments than the amount of rainfall. This possibility is supported by erosion studies in high-mountain environments that have suggested a direct relationship between tectonically controlled terrain steepness and the efficiency of erosion (Molnar and England, 1990; Willet, 1999; Montgomery and Brandon, 2002; Ouimet et al., 2009). An alternative possibility is, however, that the combined effects of rainfall amount and distribution patterns and covarying differences in vegetation cover determine the patterns of erosion and hence the landscape evolution of rift basins, especially if the steep topographic gradients between the basin floors and the rift shoulders are taken into account. Finding answers to some of these questions is important, because rift zones are valuable archives of climate and evolution as they form pathways for migration and speciation, as well as providing restricted environments in which records of environmental change can be preserved (Cohen, 2003; Trauth et al, 2005; Sepulchre et al., 2006; Behrensmeyer, 2006; Spiegel et al., 2007; Wichura et al., 2011). They

can also be important locations for natural resources including hydrocarbons (Tiercelin et al., 2012), metalliferous deposits (Van Schmus and Hinze, 1985), freshwater (Odada, 2013).

The East African Rift system (EARS) is an excellent region (Figure 1.1) in which to study the rich interactions between active rifting, rift shoulder uplift, tectonic exhumation, erosion, and sedimentation. Numerous studies have been conducted in East Africa to elucidate the timing of rifting, the mechanisms involved, the impact of tectonics on sedimentary processes, and the evolution of biota, especially hominins (Potts, 1998; 2013; Trauth et al, 2005; Behrensmeyer, 2006; Sepulchre et al., 2006; Cerling, 2014; Maslin et al., 2015). In addition, since the EARS is located in a region that is influenced by the African-Indian Monsoon and by moisture-bearing winds originating in the Congo Basin, this region has been a focus of climate and paleoclimate studies investigating the influence exerted by climate and tectonics on rainfall, over a range of time scales (Feakins et al., 2005; Sepulchre et al., 2006; Wichura et al., 2010). Despite the breadth and depth of previous investigations into the EARS, there is continuing debate concerning the relationship between the development of the East African rift basins and volcanism associated with mantle-plume dynamics (Ebinger and Sleep, 1998; Nyblade and Brazier, 2002; Koptev et al., 2015). The resulting rifting scenarios have either invoked a north-to-south migration (and hence southward younging) of volcanism and rift-basin formation (i.e., Ebinger and Sleep), or an unsystematic, aerially widespread formation of diachronous (Morley et al., 1992) or coeval basins (Koptev et al., 2015). As such, the evolution of the Kenya Rift provides a crucial link in rift-basin formation between the northern Kenyan and Ethiopian rifts and the Tanzanian rift basins (Tiercelin and Lezzar, 2002; Ebinger and Scholz, 2012). Unfortunately, the early vestiges of extensional processes that would be needed to unambiguously link the different manifestations of rifting over different timescales are often buried under younger basin deposits or have been obliterated on the rift shoulders by erosional processes. Low-temperature thermochronology applied to basement lithologies exposed along the principal rift-bounding faults and the rift shoulders may therefore be especially helpful in elucidating the early stages of extensional processes and, when combined with geological and geophysical data, may furnish new insights into the full spectrum of thermally controlled extensional processes and ensuing environmental changes.

In light of the previous studies and research hypotheses, the motivation of this dissertation was focused on two main objectives. ***The first objective*** was to better constrain the onset of the tectonic evolution of the Kenya Rift on million-year timescales and to evaluate the regional tectono-thermal history in light of previous studies and current models of how the rift evolved. For this purpose I first refined the tectono-thermal evolution of the Kenya Rift by combining low-temperature thermochronology and thermal modeling with geophysical and stratigraphic data and results obtained from previous thermo-chronologic investigations. The ***second objective*** of my study was to assess erosion processes along the rift escarpments and on the rift-shoulder sectors. I therefore analyzed basin-wide erosion rates using the ter-

restrial cosmogenic nuclide ^{10}Be to determine erosion rates over the past several millennia. Overall, I strived to answer the following questions that examine the interactions between tectonics, topography, erosion, and climate on different spatiotemporal scales:

When did extensional processes begin in the eastern branch of the East African Rift? How do pulses of thermo-tectonic events relate to extension, erosion and sedimentation that have been inferred to have driven Cenozoic surface processes?

What are the principal factors modulating erosion in the rift landscape? Are the factors controlling erosion sustained over time or is there a change in form and rate, especially during wetter periods in the geological past?

Previous work on the tectonic setting, present-day and past climate conditions, and vegetation in the East African Rift are summarized below, together with a very brief discussion of the dating techniques used in this research.

1.2 Tectonics, climate, and vegetation through time in the EARS

1.2.1 Tectonic and geodynamic setting

The EARS is one of the most spectacular topographic expressions of ongoing rifting on Earth (Fig. 1.1). It stretches over a length of more than 4000 km from the Gulf of Aden to Mozambique and follows reactivated Proterozoic shear zones in a generally north-south direction. Starting from a position below sea-level in the Afar Depression, the rift traverses the Ethiopia Dome and continues into the Turkana Depression of northern Kenya at an elevation of about 400 m. At approximately 3°N the rift splits into the eastern branch (the Kenya Rift), and the western branch containing the large freshwater lakes such as Lake Albert, Lake Tanganyika, Lake Rukwa, and Lake Malawi (Fig. 1.1). The two branches of the rift, together with the Tanzania Craton and Lake Victoria located between them, form part of the approximately 1300 km-wide (in an E-W direction) and 1200-m-high East African Plateau. This elevated region is underlain by a pronounced negative Bouguer gravity anomaly, reflecting the presence of the underlying mantle plume responsible for generating the dynamic topography (e.g., Achauer et al., 1994; Smith, 1994; Simiyu and Keller, 1997; Nyblade and Brazier, 2002; Moucha and Forte, 2011). The mantle-driven uplift of this region is inferred from paleontological and geologic-geomorphic evidence to have started between about 17 Ma and 13 Ma (Veldkamp et al., 2007; Wichura et al., 2010; 2015); the mantle anomaly is further manifested by voluminous volcanic flows and edifices, and by associated high heat flow (Wheildon et al., 1994). The highest sectors of the greater rift region, however, are not directly associated with the long-wavelength plateau uplift. They are either part of the volcanic edifices on the rift shoulders (Mt. Kenya, Mt. Kilimanjaro) or they are part of the structurally controlled relief, including the Rwenzori Mountains of the western rift branch, or rift-shoulder areas. At about 2°30'S the Kenya Rift transitions into a fan-like extensional province in northern Tanzania, includ-

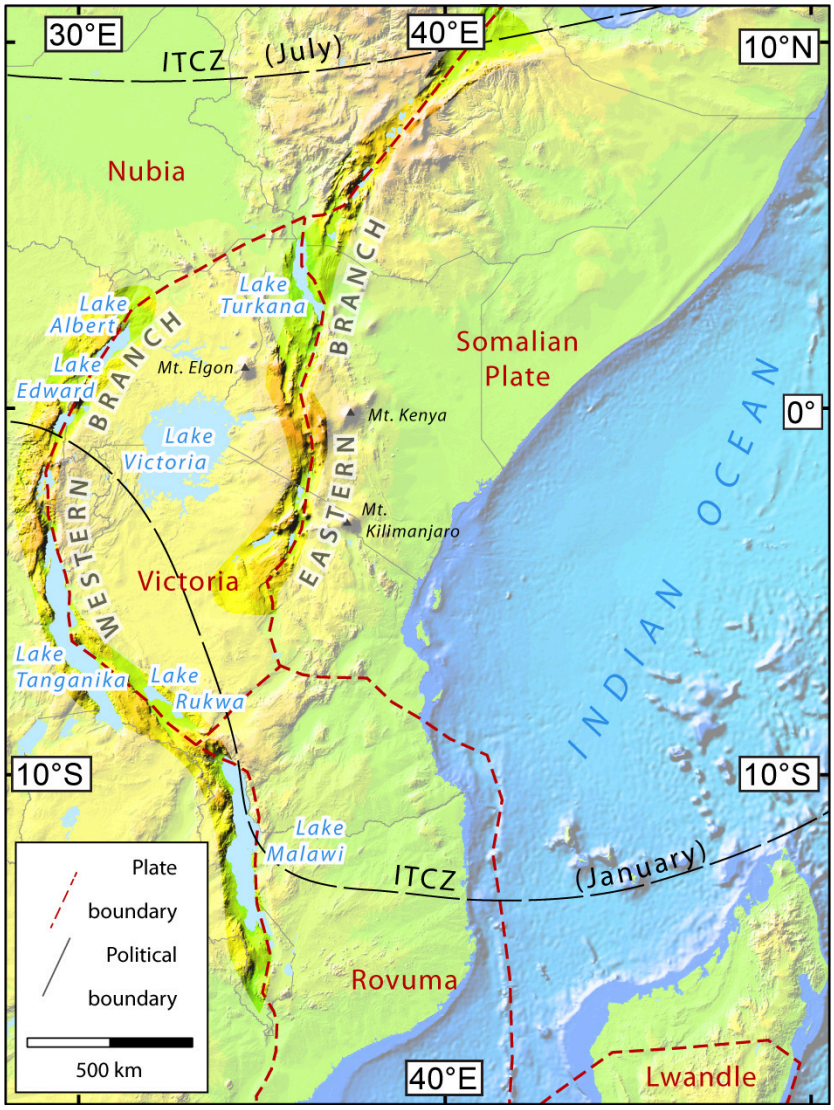

Figure 1.1 – Digital elevation map of the East African Rift System showing principal plate boundaries (red-dashed lines), rift lakes, prominent volcanic edifices, and boundaries of the Intertropical Convergence Zone (dashed black lines). Plate boundaries are marked in red-dashed lines, modified by S. Riedl after Stamps et al. (2008).

ing the Manyara and Pangani rifts, while the western branch continues southward into the Malawi Rift and then on to Mozambique (Brazier et al., 2000; Chorowicz, 2005). The kinematics of rifting in East Africa is accommodated by the motion of several lithospheric plates that have recorded extension rates measured by GPS of up to 3 mm/yr (Stamps et al., 2008). The plates involved are the Victoria, Rovuma and Lwandle plates, between the larger Somalia and Nubia plates. The western branch follows the developing plate margin between the Nubia, Victoria, Rovuma and Lwandle plates, while the eastern branch straddles the boundary between the Victoria, Rovuma and Somalia plates (Figure 1.1).

Numerous investigations carried out during recent decades have provided constraints on the tectonic evolution of the region over the last 30 Ma (Williams, 1970; King, 1978; Jones and Lippard; 1979, Baker, 1988; Foster and Gleadow, 1996; Spiegel et al., 2007). Although the more recent tectonic history of the Kenya Rift is generally well known (Baker and Wohlenberg, 1971; Williams, 1970; Crossley, 1979; Chapman et al., 1978; Baker et al., 1988; Morley et al., 1992; Smith, 1994), the exact timing of the onset of early Cenozoic extension and the associated exhumation processes remain controversial and only poorly constrained. The Kenya Rift of the EARS comprises the asymmetric northern (Elgeyo), central (Mau) and southern (Nguruman) rift segments, which are bounded by major escarpments on their western margins (Figure 1.1). These escarpments reflect fault movements during the Miocene stage of extension and form the western boundaries of asymmetric rift basins that have experienced major tectonic subsidence on their (deepest) western sides (Mugisha et al., 1997; Hautot et al., 2005). The eastern margins of the rift consist of former monoclinal downwarps that were subsequently segmented by antithetic faults and now constitute a full-graben morphology (Crossley, 1979; Baker et al., 1988; Strecker et al., 1990; Mugisha et al., 1997; Bosworth and Maurin, 1993).

1.2.2 Climate

This section reviews the characteristics of past and present-day climates in the Kenya Rift region. These are considered to be important because the amount and distribution of rainfall are closely related to tectonically driven surface uplift or subsidence and reflect the orographic precipitation along the rift and its shoulder areas, over long periods of time. However, over shorter periods the effects of climatic changes and variability on erosion processes and landscape evolution are probably more important as abrupt changes can occur on centennial to millennial timescales (e.g., Wolff et al., 2011). In either case the climatic conditions influence the evolution and erosional efficacy of fluvial networks, as well as soil-formation processes and the development of vegetation cover, which in turn can also influence the susceptibility of a landscape to erosional processes.

Present-day climate

The geographical tropics are the low-latitude regions between the equator and the Tropics of Capricorn (23.5°S) and Cancer (23.5°N). The tropical climate zone, however, can extend beyond the latitudinal limits of the geographical tropics. According to Köppen's climate classification, the tropics are characterized by mean-annual temperatures greater than ~18°C for the coldest month of the year (Köppen, 1936; McGregror and Nieuwolt, 1998). This applies mostly to lowland areas, where the differences between the coldest and hottest months can be less than 4°C. Alternating dry and wet seasons are the most important characteristic of the climate in these low-latitude regions. Along the equator, precipitation is the most important climatic factor, rather than temperature (McGregror and Nieuwolt, 1998). These patterns are related to a number of features of atmospheric circulation that drive the seasonal variations of the Intertropical Convergence Zone (ITCZ), where the trade winds of the northern and southern hemisphere converge. The ITCZ is controlled by seasonal changes in insolation (Griffiths, 1972; Nicholson, 1988). Heating over the African continent funnels moist air from the equatorial Atlantic into western and central Africa during the northern summer (Hastenrath, 1984; de Menocal, 1995). Regional atmospheric circulation reverses during the northern winter, when dry, variable northeast trade winds blow over subtropical Africa, Arabia, and Southeast Asia (McGregror and Nieuwolt, 1998). The seasonal development of the tropical precipitation belt is driven by the position of, and fluctuations in, the ITCZ and the Congo Air Boundary stream (Figure 1.1) (Nicholson, 2001; www. iridl.ldeo.columbia.edu). In addition to these regional processes, the wind and precipitation patterns of tropical Africa are overprinted by climate oscillations such as the El Niño Southern Oscillation (ENSO) (McGregror and Nieuwolt, 1998; Wolff et al., 2011).

Sea-surface temperature fluctuations in the western Indian Ocean associated with the Indian Ocean Zonal Mode (Saji et al., 1999; Webster et al., 1999), the presence of orographic barriers (such as rift escarpments, Mt. Kenya, Mt. Kilimanjaro, Mt. Elgon, etc.), and large water bodies (e.g., lakes Turkana, Victoria, Tanganyika), also affect the atmospheric circulation and precipitation in the East Africa (Nicholson, 1996).

The climate in equatorial East Africa ranges from the tropical humid coastal sectors, through the dry heat of the hinterland and plains of East Africa, to cool and temperate conditions on the plateaus and in mountainous areas. Average annual precipitation varies from ~4 mm/yr in the most arid regions (the northern plains) to ~4000 mm/yr in the temperate highlands (TRMM 2B31, http://trmm.gsfc.nasa.gov/). Most regions in equatorial East Africa have two rainy seasons, one between March and May (the "long rains") and the other between October and November (the "short rains") (Morgan, 1971; Griffiths, 1972, East African Meteorological Department, 1975). The climate in the Kenya Rift zone is affected by the movement of air masses from the Congo Basin, and also by the tropical monsoon and trade winds (Camberlin and Philippon, 2002). As a result of its equatorial position and the presence of orographic

barriers, the rift basin experiences high levels of evaporation and overall aridity, while orographic precipitation is typical of the rift flanks (Bergner et al., 2009 and references therein).

Past changes in climate

Cenozoic environmental changes in East Africa have been the focus of many investigations that have led to a better understanding of the influence of climatic changes on the evolution of hominids and other mammals (Cerling, 1980, 1985, 2010; Beherensmeyer, 2006; Maslin et al., 2015). Some studies have found links between the continental and marine environmental records, using sedimentary archives from East African lakes and offshore areas (Cohen et al. 2003; Behrensmeyer, 2006; Wolff et al., 2011). Lake-sediment records, together with climate modeling and high-precision $^{40}Ar/^{39}Ar$ dating of intercalated volcanic ashes, have furthermore helped to identify the sedimentary processes and associated hydrological changes that are due to climatic changes, fault activity, and volcanism (Feakins et al., 2005; Trauth et al. 2005; Behrensmeyer, 2006; Zachos, 2001; Tiercelin, 1987; Tierney et al., 2011; Tiercelin et al., 2012). The pronounced effect of climate change on the hydrological budget of lakes must have co-varied with the potential stream power of rivers draining into the basins and the production of sediments. The impact that climatic changes have on landscape evolution depends on the period of time over which the mechanisms behind these changes operate. The principal driving forces of changes in the East African climate on million-year timescales are clearly mainly related to spatially extensive plateau uplift and rift-shoulder formation, which can affect not only the topography but also atmospheric circulation patterns (Sepulchre et al., 2006; Levin et al., 2009). For example, associated with the initiation of the Cenozoic East African Rift System during the Eocene-Oligocene, East Africa was affected by major crustal uplift, resulting in the formation of the East African Plateau (Veldkamp et al., 2007; Wichura et al., 2010; Wichura et al. 2011; Moucha and Forte, 2011; Wichura et al., 2015). This involved uplift of the Earth's surface from close to sea level to mean elevations of about 1000 m. This dramatic change in the regional topography led to a major reorganization of atmospheric circulation and precipitation patterns, resulting in aridification and other important paleoenvironmental changes in equatorial East Africa (Sepulchre et al., 2006 and references therein). In contrast, changes in the Earth's orbital parameters (such as eccentricity, obliquity, and precession) over periods of twenty-thousand years to several hundred-thousand years have been the major drivers behind changes in the Earth's climate (Milankovitch, 1941; Berger, 1979) that have been repeatedly superimposed on the evolving rift system and caused pronounced changes in its hydrological regime (e.g., Trauth et al., 2005 and references therein). Such orbital parameters control variations in both the temporal and spatial distribution of energy received from the sun. Eccentricity cycles (with 100 kyr cyclicity), together with obliquity cycles (41 kyr cyclicity) and precession cycles (23 kyr cyclicity) have been linked to the growth and shrinkage of high latitude ice caps (i.e., to glacial-

interglacial cycles) (Milankovitch, 1941; Hays et al., 1976; Imbrie and Imbrie, 1980; Huybers and Wunsch, 2005). Low-latitude climates are, in contrast, primarily influenced by the precession cycles that drive the monsoonal seasons (Berger and Loutre, 1997). Alternating wet and dry cycles described from various East African sedimentary archives dating back to 3 Ma have, for example, been attributed to precession cyclicity (e.g., Deino et al., 2006; Ashley, 2007; Trauth et al., 2003, 2007). Finally, the principal forces affecting the climate on millennial timescales, especially in the East African region, are the intensity of the ENSO, variations in the North Atlantic dipole, and changes to stratospheric winds and atmospheric circulation patterns (McGregror and Nieuwolt, 1998). The large variations in rainfall identified from sedimentary proxy records have been attributed to changes in ENSO-related precipitation (e.g., Russell and Johnson, 2005; Wolff et al., 2011). In view of the many factors that can influence climate over different timescales, it is clear that climatic changes must have had a profound impact in the EARS, especially with regard to lake-level changes and associated variations in base level, erosion rates, and short-term changes in vegetation cover.

1.3 Vegetation

In view of the influence that climate exerts on soil formation, the development of vegetation and the susceptibility of a landscape to erosion (e.g., Langbein and Schumm, 1958), a description is included below of the relevant characteristics of East African (mainly Kenyan) vegetation. The spread and speciation of vegetation in the rift area are affected by variations in climate and temperature that correspond directly with the elevation and morphology of the moist, high-mountain areas and the dry lowlands between the rift shoulders and escarpments. Vegetation and precipitation are therefore highly correlated with topography (Olago, 2001), which is reflected in vegetation belts that range from mountain forests to lowland plant assemblages (Bonnefille, 2010).

Satellite-derived data (e.g., MODIS products) have been combined with results from botanical investigations to help explain the relationship between biomass distribution and the density of different plant populations in East Africa over recent decades (ORNL DAAC, 2011). This has improved our understanding of the anthropogenic impact on soil conditions and erosion. Such information can ultimately help to identify how quickly erosion rates respond to changes in vegetation density.

Present-day vegetation

Over the last two hundred years the East African region as a whole, and Kenya in particular, has experienced significant economic developments that are associated with changes in the land surface due to the expansion of both agriculture and human settlements (Verschuren et a., 2000; Nicholson, 1988). Studies of recent pollen records from Kenya have attempted

to assess short-term vegetational responses to these changes (e.g., Lamb, 2003). The results of such studies, together with changes of water levels in the rift basins, are helping to elucidate the response of vegetation to human activity and climate variability. However, anthropogenic effects need to be considered in conjunction with those due to climate-induced changes (Lamb, 2003). Many studies have focused on precipitation, temperature, and the intensity and timing of the dry season, considering these to be the principal influences on plant distribution within the African tropical zone (Nicholson, 2001; Olago, 2001; Street-Perrot and Perrot, 1993). The East African topography varies from below sea level to over 6000 m asl and equatorial East Africa consequently has a complex patchwork of climate regimes that are sensitive to climatic fluctuations over a range of temporal and spatial scales (Mills et al., 2014). The rift-valley floor and lowland areas form a dry north-south corridor in which the prevalent vegetation is well adapted to relatively arid conditions. This area also forms a migration corridor for the plants and animals that take advantage of the water in rivers and lakes along the rift valley during both wet and dry seasons (Bonnefille, 2010; Trauth et al., 2005). In contrast, the high mountains and rift escarpments support more dense vegetation ranging from grasslands to dense forests. The vegetation therefore generally varies from savannah or scrubland at low elevations (<1000 m asl), through woodlands at intermediate elevations ($\sim$1000-2000 m asl), to forests at high elevations (>2000 m asl), and to sub-temperate afro-alpine grasslands above 3000 m elevation (White, 1983; Bonnefille, 2010). East Africa is known for its extensive savannahs along the rift zone, which comprise grasslands with sparse tree growth and open canopies. Those parts of tropical Africa with precipitation in excess of 0.8 m/yr are considered to be unstable environments for savannah grasslands, apparently unable to support the co-existence of trees and grasses (Sankaran et al., 2005). Stable savannahs occur where precipitation is below ~0.5 m/yr, with a transition zone in between (0.5-0.8 m/yr) to unstable savannahs where denser vegetation mosaics exist (Sankaran et al. 2005). This information becomes important when attempting to extrapolate the predominant historical vegetation cover in East Africa over millennial timescales. Finally, vegetation is also important in protecting steep hillslopes against erosion in densely vegetated areas with pronounced relief, as shown (for example) in the classic study by Langbein and Schumm (1958). This is therefore also an important issue if erosional processes are to be considered over periods ranging from tens of years to thousands of years.

Past changes in vegetation

Multi-proxy records from East Africa show that the climate of this region changed considerably during the Cenozoic in response to global climate changes. The oldest terrestrial records of Cenozoic vegetation in Africa are from the Eocene (ca. 47 Ma) of Tanzania. These records show evidence of periods that were characterized by prolonged dry seasons that encouraged the development of woodland vegetation and restricted the spread of rainforests along the

equator into East Africa (Bonnefille, 2010). The prolonged dry seasons have been attributed to the global climate changing from warm, wet conditions to cooler dry conditions, which occurred before the main tectonic activity started in this area (Sepulchre et al., 2006). However, our understanding of these relationships is still at an early stage. A valuable future research project would therefore be to compare the macroflora and paleobotanical vegetation records from the EARS with pollen and $\delta^{18}O$ records from marine and lacustrine sediments, (e.g., Hessler et al., 2010; Garcin et al., 2012; Feakins et al., 2013) in order to obtain a better correlation between vegetation changes and climate variability. The expansion of savannah environments in East Africa during wet periods started at about 10 Ma and their continuous existence in this region has been recognized since at least 6 Ma (Bonnefille, 2010; Cerling et al., 2011). The expansion of C_4 plants during the late Miocene (11-5 Ma) and again during the Plio-Pleistocene (4.3-1.4 Ma) interpreted from $\delta^{13}C$ data (from pedogenic carbonate, e.g., Quinn et al., 2007) and pollen data (from cores of marine sediments), also indicates significant changes in the vegetation mosaics of East Africa (Feakins et al., 2013) that were, at least during the Plio-Pleistocene, associated with increasing aridity (Feakins et al., 2005; 2013). Pollen records obtained from various lacustrine sediment cores in East Africa have revealed abrupt changes in vegetation cover during cold intervals (Heinrich events, HS), which are expressed by reductions in biomass (Hessler et al., 2010). The direct relationship between climate and vegetation cover is important when assessing variations in the vegetation, in the distribution patterns of vegetation, and in co-varying surface processes, during periods of climatic variability.

1.4 Techniques to determine the onset of extensional exhumation and erosion rates

Low-temperature thermochronology -in this case apatite fission-track (AFT), apatite (U-Th)/He (AHe) and zircon (U-Th)/He (ZHe) dating, and time-temperature history modeling are powerful tools for determining the cooling history of rocks exposed along major rift escarpments (e.g., Fitzgerald et al., 1992; Reiners, 2003; Stockli, 2005). These three dating techniques can be used to determine cooling from temperatures of more than 180°C (ZHe), 120°C (AFT) and 75°C (AHe) to surface temperatures, using Dodson's simple closure-temperature concept (Dodson, 1973). If the geothermal gradient and the age at which the mineral reached its closure temperature are known, the time that the mineral took to reach the surface can also be determined. Samples collected for thermochronological analysis along vertical elevation profiles in a rift environment can therefore be used to document different episodes of cooling, as well as possible re-heating and renewed cooling associated with extensional exhumation.

Basin-wide erosion rates on millennial timescales can be determined by detrital ^{10}Be analysis on the quartz fraction of river sands. The ^{10}Be is a cosmogenic nuclide that accumulates

over time in quartz that is exposed to cosmic radiation (e.g., von Blanckenburg, 2005 and references therein). The production rates of cosmogenic nuclides for the study area, which depend (among other factors) on elevation and latitude, need to be known in order to be able to determine erosion rates. The underlying assumptions are that sediments in river channels rapidly become mixed and that long-term storage in floodplains is minimal.The ^{10}Be concentrations in detrital quartz can then be translated into average erosion rates for the upstream drainage basin. For this study, detrital quartz samples were collected for ^{10}Be analysis, primarily along the Nguruman Escarpment (western rift margin of the southern Kenya Rift), the Loita Plains of the eastern rift shoulder, and various catchment areas along the Elgeyo Escarpment (western rift margin of the northern Kenya Rift) (Fig. 1.1).

Chapter 2

Cenozoic extension in the Kenya Rift from low-temperature thermochronology: Links to diachronous spatiotemporal evolution of rifting in East Africa

Abstract

The cooling history of rift shoulders and the subsidence history of rift basins are cornerstones for reconstructing the morphotectonic evolution of extensional geodynamic provinces, assessing their role in paleoenvironmental changes and evaluating the resource potential of their basin fills. Our apatite fission track and zircon (U-Th)/He data from the Samburu Hills and the Elgeyo Escarpment in the northern and central sectors of the Kenya Rift indicate a broadly consistent thermal evolution of both regions. Results of thermal modeling support a three-phased thermal history since the early Paleocene. The first phase (~65–50 Ma) was characterized by rapid cooling of the rift shoulders and may be coeval with faulting and sedimentation in the Anza Rift basin, now located in the subsurface of the Turkana depression and areas to the east in northern Kenya. In the second phase, very slow cooling or slight reheating occurred between ~45 and 15 Ma as a result of either stable surface conditions, very slow exhumation, or subsidence. The third phase comprised renewed rapid cooling starting at ~15 Ma. This final cooling represents the most recent stage of rifting, which followed widespread flood-phonolite emplacement and has shaped the present-day landscape through rift shoulder uplift, faulting, basin filling, protracted volcanism, and erosion. When compared with thermochronologic and geologic data from other sectors of the

East African Rift System, extension appears to be diachronous, spatially disparate, and partly overlapping, likely driven by interactions between mantle-driven processes and crustal heterogeneities, rather than the previously suggested north-south migrating influence of a mantle plume.

2.1 Introduction

Continental rift systems are first-order tectonic features that record the early stages of continental breakup. In magmatically controlled rifts, long-wavelength crustal updoming and the development of dynamic topography prior to the onset of volcanism and normal faulting underscore the role of mantle-driven, thermally controlled processes in the evolution of these regions (e.g., Crough, 1983; Ebinger and Sleep, 1998; Moucha and Forte, 2011). In the East African Rift System (EARS), such changes in topography and relief have had far-reaching consequences, including impacts on atmospheric circulation patterns that in turn affect rainfall patterns, drainage systems, and surface processes (e.g., Levin et al., 2009; Sepulchre et al., 2006; Ebinger and Scholz, 2012; Wichura et al., 2010, 2015). In addition, the interplay between extensional tectonics and superposed changes in climate has given rise to gateways and migration corridors for hominids and other mammals, thus fostering speciation (Bobe and Behrensmeyer, 2004; Bailey and King, 2011; Bailey et al., 2011).

Uplift, volcanism, and normal faulting in the EARS are hallmarks of one of the largest magmatic extensional zones on Earth (Burke, 1996). Composed of the largely amagmatic western and the magmatic eastern branch, the ~5000km long EARS has generated a series of transiently linked and isolated rift basins (Tiercelin and Lezzar, 2002; Ebinger and Scholz, 2012). The areally extensive mantle anomaly that underlies the EARS (e.g., Simiyu and Keller, 1997; Ebinger and Sleep, 1998; Achauer and Masson, 2002) helps support average elevations of ~1000m (Moucha and Forte, 2011). As such, understanding the mechanisms of rifting and its spatiotemporal evolution is critical for exploring how geodynamic and surface processes are potentially linked with topographic development, magmatic evolution, and long-termenvironmental and biotic impacts in rift systems. Changes in each of these aspects over time throughout the EARS have been difficult to quantify, but valuable information has been obtained from the sedimentary and volcanic rift-basin strata (e.g., Frostick and Reid, 1990; Morley et al., 1992; Pickford and Senut, 1994; Renaut et al., 1999; Odada and Olago, 2002; Saneyoshi et al., 2006; Ebinger and Scholz, 2012; Tiercelin et al., 2012; Roberts et al., 2012). Unfortunately, many of the rift basins do not allow for a direct inspection of such deposits, because old strata either lie below thick volcano-sedimentary sequences or areally extensive lakes (e.g., Flannery and Rosendahl, 1990; Cohen et al., 1993; Scholz and Finney, 1994; Hautot et al., 2000) or because differential faulting, uplift, and erosion along the rift flanks have been insufficient to expose such deposits. For these reasons, many studies of the spatiotem-

poral trends in rift-basin formation have relied on the combined analysis of geophysical data, field observations, and isolated drill-core data.

Low-temperature thermochronometry, such as apatite fission track and apatite and zircon (U-Th)/He dating, combined with thermal history modeling, constitute powerful alternative tools to investigate cooling as a proxy for tectono-thermal and climate-driven erosion processes in rift settings (Fitzgerald, 1992; Foster and Gleadow, 1992, 1996; van der Beek et al., 1998). Thermochronology studies have been carried out throughout the EARS aimed at unraveling the history of basin formation, rift-shoulder exhumation, and different tectono-thermal episodes associated with mantle-plume activity. These studies have addressed the tectonic evolution of the western branch of the EARS in the Rwenzori Mountains (Bauer et al., 2010, 2012) and the Malawi and Rukwa rifts (van der Beek et al., 1998; Roberts et al., 2012), and the evolution of the eastern branch in Ethiopia (Pik et al., 2008), northern Tanzania (Noble et al., 1997; Mbede, 2001), and Kenya (Wagner et al., 1992; Foster and Gleadow, 1992, 1996; Spiegel et al., 2007). In the greater Turkana region and the western rift-shoulder areas of northern Kenya (Figure 2.1), these investigations have provided helpful constraints on the regional onset of Mesozoic and early Cenozoic rifting (Foster and Gleadow, 1996; Spiegel et al., 2007). However, the spatial extent of the related tectono-thermal events, the formation of older rift basins underlying the late Cenozoic rifts, and the role of their structures in influencing Miocene to Recent rifting are unclear.

The onset of rifting in East Africa has been associated with a southward-directed migration of volcanism, which in turn has been inferred to be linked with the northward motion of the African plate over a mantle plume (Ebinger and Sleep, 1998; Nyblade and Brazier, 2002). Accordingly, the onset of tectonic activity in the eastern branch of the rift is also thought to have followed this temporal trend from Ethiopia to northern Tanzania (Nyblade and Brazier, 2002). In contrast, Zeyen et al. (1997) proposed that the onset of extension was less systematic, and largely dictated by the spatially variable mechanical properties of the lithosphere and crust. The notion that rifting and volcanism did not follow a systematic, southward migration has been recently emphasized again by numerical modeling (Koptev et al., 2015) and by a synopsis of the age of volcanism in the different sectors of the EARS, from which a synchronous onset of volcanic activity in East Africa has been proposed (Michon, 2015). Furthermore, studies of noble gases in East African lavas and xenoliths suggest the existence of separate plume heads in Ethiopia and Kenya (Halldórsson et al., 2014). As the Kenya Rift is located between the Tanzania and Turkana-southern Ethiopia extensional provinces, it constitutes an important link between different extensional sectors in the volcanically active eastern branch of the EARS and is thus in a crucial location to further test these ideas.

Here we report 15 apatite (U-Th)/He (AHe), 13 apatite fission track (AFT), and 5 zircon (U-Th)/He (ZHe) ages from basement rocks that were collected along three elevation transects at the Elgeyo escarpment and the Samburu Hills (Nyiru Range) on the eastern and western rift

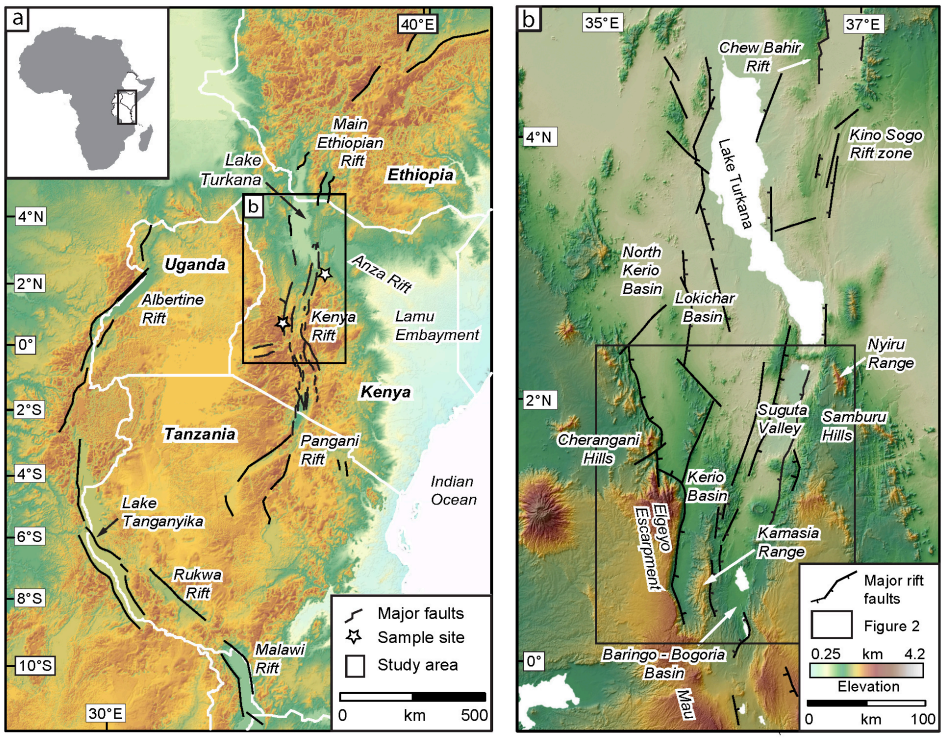

Figure 2.1 – (a) Location of the East African Rift System. Black box denotes study region in the northern and the northern sector of the central Kenya Rift. White stars denote location of sampling traverses. Grey lines denote political boundaries. (b) Digital elevation model including an overview of southern Ethiopia, the northern Kenya Rift, and northernmost sectors of the central Kenya Rift.

shoulders and steep rift flanks of basins in northern Kenya (Figures 2.1 and 2.2). Following thermal modeling of our data using the HeFTy (Ketcham, 2005; Ketcham et al., 2009) and QTQt software programs (Gallagher et al., 2009; Gallagher, 2012), we use the cooling histories to help elucidate the Cenozoic tectono-thermal evolution of the Kenya Rift shoulders and its implications for the overall structural evolution of the EARS.

2.2 Geological setting and tectonic history

In Kenya, the EARS is characterized by asymmetric rift basins, central volcanoes, and high rift shoulders (up to ~2000m above sea level (asl) in western Kenya) bounded by escarpments where late Proterozoic crystalline basement rocks are exposed (Maboko et al., 1985; Smith, 1994; Smith and Mosley, 1993; Shackleton, 1993). Our study area comprises the eastern shoulders of the northern Kenya Rift and the transition between the northern and central Kenya rifts along the western rift margin (Figure 2.1).

Geophysical data, stratigraphic information, and dated volcanic lava flows have furnished information on the early rifting history in northern Kenya, which began during the late Meso-

zoic (Foster and Gleadow, 1992, 1996; Morley et al., 1992; Wagner et al., 1992; Ebinger et al., 2000; Tiercelin et al., 2004, 2012). These early episodes of extension affected areas between the Indian Ocean and the Lake Turkana region, leading to the accumulation of thick lacustrine, fluvial, and eolian strata in the NW-SE oriented Cretaceous Anza Rift (Figure 2.1). In its central part, the buried Anza Rift was active during the late Cretaceous, whereas it continued to be active into the late Tertiary in the northern Lamu Embayment (Figure 2.1), in the vicinity of the present-day coast of the Indian Ocean (Bosworth and Morley, 1994). Farther west, the Anza Rift is inferred to transition into the eastern sectors of the Cretaceous Central African Rift Zone (Schull, 1988).

Subsequent Cenozoic extension in northern Kenya is recorded in the Turkana-Lokichar rift zone (Figure 2.1b) but was preceded by volcanism at about 35 Ma, followed by Oligocene normal faulting and the formation of several halfgraben basins (Morley et al., 1992). These basins span the region between the Ugandan border and Lake Turkana (Figure 2.1), and they host sedimentary fills 5 to 8 km thick that include intercalated volcanic rocks (Morley et al., 1992; Tiercelin et al., 2012). However, apatite (U-Th)/He and fission track data from the western rift flank (Cherangani Hills of northern Kenya) and from the present-day eastern rift flank southeast of Lake Turkana (Figures 2.1 and 2.2) only reveal clear episodes of cooling during the late Cretaceous to Paleocene and during the late Neogene (Foster and Gleadow, 1996; Spiegel et al., 2007).

Today, the northern Kenya Rift encompasses the wide, early Cenozoic Turkana-Lokichar rift zone, but the Miocene to Recent manifestations of rifting are primarily located in the eastern sector of this extensional province, between approximately 1°N and 4.5°N latitude. This region is characterized by the active, down-to-theeast halfgraben basin of the NNE-oriented Suguta Valley (Bosworth and Maurin, 1993; Saneyoshi et al., 2006; Melnick et al., 2012) and the northern sector of the NNE-oriented Elgeyo Escarpment farther west (Figure 2.1b). The rift floor in the Suguta Valley is at ~300masl, whereas the antithetically faulted monocline on the eastern rift margin has an average elevation of ~1400m asl (Bosworth and Maurin, 1993). There, the rift shoulder exposes gneissic Precambrian basement in the Samburu Hills, our first study site, which locally reach up to 1900m asl (Figures 2.1 and 2.2). To the north of the Suguta Valley is the active Kino Sogo rift zone; this extensional sector transitions northward into the Chew Bahir Rift of southern Ethiopia, which is an integral part of the Main Ethiopian Rift (Figure 2.1).

The Elgeyo Escarpment, our second study site, is located along the western margin of the northern Kenya Rift and the northernmost sector of the NNW oriented central Kenya Rift, where the escarpment transitions southward into the Mau Escarpment (Figure 2.1b). The Elgeyo Escarpment is one of the most prominent fault-line escarpments of the Kenya Rift. In its southern sector, the escarpment is ~900m higher than the adjacent Kerio sedimentary basin (Figure 2.2). The Elgeyo Escarpment is related to a down-to-the-east normal fault, which ex-

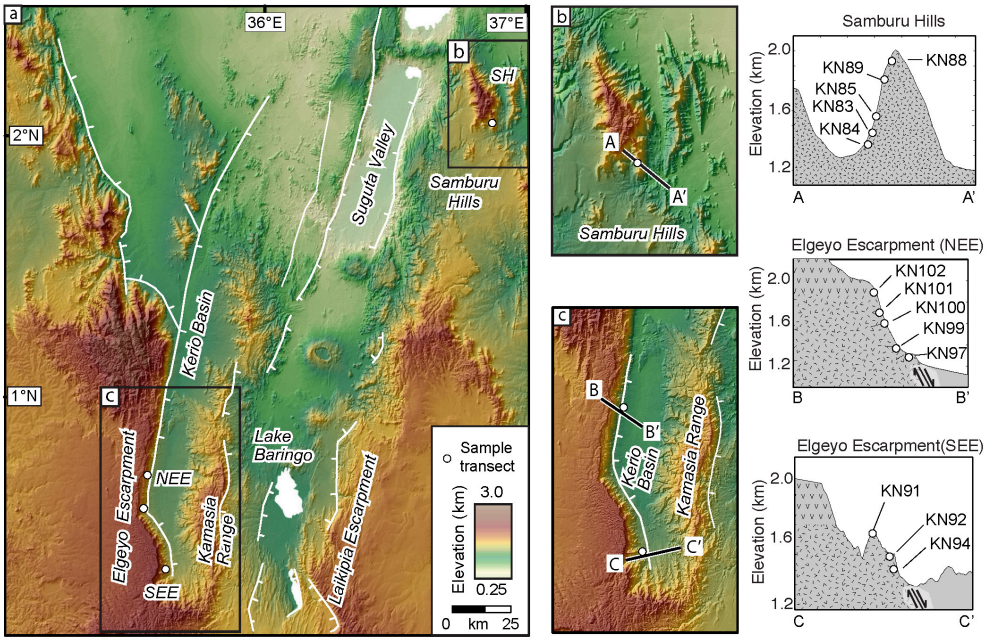

Figure 2.2 – Figure 2. Digital elevation model of the study area and location and elevation of thermochronology sampling transects. Circles denote each thermochronologic sample analyzed with sample names as labels. (a) Study area, including Samburu Hills (SH), Northern Elgeyo Escarpment (NEE) and Southern Elgeyo Escarpment SEE). (b)Samburu Hills region. (c) Elgeyo Escarpment. Profiles on right show schematic elevation transects and simplified geology along the SH, NEE, and SEE sampling transects.

poses steeply eastward dipping Proterozoic gneisses of the pan-African orogeny (Chapman et al., 1978; Maboko et al., 1985; Hetzel and Strecker, 1994). The Cenozoic faults along the Elgeyo Escarpment follow the gneissic foliation and change in strike, where the foliation is cut by NW striking Proterozoic dextral shear zones (Strecker et al., 1990; Shackleton, 1993). These reactivated shear zones influence the geometry and areal distribution of strata of the Kerio sedimentary basin (Mugisha et al., 1997). The basement shear zones are overlain by arkosic sandstones, conglomerates, and lacustrine shales of unknown age, and up to 150m thick, 14 Myr old phonolites (Lippard, 1973; Ego, 1994; Supplementary Figure A1) that also cap the western rift shoulder. Faulting along the Elgeyo Escarpment in this sector postdates the emplacement of the middle Miocene phonolite flows and generated the westward tilted Kamasia fault block to the east (Figure 2.2), which in turn is delimited by a major down-to-the-east normal fault to the east (e.g., Chapman et al., 1978). The Kamasia Range thus forms the barrier between the Kerio Basin and the Baringo Basin farther east, which now hosts the active volcano-tectonic axis of this part of the Kenya Rift.

2.3 Methodology

We constrain the Cenozoic cooling of the Precambrian Mozambique Belt gneisses exposed on the western and eastern rift shoulders of the northern Kenya Rift and the northernmost sector of the central Kenya Rift using apatite fission track thermochronology (AFT; apatite partial annealing zone, PAZ, ~60 to ~120°), apatite (U-Th-Sm)/He thermochronology (AHe, partial retention zone, APRZ ~40°C-85°C), and zircon (U-Th)/He thermochronology (ZHe; ZPRZ ~120 to ~200°C) (assuming that zircons remained in this temperature range for about 90 Myr (e.g., Reiners and Brandon, 2006; Wolf et al., 1998; Ketcham et al., 1999; Reiners, 2005)). We collected seven samples (KN83 through KN89) along a W-E oriented profile between 1300 and 1900m asl in the Samburu Hills (SH), on the eastern rift flank (Figure 2.3, Tables 2.1 and 2.2, and Table A1 in the supporting information). On the western flank, we collected one steep profile across the northern Elgeyo Escarpment (NEE) and one across the southern Elgeyo Escarpment (SEE) (Figure 2.2). The NEE profile comprises six samples (KN97 through KN102) collected between 1280 and 1850 m asl, and the SEE profile comprises five samples (KN53, KN55, KN91, KN92, and KN94) collected between 1350 and 1780 m asl. The Elgeyo escarpment profiles are separated by ~50 km and were collected perpendicular to the main fault-line escarpment (Figure 2.2). In addition, sample KN50 was collected between the two profiles and analyzed for AFT, although it was not used to help constrain the thermal modeling.

Mineral separation and sample preparation for AFT, AHe, and ZHe analyses followed standard procedures (e.g., Dobson, 2006) and are briefly described below. Eighteen samples yielded enough apatite for AFT and AHe analysis, and six samples were analyzed with the ZHe method.

2.3.1 Apatite Fission Track Analysis

AFT samples were analyzed with a Leica DMRM microscope at the University of Potsdam. Approximately 20 good-quality grains per sample were randomly selected and dated using the external detector method and the zeta calibration technique (Hurford and Green, 1983) (see Table 2.1). The pooled age is reported ($\pm 1\sigma$) when samples pass the chi-square test (P(χ^2) $\geq$5%) (Galbraith, 1981); for KN50, the central age is reported because the sample failed this test. We also report confined track-length distributions of seven AFT samples (see details in Table 2.1). ^{252}Cf irradiations were performed (see supporting information) to obtain a larger number of horizontally confined tracks for track-length measurements (e.g., Donelick et al., 2005). The angle between the confined tracks and the crystallographic c axes was routinely measured. The size of the etch-pit diameter parallel to the c axis (Dpar) was also determined, as it is a kinetic parameter used in thermal history modeling (Donelick et al., 1999; Ketcham et al., 1999) At least four Dpar values were measured per crystal; the data were corrected following Sobel and Seward (2010).

2.3.2 Apatite (U-Th-Sm)/He Analysis

The AHe method is based on the accumulation of alpha particles produced by U, Th, and Sm series decay (Ehlers and Farley, 2003). Ages are corrected for alpha ejection near the margins of the crystal assuming a homogenous distribution of U, Th, and Sm (Farley et al., 1996; Ehlers and Farley, 2003). Samples were analyzed at the Scottish Universities Environmental Research Center (SUERC) following the procedure described by Foeken et al. (2006). We analyzed between 1 and 3 apatite crystals of similar radius per sample (Table S1). Corrections for He recoil loss were made following the procedures of Farley and Stockli (2002). The correction factor (Ft) was calculated based on the retention and stopping distance of the alpha particle in the crystal and the size of each grain analyzed. The reproducibility of the 3He spike was determined from three daily measurements against an accurately known ^{4}He standard. Standard ^{4}He abundance measurements have within-run precision of better than 0.1% (1σ) and between-run precision of 0.2% (1σ) (Persano et al., 2002).

U, Th, and Sm analyses were performed on a VG plasma Quad PQ2 + inductively coupled plasma-mass spectrometry. After ^{4}He analysis, each crystal was dissolved and spiked with ~0.45 ng ^{230}Th and 0.20 ng ^{235}U with approximately 2mL of HNO3. Total analytical uncertainty on all ages was approximately 1-3% (1σ), which is dominated by the uncertainty in the U and Th spike concentrations (e.g., Dobson, 2006; Foeken et al., 2006), He determinations, blank corrections, and uncertainties on grain-size measurements for α-correction.

2.3.3 Zircon (U-Th)/He Analysis

The (U-Th)/He analysis of zircons is also based on the accumulation and diffusion of alpha particles produced by the decay of U and Th. After mineral-separation at the University of Potsdam, we used the facilities at SUERC following analytical procedures described by Foeken et al. (2006) and Dobson (2006). Seven samples with one to three single-crystal aliquots each were analyzed. With respect to the Ft correction, we followed procedures described in Farley and Stockli (2002), and we again assumed a uniform distribution of U and Th. Total analytical uncertainty is dominated by the uncertainty in the U and Th spike concentrations (Dobson, 2006; Foeken et al., 2006), He determinations, and blank corrections.

2.3.4 Age-Elevation Relationships and Thermal History Modeling

The relationship between thermochronologic ages and elevations of different samples along an elevation profile are commonly used to determine rates and amounts of exhumation (e.g., Dobson et al., 2009; Foeken et al., 2006). However, the thermal structure of the uppermost crust could be influenced by topography, erosion, faulting, and advection (e.g., Ehlers and Farley, 2003; Gallagher et al., 2005), which complicate direct interpretations of the slope of age-elevation plots (e.g., Valla et al., 2010; van der Beek et al., 2010).

To determine the Cenozoic cooling history recorded by samples within our age-elevation profiles, we used two different thermal modeling approaches. We performed forward and inverse Monte Carlo modeling of time-temperature paths combining AFT and ZHe data using the HeFTy 1.8.2 software (Ketcham, 2005) for individual samples, and we used the QTQt software (Gallagher et al., 2009; Gallagher, 2012) to derive integrated cooling constraints from multiple samples within an age-elevation transect. AHe data were not used for modeling due to the high dispersion of single-grain ages, as discussed in the results' section.

The HeFTy program is effective for assessing the thermal history of a single sample. The output reflects the goodness of fit of the models, which allows for testing different cooling histories. However, the program has not yet been adapted for modeling multiple samples within an elevation profile. In contrast, the QTQt program is well suited for the latter task. Therefore, we use the HeFTy results to determine approximate constraints that can be applied during QTQt modeling of the complete profile.

To resolve the Cenozoic thermal history of the rocks along each profile, we tested two contrasting thermal history scenarios: monotonic cooling versus Neogene reheating and cooling. We used the HeFTy and QTQt programs to predict time-temperature paths for these two scenarios that are consistent with our AFT age and track-length distribution data and our ZHe ages. Additionally, we used geological constraints, such as the initiation of volcanism north of the study area (Morley et al., 1992; Ebinger and Sleep, 1998), to provide some brackets on possible cooling paths.

2.4 Results

2.4.1 Apatite Fission Track Dating Results

The apatite fission track cooling ages are shown in Table 1. Over the 400m elevation range of the Samburu profile (SH), samples KN89, KN85, and KN83 yielded ages ranging from 39.4 $\pm$ 3.0 Ma to 50.3 $\pm$ 8.0 Ma. Although the elevation difference is small, this section provides the best relief and outcrop conditions in the area. Mean track lengths from samples KN83 and KN85 are 12.2 and 11.9 μm, respectively; sample KN89 did not yield a meaningful number of track lengths (n = 2; Table 1). Samples from the northern Elgeyo transect (NEE, four samples) yielded ages ranging from 26.2 $\pm$ 3.0 Ma to 38.8 $\pm$ 3.0 Ma, with mean track lengths of 11.2 to 11.8 μm that were measured from three out of the four samples (KN99, KN100, and KN102). The southern Elgeyo transect comprises six samples with an age range between 4.6 $\pm$ 1.0 Ma and 9.2 $\pm$ 2.0 Ma. No confined track lengths were found in those samples. In comparison to the AFT ages of the NEE and SH profiles, the young AFT ages of this transect together with the lack of a clear increase in age with elevation may be related to reheating as a result of nearby fluorite mineralization associated with the emplacement of Miocene lava flows. The fluorite mineralization shows ENE to east trending growth fibers in the plane of the steeply

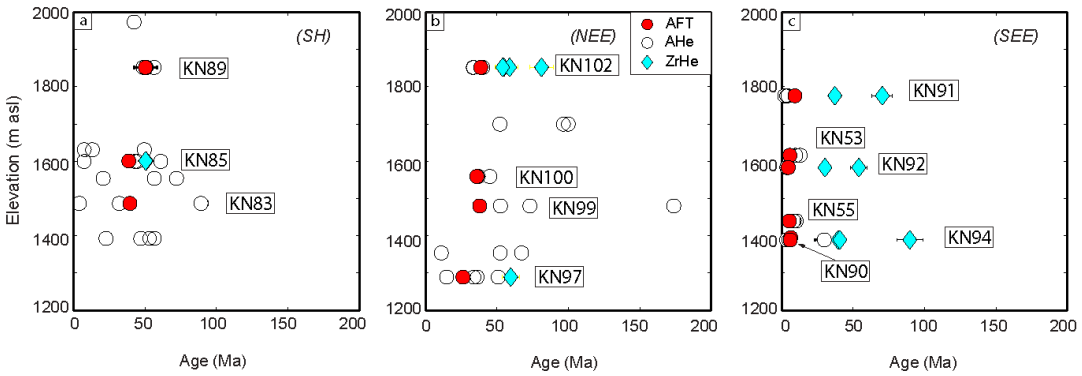

Figure 2.3 – Age-elevation plots of the thermochronologic data. White circles denote AHe ages (not interpreted in the thermal modeling). Red circles represent AFT ages and blue diamonds denote ZHe ages; (a) Samburu Hills (SH), (b) Northern Elgeyo Escarpment (NEE), (c) Southern Elgeyo Escarpment (SEE).

east dipping foliation (Aljabri, 1992; Hetzel and Strecker, 1994; Ogola et al., 1994). As fluorite mineralization involves temperatures between 120 and 260°C (e.g., Richardson and Holland, 1979), AFT ages were likely at least partially reset, and therefore, we do not use those data to model the tectono-thermal history in this part of the study area.

2.4.2 Apatite (U-Th-Sm)/He Results

We report 54 single-grain AHe ages from 15 samples (Table A1). In most samples, several single-grain AHe ages are older than the AFT age from the same sample, and only a few aliquots yield younger AHe ages (Table S1 and Figure 2.3). With respect to calibration and operation of the analytical machines, Ft corrections on potential nonideal geometries, and grain-size measurement uncertainties, none can explain independently the dispersion of the data. Below we consider other possibilities.

Because prominent zonation in U and Th can also affect AHe ages, we examined the distribution of induced tracks in the micas of AFT samples that were also analyzed with the AHe method to assess the variability of the U distribution within single grains. Many of the samples contained numerous grains with pronounced U zoning, often with U-rich rims, although U-rich cores relative to the rims are required to explain ages that appear too old. Two samples (KN53 and KN55) were also characterized by very high crystal-dislocation densities. During AFT analysis, such crystals were not analyzed. However, these characteristics can help explain the high age dispersion within the AHe data.

Particularly, in the case of slowly cooled apatites, differing amounts of radiation damage reflected by variable effective uranium ("eU") have been invoked to explain widely dispersed AHe ages (e.g., Flowers, 2009) or AHe ages that are older than AFT ages (e.g., Green et al.,

Table 2.1 – Apatite Fission Track (AFT) Data from the Kenya Rift

Apatite Fission Track (AFT) data from the Kenya Rift [a]

Sample	Latitude (°N)	Longitude (°E)	elev m asl	Lithology	Xl	Rho-S x10^6	NS	Rho-I x10^5	NI	P(χ^2) %	RhoD x10^6	ND	Age[b] Ma	±1σ Ma	Dpar mean	Dpar SD	n lengths	Mean length µm	SD µm	Analyst
Central Elgeyo Escarpment																				
KN50	35.540	0.560	1260	gneiss	20	1.497	279	2.873	1454	3	1.222	4978	43.2	3	2.3	0.2	0	-	-	AB
Southern Elgeyo Escarpment																				
KN53	35.600	0.310	1616	gneiss	20	2.173	68	0.566	2612	82	1.185	4978	5.7	1	2.3	0.2	5	13.2	3.6	AB
KN55	35.620	0.310	1440	gneiss	20	4.108	99	1.057	3849	100	1.136	4978	5.4	1	2.3	0.2	0	-	-	AB
KN90	35.628	0.360	1395	gneiss	18	1.583	32	0.393	1289	100	1.365	5713	6.3	1	1.9	0.2	0	-	-	AB
KN91	35.599	0.305	1776	gneiss	20	0.965	40	0.356	1086	100	1.359	5713	9.2	2	2.0	0.2	0	-	-	AB
KN92	35.611	0.302	1583	gneiss	23	1.880	44	0.346	2392	97	1.353	5713	4.6	1	1.9	0.2	0	-	-	AB
KN94	35.631	0.312	1389	gneiss	20	1.497	279	2.873	1454	100	1.347	5713	6.0	1	2.2	0.3	0	-	-	AB
Northern Elgeyo Escarpment																				
KN97[c]	35.552	0.660	1289	gneiss	20	1.340	95	1.326	960	66	1.438	5713	26.2	3	2.1	0.2	0	-	-	AB, VT
KN99	35.548	0.661	1480	gneiss	17	2.281	45	0.555	1850	89	1.426	5713	38	2	2.2	0.1	65	11.2	2.1	AB, VT
KN100	35.545	0.661	1559	gneiss	16	3.107	269	4.271	1957	99	1.420	5713	36	3	2.2	0.2	56	11.8	1.87	AB
KN102[c]	35.539	0.660	1852	gneiss	20	1.404	193	2.102	1289	10	1.407	5713	38.8	3	2.1	0.2	101	11.2	2.0	AB, VT
Samburu Hills																				
KN83	36.868	2.033	1487	gneiss	20	2.087	327	3.228	2114	30	1.401	5713	39.4	3	2.1	0.3	40	12.2	1.9	AB, VT
KN85[c]	36.870	2.033	1601	gneiss	20	1.836	195	1.836	1289	100	1.389	5713	38.7	3	2.2	0.2	100	11.9	1.9	AB, VT
KN89	36.879	2.036	1852	gneiss	11	0.574	56	1.144	281	100	1.371	5713	50.3	8	1.7	0.3	2	12.4	0.2	AB

[a] Sample preparation and analysis similar to that used by Sobel & Strecker (2003). All apatites were etched in 5.5 mol Nitric acid for 20 seconds at 21°. Samples analized with a Leica DMRM microscope with drawing tube located above a digitalizing tablet and a kinetek computer-controlled stage driven by the Ftstage program (Dumitru, 1993). Analysis was performed with reflected and transmited light at 1250x magnification. Samples were irradiated at Oregon State University. Following irradiation, the mica external detectors were etched with 21°C, 40%hydroflouric acid for 45 minutes. The pooled age is reported for samples with P(χ2) grater than (less than) 5% as they pass (fail) the χ2 test. Age errors are presented as one sigma, calculated using the zeta calibration method (Hurford and Green, 1983), AB:369.5±7.9, unpublished, 2012.

[b] Pooled age is reported for most of the samples, except for sample KN50, central age is reported

[c] ^{252}Cf irradiations on additional grain mount of the sample

2006; Hansen and Reiners, 2006; Gautheron et al., 2009). Higher eU in apatite leads to more radiation damage, higher He retentivity, and hence a higher effective closure temperature and a greater accumulation of He for a given cooling history (Flowers et al., 2007). Alternatively, variations in the effective diffusion domain size could influence the closure temperature of the crystal (Gautheron et al., 2009). To explore these possibilities, we plotted AHe age versus eU and versus grain size. However, the ages do not show a clear correlation with either parameter (Figure A2 in the supporting information).

Radiation damage and variable eU problems are commonly discussed in cases with AHe ages that are much older (>100 Ma) (e.g., Flowers, 2009) than those in this study. However, prolonged residence time at a low temperature (i.e., ~80-100°C) prior to late burial heating has been shown to exert a strong influence on ^{4}He retentivity and hence on the effective closure temperature (Fox and Shuster, 2014). In our study, the basement rocks are ~500 Myr old and are related to the Panafrican orogeny (Maboko et al., 1985; Smith, 1994). Between these early tectonic processes and the initiation of Cenozoic rifting (e.g. Foster and Gleadow, 1996; Spiegel et al., 2007), the samples remained at a relatively constant position below the surface (~3 km). This thermal history is quite analogous to the Grand Canyon (Fox and Shuster, 2014), suggesting that AHe results from there are applicable to our study. The extremely long residence time of samples at depths of a few kilometer led to a variable and large amount of accumulated radiation damage, which caused higher ^{4}He retentivity and hence anomalously old AHe ages. Such a scenario provides a better explanation for the old ages in our study than variations in grain size, eU, zonation, or analytical problems.

2.4.3 Zircon (U-Th)/He Results

We analyzed a subset of samples from each of our three elevation profiles for ZHe. From the Samburu Hills profile, we analyzed samples KN85 and KN83. Two aliquots from sample KN85 provide a ZHe mean age of 50.6 $\pm$ 5.2 Ma. From sample KN83, the anomalously young age (1.5 Ma) is paired with very low He and high U and Th concentrations. Induced tracks in the external detector from occasional zircons included in the AFT grain mount of the same sample show that many of these zircons are strongly zoned and have U-rich rims. Therefore, data from this sample was not plotted in the age-elevation plot and not used for thermal modeling (Figure 2.3a). From the Northern Elgeyo Escarpment profile, samples KN97 and KN102 yielded ZHe ages of 59.7 $\pm$ 6.1 Ma (single aliquot) and mean age of 55.9 $\pm$ 5.6 Ma (three aliquots), respectively. A fourth aliquot of sample KN102 was discarded due to the low reproducibility of the age (Table 2.2). From the Southern Elgeyo Escarpment profile, samples KN91, KN92, and KN94 (Figure 2.3c) have mean ages of 53.9 $\pm$ 5.5 Ma (two aliquots), 42.2 $\pm$ 4.3 Ma (two aliquots), and 56.7 $\pm$ 5.8 Ma (three aliquots), respectively.

Table 2.2 – (U-Th)/He Ages of Zircon (ZHe) in The Kenya Rift

(U-Th)/He Ages of Zircon (ZHe) in The Kenya Rift.

Sample	Latitude (°N)	Longitude (°E)	Elev m asl	U (ng)	Th (ng)	4He (cc)	Ft	Corrected age Ma	error (1σ) Ma	mineral
					Southern Elgeyo					
KN91	35.599	0.305	1776	6.7	91.9	6.87E-07	0.85	70.5	7.2	Zircon
KN91	35.599	0.305	1776	7.0	88.5	3.48E-07	0.85	37.3	3.8	Zircon
KN92	35.611	0.302	1583	14.0	34.2	1.07E-07	0.78	30.4	3.1	Zircon
KN92	35.611	0.302	1583	5.1	18.7	9.63E-08	0.74	54.0	5.5	Zircon
KN94	35.631	0.312	1389	9.5	41.7	1.74E-07	0.82	39.6	4.1	Zircon
KN94	35.631	0.312	1389	6.0	23.9	2.29E-07	0.82	89.8	9.2	Zircon
KN94	35.631	0.312	1389	9.1	42.3	1.74E-07	0.79	40.8	4.2	Zircon
					Northern Elgeyo					
KN97	35.552	0.660	1289	3.6	7.5	5.03E-08	0.83	59.7	6.1	Zircon
KN102	35.539	0.660	1852	15.9	28.6	1.83E-07	0.84	54.9	5.6	Zircon
KN102	35.539	0.660	1852	0.3	0.9	5.79E-09	0.82	58.9	6.1	Zircon
KN102	35.539	0.660	1852	8.6	18.5	1.64E-07	0.81	81.3	8.3	Zircon
KN102	35.539	0.660	1852	13.7	32.7	1.94E-07	0.82	54.1	5.5	Zircon
					Samburu Hills					
KN85	36.870	2.033	1601	1.7	1.5	9.06E-09	0.78	50.8	5.2	Zircon
KN85	36.870	2.033	1601	1.3	1.0	6.54E-09	0.81	50.5	5.2	Zircon

2.4.4 Thermal History Modeling of Elevation Transects

We performed thermal modeling on the NEE and SH transects. Thermal models that incorporated the AHe data were incompatible with the AFT data. Because of the large AHe age dispersion, low reproducibility of ages, and strongly likelihood of variable ^{4}He retentivity (as discussed previously), we decided to base the thermal modeling and our interpretations on only the AFT and ZHe data. (see Table A1 and Figure A2).

Our general approach was to first model an individual sample from an elevation profile (sample KN85 from profile SH, elevation 1600 m, and sample KN102 from profile NEE, elevation 1852 m; Figure 2.3) using the HeFTy program. The HeFTy modeling results were used as the basis for defining a common thermal history of the samples (e.g., Prenzel et al., 2013) along the vertical profile. Next, we used QTQt to model the three samples from the SH profile simultaneously and the four samples from the NEE profile simultaneously. Monotonic cooling and reheating paths were tested with both programs. Constraint boxes were first defined to observe preferential cooling paths of the analyzed samples. In subsequent runs, the constraint boxes were shifted to examine the reliability of inflection points representing changes in modeled cooling rates and to allow for reheating.

Input parameters for modeling included AFT data (age, c axis nonprojected track lengths, and Dpar values), the ZHe data, and present-day surface temperatures. Acceptable-fit paths (goodness of fit >0.05) from the HeFTy models of individual samples were considered for interpretation.

2.4.5 Thermal Modeling of Data From the Samburu Hills

For our thermal modeling of the Samburu Hills (SH) data, we first ran models with monotonic cooling paths using both the HeFTy and QTQt programs (Figures 2.4a and 2.4b). We defined a first constraint box with a temperature range from 135 to 15°C for HeFTy (Figure 2.4a) and for QTQt (Figure 2.4b) over a time range from 15 Ma to the present. Second constraint boxes were defined between ~130 and 30°C at ~30 to 20 Ma. Third constraint boxes were defined between 230 and 160°C at ~75 to 45 Ma to be compatible with the AFT and ZHe cooling ages. HeFTy models always end with a temperature constraint at the present day ranging from 25 to 15°C. The QTQt models end at present-day temperatures from 0° to 50°C.

A second set of models was run to test if the thermochronologic ages are compatible with either a reheating event during the Paleogene, the onset of volcanism in the late Eocene-early Oligocene, or early exhumation. The track-length distribution of sample KN85 (Figure 2.4a) suggests that reheating could be possible. Geologically, reheating could be associated with volcanism prior to or during the early stages of rifting. To allow for this possibility, we reduced the temperature limits of the second boxes to 100°C and 10°C, thus permitting paths to reach lower temperatures at an earlier phase in the cooling history and extending the duration of

this interval to between 40 and 20 Ma (Figure 2.4c). Other constraints were similar to the first run.

Well-fitting HeFTy models for monotonic cooling of sample KN85 (Figure 2.4a) suggest that a first episode of relatively rapid cooling (12°C/Myr) occurred from ~60 to 50Ma. Subsequently, very slow cooling (~1.5°C/Myr) took place from~45Ma to ~15Ma, followed by cooling to the present. As themodel results are not well constrained over this final timeframe, we refrain from interpreting this cooling trend further. Because the model results rely on the calculating paths through the lowest temperature part of the PAZ and below the PAZ, where not much control on the thermal history exists, it is not known if cooling may have accelerated or not.

Using QTQt, we obtained results for the entire profile (Figure 2.4b) that are broadly similar to the HeFTy results obtained for sample KN85 (Figure 2.4a). Rapid cooling from about 65 to 50Ma (~10 °C/Myr) is followed by slow reheating (<1°C/Myr) from ~40 to ~20Ma. The model reveals a slight acceleration of cooling (~3°C/Myr) at ~15Ma as part of a final continuous cooling episode, which has lasted to the present. Acceptable fits also permit an isothermal path without reheating from as early as ~50Ma to as late as ~20Ma. Despite some potential reheating of the uppermost samples within the transect between 40 and 20Ma, the thermal histories for the different samples in the SH appear to have experienced similar t-T paths and are consistent with previous studies in the region (e.g., Foster and Gleadow, 1992, 1996). Acceptable fits for the reheating model using HeFTy (Figure 2.4c) follow a broader swath than for the monotonic cooling model (Figure 2.4a). The best fitting path shows that reheating is plausible. This scenario (Figure 2.4c) shows rapid cooling (~10°C/Ma) from 55 to 40Ma. Cooling was followed by an ~20Ma interval at a near-constant temperature. A short-lived earlyMiocene pulse of reheating to temperatures as high as 100°C could have occurred, although a broad range of other paths that do not include reheating lie within the acceptable-fit envelope. Final cooling occurred from ~15Ma to the present.

The QTQt reheating model results for the entire profile in the reheating scenario (Figure 2.4d) show similar changes in the cooling rates. A first rapid cooling from ~65 to 50 Ma, reheating from ~50 to 35 Ma of ~2 °C/Myr (particularly for the uppermost samples in the profile), then slow cooling from 35 to ~15 Ma, and final cooling from ~15 Ma until the present (Figure 2.4d). These results are quite similar to the previous QTQt modeling scenario (Figure 2.4b).

From these two sets of models (monotonic cooling and reheating) and the general geologic context of the region, we conclude that reheating is permissible, but not required by the thermochronologic data. The differences between the two models suggest that the magnitude and timing of such a reheating event can only be loosely constrained (Figures 2.4c and 2.4d).

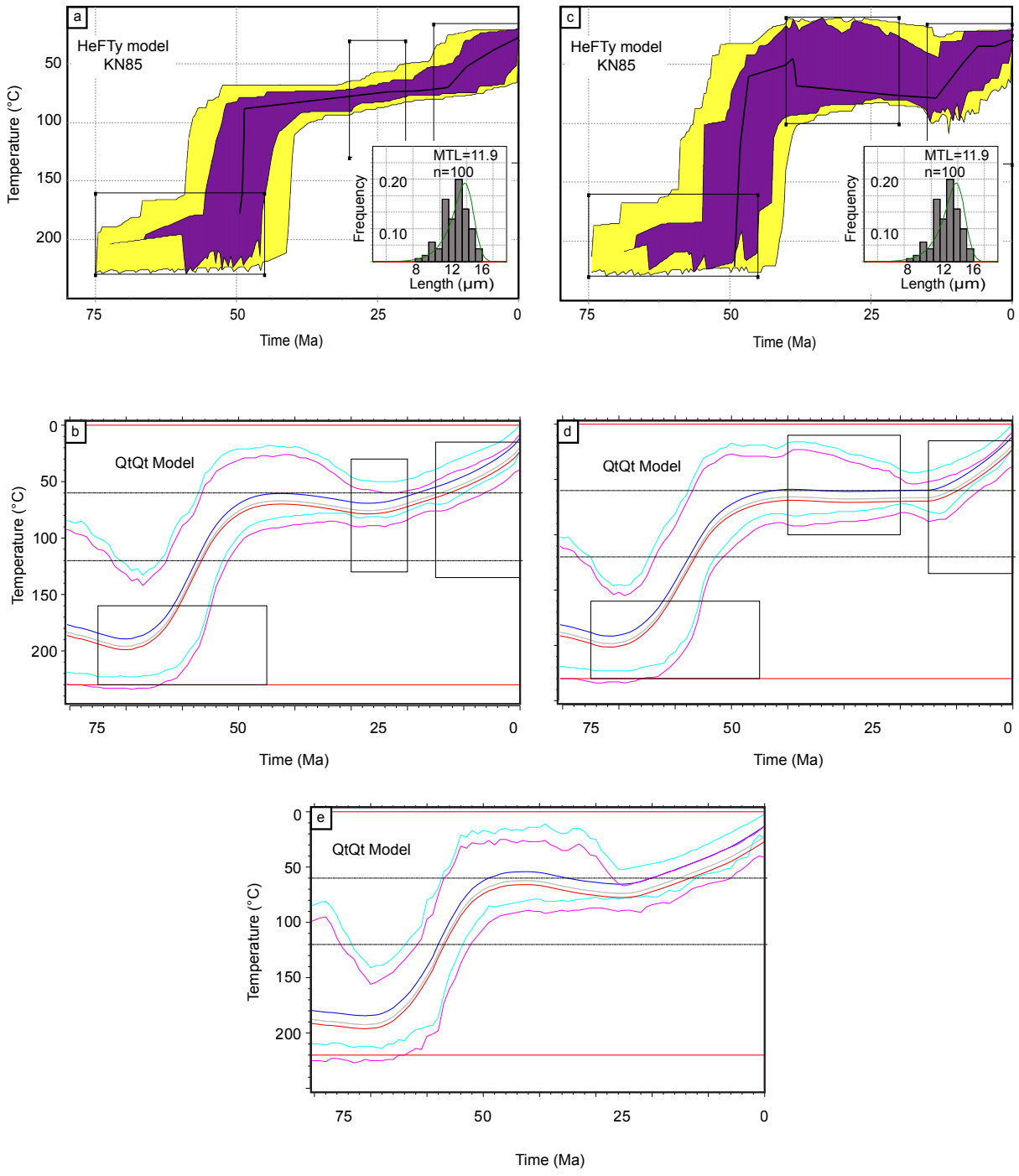

Figure 2.4 – TThermal modeling results for the Samburu Hills (SH) samples. (a and c) Time temperature model for sample KN85 from the Samburu Hills (SH) using HeFTy software (Ketcham, 2005) with acceptable (yellow) and good (purple) time-temperature pathway envelopes and best fit shown with black line. The modeling scheme in Figure 4a only permits monotonic cooling while Figure 4c permits reheating between 40 and 20 Ma. (b and d) Time- temperature histories derived from QTQt modeling, with time-temperature constraints in B similar to those in A and with constraints in D similar to those in Figure 4c. (e) Time-temperature history paths derived from QTQt with no constraint boxes; red box defines the limits of the modeling, 0°C-220°C and 0-80 Ma. Blue and red lines correspond to the uppermost and lowermost sample; cyan and magenta lines correspond to 95% confidence intervals for uppermost and lowermost samples, respectively.

2.4.6 Thermal Modeling of Data From the Northern Elgeyo Escarpment

Thermal models were run for the Northern Elgeyo Escarpment (NEE) profile in a similar manner as described above for the Samburu Hills profile. For the HeFTy (Figure 2.5a) and QTQt (Figure 2.5b) monotonic cooling models of sample KN102, the first constraint boxes were set to 160 to 10°C at 15 Ma to the present day. Second constraint boxes were set to ~150 to 30°C at 40 to 20 Ma for HeFTy and for QTQ, based on the AFT ages, sedimentary evidence in the hanging wall, and volcanic flows on top of the footwall. Third constraint boxes were set to 220 to 160°C at 75 to 40 Ma, based on an early to middle Tertiary regional extension with minor strain, which is also associated with the latest stages of extension of the Anza Rift in the north (Foster and Gleadow, 1996). Again, HeFTy models always end with a constraint at the present-day surface temperature, ranging from 25 to 15°C, and QTQt models terminate at present-day temperatures ranging from 0° to 50°C.

The second reheating model used similar constraints as the monotonic model, but with slight changes in the time-temperature limits of the boxes. The second constraint box shows the most pronounced change, extending the range of temperatures from 120 to 10°C over a time range from 49 to 20 Ma in the HeFTy and QTQt models (Figures 2.5b and 2.5d). This additional constraint permits reheating (by allowing for cooling to lower temperatures at an earlier period), which could be due to basaltic volcanism in the region starting in the northwest sector of Lake Turkana at ~37 Ma (i.e., Zanettin et al., 1983; McDougall and Brown, 2009) and farther south during the early Miocene (Samburu Basalts, ~20-11 Ma) (Hackman et al., 1990) (Figure S1).

HeFTy results for the monotonic cooling model for sample KN102 (Figure 2.5a) display similar cooling paths as modeled for sample KN85 in the Samburu Hills (Figure 2.4a). Rapid cooling (>20°C/Ma) from ~55 to 50 Ma is followed by very slow cooling (1.5°C/Myr) from 45 to 10 Ma, and finally moderate cooling of >2.0°C/Myr until the present (Figure 2.5a). QTQt results from the entire profile at the Elgeyo Escarpment are broadly consistent with the HeFTy results, also showing rapid (>20°C/Myr) cooling from ~60 to 55 Ma. But rather than very slow cooling from ~50 to 15 Ma, the results show reheating (Figure 2.5b). This reheating is followed by final cooling (~3°C/Ma) from 15 Ma to the present.

The HeFTy thermal model involving reheating (Figure 2.5c) shows many similarities to the HeFTy model of monotonic cooling (Figure 2.5a). The best fit of the reheating model exhibits relatively fast cooling rates (~15°C/Ma) from ~60 to 50 Ma and moderately fast cooling from ~50 to 30 Ma. Slight reheating follows from ~30 to 10 Ma; this reheating is followed by rapid cooling to the surface until the present. As observed for sample KN85 from the Samburu Hills (Figures 2.4a and 2.4c), the broad envelope of the acceptable cooling paths shows that this model is not as tightly constrained as the monotonic cooling scenario (Figure 2.5a). The second QTQt model has constraint boxes that were set between 160 to 10°C at 15 to 0 Ma, 120 to 10°C at 40 to 20 Ma, and 220 to 160°C at 75 to 45 Ma. The results show reheating

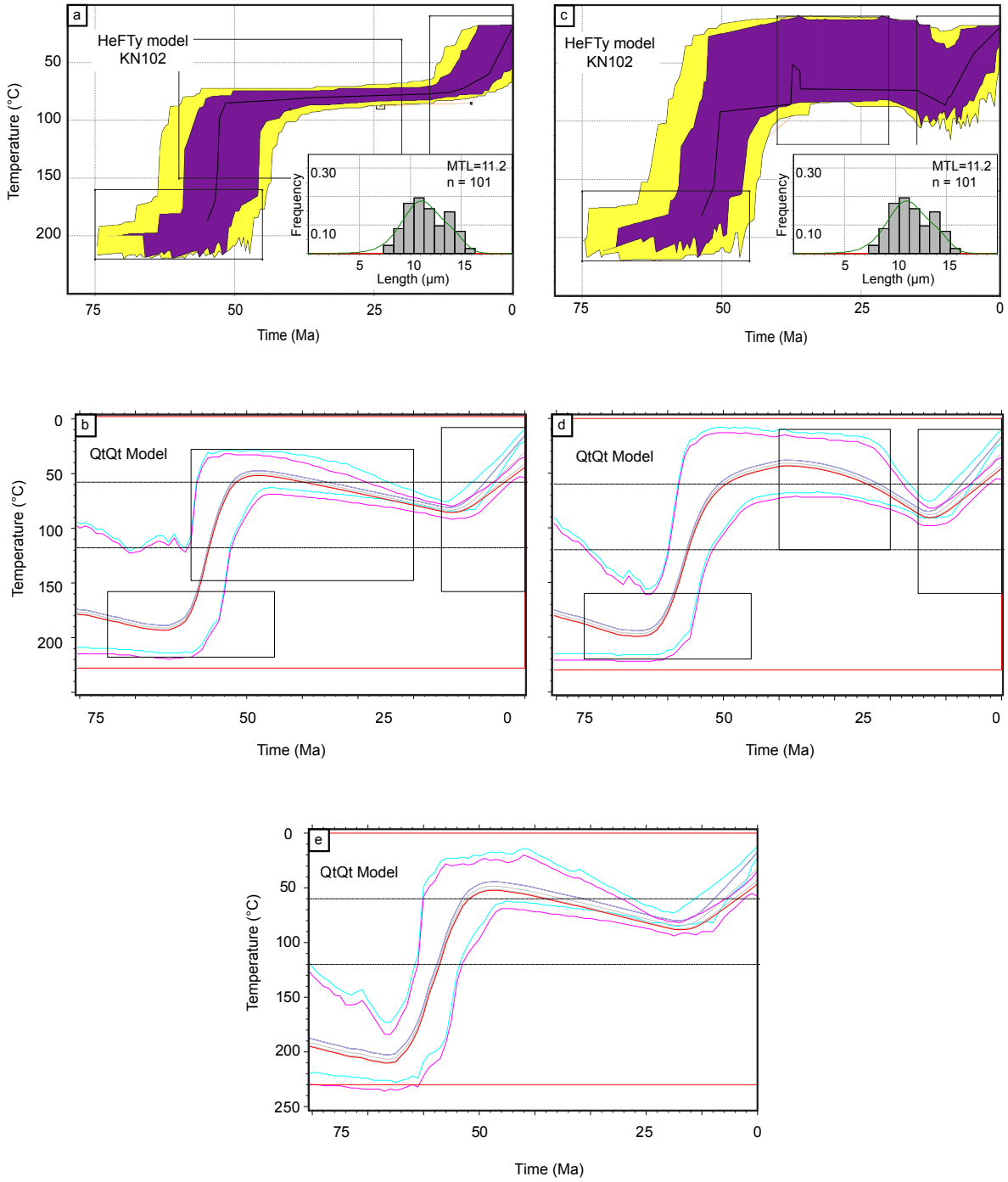

Figure 2.5 – Thermal modeling results for the northern Elgeyo Escarpment (NEE) samples. (a and c) Time temperature model for sample KN102 from the Northern Elgeyo Escarpment (NEE) using HeFTy software with acceptable (yellow) and good (purple) time-temperature pathway envelopes and best fit shown with black line. Figure 5a requires monotonic cooling while C permits reheating between 35 and 15 Ma. (b and d) Time-temperature histories derived from QTQt modeling, with time-temperature constraints in Figure 5b similar to those in Figure 5a and with constraints in Figure 5d similar to those in Figure 5c. (e) time-temperature history paths derived from QTQt with no constraint boxes; red box defines the limits of the modeling, 0°C-220°C and 0-80 Ma.

constrained to a shorter time window between ~35 and 10 Ma, even if the result looks forced by the constraint (Figure 2.5d). For the remaining time windows, the QTQt modeling results agree with those from HeFTy.

2.4.7 Unconstrained Thermal Modeling of Elevation Profiles

In addition, we ran QTQt models for both regions without using any constraint boxes (Figures 2.4e and 2.5e) to explore best fitting thermal histories when the program is set to freely search for acceptable solutions. The results do not differ substantially from the results of the constrained model runs described above. These results overall show that between periods of rapid cooling, the Samburu Hills profile may have experienced limited reheating, while the Northern Elgeyo Escarpment is likely to have experienced reheating. Ultimately, the modeling results are consistent, independent of the choice of the constraint boxes. Therefore, the input data, i.e., the ages and track lengths, guide the basic shape of the paths, rather than the user-defined constraint boxes. Other modeling results, including scenarios with short pulses of reheating, are provided in the supplementary material (Figure A3). Overall, results of the modeling with single (HeFTy) and multiple (QTQt) samples suggest a similar thermal history for the eastern and the western flanks of the northern and central Kenya Rift sectors, with clear periods of rapid cooling between ~65 and 50 Ma and from ~15 Ma to today, with either stable temperatures or reheating in between (Figures 2.4 and 2.5).

2.5 Discussion

Our new thermochronological data and thermal modeling results from the Samburu Hills and the Elgeyo Escarpment of Kenya define three Cenozoic stages of thermal evolution: (1) rapid cooling between ~65 and ~50 Ma, (2) subsequent slow cooling or slight reheating during the Oligo-Miocene, and (3) renewed rapid cooling after 15 Ma. Below, we address these different cooling stages with respect to rift evolution in Kenya and within the broader context of regional extensional processes in East Africa.

2.5.1 Paleocene to Eocene (65-50 Ma) Rapid Cooling

Our HeFTy and QTQt thermal modeling of samples from the Samburu Hills elevation profile on the eastern side of the rift valley and from the Elgeyo Escarpment on the western side yielded similar results, documenting rapid, early Cenozoic regional cooling (>50°C) between ~65 and 50 Ma (Figures 2.4 and 2.5). These results are in good agreement with previous modeling of apatite fission track and length parameters from samples collected in the Cherangani Hills and the basement rocks SE of Lake Turkana, which revealed 60 to 70°C of cooling between approximately 60 and 50 Ma (Foster and Gleadow, 1996; Spiegel et al., 2007). This

cooling appears to have been coeval with renewed extension and tectonic subsidence in the Anza Rift (i.e., Morley et al., 1999; Bosworth and Morley, 1994; Morley, 2002), which is inferred to have been associated with flexural upwarping of rift flanks in that region (Foster and Gleadow, 1996).

2.5.2 Eocene Through Middle Miocene Monotonic Slow Cooling or Reheating

Our results show that very slow cooling or reheating occurred between ~45 and 15 Ma in the Samburu Hills and at the Northern Elgeyo Escarpment, with temperatures ranging between ~60° and 90°C from the Eocene through the middle Miocene. Similar results were reported by Foster and Gleadow (1996) and Spiegel et al. (2007), with very slow cooling along both the western (Cherangani Hills) and eastern (Ndoto Mountains) rift shoulders from the Eocene through the middle Miocene.

The models show that minor reheating is likely to have occurred from Eocene to middle Miocene time (~45 to 15 Ma) for the Northern Elgeyo Escarpment samples, and is permitted, but not required for the Samburu Hills samples over a similar time interval. The Miocene phonolites are too young to explain this reheating. However, for the Northern Elgeyo Escarpment, reheating is compatible with geological interpretations of the early Cenozoic rifting phase in the Kerio Basin (Figure 2.1a) based on seismic reflection data (Mugisha et al., 1997; Hautot et al., 2000). The seismic reflection data document an early (as of yet undated) stage of tectonically controlled basin subsidence beneath the Neogene Kerio Basin followed by regional thermal basin subsidence and sedimentation within a sag basin (Morley et al., 1992; Mugisha et al., 1997; Morley and Ngenoh, 1999; Hautot et al., 2000). Thermo-chronological and geophysical evidence for protracted subsidence in this sag basin is corroborated by regional pinch-outs of fluvial and organic-rich lacustrine sediments exposed along the Elgeyo Escarpment (Morley et al., 1992; Mugisha et al., 1997; Ego, 1994; Renaut et al., 1999) and the regional extent and thickness of the overlying <14.5 Ma phonolites that cover the present-day eastern and western rift shoulders (Lippard, 1973). Alternatively, reheating could have been associated with the thermal impact of a mantle plume beneath the Tanzanian Craton since the Eocene-Oligocene (Ebinger and Sleep, 1998; George et al., 1998; Pik et al., 2008).

In this context, it is interesting that our thermochronologic data obtained from the Samburu Hills on the eastern rift shoulder exhibit a similar cooling history as samples from the Cherangani Hills on the western rift shoulder (Foster and Gleadow, 1996; Spiegel et al., 2007) (Figure 2.6), with reheating permitted, but not required. Due to their locations on the rift shoulders, neither area was affected by reheating related to subsidence and sedimentation within a sag basin. Thermal impacts of a mantle plume beneath the Tanzanian Craton since the Eocene-Oligocene (Ebinger and Sleep, 1998; George et al., 1998; Pik et al., 2008) remain a possibility, but clearly did not strongly influence the thermal evolution of the area as recorded in our samples.

2.5.3 Middle Miocene-Recent Renewed Cooling

Our thermal modeling shows a renewed, rapid cooling event starting at ~15 Ma in the Samburu Hills and the northern Elgeyo Escarpment, with rocks cooling from temperatures of ~60°C in the Samburu Hills and from ~90°C at the northern Elgeyo Escarpment. This accelerated cooling is compatible with the tectono-magmatic and sedimentary evolution of the northern and central Kenya rifts. Extensional faulting and the generation of transfer faults guided by foliation and inherited brittle shear zones in the Proterozoic basement gneisses affected the <14.5 Myr old phonolites as well as undated lacustrine shales, arkosic sandstones, and conglomerates (Hetzel and Strecker, 1994; Ogola et al., 1994; Ego, 1994), now exposed on the rift shoulders at the Elgeyo escarpment (Figure 2.6). These processes were responsible for the formation of a second rift basin superposed on the Paleogene basin (Figure 2.6). This younger basin has the geometry of a down-to-the-east halfgraben, which hosts the present-day Kerio Basin. The Neogene phase of extension generated an additional 2 km of sedimentary and volcanic fill in addition to the 4 km of basin deposits that had been deposited during Paleogene rifting, with the corresponding bounding fault being located farther west (Mugisha et al., 1997; Morley and Ngenoh, 1999; Hautot et al., 2000), (Figure 2.6).

2.5.4 Regional Implications for Rifting in East Africa

Our thermochronological results from the Elgeyo and Samburu sites in the northern and central Kenya Rift sectors agree with the well-documented, regionally widespread Paleogene episode of extension in the Turkana region (Morley et al., 1992; Foster and Gleadow, 1996; Morley et al., 1999; Morley, 2002; Tiercelin et al., 2012). East of the present-day Elgeyo Escarpment, Paleogene normal faulting and coeval sedimentation along the proto-Kerio Basin had been previously inferred based on a pronounced negative Bouguer gravity anomaly, reflecting a thick sedimentary fill, thought to be incompatible with the amount of Neogene extension and tectonic basin subsidence (Morley et al., 1992; Mugisha et al., 1997). As neither currently available geophysical, geological, nor thermo-chronological data suggest similar coeval Paleogene extension processes in the central and southern sectors of the Kenya Rift, it appears that early Cenozoic rifting in Kenya was focused in the greater Turkana region (i.e., Morley et al., 1992; Foster and Gleadow, 1992; Foster and Gleadow, 1996; Morley and Ngenoh, 1999; Spiegel et al., 2007), the Anza Rift, where Mesozoic extensional faults were reactivated (i.e., Morley et al., 1992; Bosworth and Morley, 1994), and regions as far south as the transition between the central and northern Kenya rifts (this study).

Thermo-chronologic data from other sectors of the EARS reveal spatially disparate and diachronous cooling histories (Figure 2.7). Approximately 300 km to the southeast of the Elgeyo region, the Pangani Rift of northern Tanzania is the closest manifestation of Paleocene-Eocene extensional processes in the southern continuation of the eastern branch of the EARS.

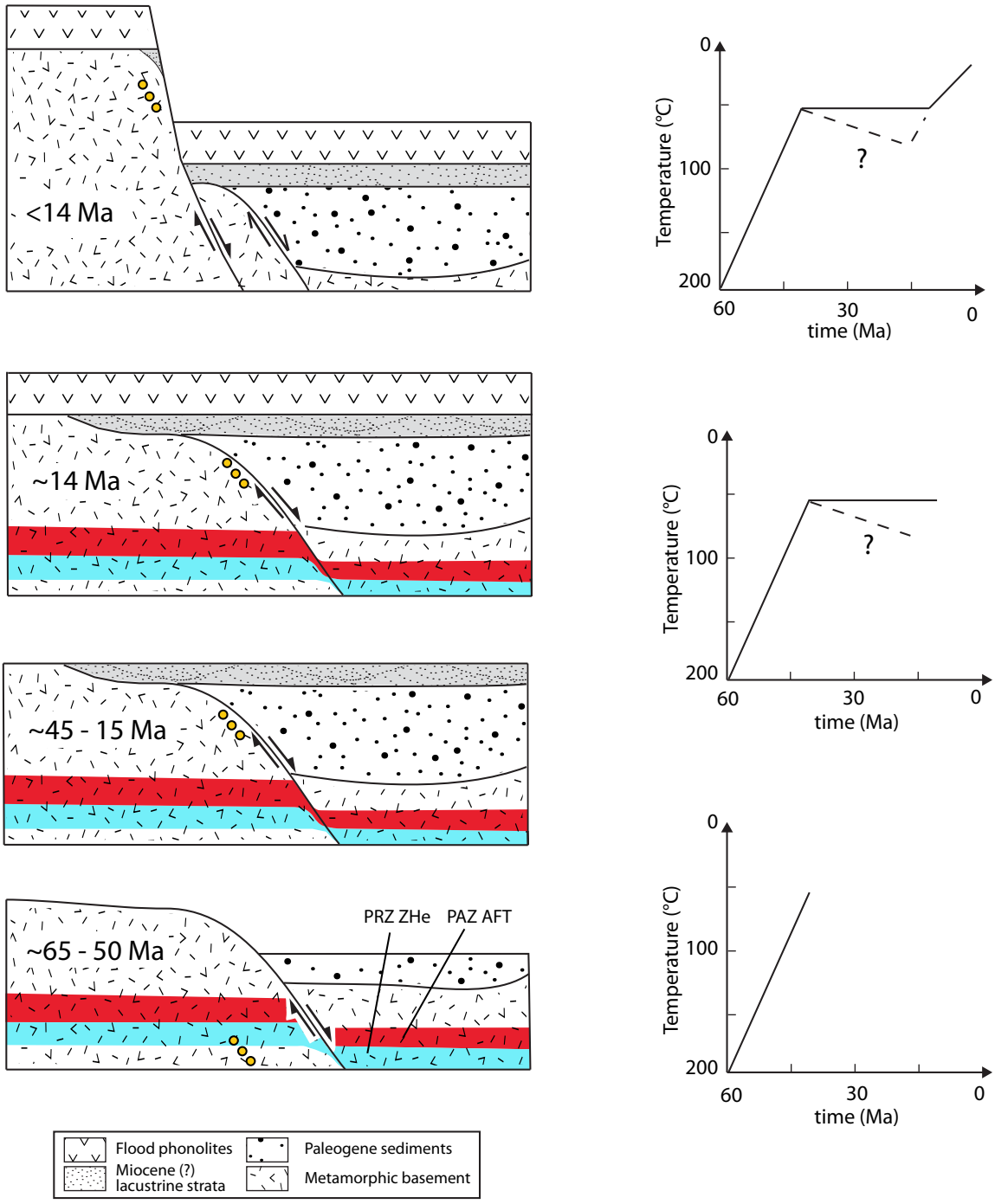

Figure 2.6 – Cartoon of the structural and thermal evolution of the Kenya Rift along the Elgeyo Escarpment of the Kerio Valley in the transition between the central and northern Kenya rifts. Episodes of cooling occurred from ~65 to 50 Ma and from 15 to 0Ma. Tectonic quiescence or minor reheating occurred between ~45 and 15 Ma. From bottom to top, circles denote the approximate position of the analyzed samples from ~50 Ma to present-day (surface). Blue band represents the inferred position of the partial retention zone for ZHe (PRZ); red band represents the apatite fission track partial annealing zone (PAZ).

Apatite fission track data indicate that a phase of rapid cooling began during the late Cretaceous and continued throughout the Paleogene (Noble et al., 1997; Mbede, 2001), although no thermal modeling was performed to better constrain the timing. In the western branch of the EARS, the Rwenzori Mountains and the Albertine Rift of Uganda have a distinctly different late Cretaceous to Cenozoic thermal history, with very slow cooling of<0.5 °C/Myr from the late Cretaceous through the middle Eocene (70 to 40Ma), and faster cooling (~1 to 4 °C/Myr) from themiddle Eocene at least through the Oligocene (Bauer et al., 2013). The Malawi Rift in Tanzania (western branch of the EARS) records a broadly similar history as the Rwenzoris Mountains over that time interval, with slow cooling from the Cretaceous through the Paleocene, and more rapid cooling (~0.5 to 1°C/Myr) starting after ~40Ma (van der Beek et al., 1998).

Sedimentologic, geomorphic, and geochronologic studies from different sectors of the EARS also suggest diachronous, yet partly overlapping rift-related exhumation in East Africa (Figure 2.7). For example, the Lake Rukwa region of the western branch and the rift basins west of Lake Turkana record an Oligocene onset of rifting (Morley et al., 1992, 1999; Roberts et al., 2012). Our new data from the Elgeyo Escarpment combined with field observations by Chapman et al. (1978) and geophysical data from the Kerio Basin (Mugisha et al., 1997) also suggest an earlier onset of extensional processes in this región, while the present-day morphologic characteristics of northern and central Kenya rifts are the result of renewed normal faulting after 12 Ma, coeval with extension recorded in the Central Tanganyika Basin (Chapman et al., 1978; Baker et al., 1988; Strecker et al., 1990), and the Albertine and southern Kenya rifts record the formation of extensional basin fills after approximately 9 and 7 Ma, respectively (Crossley, 1979; Pickford and Senut, 1994; Lezzar et al., 1996). At first sight, the regional data regarding extension the EARS summarized in Figure 2.7 suggest an earlier onset of extension based on thermochronological data compared to stratigraphic information. This is probably an artifact, because sediments and volcanic rocks associated with Paleogene rifting have subsided, and coeval removal of rift-related deposits from exposed fault blocks and rift-shoulder areas precludes inspection of the early sedimentological vestiges of rifting. This problem is well emphasized by the Paleogene onset of rifting in the Kenyan Kerio Valley, where eroded sedimentary deposits from rift-shoulder areas have only been imaged by geophysical techniques (Mugisha et al., 1997).

In any case, the available thermochronologic and geologic data reveal a spatially disparate and diachronous evolution of Cenozoic rifting in East Africa, with clear differences in the onset of rifting in the western and eastern branches of the EARS. This spatiotemporal pattern of extension is inconsistent with tectonic models of rifting in East Africa that are based on a southward directed migration of volcanism and cogenetic extension (McConnell, 1972; Ebinger and Sleep, 1998; Ebinger et al., 2000; Nyblade and Brazier, 2002; Morley, 2010). In light of the pronounced geophysical anomalies, evidence for mantle advection, and the evolu-

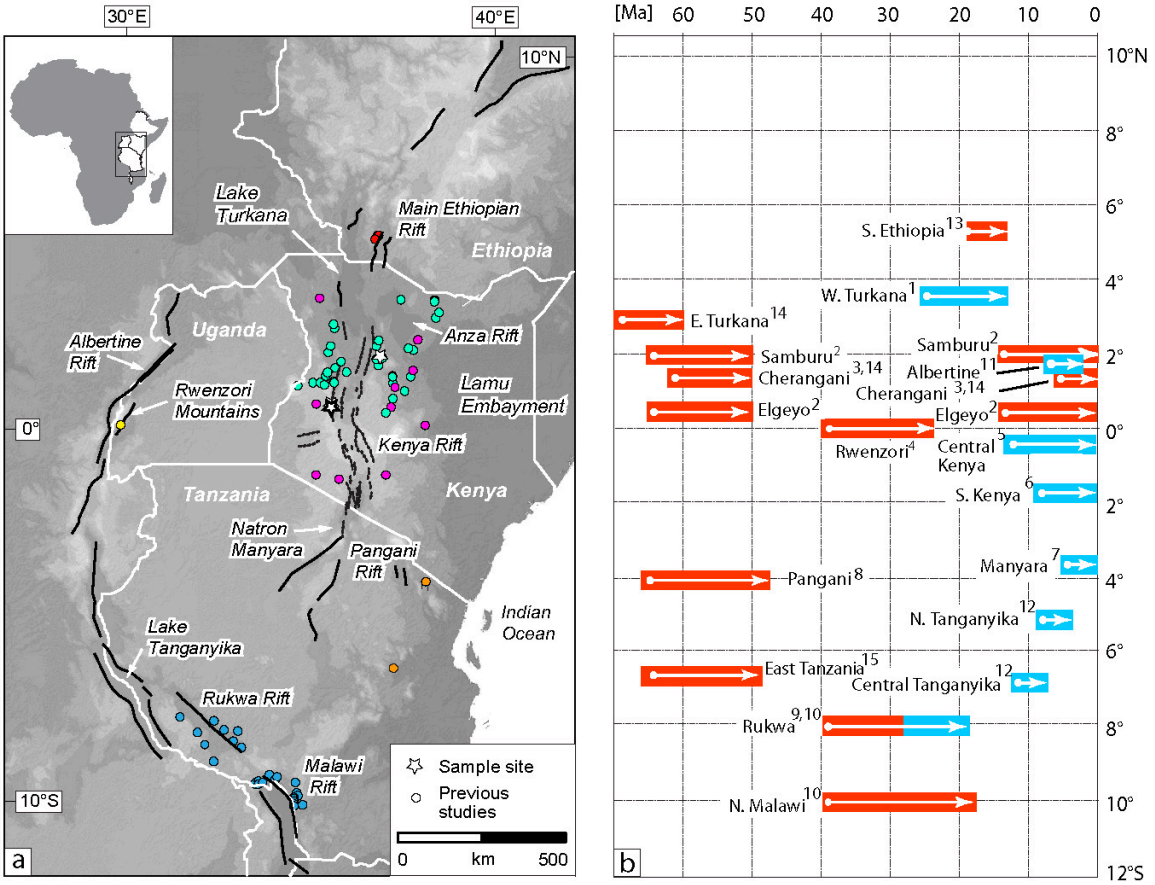

Figure 2.7 – (a) Locations of thermochronological and geological studies throughout the EARS. Thermochronological study sites are color coded: Pik et al. (2008) (red), Bauer et al. (2013) (yellow), Foster and Gleadow (1996) and Spiegel et al. (2007) (cyan), Wagner et al. (1992) (magenta), van der Beek et al. (1998) (blue), and MBede (2001) (orange). White outlines denote political boundaries. (b) Chronogramdepicting the onset of rapid cooling from thermochronology studies (red) and known extensional periods from structural constraints and basin stratigraphy (blue) in East Africa, compiled from different sources: (1) Morley et al. (1992), (2) this study, (3) Spiegel et al. (2007), (4) Bauer et al. (2013), (5) Mugisha et al. (1997), (6) Crossley (1979), (7) Foster et al. (1997), (8) MBede (2001), (9) Roberts et al. (2012), (10) van der Beek et al. (1998), (11) Pickford and Senut (1994), (12) Lezzar et al. (1996), (13) Pik et al. (2008), (14) Foster and Gleadow (1996), and (15) Noble et al. (1997). Arrows indicate onset of extension, although the length of the arrows does not always reflect the full length of extensional processes at the particular location. Thermochronology study sites indicate onset of cooling inferred to represent tectonically controlled exhumation by normal faulting..

tion of dynamic topography associated with regional domal uplift (i.e., White and McKenzie, 1989; Simiyu and Keller, 1997; Prodehl et al., 1997; Achauer and Masson, 2002; Mechie et al., 1997; Sepulchre et al., 2006; Moucha and Forte, 2011; Wichura et al., 2015), the timing of extension throughout East Africa likely reflects a large-scale, mantle-driven process that generated differential stresses (e.g., Crough, 1983; Zeyen et al., 1997) and the formation of rift basins in areas characterized by pronounced lithospheric and crustal-scale anisotropies and weaknesses (i.e., Ashwal and Burke, 1989; Ebinger and Sleep, 1998; Smith and Mosley, 1993; Smith, 1994). As such, our new data from the Kenya Rift, combined with the synopsis of geological and thermo-chronological studies in East Africa, is compatible with recent numerical modeling results (Koptev et al., 2015) that predict a regionally overlapping initiation of amagmatic and magmatic rifting sectors in East Africa following the asymmetric impingement of a single mantle plume (i.e., Halldórsson et al., 2014) at the base of the lithosphere of the eastern sector of the Tanzania Craton.

2.6 Conclusions

Our new AFT and ZHe data from both escarpment and rift shoulders from the northern and central sectors of the Kenya Rift help to define two distinct stages of rapid cooling from ~65 to 45 Ma and from ~15 Ma to the present day, separated by a long phase of near-isothermal conditions or minor reheating. The initial stage of rapid cooling likely reflects the initiation of Cenozoic rifting, followed by a period of relative quiescence, and then renewed rift activity since the middle Miocene. While our thermal modeling results are consistent with those reported from the northern Kenya Rift and the Pangani Rift (e.g., the eastern branch of the EARS), they contrast markedly with those reported from the western branch (Rwenzori Mountains, and the Rukwa and Malawi rifts). As such, we suggest that the spatiotemporal evolution of rifting in the EARS is compatible with the impact of mantle upwelling, ensuing crustal uplift, and extensional fracture propagation guided by crustal heterogeneities, rather than being related to the southward progression of mantle-plume activity.

Acknowledgments V.T.A was supported by the DFG Graduate School GRK1364 Shaping Earth's Surface in a Variable Environment, funded by the Deutsche Forschungsgemeinschaft (DFG) through a grant to M.R.S. (grant STR 373-20/1). We thank the Government of Kenya and the University of Nairobi for research permits and logistical support. T.F.S. was supported by the DFG's Emmy-Noether-Programme (grant number SCHI 1241/1-1). We thank Matthias Bernet, Lydia Olaka, Henry Wichura, and Rod Brown for discussions. The data for this paper are available by contacting the corresponding author.

Chapter 3

Effect of vegetation cover on millennial-scale landscape denudation rates in East Africa

Abstract

The mechanisms by which climate and vegetation affect erosion rates over various time scales lie at the heart of understanding landscape response to climate change. Plot-scale field experiments show that increased vegetation cover slows erosion, implying that faster erosion should occur under low to moderate vegetation cover. However, demonstrating this concept over long time scales and across landscapes has proven to be difficult, especially in settings complicated by tectonic forcing and variable slopes. We investigate this problem by measuring cosmogenic ^{10}Be-derived catchment-mean denudation rates across a range of climate zones and hillslope gradients in the Kenya Rift, and by comparing our results with those published from the Rwenzori Mountains of Uganda. We find that denudation rates from sparsely vegetated parts of the Kenya Rift are up to 0.13 mm/yr, while those from humid and more densely vegetated parts of the Kenya Rift flanks and the Rwenzori Mountains reach a maximum of 0.08 mm/yr, despite higher median hillslope gradients. While differences in lithology and recent land-use changes likely affect the denudation rates and vegetation cover values in some of our studied catchments, hillslope gradient and vegetation cover appear to explain most of the variation in denudation rates across the study area. Our results support the idea that changing vegetation cover can contribute to complex erosional responses to climate or land-use change and that vegetation cover can play an important role in determining the steady-state slopes of mountain belts through its stabilizing effects on the land surface.

3.1 Introduction

Over the past decade, new approaches for quantifying landscape denudation rates over multiple time scales have helped to reveal the relative importance of tectonic and climatic factors in controlling landscape denudation (Montgomery and Brandon, 2002; Molnar, 2004; Wittmann et al., 2007; Champagnac et al., 2012; Kirby and Whipple, 2012; Carretier et al., 2013; Scherler et al., 2014). Steeper slopes and higher runoff are generally expected to increase hillslope sediment flux and denudation rates (Gilbert, 1877; Wischmeier and Smith, 1965; Kirkby, 1969; Summerfield and Hulton, 1994; Roering et al., 1999), while steeper river channels and higher discharge increase the erosional potential and sediment-transport capacity of rivers (Howard, 1994; Whipple and Tucker, 2002). In areas with relatively uniform and stable climatic conditions, denudation rates are thus positively correlated with hillslope angles, river steepness, or other measures of landscape relief (e.g., Ahnert, 1970; Granger et al., 1996; Montgomery and Brandon, 2002; Binnie et al., 2007; Harkins et al., 2007; Wittmann et al., 2007; Ouimet et al., 2009; DiBiase et al., 2010; Cyr et al., 2010; Roller et al., 2012; Miller et al., 2013; Scherler et al., 2014). Tectonic activity can induce faster denudation when higher uplift rates lead to river incision and consequent hillslope steepening (Willett, 1999). A functional relationship between denudation rates and precipitation or effective precipitation, however, is not always apparent. Whereas some studies have shown positive correlations between millennial-scale denudation rates and precipitation (Moon et al., 2011; Bookhagen and Strecker, 2012; Kober et al., 2007; Heimsath et al., 2010), most have revealed no clear correlation (Riebe et al., 2001; von Blanckenburg, 2005; Safran et al., 2005; Binnie et al., 2010; Insel et al., 2010; Portenga and Bierman, 2011; Scherler et al., 2014). This disagreement may arise because the effect of precipitation on denudation is modulated by other factors, including the density of the vegetation cover (Langbein and Schumm, 1958; Kirkby, 1969; Dunne et al., 1978; Dunne, 1979; Collins et al., 2004; Istanbulluoglu and Bras, 2005; Vanacker et al., 2007; Molina et al., 2008).

Over shorter time scales of up to decades or centuries, plot-scale studies provide important insights into the mechanisms through which vegetation cover affects erosion processes and denudation rates. These studies have shown that both the type and density of vegetation cover increase the resistance of soil to erosion through the binding effects of roots, the formation of soil aggregates, the resistance to flow exerted by leaf litter and stems, and the protection of the surface from rainsplash (e.g., Dunne et al., 1978, 2010; Wainwright et al., 2000; Gyssels and Poesen, 2003; Durán Zuazo et al., 2008). Higher infiltration rates in densely vegetated areas with thick soils also decrease the likelihood of overland flow, which can rapidly denude slopes (Horton, 1933, 1945; Abrahams et al., 1995; Prosser and Dietrich, 1995). Although plot-scale experiments and modeling studies demonstrate continued increases in denudation with decreasing vegetation cover under imposed rainfall (e.g., Nearing et al., 2005), in natural systems sparse vegetation often correlates with low precipitation, limited bioturbation (Gyssels and Poesen, 2003; Gabet et al., 2003; Pelletier et al., 2011),

and potentially lower soil-production rates (Jenny, 1941; Dixon et al., 2009a, 2009b; Roering et al., 2010), which together can minimize sediment transport. This general pattern in natural systems has been used to argue for an expected peak in denudation at intermediate values of precipitation and vegetation (e.g., Langbein and Schumm, 1958), although numerous other forms of this relationship, sometimes with multiple peaks, have been proposed for different climate regimes (summarized in Wilson, 1973). Nonetheless, variations in tectonic forcing, rock strength, storminess, temperature-dependent erosion processes, and anthropogenic land-use changes make direct tests of the effects of vegetation cover on denudation rates at catchment scales challenging.

Catchment-mean denudation rates derived from cosmogenic nuclides may provide an alternative to better understand how climate, tectonics, lithology, and any complicating influence of vegetation affect denudation rates (Bierman and Steig, 1996; Granger et al., 1996). The relatively long averaging time scale of the technique (typically ranging from several thousand to several hundreds of thousands of years) decreases sensitivity of the measurements to recent (e.g., human) disturbances (Bierman and Steig, 1996; Brown et al., 1998; von Blanckenburg, 2005; Vanacker et al., 2007), which is a primary concern when attempting to use contemporary measurements to infer long-term erosion rates (e.g., Milliman and Meade, 1983). Indeed, Bierman and Steig (1996) calculated a change in cosmogenic basin-average denudation rates of $<$30% for recent soil loss of 0.5 m. The potential for these measurements to average over broad spatial scales also provides greater possibilities for deriving spatially representative denudation rates, which are critical for investigating interactions among erosion, climate, and tectonics (Granger et al., 1996). Nonetheless, a recent multivariate linear regression analysis of a global compilation of cosmogenic catchment-mean denudation rates found vegetation cover to be unimportant in explaining denudation-rate variations (Portenga and Bierman, 2011). The absence of any discerned effect may result from (1) the difficulty of finding metrics that quantify aspects of vegetation cover that may affect denudation, (2) vegetation cover having indeed minimal effects on denudation rates, or (3) the relationship between vegetation cover and denudation rate being highly nonlinear.

Here, we present new cosmogenic catchment-mean denudation rates from a range of climatic zones in the eastern branch of the East African Rift system (Kenya Rift; Fig. 3.1). Together with published denudation rates from the Rwenzori Mountains in the western branch of the rift system in Uganda (Fig. 3.2; Roller et al., 2012), we explore how hillslope gradient, precipitation, lithology, and vegetation cover influence denudation rates. In particular, we investigate whether or not a clear signal of hillslope stabilization by vegetation cover can be discerned across a landscape with widely varying slopes and climate regimes.

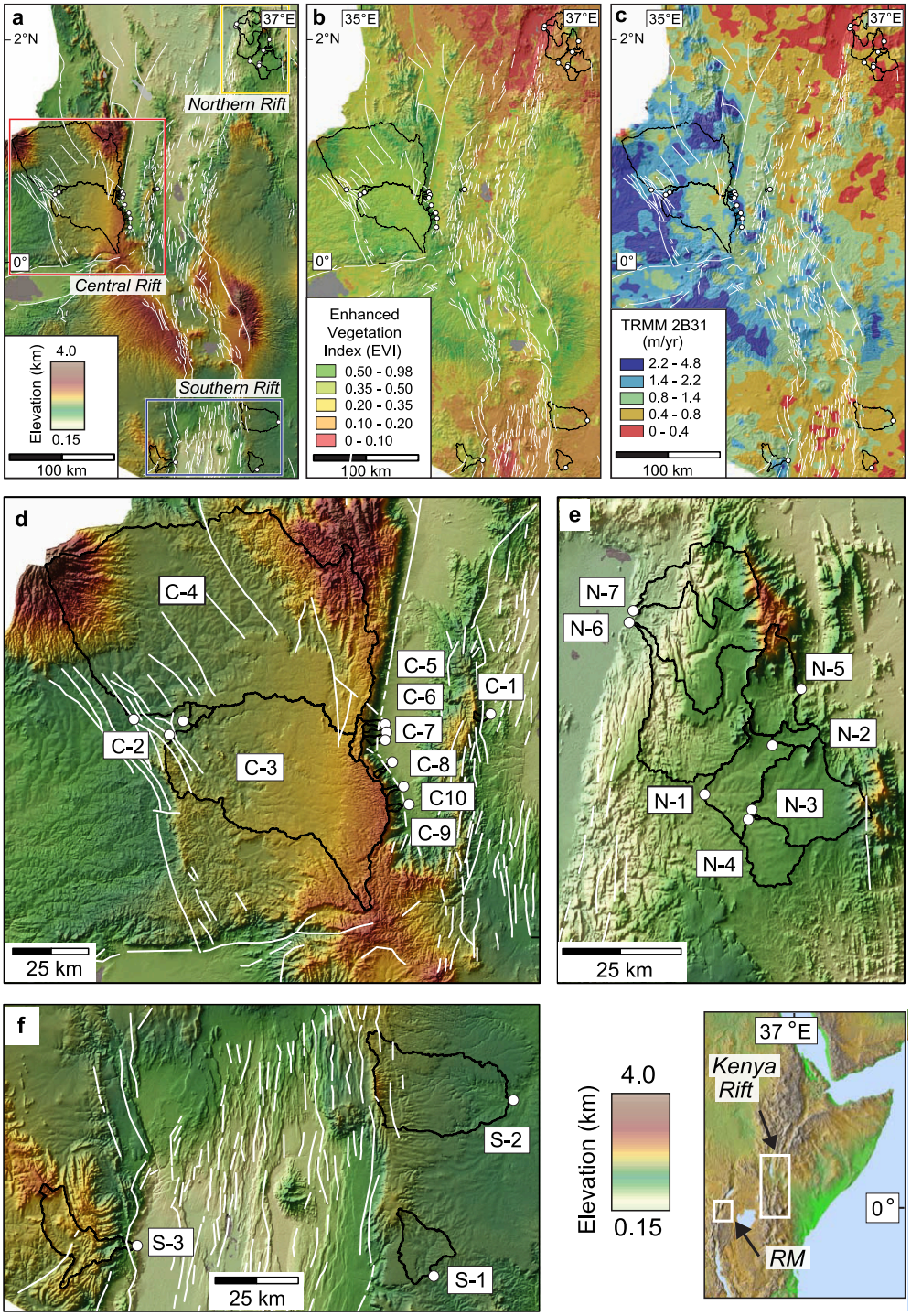

Figure 3.1 – The Kenya Rift area and sample sites. (a) Digital elevation model (SRTM 90-m resolution) showing the location of samples and catchments. (b) Vegetation cover represented by the enhanced vegetation index (EVI). (c) Mean annual precipitation derived from calibrated TRMM 2B31 rainfall averaged from 1998 to 2007. Black lines outline river catchments and white circles correspond to sample sites. Zoomed in views illustrate topography, sampled drainage basins (with sample numbers), and faults (white lines) in the (d) Central Rift sector, (e) Northern Rift sector, and (f) Southern Rift sector.

3.2 East African Rift

The present-day topography of the Kenya Rift is characterized by steep rift escarpments and low-relief rift shoulders (Fig. 3.1). This topography results from regional domal uplift, which had been accomplished by the middle Miocene, followed by extension and formation of the rift after ca. 13.5 Ma (Smith, 1994; Hetzel and Strecker, 1994; Wichura et al., 2010). Although extensive areas of the rift are covered by Neogene and Quaternary volcanic rocks, Proterozoic basement rocks (predominantly quartzitic gneisses, but also quartzites, migmatites, and schists) are exposed at the steep Elgeyo (northern rift) and Nguruman (southern rift) escarpments and on rift shoulder areas, while Miocene to recent sediments are found in the main rift and major river valleys draining the rift-shoulder areas (BEICIP, 1987; Ackerman and Heinrichs, 2001). Our study area includes three principal morphotectonic units in the Kenya Rift, which we refer to as the northern, central, and southern rifts (Fig. 3.1A).

The Rwenzori Mountains of Uganda have also evolved since Miocene time and now reach elevations over 5 km (Ebinger, 1989; Chorowicz, 2005; Bauer et al., 2010, 2012). The Rwenzori Mountains consist of an Archean basement complex composed of gneisses, schists, quartzites, and amphibolites (Bauer et al., 2010). Unlike the catchments we studied in the Kenya Rift, high-elevation regions within the Rwenzori Mountains have experienced repeated glaciations (Osmaston and Harrison, 2005; Hastenrath, 2009). Despite the steep slopes that characterize much of the Rwenzori Mountains, Roller et al. (2012) interpreted the positively skewed hillslope distributions together with consistent cosmogenic nuclide concentrations across different grain sizes to argue for limited rockfalls or other mass movements in the region over millennial time scales.

Overall, the East African Rift lies in an equatorial zone characterized by seasonal shifts in the Intertropical Convergence Zone (ITCZ) and the Congo Air boundary (Nicholson, 1996). Precipitation patterns and amounts are influenced by the elevation of the East African Plateau, the volcanic edifices, the uplifted shoulder regions of the individual rift basins, and by high evapotranspiration (Nicholson, 1996; Sepulchre et al., 2006; Bergner et al., 2009). Considering that the main characteristics of the present-day topography in the rift-shoulder areas (Figs. 1 and 2A) were formed by Neogene volcano-tectonic processes (e.g., Wichura et al., 2010), tectonically induced changes to the regional topography and hence, precipitation patterns, have probably been minor since that time. Annual precipitation ranges from 0.003 m/yr in the arid northern Kenya Rift to 4 m/yr in the Rwenzori Mountains and in the humid western highlands of the Kenya Rift (Figs. 1C and 2C). Recurring humid periods from the Miocene to the Quaternary (deMenocal et al., 2000; Trauth et al., 2005; Tierney et al., 2011; Garcin et al., 2012) were accompanied by shifts in vegetation between open wooded grasslands and grasslands (Bonnefille, 2010; Cerling et al., 2011). More recently, land-use changes in the Kenya Rift have led to reductions in vegetation cover due to grazing and crop cultivation (Ovuka, 2000; Fleitmann et al., 2007). These land-use changes strongly influence

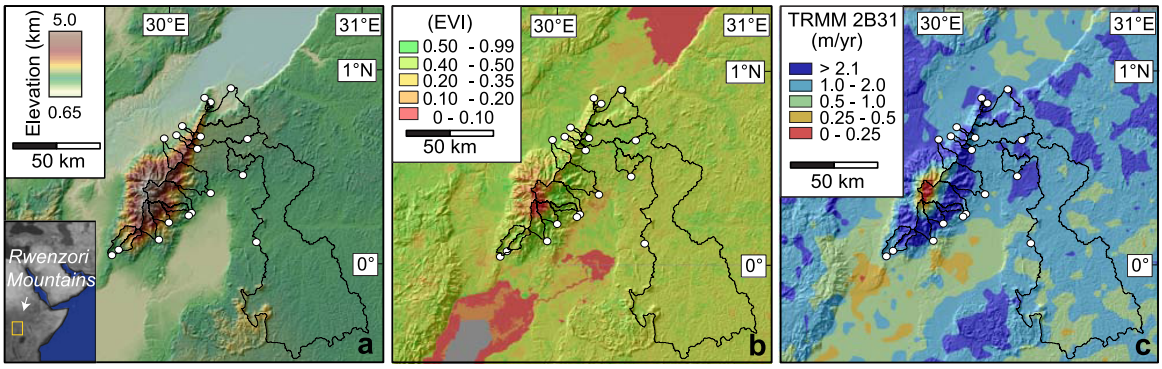

Figure 3.2 – Rwenzori Mountains area and sample sites. (a) Digital elevation model (SRTM 90-m resolution) showing the location of samples and catchments. (b) Vegetation cover represented by the enhanced vegetation index (EVI). (c) Mean annual precipitation derived from calibrated TRMM 2B31 rainfall averaged from 1998 to 2007. Black lines outline river catchments and white circles correspond to sample sites.

modern sediment yields, with the most disturbed areas yielding erosion rates several orders of magnitude higher than those in lightly or undisturbed sites (Dunne, 1979).

3.3 Methods

3.3.1 Sampling Methods and Assessing Catchment Characteristics

We determined catchment-mean denudation rates from in situ-produced cosmogenic ^{10}Be concentrations in detrital quartz sand collected from 20 streams in the Kenya Rift (Fig. 3.1; see Appendix B). River catchments were selected to avoid the influence of faults (Fig. 3.1). We sampled catchments with a minimum drainage area of 5 km^2 to help ensure sufficient mixing of river sands (e.g., Bierman and Steig, 1996; Portenga and Bierman, 2011), and we distributed our sampling within the different sectors of the rift to ensure that we obtained samples across a wide range of climate zones, vegetation zones, and mean hillslope gradients. When calculating topographic, climatic, and vegetation properties of the catchments, we only considered the areas that are underlain by quartz-bearing rock types, as denudation from those areas alone is recorded in the cosmogenic nuclide analysis. Within those regions, we assumed a uniform distribution of quartz.

Hillslope gradients and the relief of the contributing areas for each catchment from Kenya (see Appendix B) and the Rwenzori Mountains (see Appendix B) were extracted from 90-m-resolution Shuttle Radar Topography Mission (SRTM) data. We chose a 2 km moving window to calculate relief, because this is large enough to capture the valley-ridge top elevation difference for many of the catchments. For most catchments, gradient and relief values do not have a normal distribution (see Appendix B). To ensure consistency in the interpretation of

results, we therefore used median gradient and relief values when analyzing trends in the data.

We used two data sets to characterize vegetation cover across our sampled catchments in the Kenya Rift and those sampled by Roller et al. (2012) in the Rwenzori Mountains: the enhanced vegetation index (EVI) and the vegetation continuous fields (VCF). The EVI was developed to provide a satellite-based measure of vegetation cover that remains sensitive in areas of high biomass and reduces atmospheric influences (Huete et al., 2002). The EVI is sensitive to variations in the near-infrared band, and hence it reflects variations in canopy structures (Huete et al., 2002). We calculated average enhanced vegetation index (EVI) values for each catchment based on the MODIS sensor subsetted land products, collection 5, with 250 m resolution and 16 days temporal intervals (ORNL DAAC, 2012). We averaged the EVI products available from April 2000 to April 2012 (276 images) for the Kenya Rift and the Rwenzori Mountains. In addition, we used the vegetation continuous fields (VCF) collection MOD44B V005, which provides a rough representation of surface vegetation cover (divided into percent tree cover, percent non-tree cover [herbaceous], and bare), to characterize vegetation type within each catchment. Both of these vegetation-cover data sets are imperfect for comparison with cosmogenic nuclide-derived denudation rates, because the satellite products characterize modern vegetation cover, while the cosmogenic nuclide data are averaged over many millennia. Nonetheless, we used the remotely sensed vegetation data to explore to a first order how vegetation cover may influence denudation rates.

Annual precipitation for each catchment was based on 5 x 5 km resolution, calibrated, satellite-derived Tropical Rainfall Measuring Mission (TRMM) 2B31 precipitation data averaged over the years of 1998-2009. To obtain a measure of the distribution of yearly rainfall, particularly with respect to the importance of storm events, we used a 90^{th} percentile rainfall threshold to define the number of extreme hydrometeorological events from 1998 to 2009.

3.3.2 Cosmogenic Nuclide Sample Preparation and Analysis

Quartz grains ranging from 250 to 500 μm in size from each sample were first concentrated through magnetic techniques and then cleaned for 12 h in a 1:1 hydrochloric acid and water solution. Next, samples were leached at least 4 times with a 1% hydrofluoric acid solution in a heated ultrasonic bath to remove unwanted minerals like feldspars (see procedure described in Kohl and Nishiizumi, 1992). These initial sample preparation steps were performed at the University of Potsdam, and they yielded between 10 and 80 g of clean quartz for each sample (Table 3.1). Sample dissolution in hydrofluoric acid, addition of ^{9}Be carrier, isolation of Be through ion-exchange chromatography, oxidation, mixing of BeO with niobium powder, and target packing were performed in a clean laboratory at the GeoForschungsZentrum (GFZ) Potsdam. Ratios of ^{10}Be/^{9}Be were measured at the Center for Accelerator Mass Spectrometry at Lawrence Livermore National Laboratories in the United States, and resulting values were

converted into ^{10}Be concentrations, which are reported along with analytical errors in Table 3.1. We relied on the original ICN standard (07KNSTD3110) as reference and used a value of 5.0 x 10^{-7}yr-1 for the decay constant for ^{10}Be (Chmeleff et al., 2010), which is equivalent to the ^{10}Be half-life of 1.387 $\pm$ 0.012 yr (Korschinek et al., 2010).

To determine ^{10}Be production rates for the quartz-bearing contributing areas of each catchment, we averaged the production rates calculated for every 90 m pixel from SRTM elevation data, including variations in altitude, latitude, spallation and muon production, and topographic shielding (for details, see Scherler et al., 2014). We calculated erosion rates using the numerical functions from the CRONUS online calculator (Balco et al., 2008). All erosion rates we present here are based on the time-dependent version of the production-rate scaling model after Lal (1991) and Stone (2000), denoted "Lm" in Balco et al. (2008).

3.4 Results

The sampled catchments in Kenya yielded denudation rates between 0.001 and 0.132 mm/yr (Table 3.1). Median hillslope gradients (m/m) ranged from 0.03 to 0.30, and mean annual precipitation was between 0.2 and 2.4 m/yr (Table 3.2). Calculated EVI spanned dimensionless values between 0 and 0.5 in the Kenya Rift, representing sparse to dense vegetation (Figs. 1B and 3; Table 3.2). In the Rwenzori Mountains, denudation rates ranged from 0.007 to 0.077 mm/yr, median hillslope gradients ranged from 0.03 to 0.37, mean annual precipitation was between 1.3 and 2.8 m/yr, and EVI ranged from 0.39 to 0.54 (Fig. 3.2B; Table 3.2).

The VCF data indicate that the vegetation cover of most sampled catchments is characterized by at least 50% herbaceous cover (Fig. 3.4). Additionally, those catchments with EVI values below 0.2 are characterized by at least 20% bare soil/rock, and those with EVI values above 0.4 are characterized by at least 40% trees (Fig. 3.4). Despite the well-known impacts of humans on the natural vegetation (as well as modern erosion rates) in East Africa (Dunne et al., 1978; Dunne, 1979), there is a positive correlation between mean annual precipitation and EVI in our sampled catchments (R^2 = 0.642; Fig. 3.5).

In comparing the denudation-rate data from the Rwenzori Mountains with our data, we excluded five samples from glacially influenced catchments where denudation rates may be overestimated due to ice/snow shielding; Roller et al. (2012) excluded the same samples when analyzing their data. Considering the remaining samples from East Africa, we find poor linear correlations of denudation rates with median gradient (R^2 = 0.266; Fig.3.6A), EVI (R^2 = 0.050; Fig. 3.6C), mean annual precipitation (R^2 = 0.042; Fig. 3.6D), and extreme rainfall events (R^2 = 0.004; Fig. 3.6E). The best correlation (R^2 = 0.479) is with mean basin relief (Fig. 3.6B). Interestingly, the combined data from East Africa yield what appear to be two distinct scaling relationships: one showing denudation rates that increase rapidly with median gradient, and another showing denudation rates that increase more slowly with median gradient (Fig.

Table 3.1 – Cosmogenic nuclide analytical data for samples from the Kenya Rift.

Sample ID	Elevation	Latitude	Longitude	Sample weight	^{10}Be atoms[a] x 10^3	^{10}Be atoms x 10^3 (1σ)	Surface Production rate[b]		Denudation rate	Denudation rate uncertainty	Integration time	Corrected denudation rate[c]
							Muogenic	Spallogenic				
	(masl)	(°N)	(°E)	(g)	(atoms/g_{qtz})	(atoms/g_{qtz})	(atoms/(g_{qtz}*yr))	(atoms/(g_{qtz}*yr))	(mm/yr)	(1σ)	(kyr)	(mm/yr)
Southern Rift												
S-01	1707	-1.876	36.779	37.189	2243	34	0.3	10.9	0.0030	0.0003	201	0.0032
S-02	1567	-1.446	36.971	52.970	3890	51	0.3	9.9	0.0014	0.0001	437	0.0015
S-03	2246	-1.809	36.045	50.261	874	14	0.4	14.6	0.0111	0.0009	54	0.0130
Central Rift												
C-01	1400	0.658	35.883	13.947	48	2.8	0.3	8.0	0.1315	0.0112	4.6	0.1550
C-02	1830	0.633	34.999	38.303	806	16	0.3	12.1	0.0101	0.0008	60	0.0122
C-03	2010	0.612	34.962	42.848	2320	27	0.3	11.2	0.0029	0.0003	204	0.0040
C-04	2244	0.655	34.839	49.257	1422	15	0.3	13.7	0.0062	0.0005	97	0.0079
C-05	1511	0.631	35.569	38.217	78	2.2	0.3	9.4	0.0877	0.0062	6.8	0.1058
C-06	1540	0.608	35.579	78.575	78	2.1	0.3	9.6	0.0885	0.0062	6.8	0.1100
C-07	1540	0.582	35.570	44.168	73	2.1	0.3	9.6	0.0950	0.0067	6.3	0.1215
C-08	1657	0.513	35.586	45.889	432	10	0.3	10.4	0.0174	0.0013	34	0.0228
C-09	1621	0.395	35.640	44.682	202	4.7	0.3	9.9	0.0358	0.0026	17	0.0465
C-10	1803	0.442	35.628	78.257	199	2.8	0.3	11.3	0.0407	0.0028	15	0.0519
Northern Rift												
N-01	1306	1.812	36.715	30.350	714	15	0.3	8.3	0.0086	0.0007	70	0.0091
N-02	1415	1.908	36.837	29.871	1122	25	0.3	8.8	0.0052	0.0004	116	0.0054
N-03	1405	1.792	36.799	29.645	1053	11	0.3	9.3	0.0058	0.0005	103	0.0063
N-04	1347	1.773	36.794	29.500	705	9.4	0.3	8.7	0.0086	0.0007	70	0.0090
N-05	1555	2.005	36.890	27.005	169	3.3	0.3	10.3	0.0422	0.0029	14	0.0444
N-06	1318	2.125	36.588	29.957	237	4.6	0.3	7.7	0.0245	0.0017	24	0.0257
N-07	1258	2.148	36.594	32.619	65	1.8	0.3	8.5	0.0962	0.0066	6.2	0.1050

[a] Standard used for normalization was 07KNSTD3110; ^{10}Be/^{9}Be ratio for standard=2.85e-12

[b] Production rate according to time-dependent Lal/Stone scaling, see details in Balco et al. (2008).

[c] Corrected for chemical erosion using relationship reported in Riebe and Granger (2013).

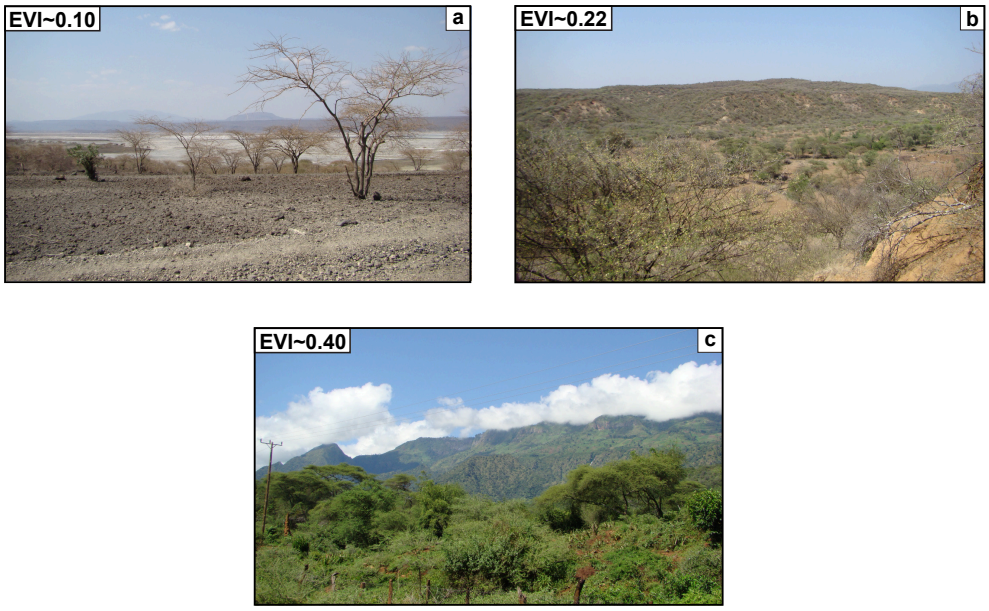

Figure 3.3 – Differences in vegetation cover and corresponding EVI values in the Kenya Rift.

3.6A). In the following discussion, we explore whether any of the catchment characteristics can explain these two scaling relationships.

3.5 Discussion

3.5.1 Biogeomorphic and Geologic Controls on Denudation-Rate Patterns

As has been demonstrated in a global compilation of cosmogenic catchment-mean denudation rates, mean basin slope is the most powerful regressor in explaining denudation-rate variations, but a host of other catchment characteristics also contribute to variations (Portenga and Bierman, 2011). Our bivariate analyses of denudation rates versus various catchment properties from East Africa yield relatively poor to moderate correlations for the full data set (R^2 values ranging from 0.004 to 0.479; Fig. 3.6). However, the two distinct scaling relationships (one steep and one shallow) in the plot of denudation rate versus hillslope gradient (Fig. 3.6A) suggest that there may be a threshold value in one or more catchment characteristics and/or a fundamental change in hillslope/erosion processes across the two groups of data that influences the sensitivity of denudation rates to median gradient. As such, we next explore whether different processes, rock types, or threshold values in climatic/vegetation characteristics separate the two scaling relationships.

One potential explanation for the two different scaling relationships could be differences in chemical weathering across the different climate zones. Chemical weathering can increase

Table 3.2 – Kenya Rift and Rwenzories catchment characteristics & morphometric parameters.

Sample ID	Elev.	Lat.	Long.	Median slope	Median gradient	Median relief[a]	Mean annual rainfall[b]	EVI	Trees[c]	Herba-ceous[c]	Bare[c]	Catch-ment area[d]	Quartz-bearing lithology[e]	Percent lithology[e]			Denuda-tion rate	Denuda-tion rate	Corrected denudation rates[f]
	(masl)	(°N)	(°E)	(°)	(m/m)	(m)	(mm/yr)		(%)	(%)	(%)	(km^2)		basement	sediment	volcanics	(mm/yr)	(1σ)	(mm/yr)
Southern Rift																			
S-01	1707	-1.876	36.779	1.99	0.03	67	578	0.26	11	86	3.0	63	1	100	0	0	0.0030	0.0003	0.0032
S-02	1567	-1.446	36.971	1.93	0.03	84	769	0.25	12	85	2.3	92	1	0	100	0	0.0014	0.0001	0.0015
S-03	2246	-1.809	36.045	7.23	0.13	284	1112	0.33	36	64	0.1	248	2, 3	77	23	0	0.0111	0.0009	0.0130
Central Rift																			
C-01	1400	0.658	35.883	9.91	0.17	762	1189	0.28	10	82	7.4	6.1	4,5	34	66	0	0.1315	0.0112	0.1550
C-02	1830	0.633	34.999	2.23	0.04	161	1389	0.34	17	83	0.1	4.4	6	100	0	0	0.0101	0.0008	0.0122
C-03	2010	0.612	34.962	3.33	0.06	143	2416	0.37	19	81	0.1	616	4,7	100	0	0	0.0029	0.0003	0.0040
C-04	2244	0.655	34.839	2.97	0.05	118	1868	0.36	23	77	0.2	3644	2,4,5,7	98	2	0	0.0062	0.0005	0.0079
C-05	1511	0.631	35.569	8.60	0.15	810	1379	0.32	13	83	3.8	8.1	8,9	34	66	0	0.0877	0.0062	0.1058
C-06	1540	0.608	35.579	9.96	0.17	800	1618	0.32	14	81	5.6	12	8,9	33	67	0	0.0885	0.0062	0.1100
C-07	1540	0.582	35.570	10.67	0.18	779	1856	0.34	14	82	4.4	10	8,9	32	68	0	0.0950	0.0067	0.1215
C-08	1657	0.513	35.586	17.70	0.30	1120	2062	0.38	20	76	3.5	6.8	8,9	57	43	0	0.0174	0.0013	0.0228
C-09	1621	0.395	35.640	17.89	0.30	959	1989	0.39	21	79	0.0	6.4	8,9	87	12	0	0.0358	0.0026	0.0465
C-10	1803	0.442	35.628	14.40	0.25	1053	1844	0.43	33	67	0.0	5.7	8,9	64	36	0	0.0407	0.0028	0.0519
Northern Rift																			
N-01	1306	1.812	36.715	1.64	0.03	80	445	0.15	1.8	66	32	533	2,5,10	43.2	56.8	0	0.0086	0.0007	0.0091
N-02	1415	1.908	36.837	1.86	0.03	126	288	0.15	0.6	59	41	29	2,10	61	39	0	0.0052	0.0004	0.0054
N-03	1405	1.792	36.799	1.70	0.03	86	534	0.19	3.0	70	27	263	2	26.7	73.3	0	0.0058	0.0005	0.0063
N-04	1347	1.773	36.794	1.20	0.02	62	308	0.17	2.5	69	28	113	2,5	23	77	0	0.0086	0.0007	0.0090
N-05	1555	2.005	36.890	5.12	0.09	400	341	0.22	11	65	24	145	2,5	100	0	0	0.0422	0.0029	0.0444
N.06	1318	2.125	36.588	3.86	0.07	248	307	0.15	1.9	55	43	229	2,5	89	11	0	0.0245	0.0017	0.0257
N-07	1258	2.148	36.594	7.32	0.13	638	611	0.17	4.1	51	45	83	2,5	59	41	0	0.0962	0.0066	0.1050
Rwenzori Mountains																			
294	2121	0.591	30.142	19.10	0.32	1031	1700	0.54	46	53	< 1	1.2	6	100	0	0	0.061	0.0053	0.077
295-1	2206	0.656	30.166	21.69	0.36	886	1450	0.53	48	51	< 1	12	6,12	100	0	0	0.062	0.0046	0.075
295-2	2206	0.656	30.166	21.69	0.36	886	1450	0.53	48	51	< 1	12	6,12	100	0	0	0.058	0.0049	0.070
300	1537	0.807	30.233	12.70	0.22	746	2150	0.46	23	76	< 1	1.1	6	100	0	0	0.047	0.0034	0.063
311a	2242	0.661	30.048	22.19	0.37	1049	1750	0.50	64	35	< 1	19	6,12	100	0	0	0.077	0.0060	0.098
311b	2242	0.661	30.048	22.19	0.37	1049	1750	0.50	64	35	< 1	19	6,12	100	0	0	0.070	0.0053	0.089
316	2408	0.641	29.977	21.38	0.36	990	1860	0.48	57	42	< 1	90	5,6	93.2	7	0	0.052	0.0040	0.066
321	1767	0.712	30.080	17.95	0.30	978	2330	0.50	58	41	< 1	10	5,6,12	94.1	6	0	0.066	0.0048	0.090
337	1326	0.836	30.227	15.85	0.27	651	2700	0.46	26	73	< 1	8	6	100	0	0	0.033	0.0024	0.047
359	2045	0.365	30.215	16.02	0.27	753	2530	0.49	39	65	< 1	266	5,6,11,12	98.2	2	0	0.042	0.0032	0.057
375	2072	0.267	30.110	17.93	0.30	778	2760	0.48	40	59	< 1	51	5,6,12	92.8	7	0	0.044	0.0033	0.063
398	2075	0.081	29.749	16.34	0.28	721	2090	0.45	53	46	< 1	60	6,12	100	0	0	0.042	0.0032	0.055
399	1839	0.041	29.720	15.57	0.27	683	2010	0.46	43	56	< 1	161	5,6,12	94	6	0	0.030	0.0027	0.039
9	1617	0.643	30.393	4.61	0.08	109	1660	0.51	29	70	< 1	296	6,12,13	80.8	0	19	0.019	0.0014	0.024
28	1417	0.101	30.462	6.81	0.12	108	1260	0.46	35	64	< 1	125	6,12,13	93.2	0	7	0.009	0.0006	0.010
24	1356	0.901	30.339	4.54	0.08	138	1460	0.39	37	72	< 1	5203	5,6,11,12	98.4	0.5	1	0.007	0.0005	0.009
538	1211	0.459	30.380	8.61	0.15	400	1900	0.50	61	38	< 1	320	5,6	61.2	38	0.8	0.052	0.0036	0.067

[a] Calculated with 2-km radius window.
[b] From TRMM calibrated data.
[c] From VCF (Vegetation Continuous Field, see methods).
[d] Contributing area
[e] 1: Undifferentiated sediments (Neogene); 2: Quartzite; 3: Holocene deposits; 4: Undifferentiated metamorphics; 5: Undifferentiated sediments; 6: Gneiss, granite, granodiorite; 7: migmatites; 8: Para-gneiss; 9:Quaternary-Tertiary sediments; 10: alluvial deposits;11: Amphibolite;12: Undifferentiated schist;13: volcanics
[f] Corrected for chemical erosion using relationship reported in Riebe and Granger (2013).

the residence time of quartz within vertically mixed soils, slowing exhumation of quartz through the uppermost meters of the surface, and resulting in biased (slower) rates (e.g., Riebe and Granger, 2013). Assuming that annual precipitation is an appropriate proxy for the extent of chemical weathering within a given region, we can correct our data for the presumed effects of chemical weathering based on relationships proposed in Riebe and Granger (2013).

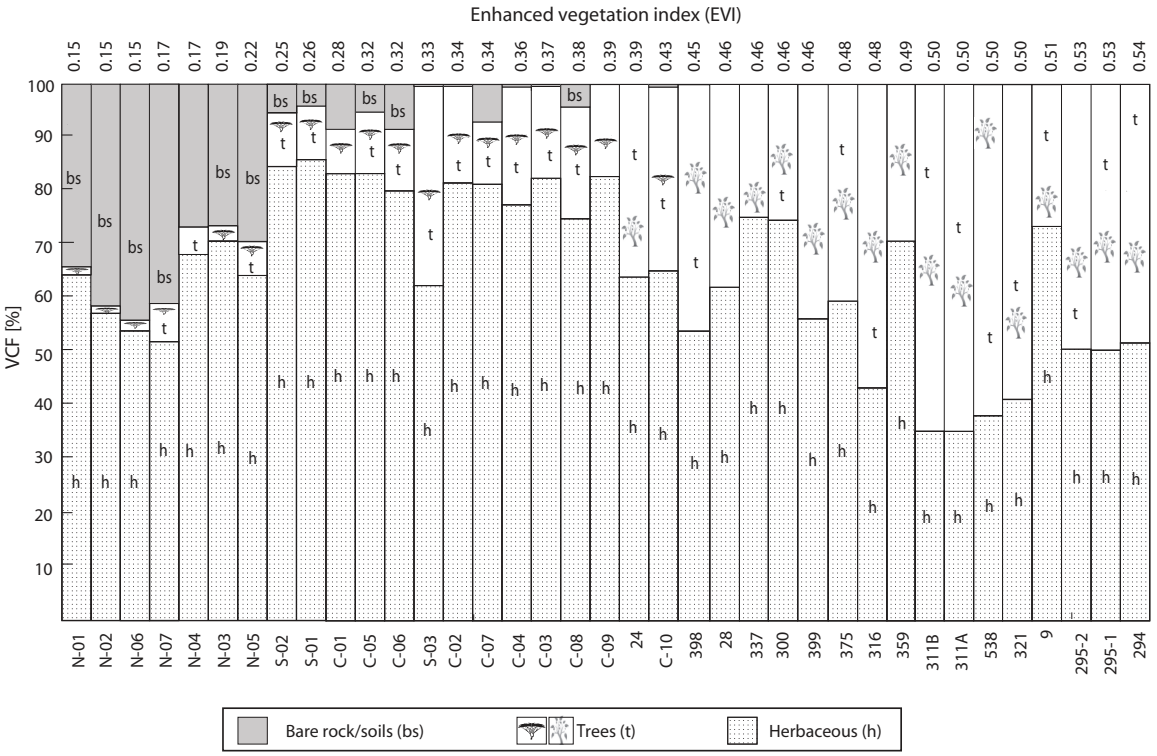

Figure 3.4 – Vegetation continuous fields (VCF) data summarized for each of the studied catchments in the Kenya Rift and the Rwenzori Mountains. Catchments are sorted from left to right according to their mean EVI value (shown on top). Sample names are shown at the bottom of each column. Note that sample names starting with N, C, and S correspond to the northern, central and southern rift sectors. Sample names without a preceding letter are from the Rwenzori Mountains.

However, the corrected data show only a slight increase in denudation rates for wetter catchments (Table 1; Fig. 3.7A) and do not eliminate the separation of the two scaling relationships.

The influence of human activity in the region for at least the past several thousand years in East Africa is another source of concern with respect to anthropogenically induced faster denudation and changes in land use (e.g., Dunne et al., 1978; Dunne, 1979). For example, Ba/Ca ratios in corals along Kenya's coast document a continuous increase of suspended sediment load in rivers draining eastern Kenya beginning at ca. A.D. 1900, which has been related to intensified land use (Fleitmann et al., 2007). As described earlier, recent soil erosion of up to 0.5 m could affect catchment mean denudation rates by ~30% (Bierman and Steig, 1996). However, because the highest denudation rates from the sparsely vegetated areas (which would be most affected by human disturbances due to their shorter integration times of ~4.6-7 kyr.; Table 2) are more than 5x higher than densely vegetated areas with equivalent hillslope gradients, human impact on our erosion-rate measurements is likely small relative to the size

of the signal, and it cannot explain the existence of the two scaling relationships. Furthermore, the full range of cosmogenic nuclide-derived denudation rates from East Africa (0.001-0.13 mm/yr) does not greatly exceed denudation rates based on modern sediment yields from catchments in the Kenya Rift with little to no human disturbance (0.007-0.075 mm/yr, assuming rock with a density of 2.65 g/cm^3 was eroded; Dunne et al., 1978; Dunne, 1979). This similarity supports our contention that human disturbance has limited influence on our denudation-rate results. That disturbance may be more important with respect to the EVI values, but as noted earlier, the strong positive correlation with precipitation (R^2 = 0.642; Fig. 3.5) supports the idea that much of the variation in vegetation cover is still a result of natural forcing.

Differences in lithology, vegetation cover, or rainfall could alternatively produce the two scaling relationships in the hillslope-gradient- denudation-rate data, with strong rock/soil (Dunne et al., 1978; Molnar et al., 2007; Hahm et al., 2014), dense vegetation (Dunne et al., 1978; Dunne, 1979; Collins et al., 2004; Vanacker et al., 2007), or a low frequency of intense storms (Tucker, 2004; Lague et al., 2005; Molnar et al., 2006; Turowski et al., 2009; DiBiase and Whipple, 2011) requiring a steeper gradient to achieve a given denudation rate. Although the quartz contributing regions are dominated by resistant metamorphic rocks (e.g., gneiss, quartzite, and migmatite), some catchments are underlain by significant proportions of Miocene to recent sediments (Fig. 3.7B; Table 2; see Appendix B; Smith, 1994; Bauer et al., 2012), which may contribute to higher denudation rates. Indeed, our fastest-denuding catchments that lie on the steep scaling relationship (C-01, C-05, C-06, C-07, and N-07) are underlain by 41%-68% sediments (Fig. 3.7B; Table 2). However, three samples that lie on the shallow scaling relationship (S-03, C-08, and C-10) are underlain by 23%-43% sediments (Fig. 3.7B; Table 2), making it difficult to explain the two scaling relationships based on lithologic differences alone.

The apparently minor influence of lithology (and sediments in particular) in explaining the two scaling relationships is counterintuitive, but it can be explained by considering that the portions of the catchments in Kenya covered by sediments have very low slopes (typically only up to a few degrees; see Appendix B); hence, those areas are unlikely to contribute much sediment despite their high erodibility. Indeed, the quartz contributing area of catchment S-02 is characterized by 100% sediments, but it has a very low median gradient of 0.03 (1.7°) and a denudation rate of only 0.001 mm/yr. In contrast, catchment 538 in the Rwenzori Mountains has slopes up to ~9° in the areas underlain by sediments (see Appendix B), suggesting that in that case, incision through the highly erodible sediments may contribute to faster denudation rates.

Differences in fracture/joint density can also contribute to variations in rock strength and hence erodibility (Molnar et al., 2007), but without detailed field surveys, this factor is difficult to quantify. Still, given the similar tectonic setting across our field area and our avoidance of

catchments crossed by faults, we do not expect significant differences in rock fracture density. Indeed, the regionally extensive faults that bound the rift-shoulder areas in northern Kenya are fault-line scarps, where mechanically more affected rocks in the vicinity of the former fault scarps have been removed (Hetzel and Strecker, 1994; Mugisha et al., 1997).

With respect to climatic properties of the catchments, we find no threshold value in annual precipitation (Fig. 3.7C) that appears to separate the different scaling relationships. However, considering vegetation cover, the steep scaling relationship (with lower gradients for a given denudation rate) includes samples from the most sparsely vegetated environments in the Kenya Rift (EVI < 0.35), while the shallow scaling relationship includes samples from the most densely vegetated parts of the western Kenya Rift and all of the samples from the Rwenzori Mountains (EVI > 0.35; Fig. 3.7D).

Two samples appear to be outliers in this division according to EVI. One sample from the Rwenzori Mountains (catchment 538) has a high EVI (0.50) but appears to lie on the steep scaling relationship. Although we cannot identify the reason for its higher denudation rate with certainty, within the Rwenzori data set, it is the only catchment with a significant exposure of relatively easily erodible Miocene to recent sediments (38%, vs. 0%-7.2% for all other catchments; Table 2; see Appendix B). In contrast, one relatively sparsely vegetated catchment from the Kenya Rift (S-03) appears to lie on the shallow scaling relationship, but its 23% sediment cover (Fig. 3.7B; Table 2) does not help to explain its relatively low denudation rate. Importantly, S-03 is the one catchment from the Kenya Rift with both a prominent knickpoint in the river profile and quartz-bearing rocks both upstream and downstream from the knickpoint (see Appendix B). If a higher proportion of sediment is derived from the steep, lower section of the catchment (which is wetter and more densely vegetated) compared to the gently sloping upper part, then the catchment characteristics such as slope, vegetation cover, and precipitation that we compare with denudation rates should also be weighted toward the characteristics within the steeper section. As such, the "effective" catchment characteristics would have a higher mean gradient, higher average EVI, and higher average yearly precipitation. Because the EVI averaged for the whole catchment is 0.33, it would only take a small increase in the proportion of sediment derived from the steeper part of the catchment to make the effective EVI fall above 0.35, and hence no longer appear to be an outlier.

Despite these two potential outliers, if we reanalyze our data after separating it into two groups (EVI > 0.35 and EVI < 0.35), some stronger correlations emerge. The more sparsely vegetated areas show a positive linear correlation with mean gradient (R^2 of 0.806, or 0.923 if sample S-03 is excluded), and the more densely vegetated areas show a positive linear correlation with an R^2 value of 0.666, or 0.779 if sample 538 is excluded (Fig. 3.7E). Also, when comparing denudation rates to mean annual precipitation, the sparsely vegetated areas show an improved positive linear correlation with an R^2 of 0.333 (or 0.384 if sample S-03 is excluded), while the densely vegetated area shows no correlation (R^2 of 0.002, or 0.006 if sample 538 is

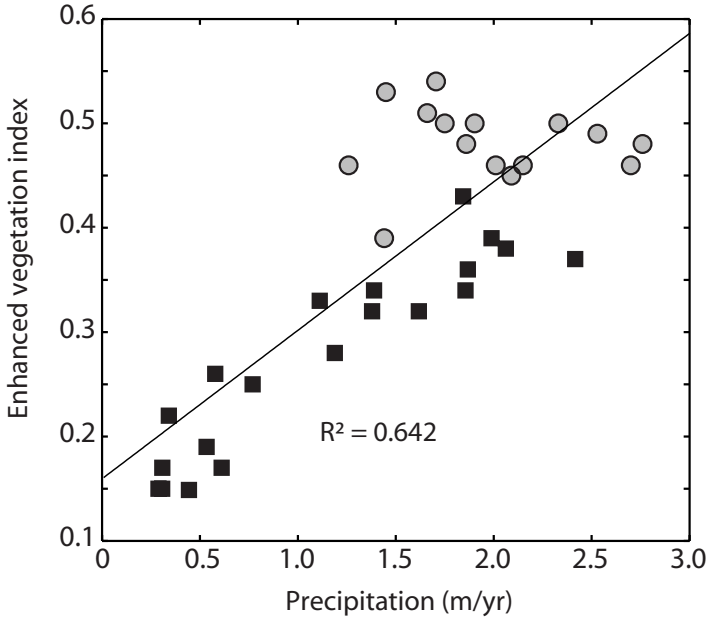

Figure 3.5 – Correlation between Enhanced Vegetation Index (EVI) and mean annual precipitation (m/yr) for sampled catchments in the Kenya Rift and the Rwenzori Mountains. Black squares for the Kenya Rift catchments, gray circles for the Rwenzori Mountain catchments.

excluded; Fig. 3.7F). Similar results were derived concerning the role of vegetation cover in Kenya on modern sediment yields, whereby more sparsely vegetated areas (in this case, areas more strongly affected by crop planting and grazing) were more sensitive to changes in runoff and slope compared with densely forested areas (Dunne, 1979). While other factors (lithology in particular) surely contribute to the variability in the data, our ability to separate the data along the two scaling relationships in the hillslope-gradient-denudation-rate plot according to a specific EVI value suggests that vegetation cover may be a primary factor explaining the two scaling relationships.

This interpretation of the importance of vegetation cover relies on the measurements for the steepest catchments in the Kenya Rift (samples C-08, C-09, and C-10) being robust. We have no reason to believe that they are unreliable; compared to the catchments we sampled farther north along the escarpment (C-01, C-05, C-06, and C-07), they have similar morphology and a similar distribution of rock types (Fig. 3.1D; see Appendix B), and we observed nothing in the field that would lead us to suspect that the measurements would be questionable. The EVI value of 0.35 that separates the different scaling relationships in our data corresponds to a change from predominantly herbaceous vegetation cover with at least some bare rock/soil and generally $<$20% trees at EVI values of $<$0.35 to 20%-64% trees and no bare rock/soil at higher EVI values (Fig. 3.4). While the distinct EVI value that separates the denudation- rate data in East Africa may point toward a threshold behavior of the sys-

tem associated with a change in erosion processes, we emphasize (1) that modern vegetation indices do not capture potentially important regional and/or time-integrated variations in vegetation cover on cosmogenic time scales, and (2) that recent changes in land use (and vegetation cover) may not strongly affect cosmogenic denudation rates. Also, other catchment differences with respect to lithology, climate, biology, soil type, and erosional processes exert additional influence on denudation-rate patterns in the data. For these reasons, we suggest that, although our data support a change in the effectiveness of dense vegetation cover in stabilizing hillslopes, the exact values reported here are likely to differ from those that may be identified in other landscapes, and that more extensive data sets may reflect transitional rather than threshold behavior. Indeed, more transitional behavior has been revealed in modern sediment yields as a function of different land-use types (Dunne, 1979).

3.5.2 Denudation Rates under Changing Climate Conditions

The integration time scale for cosmogenic denudation is equal to the absorption depth scale (i.e., ~60 cm in silicate rock; von Blanckenburg, 2005) divided by the denudation rate. Because the integration times of our samples from East Africa range from 4.6 to 437 kyr (Table 1), samples from slowly denuding regions are averaged over episodes in the past that were more humid than today, as indicated by periods of high lake levels (e.g., Garcin et al., 2012) with increased forest cover and decreased grasslands/ savannahs (deMenocal et al., 2000; Hessler et al., 2010; Bonnefille, 2010; Tierney et al., 2011; Wolff et al., 2011). Therefore, as we discussed already, our comparison with modern vegetation cover does not capture the time-integrated effects of vegetation shifts. A similar problem exists when attempting to compare variations in modern precipitation with denudation rates based on cosmogenic nuclides (e.g., Bookhagen and Strecker, 2012; Kober et al., 2007; Riebe et al., 2001; von Blanckenburg, 2005; Safran, et al., 2005; Portenga and Bierman, 2011; Scherler et al., 2014). However, if we assume that shifts in climate resulted in overall denser or sparser vegetation without significant changes in the relative distribution of vegetation cover, an idea supported by pollen records in East Africa (i.e., Hessler et al., 2010), then we can still use the modern vegetation indices to assess relative amounts of vegetation cover over similar integration times. For a given denudation rate, which corresponds to a specific integration time, more densely vegetated catchments have higher gradients compared with more sparsely vegetated ones (Fig. 3.7E). Viewed from this perspective, the stabilizing effect of dense vegetation (requiring a steeper hillslope gradient to achieve a given denudation rate) persists even when we consider a range of different integration times (multiple pairs of data points).

Although the cosmogenic data that we analyze often average denudation rates over several climate cycles, the behavior of the system that we infer, with maximum denudation rates occurring under low to moderate vegetation cover, provides insights into the ways in which shifts in climate and vegetation affect landscape denudation rates. For a given hillslope gradi-

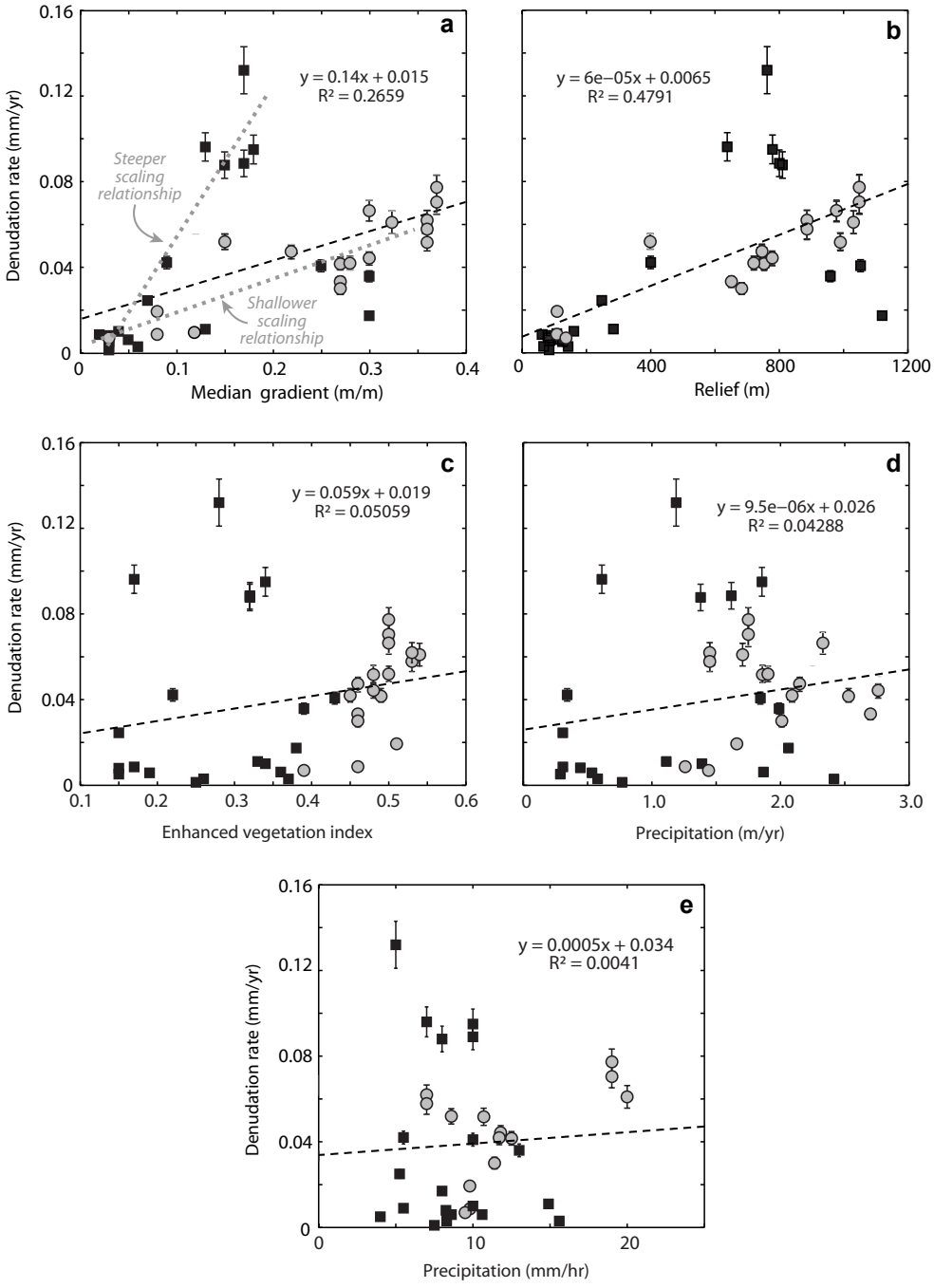

Figure 3.6 – Bivariate linear regression analyses of catchment mean denudation rates versus (a) median catchment gradient, (b) mean relief, (c) enhanced vegetation index (EVI), (d) mean annual precipitation, and (e) extreme events. Black squares for the Kenya Rift catchments, gray circles for the Rwenzori Mountain catchments. What appear to be two distinct scaling relationships (one steep and one shallow) in (a) are highlighted with dashed gray lines.

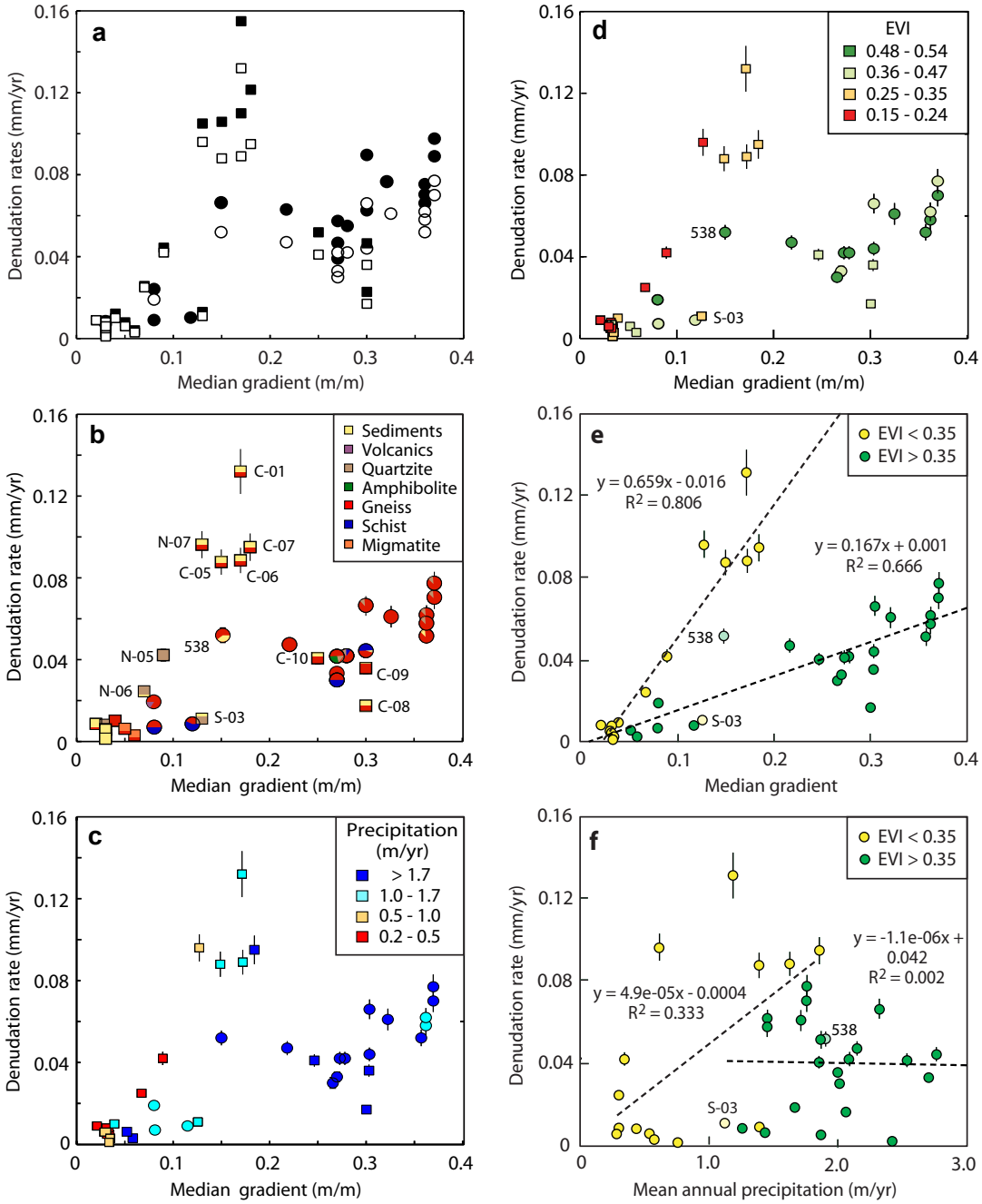

Figure 3.7 – Analysis of various catchment characteristics with respect to the two main scaling relationships in the plot of denudation rate versus median gradient illustrated in Figure 6a. (a) Plot of denudation rates that are uncorrected (open symbols) and corrected (filled symbols) for the effects of chemical weathering, based on the relationship proposed by Riebe and Granger (2013). Squares for the Kenya Rift catchments, circles for the Rwenzori Mountain catchments. Relationship between cosmogenic catchment mean denudation rates and median hillslope gradients for East Africa with points colored according to (b) the underlying lithology of the catchment, (c) mean annual precipitation, and (d) EVI. Squares for the Kenya Rift catchments, circles for the Rwenzori catchments. A threshold EVI value (0.35) appears to divide the data according to the two different scaling relationships. Two outliers (538 and S-03) are discussed in the text. More sparsely vegetated catchments (EVI < 0.35) show a greater sensitivity to (and better correlation with) both (e) hillslope gradient and (f) mean annual precipitation compared to more densely vegetated catchments (EVI > 0.35).

ent, the highest denudation rates occur in areas with intermediate vegetation cover (e.g., EVI < 0.35). In these regions, we anticipate that increased precipitation should initially increase denudation rates, but only until the vegetation cover densifies and lowers hillslope erodibility, provided that soils are thick enough to support denser vegetation (e.g., Knox, 1972). Supporting this inference, Dunne (1979) reported that long-term erosion rates in southern Kenya calculated from late Cenozoic erosion surfaces were lower during the wetter period that preceded the Quaternary.

The effect of vegetation cover on surface erodibility further implies that vegetation helps to control the shape and relief of mountain ranges, with densely vegetated mountains requiring higher slopes to achieve the same denudation rate as compared to more moderately vegetated ones, if all other factors are roughly equal.

3.6 Conclusions

Our new denudation-rate data from the Kenya Rift combined with previously published data from the Rwenzori Mountains show that variations in vegetation cover may explain differences in denudation rates across East Africa in a pattern consistent with our understanding of how vegetation cover affects surface erodibility: Areas with dense vegetation cover (EVI $>$ 0.35) yield relatively low denudation rates for a given hillslope gradient compared to those with lower values of vegetation cover. While this "threshold" value in EVI appears to explain the separation of our data along two scaling relationships in hillslope gradient versus denudation rate, a more extensive data set may reveal more transitional behavior. Also, we cannot rule out lithologic differences as contributing to the large difference in the scaling relationships. Nonetheless, if these results are applicable to other regions, the stabilizing effect of vegetation cover should exert a fundamental influence on the steady-state slopes of mountain belts and also help to explain complex erosional responses to changes in climate (or land use), particularly if they induce rapid changes between densely and sparsely vegetated conditions.

Aknowledgments Torres Acosta was supported by the Deutsche Forschungsgemeinschafts (DFG) Graduate School GRK1364 "Shaping Earth's Surface in a Variable Environment", funded by the DFG through a grant to Strecker (grant STR 373-20/1). We thank the government of Kenya and the University of Nairobi for research permits and support. Schildgen was supported by the DFG's Emmy Noether Programme (grant SCHI 1241/1-1). We thank S. Roller for providing raw data from the Rwenzori Mountains. We thank Will Ouimet, Jean Dixon, and Christoff Andermann for discussions, Tom Dunne, Arjun Heimsath, and Editor Eric Kirby for their very thorough and constructive reviews, and Darryl Granger for his constructive review of an earlier version of the manuscript.

Chapter 4

Climate-controlled variability of Holocene erosion rates in the northern Kenya Rift

Abstract

Fluvial terrace deposits from the Baragoi River in the Suguta Valley (northern Kenya Rift) reflect the importance of climatic change on denudation rates over time, as revealed in the concentration of cosmogenic ^{10}Be in detrital quartz grains. We report paleo-denudation rates from early Holocene (~11 ka) fluvial sediments that are at least six times faster than the present, whereas paleo-denudation rates from the middle Holocene (~8.5 ka) are only two times faster than present-day rates. These rate changes during the course of the African Humid Period (~14.5-5.5 ka) may reflect a strong increase in precipitation, runoff and erosivity in the beginning of the arid-humid transition at about 11 ka. These changes resulted in the filling of the Suguta Valley with an extensive (~2150 km^2) lake with an overflow toward Lake Turkana in the north, coeval with the maximum highstand of other lakes in East Africa at that time. Precipitation at least 20% higher than today and a probable higher fluvial transport capacity during this wet period may explain the higher denudation rates during the early-mid Holocene, before the landscape stabilized again.

4.1 Introduction

Climate change in tropical and subtropical regions associated with rapid changes in precipitation, erosion, soil degradation, and vegetation cover is the focus of many recent research efforts to better understand the impact of Global Change on surface processes (e.g., Trenberth, 2011; Pelletier et al., 2015). Paleo-environmental changes recorded by proxy indicators in marine and terrestrial sediments may serve as powerful analogs of landscape response to both

present-day climate variability and future climate change (Shanahan et al., 2009; Tierney et al., 2013). In this context the sedimentary basins of the East African Rift System (EARS) have recorded the impacts of past climate oscillations on surface processes in a tropical region and may furnish valuable information on how future shifts in rainfall and vegetation patterns may impact the environment (Verschuren et al., 2000; Tierney et al., 2008; Wolff et al., 2011). The equatorial Kenya Rift of the eastern branch of the EARS is well suited for such comparative studies, as sedimentary basins of different size, past and present-day environmental conditions host sedimentary sequences that record the details of climatic variability and changing erosional regimes (Behrensmeyer, 2006; Bergner et al., 2003; Trauth et al., 2005; Wolff et al., 2011). To date, there is only limited knowledge about past erosional processes in East Africa with respect to the erosion mechanisms, erosion rates, and how such changes may have been related to fluctuations in the amount and distribution of rainfall.

In other regions that have shown to be very sensitive toward climate change it has been suggested that increased rainfall and greater runoff availability may result in an acceleration of erosion rates (Summerfield and Hulton, 1994; Montgomery et al., 2001; Heimsath et al., 2010; Moon et al., 2011; Bookhagen and Strecker, 2012). However, the relationship between erosion rate and rainfall amount is not always straightforward (e.g., Safran et al., 2005; Portenga and Bierman, 2011) and uncertainty remains regarding the timing and possible lag times. This is in part due to factors such as evapotranspiration, soil production, and vegetation cover which counteract the expected increase in runoff and/or decrease the surface erodibility (e.g., Istanbulluoglu and Bras, 2005; Vanacker et al., 2007; Molina et al., 2008; Torres Acosta et al., in press).

In East Africa, various environmental indicators suggest dramatically different climate conditions in the past; these include pollen spectra and plant leaf wax carbon isotopic composition documenting the expansion of forests at the expense of grasslands and vice-versa (Vincens et al., 2007; Bonnefille, 2010; Cerling et al., 2011; Feakins et al., 2013), and lacustrine sediments that record oscillating lake levels with co-varying changes in mineralogical composition and fossil content (Trauth et al., 2003; Bergner et al., 2009; Owen et al., 2014). In the equatorial regions, these episodes were characterized by alternating periods of higher and lower precipitation (deMenocal et al., 2000; Bergner et al., 2003; Garcin et al., 2009, 2012; Hessler et al., 2010; Junginger and Trauth, 2013; Junginger et al., 2014). However, the details of past erosional regimes associated with these environmental conditions, the efficacy of sediment routing from rift-shoulder areas to the basins, and the overall nature of changing hydrological conditions are still enigmatic.

Here, we compare erosion-rates from the Baragoi River catchment at the southeastern margin of the Suguta Valley in the northern Kenya Rift (Fig. 4.1) during the African Humid Period to more recent erosion-rate estimates. Although being located at the Equator, this area of the rift is now one of the driest regions of Kenya, with 300 to 500 mm/yr precipitation, ephemeral

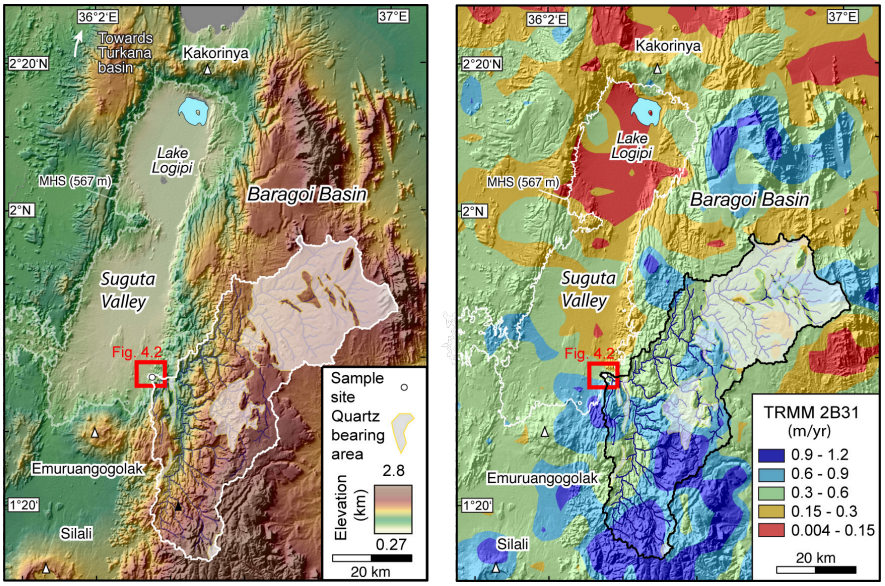

Figure 4.1 – Overview map of the Kenya Rift with the Suguta Valley and the Baragoi River drainage area A) DEM map of the drainage area, B) Precipitation map of the drainage area.

runoff (Ojany and Ogenoo, 1973), and sparse vegetation. Specifically, we compare our ^{10}Be present-day basin-wide erosion rates derived from river sands of the Baragoi River catchment in the Suguta Valley of the northern Kenya Rift to new ^{10}Be paleo-erosion rate estimates from quartzitic sands collected from well dated Holocene deltaic and sandy intercalations from lacustrine sequences (Fig. 4.1). To better define the parameters that currently influence erosion in the Baragoi River catchment and to compare this area to presently humid environments in the region of the Kenya Rift, which may be analogous to past humid conditions in northern Kenya, we furthermore report the drainage basin's morphometric characteristics (slope, relief, and mean elevation), precipitation, and vegetation cover. Our analysis demonstrates how short-lived, climate-controlled surface processes on millennial timescales fundamentally impacted erosion, sedimentation and landscape evolution in the Northern Kenya Rift during the early Holocene African Humid Period.

4.2 Principal aspects of tectonic and climatic conditions in the northern Kenya Rift

In the the Kenya Rift, numerous faulted Holocene basaltic flows and small fault scarps along the volcano-tectonic axis and at the rift flanks attest to active tectonism. In its northernmost sector, the Suguta Valley, ongoing extension inferred from both space geodetic data (Stamps et al., 2008) and from field observations of fault heave (Melnick et al., 2012) is ~4 mm/yr. Late Cenozoic normal faulting and rift-shoulder uplift have created pronounced relief contrasts,

generating accommodation space for sediments in the lowest sectors of the basins. The sedimentary fills of these basins record the erosional history of the rift-shoulder areas, which integrate the complex relationships between tectonics, changing climatic conditions, and resulting shifts in depositional environments (Dunkley et al., 1993; Saneyoshi et al., 2006; Feibel, 2011).

Today, the Kenya Rift is impacted by large seasonal shifts of the Intertropical Converge Zone (ITCZ) and the Congo Air boundary (Nicholson, 1996). Regional moisture transport and precipitation are influenced by the elevation of the East African Plateau, the rift shoulders of the East African Rift, and the effects of high evapotranspiration in those rift sectors that are bordered by orographic barriers (Nicholson, 1996; Bergner et al., 2009).

During the African Humid Period between approximately 11.8 and 8.5 ky, paleo-Lake Suguta rose more than 300 m (Truckle, 1976; Garcin et al., 2009). At that time it overflowed into the Turkana basin and was connected with the White Nile (Garcin et al., 2012 and references therein). The early Holocene lake-level change in the Suguta Valley had a far-reaching impact on the base-level of rivers with large catchments sourced in the rift-shoulder areas, leading to the formation of voluminous delta deposits intercalated with lacustrine strata in the area where the Baragoi River enters the Suguta Valley (Figs. 4.2 and 4.3).

4.3 Tectonic stratigraphic and hydrologic setting of the Suguta Valley and the Baragoi River catchment

The Suguta Valley is an asymmetric graben bordered by a major fault on the west and an antithetically faulted monocline on the east, involving multiple escarpments cut into Miocene to Quaternary volcanic and sedimentary sequences (Baker, 1963; Dodson, 1963; Bosworth and Maurin, 1993; Dunkley et al., 1993; Saneyoshi et al. 2006). The eastern rift flanks are mainly comprised of basaltic volcanic flows, intercalated with trachytes, pyroclastic material, and sediments (Dunkley et al., 1993; Saneyoshi et al., 2006). These units cover late Proterozoic gneissic basement rocks that are exposed in the rift-shoulder areas of the upper Baragoi catchment to the east at elevations of about 1700 m (Fig. 4.1). Quartz-bearing units cover approximately 900 km^2 of the Baragoi catchment out of a total area of 2103 km^2. In the southeast, at ca. 1.627°N - 36.458°E, the Baragoi River enters the Suguta Valley (Fig. 4.1) through deeply incised volcanic strata as well as delta and lake sediments that constitute the Baragoi paleo-delta. The incision has left a set of well-defined degradational terraces carved into the sediments (Fig. 4.3). The base of the terraces and the delta deposits, which coincides with the present-day river bed of the Baragoi, is composed of coarse sand and conglomeratic gravel, intercalated with silty, fossiliferous lacustrine deposits upsection (Garcin et al., 2009; Junginger et al., 2014). The exposed thickness of these units is approximately 110m (Fig. 4.3)

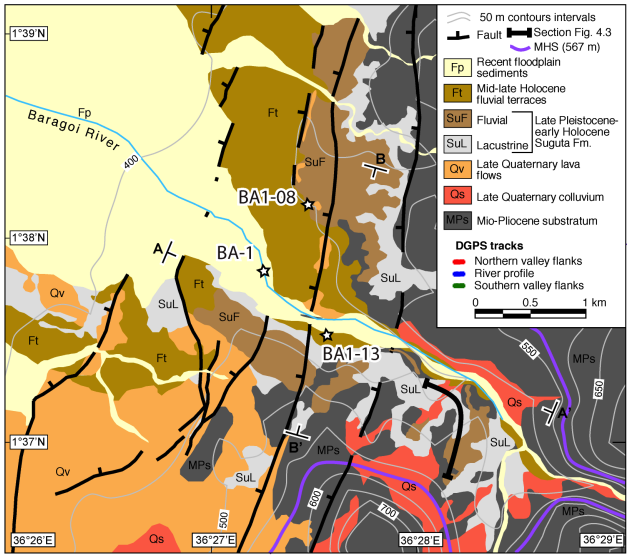

Figure 4.2 – Geological and structural map of the Baragoi paleo-delta. White starts denote sampling site. B-B' shows a cross section of the Baragoi mouth with direction NNE-SSW. A-A' shows a section along the river SSE-NNW.

The Suguta Valley is bordered to the north by the Quaternary Barrier eruptive center and to the south by the Emuroangogolak caldera volcano, which prevent external drainage conditions (Fig. 4.1). As a result, the northern Suguta Valley is covered by the shallow Lake Logipi, which is the base level for the ephemeral Baragoi River at approximately 275 m elevation. The Baragoi River carries water mainly following storms during the rainy seasons from March to May and from October to November (Morgan, 1971; Griffiths, 1972, East African Meteorological Department, 1975).

Throughout the Quaternary, the Suguta Valley has been affected by multiple volcanic eruptive events and faulting episodes (Dunkley et al., 1993). These volcano-tectonic processes generated the morphology that confined the highstand of Lake Suguta during the Holocene African Humid Period (Truckle, 1976; Dunkley et al, 1993; Garcin et al., 2009; Junginger and Trauth, 2013). Numerous regressive shorelines of the Holocene paleo-lake levels are well preserved along the flanks of the Suguta Valley, attesting to the former highstand at 570 m (Fig.4.2) during the early Holocene and the subsequent, progressive lake-level fall (Melnick et al., 2012) to the present-day position of the regional base level at 275 m.

4.4 Methods

4.4.1 Sampling of river sands and material for ^{14}C-dating

To assign an age and to determine an erosion rate for the quartz-bearing sands in the deltaic deposits of the Baragoi paleo-delta, we first chose a well-exposed, approximately 110-m-thick section of fluvial sands and conglomerates on the south side of the Baragoi River that are intercalated with silty, charcoal-bearing lacustrine strata (sample BA1-13, at 1.632°N, 36.473°E)(Fig. 4.2). The age relationships at this first outcrop are constrained by two samples of ^{14}C-dated charcoal (samples DM13-BA1 and DM13-BA2). In addition, we sampled snails in the lacustrine intervals (Melanoides tuberculata). The position of the samples was measured with high-precision Leica 1200 differential global position system. The sand sample collected for ^{10}Be analysis (BA1-13) is ~100 m beneath the overlying delta strata, but due to subsequent incision and a recent landslide (less than one year prior to sampling), the sampling site was recently exposed by a rotational slump after the rainy season in 2013.

A second quartz-sand bearing section was selected in lacustrine deposits with intercalated sands north of the Baragoi River (sample BA1-08, at 1.636°N, 36.460°E) (Fig. 4.2). The strata from this site are well correlated to the detailed stratigraphic column described by Junginger et al. (2014), which is located ~800 m to the southeast and which constrained by ^{14}C-dating of snails and charcoal. The sand sample collected for ^{10}Be analysis (BA1-08) is ~5 m beneath the overlying delta strata, but due to subsequent incision, the horizon now lies 50 cm beneath a degradational terrace surface.

Modern catchment-mean denudation rates from in situ produced ^{10}Be cosmogenic nuclide measured in detrital quartz sand was collected from the Baragoi River (sample BA-01) at the outlet of the catchment (Fig.4.2)

Sample preparation for ^{10}Be cosmogenic radionuclide analysis was carried out at the University of Potsdam and at the GeoForschungs Zentrum Potsdam (Germany), following the procedures described in Kohl and Nishiizumi (1992). AMS analyses were performed at ETH Zurich, Switzerland and at the Cologne AMS facility of the University of Cologne (Germany). Details on the procedures of the ^{10}Be analysis are reported in Torres Acosta et al., (2015).

^{14}C-analysis

Charcoal fragments of sample DM13-BA1 and DM13-BA2 were approximately 250 μm long and weighed $\geq$ 20 mg. For the snail shells, more than 10 mg per sample were collected for analysis. Sample preparation was performed at the University of Potsdam. ^{14}C-analyses were carried out at the Leibniz-Laboratory for Radiometric Dating at the Christian-Albrechts-Universität in Kiel (Germany) and at the Pozna' Radiocarbon Laboratory (Poland). The ages were calibrated with CALIB 5.0.1. (Stuiver and Reimer, 1993) and IntCal013 curve (Reimer et

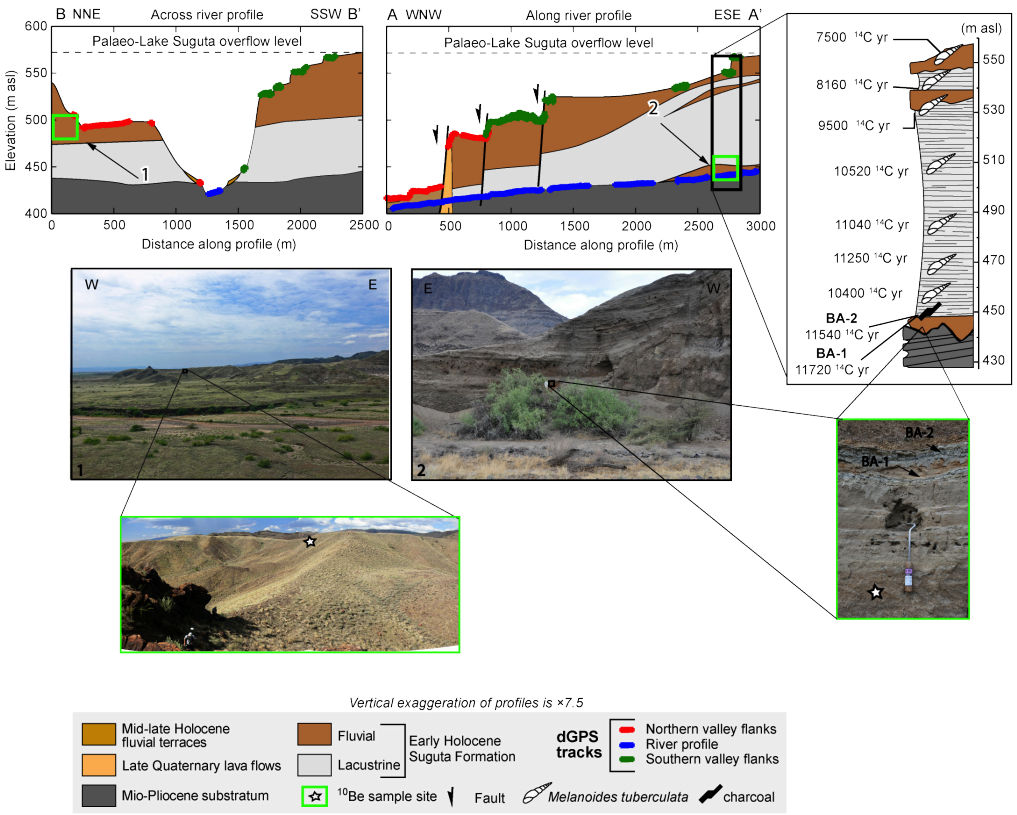

Figure 4.3 – Sampling site and sections along and across the Baragoi mouth.

al., 2004) and reported in cal. yr BP and in cal. ka BP (calendar year and kilo year before Year 1950, respectively).

^{10}Be analysis

To calculate paleo-denudation rates from the concentration of ^{10}Be in the detrital sand deposits of the deltaic strata, we must consider how post-depositional production and decay of cosmogenic ^{10}Be has altered the initial ^{10}Be concentration at the time of deposition (e.g., Schaller et al., 2002). Due to the young age of the deposit (11 kyr BP), decay of ^{10}Be in the deposit is insignificant. In terms of post-depositional production, rapid sediment deposition at the site (~25 mm/yr based on the dated stratigraphy) coupled with shielding from the lake water minimizes significant nuclide accumulation during burial. Subsequent incision through the strata has also likely resulted in minimal post-depositional production. For sample BA1-13, its very recent exposure from a depth of ca. 3 m following the slump, leads us to assume no nuclide accumulation during subsequent exposure. For sample BA1-08, collected from 50 cm beneath a degradational terrace, post-depositional production is only on the order of 10% the

surface production rate (~3.6 atoms/(g*yr)). While a precise exposure age of the degradational terrace is needed to properly calculate nuclide accumulation since incision, the total amount is likely to be very low. As such, we proceed with paleo-erosion rate calculations assuming no post-depositional accumulation. If our assumption of minimal post-depositional accumulation were wrong, and a significant amount has indeed accumulated, this would mean that our calculated paleo-erosion rates are minimum rates.

Paleo-erosion rates were calculated following Balco et al. (2008) and using the Cronus calculator (ver. 2.2; http://hess.ess.washington.edu/). We relied on the original ICN standard (07KNSTD and BEST433) as reference and used a value of 5.0 x10-7 yr^{-1} for the decay constant for ^{10}Be (Chmeleff et al. 2010) which is equivalent to the ^{10}Be half-life of 1.387 $\pm$ 0.012 Myr, (Korschinek et al., 2010).

4.4.2 Morphometric and environmental characteristics

Using an SRTM 90-m-resolution digital elevation model and ArcGIS®software we determined median slope, median relief, and mean elevation of the drainage area. In addition, for the Baragoi River catchment, precipitation data were determined from the Tropical Rainfall Measuring Mission (TRMM) 2B31 data provided by NASA (Bookhagen and Strecker, 2008); information on the present-day vegetation cover was obtained from the Moderate Resolution Imaging Spectroradiometer (MODIS) data of the USGS (ORNL DAAC, 2012).

4.5 Results

Charcoal and snail shells dated with the ^{14}C method provided ages between 7,500 and 11,700 cal yrs BP (Table 4.1). The ages of the snails were corrected taking into account a lake reservoir effect of 1900 years according to Junginger et al., (2014). The depositional age of the fluvial sediments where sample BA1-08 was collected (located at 479 m asl) is of 8,570 cal. yr. BP (set by sample BG08-31-75 located at 490 m asl., Junginger and Trauth, 2013). For sample BA1-13 (located at 440 m asl), the age must be slightly older than ~11,720 cal. yr (cf. sample DM13-BA1). Indeed, ^{14}C sample DM13-BA1 was collected ~30 cm above ^{10}Be sample BA1-13 and both sampled strata were conformable (Fig. 4.3). The stratigraphic position of these samples and their ages thus reflect the culmination of the African Humid Period in the Suguta Valley. The ages are compatible with the timing of high lake levels in the Suguta Valley and lake-level oscillations in northern Kenya during the African Humid Period (Garcin et al., 2009; 2012).

Our new paleo-denudation rates determined for samples BA1-08 and BA1-13 are 0.016 $\pm$ 0.001 and 0.062 $\pm$ 0.004 mm/yr respectively. They are therefore significantly higher than our basin-wide erosion rates of 0.011$\pm$ 0.001 mm/yr derived from present-day fluvial sands in the Baragoi River, but they are comparable to independently derived paleo-erosion rates of

Table 4.1 – Radiocarbon ages Baragoi section.

Table 4.1. Radiocarbon ages Baragoi section

Sample ID	Lat.	Long.	altitude[1]	Material[2]	^{14}C age	Reservoir corrected[3]	uncertainity	Cal. Age
	(°N)	(°E)	m a.s.l.		(yr BP)	(1900 yr)		(cal. Yr BP)
KIA 36867	1.632	36.473	540.1	M	9210	7310	50	8160
KIA 36868	1.632	36.473	532.1	M	10295	8395	55	9500
KIA 36869	1.632	36.473	501.2	M	11200	9300	60	10520
KIA 36870	1.632	36.473	489.7	M	11450	9550	60	11040
KIA 42911	1.632	36.473	~450	M	9910	9910	40	11250
DM13-BA1	1.632	36.473	~440	C	10040	-	40	11540
DM13-BA2	1.632	36.473	~440	C	10110	-	50	11720

[1] *DGPS and Garmin e-trex 30*

[2] *Melanoides tuberculata(M), Charcoal (C)*
[3] *Reservoir corrected following Junginger, (2011)*

~0.04mm/yr based on volumetric calculations of deltaic and lacustrine deposits in the Baragoi area (Garcin et al., in prep.).

The morphology of the Baragoi River drainage area is characterized by a median slope of 3.6°, a median relief of 180 m, and a mean elevation of 1296 m. The maximum relief is ~1200 m. The mean annual precipitation (MAP) is ~500 mm/yr and the enhanced vegetation cover index (EVI) is 0.15. The data are summarized in Table 4.2.

4.6 Discussion

Our paleo-erosion rates of 0.016 ± 0.001 and 0.062 ± 0.004 mm/yr suggest a two- to six-fold erosion-rate increase during the African Humid Period compared to the present-day, basin-wide erosion rate of 0.011 ± 0.001 mm/yr. Theoretically, higher erosion rates in this environment could have been associated with an increase in relief contrasts resulting from uplift along the rift flanks, including changes in river longitudinal profiles or the stream capture in the basement-rock sectors of the rift shoulders. However, there is no evidence in support of such changes in the fluvial network of the rift-shoulder catchment, nor is there any depositional, morphologic, or structural evidence for accelerated faulting during the early Holocene. In general, the rates of normal faulting and extension appear to have been steady throughout the late Pleistocene and the Holocene (Dunkley et al., 1993; Melnick et al., 2012). Assuming that the size of the Baragoi River catchment, the morphologic characteristics, the exposure of quartz-bearing rocks, and tectonic activity have not changed significantly over the short time span of the Holocene, it appears more likely that changes in climate as well as potentially in vegetation cover forced the increase in erosion rates.

Table 4.2 – Cosmogenic nuclide analytical data Baragoi samples

Sample ID	Elevation	Latitude	Longitude	^{10}Be atoms[a] x 10^3	^{10}Be atoms x 10^3 (1σ)	Surface Production rate[b]		Denudation rate	Denudation rate uncertainty	Integration time	Median slope	Median gradient	Median relief[c]	Mean annual rainfall[d]	EVI	Catchtment area[e]
						Muogenic	Spallogenic									
	(masl)	(°N)	(°E)	(atoms/g_{qtz})	(atoms/g_{qtz})	(atoms/(g_{qtz}* yr))	(atoms/(g_{qtz}*yr))	(mm/yr)	(1σ)	(kyr)	(°)	(m/m)	(m)	(mm/yr)		(km^2)
Baragoi (river sands)																
BA-01	426	1.627	36.458	470	19	0.3	9.4	0.011	0.0011	53	3.60	0.06	180	500	0.15	877
Baragoi (terraces)																
BA1-08	479	1.636	36.460	276	10	0.2	3.8	0.016	0.0013	-	-	-	-	-	-	-
BA1-13	440	1.632	36.473	77	3	0	4	0.062	0.0043	-	-	-	-	-	-	-

[a] *Standard used for normalization was 07KNSTD; BEST433*
[b] *Production rate according to time-dependent Lal/Stone scaling, see details in Balco et al. (2008).*
[c] *Calculated with 2-km radius window.*
[d] *From TRMM calibrated data (Bookhagen and Burbank, 2006;Bookhagen and Strecker, 2008)*
[e] *Contributing area*

The increase in early Holocene erosion rates is remarkable, given the fact that subsequently to a marked dry period contemporaneous with the Younger Dryas event (Junginger et al., 2014) Lake Suguta must have been characterized by a rising base level, which finally stabilized at ~300 m above the present-day position of Lake Logipi (Garcin et al., 2009) - the present-day shallow water vestige of Lake Suguta. While a drop in base level is expected to result in a wave of incision that may propagate far upstream, a rise in base level should cause deposition at the channel outlet, and aggradation along a limited upstream extent (Schumm, 1993). The base-level changes in the Suguta Valley were accompanied by the formation of the Baragoi paleo-delta deposits coupled with upstream aggradation. This aggradation is documented by thick conglomeratic fills that laterally expand to the outlet of the deeply incised Baragoi gorge in the Mio-Pliocene volcanic rocks (Fig. 4.2). These early Holocene conglomeratic and sandy fills were deposited over an erosional paleo-topography, where the Baragoi gorge had reached a level of late Pleistocene/early Holocene incision comparable to the present-day.

Our new radiocarbon dates obtained from the basal sectors of the exposed Baragoi fill record the onset of aggradation (Fig. 4.3) at ~11.7 ky. This age is in line with the well-dated sequence of laterally equivalent lacustrine strata with sandy intervals farther north analyzed by Junginger et al. (2014). Based on these relationships, we conclude that major changes involving a rise in base level and faster erosion in the upstream catchment areas must have taken place in the Suguta Valley during the early Holocene. In the context of regionally available data on the evolution of the African Humid Period (see Garcin for et al., 2012 for a review), we suggest that the high paleo-erosion rates we measured from the Holocene deposits resulted from an increase in precipitation and runoff. This inference is corroborated by the documented strong variability of the hydrologic system in northern Kenya in response to the precession-controlled changes in insolation (Garcin et al., 2009), which forced the African Humid Period between 14.5 and 5.5 ka BP.

The inference of higher erosion rates being related to a climatic shift toward wetter conditions during the African Humid Period at first appears incompatible with our earlier studies of modern erosion rates in Kenya and the Rwenzori Mountains (chapter 3). Modern erosion-rate patterns in those areas suggest that regions characterized by an Enhanced Vegetation Index of >0.35, typical of areas with higher rainfall and dense vegetation, record lower erosion rates than dry regions with scarce vegetation cover and an EVI of <0.35. More specifically, these studies revealed that for a given hillslope gradient, the highest erosion rates occur in those regions of the rift that are characterized by low amounts of rainfall and intermediate vegetation covers. Today, the Baragoi catchment is characterized by an EVI <0.35 and low erosion rates. In this context, we hypothesize that environments that are characterized by low amounts of rainfall and scarce vegetation cover would have been strongly impacted by erosive processes during the initial stages of a wetter climate episode. It can be envisaged that a shift toward a climate system with more frequent, stronger rainfall events would lead to increased stream

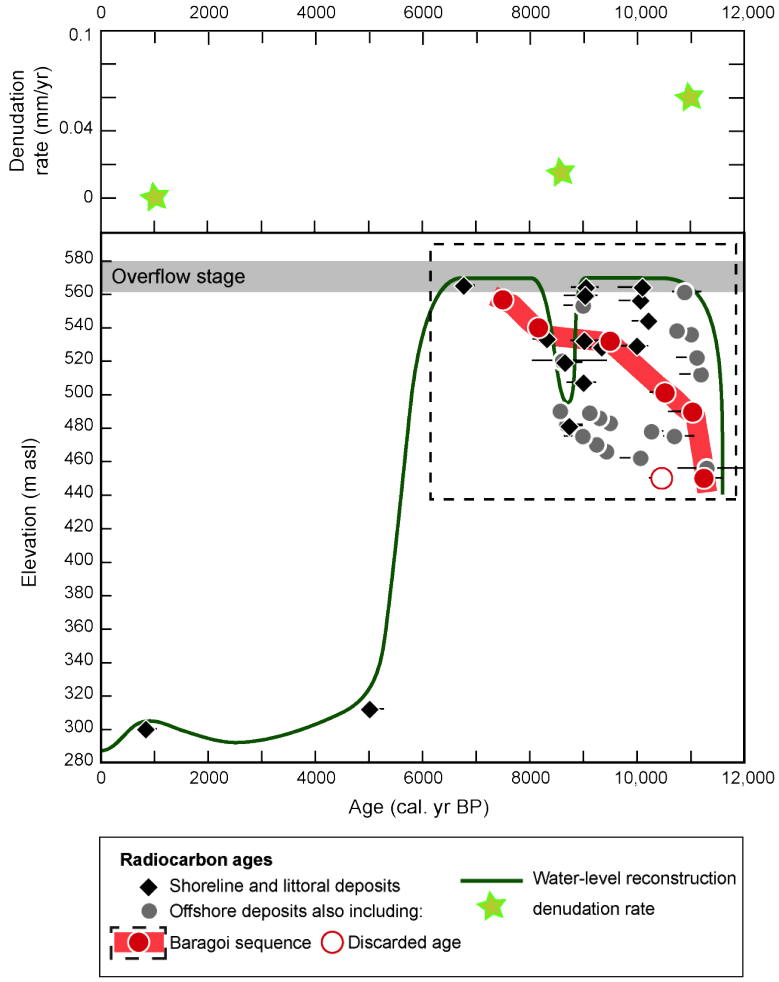

Figure 4.4 – Lake level fluctuations during the Holocene in Baragoi. Relationship between denudation rates and lake levels over time. Red dots denote radiocarbon ages of the Baragoi section. Gray circles and black diamonds denote radiocarbon ages by Junginger et al., (2014) and Garcin et al., 2009.

power, downcutting, lateral scouring, and ensuing slope failures, causing higher sediment-production rates. Such a scenario is compatible with our paleo-erosion rate data, particularly with very high erosion rates low within the stratigraphy.

To explain the decrease in erosion rates upward within the stratigraphy and to reconcile our inferred paleo-environmental scenario of humid conditions and a more erosive climate during the African Humid Period with the present-day low erosion rates in the densely vegetated humid sectors of the rift flanks (Fig. 4.4), we suggest that there is a lag time in landscape response to climatic forcing. We infer that the onset of wetter conditions during the early Holocene strongly impacted the scarcely vegetated, partly barren land surface, which resulted

from the preceding dry period contemporaneous with the Younger Dryas event, when Lake Suguta was most probably desiccated (Junginger et al. 2014), and caused initially high erosion rates. Over time, however, protracted humid conditions would have led to the establishment of more stable hillslopes associated with denser vegetation. In analogy with the present-day relationships between erosion rates and vegetation cover in Kenya, we suggest that the early Holocene changeover to wetter conditions in a climatic threshold region caused an initial strong increase in erosion rates, superseded by a transition to environmental conditions where weathering and soil formation (e.g., Knox, 1992) ultimately provided the substrate for a denser and protective vegetation cover (e.g., Bull and Kirkby, 2002), which in turn led to a decrease in erosion rates.

4.7 Conclusions

Cosmogenic ^{10}Be-derived paleo- and modern catchment-mean denudation rates of fluvial-lacustrine sediments of the Baragoi river catchment compared with reconstructed lake-levels, document coupled changes in environmental conditions and erosion rates during the early and middle Holocene in northern Kenya. Cosmogenic ^{10}Be nuclide concentrations in sand deposits of the Baragoi paleo-delta document a large increase in denudation rates during the culmination of the African Humid Period, coinciding with a rapid shift to wetter climatic conditions. We suggest that initially, increasing precipitation that resulted in the formation of a 300-m-deep lake led to greater runoff and rapid hillslope erosion. To explain the observed decrease in erosion rates during the middle Holocene (upsection), we suggest that persisting wetter conditions may have ultimately led to increased vegetation cover in the area, which would have helped to stabilize and protect hillslopes. Thus, a lag time likely existed between the onset of wetter conditions and the establishment of dense, stabilizing vegetation cover across the landscape. Present-day lower erosion rates may reflect precipitation-limited conditions in the catchment today, as the sparse vegetation likely provides little protection of the hillslopes from runoff erosion processes. We conclude that climate variability is a principal factor modulating temporal variability of denudation rates in semi-arid regions, particularly in equatorial East Africa.

Acknowledgements V.T.A was supported by the DFG Graduate School GRK1364 Shaping Earth's Surface in a Variable Environment, funded by the Deutsche Forschungsgemeinschaft (DFG) through a grant to M.R.S. (grant STR 373-20/1). We thank the Government of Kenya and the University of Nairobi for research permits and logistical support. T.F.S. was supported by the DFG's Emmy-Noether-Programme (grant number SCHI 1241/1-1). We thank Sara Savi for discussions and Görkem Sivri for sample preparation.

Chapter 5

Talas-Fergana Fault Cenozoic timing of deformation and its relation to Pamir indentation

Abstract

Regional strike-slip faults are widely distributed in continental interiors and play a major role in the distribution of far-field deformation due to continental collisions. Constraining the deformation history of the Talas-Fergana Fault (TFF), one of the largest of such faults in the Himalayan deformed interior, is vital to comprehend the hinterland kinematics of the India-Asia collision. New apatite fission track results from the northwest Tien Shan define a rapid exhumation event at ~25 Ma. This event is correlated with a synchronous pulse in the South Tien Shan, implying that both ranges experienced a simultaneous onset of rapid exhumation. We suggest that strike-slip motion along the TFF commenced at ca. 25 Ma, facilitating counter-clockwise rotation of the Fergana basin and enabling exhumation of the linked horsetail splays. Pamir indentation, located south of the Western Tien Shan, is postulated to be underway by ~20 Ma. Recently published results suggest synchronous strike-slip deformation in the western Tarim basin and eastern flank of the Pamir. Based on our results and published data we are able to connect Tarim and Pamir deformation to the onset of TFF slip. We suggest that this preexisting regional structure was responsible for transferring Pamir-induced shortening to the northwest Tien Shan.

5.1 Introduction

The Tien Shan is a ca. 2500 km long range with peaks up to 7400 m extending from Uzbekistan and Kyrgyzstan far into western China (Fig. 5.1). It is one of the best examples of an intracontinental orogen and has been intensively studied to understand the far-field effects

of continental collision (e.g., Molnar & Tapponnier 1975, Allen et al. 1991, Hendrix et al. 1994) and the role of pre-existing discontinuities in a deforming orogen (e.g., Jolivet et al. 2010; Selander et al. 2012; Macaulay et al., 2013). However, most of the scientific efforts have been focused on the Eastern (Chinese) Tien Shan (e.g., Allen & Vincent 1997; Yin, et al. 1998; Dumitru et al. 2001; Chen et al. 2007; Sun et al. 2009) and the Central (Kyrgyz) Tien Shan (e.g., Abdrakhmatov et al. 1996; Cobbold et al. 1996; Sobel et al. 2006a and b; De Grave et al. 2011; Macaulay et al. 2014); far less research has been published on the Cenozoic tectonic evolution of the Western (Kyrgyz) Tien Shan. Note that the Chinese literature typically subdivides the Tien Shan differently (e.g., Wang et al. 2011).

The ~2000 km long Talas-Fergana Fault (TFF) is one of the best examples of a reactivated intracontinental strike slip fault; it forms the most prominent morphologic feature within the Western Tien Shan. Within continental interiors, strike-slip faults often move in response to distal plate collisions and have long histories punctuated by episodic reactivation (e.g., Burtman et al. 1996; Gilder et al. 1999; Yin et al. 2002). Constraining the spatio-temporal distribution of activity along such faults is crucial for understanding how oblique deformation is accomodated in transpressional settings. In the last decade, bedrock exhumation has been used as a powerful tool to quantify transpressive deformation (e.g., Spotila et al. 2007; Niemi et al. 2013). In strike-slip settings, restraining bends and horsetail splays accommodate local contraction and focus transpressional deformation (e.g., Cunningham & Mann 2007); hence, these present an optimal target for constraining the timing of transpressive deformation.

The past few years has seen a spate of new studies focused on the geologic and geodynamic understanding of the Pamir (e.g., Cowgill 2010; Schmidt et al. 2011; Sippl et al. 2013; Sobel et al. 2013). However, the area just to the north, the Pamir-Alai basin-Tien Shan junction, has received much less attention than other parts of the India-Asia collision zone. On the other hand, these novel contributions have focused on the development of the Pamir and rarely explore the distal effects of this deformation on the Tien Shan. Although significant shortening was accommodated north of the intracontinental subduction zone (e.g., Avouac et al. 1993; Cobbold et al. 1996), the timing of these processes in the Western Tien Shan remains obscure. The scale of late Cenozoic geodynamic changes that are proposed for the Pamir area (e.g., initiation of subduction) should have had a direct effect on the development of the Tien Shan.

In this contribution we focus on constraining the timing of Cenozoic deformation in the Western Tien Shan. To do this, we present new low-temperature thermochronology data for the Chatkal, Ugam, Shandalash, Talas and Fergana Ranges (Fig. 5.1). Based on our results and integrating the database with published ages, we evaluate and constrain the onset of Cenozoic exhumation in the Western Tien Shan. The pre-existing TFF had an important role in how shortening was accommodated there, developing horsetail splays at both ends of the TFF. Finally, we integrate recent models of Pamir geodynamics, published data, and our new

results to derive a reinterpretation of the kinematic style of deformation in this part of the India-Asia collision zone.

5.2 Geologic setting

5.2.1 Western Tien Shan

In terms of topography, morphology and location the Tien Shan can be separated into three sectors: the Western, Central and Eastern Tien Shan (Fig. 5.1). At the same time, in terms of geologic history, the Western and Central Tien Shan can be divided into the North, Middle and South Tien Shan, mostly based on the Paleozoic evolution. The description and analysis of the Tien Shan Paleozoic history is out of the scope of the present contribution. Comprehensive review papers are available (e.g., Şengör et al. 1993; Wang et al. 2006a; Windley et al. 2007; Xiao et al. 2008; Burtman 2010). The geologic Tien Shan units trends roughly east - west and are represented across the different topographic Tien Shan units described previously (Fig. 5.1).

The Western Tien Shan and the Central (Kyrgyz) Tien Shan are separated by the NW-SE trending Talas-Fergana Fault (TFF, Fig. 5.1). The present day morphology of the Tien Shan is strongly influenced by Paleozoic and Mesozoic structures. According to many proposed models (e.g., Şengör et al. 1993; Wang et al. 2006a; Windley et al. 2007; Xiao et al. 2008; Burtman 2010), the Paleozoic Tien Shan represents the amalgamation of a number of terranes that formed distinctive tectonic zones. In the Western Tien Shan, three main tectonic zones can be distinguished by lithology and geologic history. The western termination of the North Tien Shan (NTS) is formed by the Talas mountains. This range predominantly consists of Precambrian and early Paleozoic metamorphosed sedimentary rocks (Voytenko & Khudoley 2012). The Middle Tien Shan (MTS) is represented by the Chatkal Ranges and lies in the northern and northwestern part of our study area. In the term Chatkal Ranges we include the Chatkal Range itself, the Shandalash Range and the Ugam Range, all located in the northwestern sector of the Tien Shan mountains. The MTS is composed of Early Paleozoic passive continental margin sedimentary sequences and Devonian-Carboniferous magmatic rocks (Seliverstov & Ghes 2001; Seltmann et al. 2011). The South Tien Shan (STS) is a late Paleozoic highly deformed accretionary belt (e.g., Biske & Seltmann 2010; Loury et al., in press). Ophiolites and related metamorphic rocks delineate a major late Carboniferous suture zone (e.g., Hegner et al., 2010) (South Tien Shan suture) along the southern margin of the Paleozoic Kazakh continent (Burtman 1975). The STS has been displaced by the right lateral TFF, forming a regional sigmoid (Lesik & Mikolaichuk 2001) and constitutes the southern (Alai Range) and eastern (Fergana Range) sectors of the Western Tien Shan (Burtman 1975). Late Paleozoic strike-slip displacement primarily occurred during the Permian, when the whole Tien Shan experienced

significant transpressional deformation (Bazhenov & Mikolaichuk 2004; Alexeiev et al. 2009; Konopelko et al. 2013; Rolland et al. 2013).

During the Mesozoic and early Cenozoic, parts of the Tien Shan were periodically reactivated in response to distal collisions (e.g., Hendrix et al. 1992; Sobel & Dumitru 1997; Dumitru et al. 2001). In the Western Tien Shan, transtensional basins formed along the TFF during the Jurassic, and accommodated thick sedimentary successions associated with significant accumulation of organic-rich clastic deposits (e.g., Burtman et al. 1996; Sobel 1999; Allen et al. 2001). Unfortunately, the extent and magnitude of Cretaceous deformation remains poorly understood in the Western Tien Shan. However, the adjacent Central (Kyrgyz) Tien Shan experienced >100 Myr period of tectonic quiescence during the late Mesozoic and early Cenozoic (Afonichev & Vlasov 1984; Bullen et al. 2003; Sobel et al. 2006b; De Grave et al. 2011; Glorie et al. 2011; Macaulay et al. 2013). This event is registered by low relief unconformities exposed at high elevations and used as structural markers of the subsequent Cenozoic deformation (e.g., Cobbold et al. 1996, Macaulay et al. 2013). In our study area, a clear example of this surface is present on the northern slope of the Chatkal Range.

During the early Cenozoic, regionally well-correlated marine transgressions occurred in the Paleocene–Eocene (Bosboom 2013; Bosboom et al. in press and refs therein). These transgressions are linked to the Paratethys sea that was open to the west, including the Amu Darya, Tajik, Fergana and Tarim basins in Central Asia (Popov et al. 2004). The Cenozoic fill of the Fergana basin is up to 8 km thick in the central part of the basin (Clarke 1984). Outcrops of Cenozoic sediments are much thinner along the basin borders. In the northern part of the basin, the outcropping section is around 1.2 km thick, mostly comprised of the Massaget Formation (~800 m). This unit is characterized by upward coarsening and thickening nonmarine red beds (Fig. 5.2). Massaget strata are strongly tilted to the south (~75°) and are cut by an impressive subhorizontal angular unconformity. The age of the Massaget Formation was traditionally considered to be Oligo-Miocene (Pg3 -N1ms) (Artyomova et al. 1971). This determination is based on unconformable relations on both the top and bottom of the unit and regional correlations. Recent biostratigraphic work (Bosboom 2013; Bosboom et al. in press and refs therein) confirms a late Eocene age for the uppermost part of the immediately underlying Fergana Group (Fig. 5.2), supporting the previous age estimates. The Pliocene? Baktriy Formation unconformably overlies the Massaget Formation. Similar time-transgressive syntectonic sequences have been described in the NW Tarim basin (e.g., Heermance et al. 2008) and in the Issyk Kul basin (Macaulay et al. 2014, Wack et al. 2014).

5.2.2 The Talas-Fergana strike-slip Fault (TFF)

The TFF extends from the western Tarim basin in the southeast to the Turgay basin in the northwest. At ~2000 km long, it is one of the largest intracontinental strike-slip faults on Earth. Traditionally, it is subdivided into two segments, the Karatau segment to the north

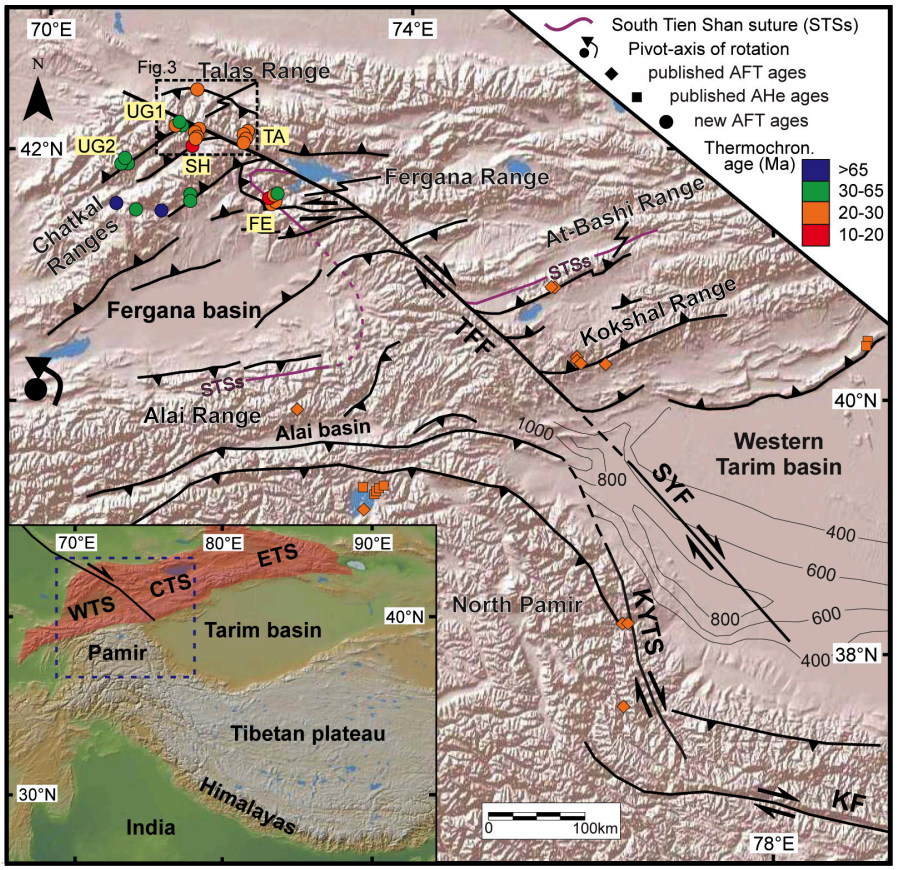

Figure 5.1 – Shaded relief image of the Tien Shan and Pamir with superimposed major structures, isopach contours for the late Oligocene-early Miocene Kezilouyi Fm. and thermochonologic data. Filled circles reflect new AFT ages, diamonds available published AFT data and squares available published apatite (U–Th)/He ages; color denote ages based on the shown scale. Only published ages between 20–30 Ma are displayed to highlight the locations where an Oligo-Miocene exhumational event was recorded. Labels in light yellow are vertical profile locations. Thermochronology ages are from Sobel & Dumitru (1997); Schmalholz (2004); Sobel et al. (2006a); Amidon & Hynek (2010); Glorie et al. (2011); De Grave et al. (2012); Chang et al. (2012) and this study. Structures modified from Vlasov et al. (1991); XBGMR (1993); Bakirov et al. (2001) and Cowgill (2010). Isopachs contours from Hao et al. (2002). Black point with large arrow shows Fergana basin pivot-axis of rotation (Thomas et al. 1993). South Tien Shan suture (STSs) drawn in purple. Dashed box shows location of Figure 3. Inset map shows location of Figure 1 in the Himalayan - Central Asian region. Transparent burnt orange polygon in inset shows the location of the Tien Shan Range. WTS is Western Tien Shan, CTS is Central (Kyrgyz) Tien Shan, ETS is Eastern (Chinese) Tien Shan, TFF is Talas-Fergana Fault, SYF is Shache-Yangdaman Fault, KYTS is Kashgar Yecheng Transfer System and KF is Karakax Fault.

and the proper Talas-Fergana segment to the south (e.g., Burtman 1980; Rolland et al. 2013). The TFF formed in the late Paleozoic –Early Mesozoic (Burtman 1980; Alexeiev et al. 2009; Konopelko et al. 2013; Rolland et al. 2013) and was reactivated in the Jurassic and Cenozoic (Bazhenov 1993; Burtman et al. 1996; Sobel 1999; Allen et al. 2001; Konopelko et al. 2013; Rolland et al. 2013). The maximum net displacement along the TFF reaches ~200 km, based on the offset of the Carboniferous South Tien Shan suture (STSs) (Fig. 5.1) and related units (Burtman 1980).

During the Cenozoic, displacement only occurred along the southern segment of the fault (Thomas et al. 1993). The overall magnitude of Cenozoic displacement is poorly constrained. The apparent offset of Cretaceous conglomerates with similar compositions suggests ~60 km of displacement (Verzilin 1968; Burtman et al. 1996). Thomas et al. (1993) suggested a Cenozoic displacement of 100 $\pm$ 60 km along the TFF based on vertical-axis rotation measured on Tertiary red beds in the Fergana basin. Given the triangular shape, the counter-clockwise sense of rotation of the Fergana basin and the Cenozoic displacement measured on the TFF, many authors proposed that much of slip on the TFF was absorbed by crustal thickening in the Chatkal Range (Cobbold & Davy 1988; Thomas et al. 1993; Burtman et al. 1996; Zubovich et al. 2010). According to Burtman (1980) and Trifonov et al. (1992), around 10 km of displacement occurred since the Pleistocene based on the offset of geomorphic markers. However, geodetic GPS shows very slow (< 2 mm/yr) active slip (Zubovich et al. 2010).

The southern termination of the Cenozoic TFF has long been considered to lie in the Kokshal range, which comprises a portion of the South Tien Shan (STS). AFT data from the Kokshal and At-Bashi ranges show that exhumation and hence deformation was underway by ~25 Ma (Sobel et al. 2006a; Glorie et al. 2011). A sequence of magnetostratigraphically-dated growth strata show that shortening in this area propagated rapidly southward into the Tarim basin between 16.3 and 13.5 Ma (Heermance et al. 2008).

Recently, a southern prolongation of the TFF has been described from the subsurface of the Tarim basin (Wei et al. 2013). Seismic reflection data show flower structures aligned across this lineament, which is named the Shache-Yangdaman right-slip Fault (SYF). This structure was active syn-depositionally with the Wuqia group (late Oligocene – late Miocene), which is subdivided into three formations: Kezilouyi, Anjuan and Pakabulake. Facies analysis and isopach patterns suggest that a 6-km-thick transtensional basin (Yecheng subbasin) formed in between the SYF and the dextral slip Kashgar Yecheng Transfer System (KYTS). Subsidence possibly commenced during deposition of the poorly dated late Oligocene – early Miocene Kezilouyi Formation (Hao et al. 2002); and was certainly rapid from 21-17 Ma during deposition of the Anjuan Formation (Wang et al. 2006b). Accumulation in the basin continued during middle to late Miocene with deposition of the over 3 km-thick Pakabulake Formation (Wei et al. 2013). The Anjuan and lower Pakabulake Formations include deep water turbiditic lacustrine strata in the subsurface (Zhou et al. 1984), suggestive of a deep, localized, rapidly

subsiding pull-apart basin (Wei et al. 2013). The seismic data suggests that the structure became inactive and then was briefly reactivated during deposition of the Pliocene (?) Xiyu Formation. The structure is now inactive and buried beneath thick Quaternary deposits, explaining why it's significance had not previously been appreciated.

5.3 Methodology and samples

5.3.1 Apatite fission track (AFT) rationale

This method relies on the fact that fission-tracks form at a constant rate from the spontaneous fission of ^{238}U and are subsequently shortened and may eventually disappear at temperatures above ca. 110°C (e.g., Gallagher et al. 1998). As a result, the track length distribution is a sensitive monitor of a crystal's thermal history. Significant annealing occurs between ca. 60-110°C, the partial annealing zone (PAZ). Where rocks were buried to sufficient depth that the temperature exceeds the total annealing temperature (Ketcham et al. 1999), the fission track clock was reset to zero and fission track data record information on the time-temperature cooling path of the sample as it cooled below this temperature during subsequent exhumation (e.g., Green et al. 1989). Track-length data are useful because they allow comparisons with forward modeling of the thermal histories (e.g., Ketcham 2005).

5.3.2 AFT methodology

AFT analysis was carried out on 26 samples; horizontal confined fission track lengths were measured in 25 of these. Kinetic properties were assessed for every crystal counted or containing confined tracks by measuring at least 4 Dpar (Donelick et al. 2005) that were averaged and corrected following Sobel & Seward (2010). AFT ages were calculated following the procedures of Galbraith (1981) using the MacTrackX software. Most AFT ages are based on ca. 20 grains. However, 3 samples contained less than 16 countable grains, resulting in AFT ages with larger errors. Ages are reported as pooled ages ($\pm 1\sigma$) because they all pass the Chi-squared test ($>=$5%). As many horizontal confined fission tracks (tracks-in-tracks) as possible were measured. To increase the number of measured horizontal confined tracks, additional mounts of 16 samples were irradiated with heavy ions (Jonckheere et al. 2007). The complete dataset and the detailed methodology description is included in the supplementary material (see Appendix D); the data is summarized in Table 1.

5.3.3 Age-elevation relationships (AERs)

AERs of samples collected at regular intervals along steep topographic profiles are commonly used to date increases in exhumation and quantify exhumation rates (e.g., Gallagher et al.

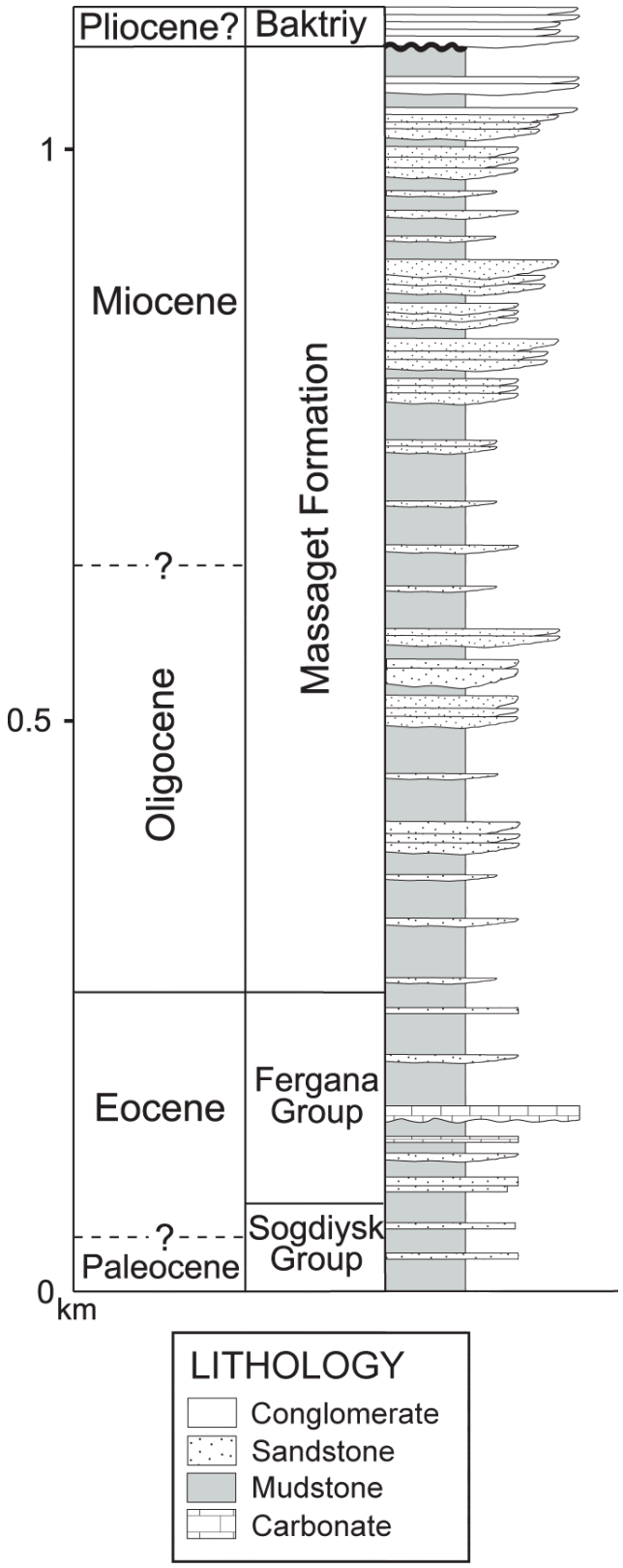

Figure 5.2 – Generalized Cenozoic stratigraphic section of the northern Fergana basin. Section simplified from log measured at the northeast corner of the basin.

2005). Typically, an increase in exhumation rate will result in a break-in-slope on an age-elevation plot (e.g., Fitzgerald et al. 1995), providing the chance of constraining the onset of that event. When possible we sampled following vertical profiles. We also collected spot samples to extend the areal coverage and spatial distribution of our dataset. Vertical profiles and spot samples will be addressed below in the geographic context of the respective ranges.

5.3.4 Thermal modeling

Thermal modeling was performed on 15 samples using the HeFTy (v.1.7.5) program (Ketcham 2005). This software models individual sample's time-temperature history by generating synthetic data, which is then compared to the observed data and evaluated using Kuiper's statistics (Ketcham 2005). The main aim of the modeling was to identify and date cooling rate variations. Input for the models includes AFT ages, Dpar values, track lengths, and the angle between each track and the crystallographic c-axis. Models were first run with minimal constraints. In cases where apparent inflection points were depicted, constraint boxes were set and shifted to test the model's goodness and reliability. Selected model results are presented below.

5.4 Results

Significant variations in thermochronological age distribution are found between ranges (Figs. 5.1 and 5.3). In the following sections we will discuss these variations systematically, starting from the north and moving towards the south.

5.4.1 Talas Range

In this range we collected a 4 sample vertical profile (TA, Fig. 5.1) near the headwaters of the Besh-Kol river, located just east of the TFF (Fig. 5.3). We sampled Proterozoic metasedimentary rocks over a vertical range of 550 m. AFT ages are tightly clustered between 25.4 $\pm$ 2.9 and 22 $\pm$ 3.1 Ma. The highest elevation sample (10TR04) presents the shortest mean track length (10.6 μm) and all samples pass the Chi-squared test. The AER (Fig. 5.4A) of these does not reveal a break-in-slope to define the onset of rapid cooling. This is probably related to the limited relief found in this zone. However, the clustering of ages across 550 m of elevation (Table 5.1) and the moderately steep slope of 0.14 mm/yr of the AER point to a relatively rapid exhumation event around the Oligo-Miocene for the Talas range. Moreover, time-temperature histories derived from thermal modeling (Fig. 5.4) of ages, track-length distributions, and Dpar (Table 1) of two samples from the Talas Range profile help to constrain the onset of rapid cooling. Thermal modelling of the bottom sample (10TR02, Fig. 5.4C) shows a rapid cooling event starting by 22 Ma; together with long confined lengths (13.6 μm),

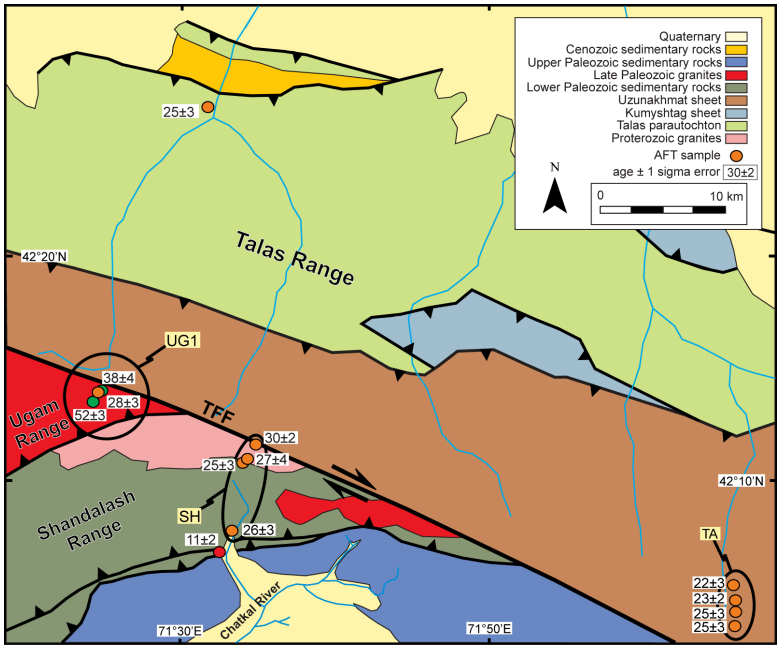

Figure 5.3 – Geologic and tectonic map of the northwestern Tien Shan (modified from Bakirov et al. (2001) and Voytenko & Khudoley (2012)) showing locations of new AFT samples; color denote ages based on same scale as Figure 1; ages with 1 sigma errors (in Ma) are in white boxes. Labels in light yellow are vertical profile locations. TFF is Talas-Fergana Fault.

this implies that it is a fully reset sample. In comparison, sample 10TR05, from 350 m higher, has shortened lengths (11.7 μm) and the time-temperature paths better defines a younger rapid cooling episode (Fig. 5.4B). We interpret the latter as a partially reset sample located at the very bottom part of the PAZ. Therefore, between these two samples we can place the lower section of the PAZ, providing a robust constrain of the initiation of rapid exhumation in the Talas Range at 23 $\pm$ 3 Ma. Modeling of sample 10TR05 also shows a younger (~5 Ma) event, but that modeled episode is not robust because is based in a just a few long track lengths. The lack of an obvious kink in the age-elevation plot is likely due to the exhumation rate and the size of the profile. To complete the picture, a fifth sample comes from the northernmost sector of the Talas Range, in the hanging-wall of the S-SW dipping frontal thrust. This sample yielded an AFT age of 25.2 $\pm$ 2.8 Ma with relative long track lengths (13.6 μm), suggesting a fully-reset sample that was cooling rapidly during the latest Oligocene-early Miocene.

5.4.2 Chatkal Ranges

In this section we will present 16 new AFT ages from the Ugam, Shandalash and Chatkal Ranges, all located west of the TFF in the Western Tien Shan. We sampled the Ugam Range in two sectors: one close to the TFF (UG1, Fig. 5.3) and a second one (UG2, Fig. 5.1) ~65 km along strike to the SW. Both profiles are in the hanging-wall of the same structure. In the

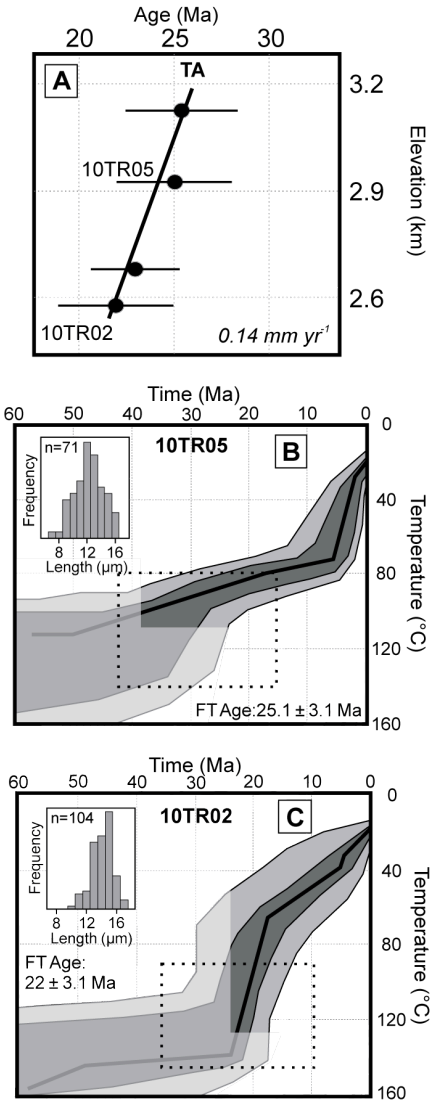

Figure 5.4 – A: Age-elevation relationships from the Talas Range vertical profile. Age errors are 1-sigma. Apparent exhumation rate based on the gradient of the AER trendline and shown in italics. B and C: Time-temperature histories obtained by thermal modeling using HeFTy software (Ketcham 2005) of samples 10TR02 and 10TR05, respectively. Unconstrained part of the models represented by transparent polygons. Dashed boxes are model input constraints. Inset shows histogram of track-length distribution.

first group, we collected 3 samples from Upper Paleozoic granites (Fig. 5.3). This location contains the northernmost samples in this study, distributed between 3456 m and 2082 m in elevation. The AFT ages range between 51.5 $\pm$ 2.8 and 27.5 $\pm$ 3.2 Ma, without a clear break-in-slope. However, the bottom sample (10UM14) has the youngest age and the longest mean track length value (12.9 μm) as expected for a sample located at a relatively lower section of an exhumed PAZ. The age (27.5 $\pm$ 3.2 Ma) is comparable to the higher-elevation samples from the neighboring Talas Range (23 $\pm$ 3 Ma), suggesting that sample 10UM14 also represents the very bottom part of the PAZ. Therefore, we conclude that the Ugam Range samples represent an uplifted PAZ with no analyzed totally reset ages. In turn, this suggests that this range has experienced less exhumation than the Talas Range.

At vertical transect UG2, we collected samples from a Carboniferous granitic pluton thrust on top of Cenozoic sedimentary rocks. Three samples distributed over a vertical separation of 626 m yielded apatite grains. The AFT ages range between 43.6 $\pm$ 3 and 30.1 $\pm$ 2.3 Ma. The mean track-length values are spread between 11.5 and 12 μm. The AFT ages together with the shortened track length values suggest that the samples spent significant time in the PAZ and were not fully-reset during the Cenozoic. Compared to the UG1, the UG2 samples represent a shallower portion of the PAZ and therefore the exhumation in this area is less significant.

The vertical profile (SH, Fig. 5.1) in the Chatkal zone lies on the south side of the Shandalash range, between its crest and the Chatkal River (Figs. 5.3 and 5.5A). In this section, Proterozoic and Lower Paleozoic rocks are thrust on top of Upper Paleozoic units. We collected 4 samples from Proterozoic granites and Cambrian tillites in this structural block. The AFT ages group between 24.5 $\pm$ 2.6 and 29.8 $\pm$ 2.4 Ma. The clustering of four ages across ca. 550 m of elevation together with the moderately steep slope (0.14mm /yr) of the AER (Fig. 5.5A) point to a rapid exhumation event occurring around the Oligo-Miocene boundary. Although this vertical profile lies to the west of the TFF, the data are remarkably similar to that derived from profile TA in the Talas Range, east of the TFF. The similar apparent exhumation rates of these two profiles is likely caused by similar tectonic rates and erosional processes. We collected a fifth sample in Devonian sedimentary rocks north of the Chatkal River, south of the other four samples (Fig. 5.3). However, this sample lies in a different structural block and shows a significantly younger AFT age (11 $\pm$ 2 Ma) and longer mean track-length value (13 μm). Therefore, we interpret it as a fully-reset age reflecting a Late Miocene exhumational event, propagating deformation locally to the south. Although we have little data reflecting this relatively young event in our study area, it is broadly represented in the Central Kyrgyz Tien Shan (Bullen et al. 2003; Sobel et al. 2006b; Macaulay et al. 2013).

Finally, we collected 5 spot samples along the Chatkal Range distributed roughly along a transect perpendicular to the tectonic strike (Fig. 5.1). A north-dipping erosional surface can be traced on the northern side of the Chatkal Range. Samples collected in this area from Carboniferous granites and Lower Paleozoic gneisses yield Mesozoic (124$\pm$7 and 120$\pm$7 Ma) AFT

ages with relatively large mean track-length values (12.8 μm). Thermal modeling of sample 10CK34 (Fig. 5.5B) suggests that these ages represent the tail end of a Late Mesozoic cooling event followed by a limited younger cooling episode. Those samples might reflect the same Late Mesozoic cooling event that is present in other parts of the Tien Shan (e.g., Dumitru et al. 2001; Jolivet et al. 2010; Glorie et al. 2011, De Grave et al. 2011). After this event, samples spent around 100 Ma at 60 – 70°C in the PAZ until an increase in the exhumation rate roughly around 25 Ma cooled them to surface temperature. Finally, we collected samples on the southern slope of the Chatkal Range from Devonian sandstones in the hanging-wall of the main south vergent thrust. These samples yield early Paleogene (65±5 and 51±6 Ma) AFT ages and pass the Chi-squared test. These are partially reset ages representing the exhumed PAZ located in southern slope.

5.4.3 Fergana Range

We sampled the range in its north-western sector (Fig. 5.1). The northern Fergana Range is crossed by a left-lateral strike-slip fault that merges with a thrust fault dipping to the east (Kalmetieva et al. 2009). The latter thrust places Paleozoic sedimentary rocks on top of Cenozoic sediments. We collected 5 samples from an 1845 m vertical profile (FE, Fig. 5.1 and 5.6A) from Late Paleozoic units. AFT Ages range between 16 $\pm$ 2 and 43 $\pm$ 3 Ma. All samples pass the Chi-squared test, representing single populations. The AER (Fig. 5.6A) presents a classic kinked profile. The bottom 4 samples are relatively young and form a steep area reflecting a high exhumation rate (0.19 mm /yr). The uppermost sample does not follow this trend; it is significantly older and probably represents the base of the PAZ. At first sight, one of the lower samples (10SU61) is too young for this trend (Figure 5.6A). However, this sample has a smaller Dpar value than the other samples. The Dpar value is a measure of the annealing kinetics of the apatite grain (Donelick et al. 2005); lower Dpar values indicate low annealing resistance (Carlson et al. 1999) and hence yield younger ages. Because Sample 10SU61 is less resistant to annealing, it has a younger age than the adjacent, more annealing-resistant samples.

The relation of the 5 samples in the AER draws a well-defined break-in-slope dating the exhumational increase at ca. 23±3 Ma (Fig. 5.6A). Thermal modeling from the highest sample (Fig. 5.6B) shows a slightly linear path with a subtle break in the slope at around 20 Ma. Thermal modeling yields time-temperature paths from sample 10SU62 (Fig. 5.6C) showing slow cooling in the Paleogene with a major increase in cooling rate at ca. 25 Ma. This event is relatively short and slow cooling is reestablished after 20 Ma. These models confirm the interpretation based on the AER, placing an increase in the cooling rate at 25 $\pm$ 3 Ma. This event correlates well with the contemporaneous deformation to the north described in the previous sections.

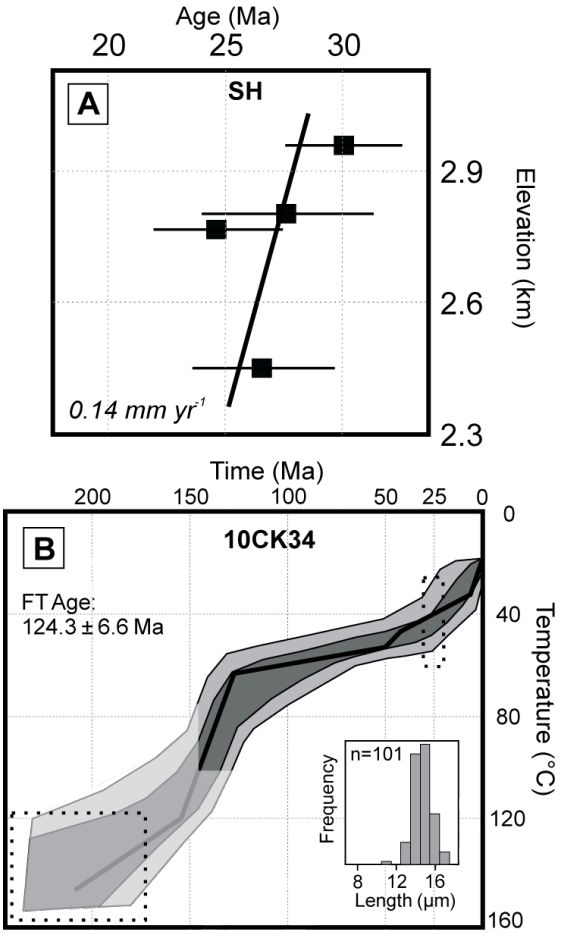

Figure 5.5 – A: Age-elevation relationships from the Shandalash Range vertical profile. Age errors are 1-sigma. Apparent exhumation rate based on the gradient of the AER trendline and shown in italics. B: Time-temperature histories obtained by thermal modeling using HeFTy software (Ketcham 2005) of samples 10CK34, collected in the axial zone of the Chatkal Range; this sample is not included in SH vertical profile. Unconstrained part of the model represented by transparent polygons. Dashed boxes are model input constraints. Inset shows histogram of track-length distribution.

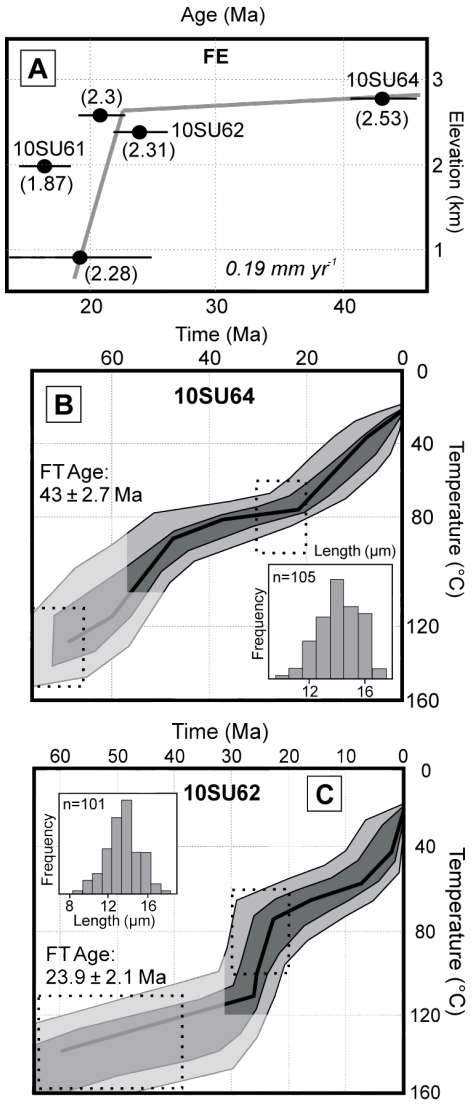

Figure 5.6 – A: Age-elevation relationships from the Fergana Range vertical profile. Age errors are 1-sigma; numbers between brackets are Dpar values. Apparent exhumation rate based on the gradient of the AER trendline and shown in italics. B and C: Time-temperature histories obtained by thermal modeling using HeFTy software (Ketcham 2005) of samples 10SU64 and 10SU62, respectively. Unconstrained part of the models represented by transparent polygons. Dashed boxes are model input constraints. Inset shows histogram of track-length distribution.

5.4.4 Interpretation

AFT ages and thermal modeling of the Talas Range samples show that the range was rapidly being exhumed by the latest Oligocene, both near the TFF and at its northern termination. Based on this data and the geometrical relation of the TFF and the structural lineaments of the Talas Range (Fig. 5.3), we interpret the zone to be a pop-up structure kinematically-related to the TFF. Many of the NE-vergent thrust faults in the Talas Range, including the frontal thrust, might be curvilinear concave-down reverse faults that steepen at depth (e.g., McClay & Bonora, 2001) rooting into the TFF. Similar structures are described in the Central (Kyrgyz) Tien Shan (e.g., Selander et al. 2012; Macaulay et al. 2013). This relation implies that the exhumation of the Talas Range is mostly controlled by a coupled strike-slip/thrust system.

The form of the Shandalash Range vertical profile (SH, Fig. 5.1 and 5.5A) suggests a rapid exhumation event commencing near the Oligo-Miocene boundary. In this sector, the geometrical relationship of the reverse faults with the main TFF (Fig. 5.3) supports the interpretation that the eastern Chatkal Ranges formed as horsetail splays connected to the TFF. Moreover, the timing of exhumation given by vertical profile SH is contemporaneous with the deformation in the Talas area, suggesting that strike-slip movement along the TFF is responsible for the uplift of the Talas pop-up structure and the development of horsetail splays in the Ugam, Shandalash and Chatkal Ranges.

In the Chatkal area the maximum exhumation is found close to the TFF. AFT ages and thermal modeling from the Ugam Range samples show that only the structural depth corresponding to the PAZ has been exhumed; no fully reset samples representing larger amounts of exhumation have been analyzed from this area. Moreover, comparing samples along strike, we can conclude that the amount of exhumation decreases while moving away from the TFF. This might be related to a lateral gradient of slip on the horsetail splays, with only limited slip to the SW and increasing towards the NE. This gradient is actually an exhumation gradient. The further from the rotation pivot point, the more shortening needed to accommodate in the Chatkal ranges.

In the Chatkal Range itself, AFT ages become relatively younger towards the southern side of the range (65 and 51 Ma), representing progressively deeper portions of an exhumed PAZ, similar to the Ugam Range. Like the Ugam and Shandalash, the Chatkal Range is bounded to the south by a north-dipping fault. As expected, exhumation is higher close to the faults. Structurally deeper rocks on the southern side of this range are exhumed to the surface, while to the north, the preserved erosion surface with late Mesozoic AFT ages (120 and 124 Ma) records far less Cenozoic exhumation.

In turn, the Fergana Range sampling site is located near the junction of active strike-slip and thrust faults (Fig. 5.1). Just from this structural setting and the sample locations, it is clear that the exhumation recorded by this vertical section should reflect the combination of strike-slip and dip-slip mechanisms. Furthermore, the timing of exhumation in this

area suggested by the AER (Fig. 5.6A) is contemporaneous with the Talas and Shandalash Ranges. Integrating all of the evidence presented above, we conclude that the north Western Tien Shan experienced a regional deformation episode near the Oligo-Miocene boundary, in which a linked strike-slip thrust system developed. Strike-slip displacement along the TFF induced several changes: it exhumed the Talas Range as a positive flower structure, exhumed the northern Fergana Range with a combination of strike-slip and reverse faulting, and developed the Ugam, Shandalash and Chatkal horsetail splays with higher exhumation close to the main strike-slip fault, as expected from a linked strike-slip thrust system. In comparison, exhumation further to the west along the strike of the Chatkal ranges must be dominantly compressional. However, deformation in the entire range should be a response to the same geodynamic driver.

5.5 Discussion

5.5.1 Talas-Fergana Fault Cenozoic chronology

According to Thomas et al. (1993), the Fergana basin experienced significant Cenozoic vertical-axis rotation. Paleomagnetic samples from the Oligo-Miocene Massaget Formation sampled at four localities around the basin show $20 \pm 11^{\circ}$ of counter-clockwise rotation in relation to the stable Issyk Kul area, located to the NE (Thomas et al. 1993). This implies that the change in declination happened during or after deposition of the coarsening-upwards Massaget Formation. Certainly the extreme tilting of Massaget beds in the northern sector of the basin suggests a strong tectonic event during deposition of the unit or shortly thereafter. Although the available age constraints for the Massaget Fm. are limited, the suggested depositional time interval overlaps with the rapid exhumation period proposed for the TFF horsetail splays. Therefore, the published paleomagnetic data and field relations lead us to consider the Massaget Formation as a syn- or pre-tectonic unit. Interestingly, the sediments on top the unconformity are subhorizontal, implying that syn-rotational deformation was almost finished before deposition of the Baktriy Formation or has continued at slower rates since then. This latter interpretation is consistent with modern GPS vector data (Zubovich et al. 2010).

The counter-clockwise sense of rotation is consistent with the right-lateral slip of the TFF. Since the Fergana basin is bounded by the TFF, we concur with Thomas et al. (1993) that the rotation was absorbed by right-lateral slip along the TFF coupled with shortening in the Chatkal ranges. Our new data suggests that much of this slip occurred during the late Oligocene - early Miocene. The documented onset of exhumation in the STS at ca. 25 Ma (Sobel et al. 2006a; Glorie et al. 2011) was synchronous with the exhumation that we have constrained at the Talas and Shandalash ranges. Even though the NW Tien Shan lies ca. 400 km away from the Kokshal and At-Bashi Ranges, they all have a synchronous Cenozoic onset

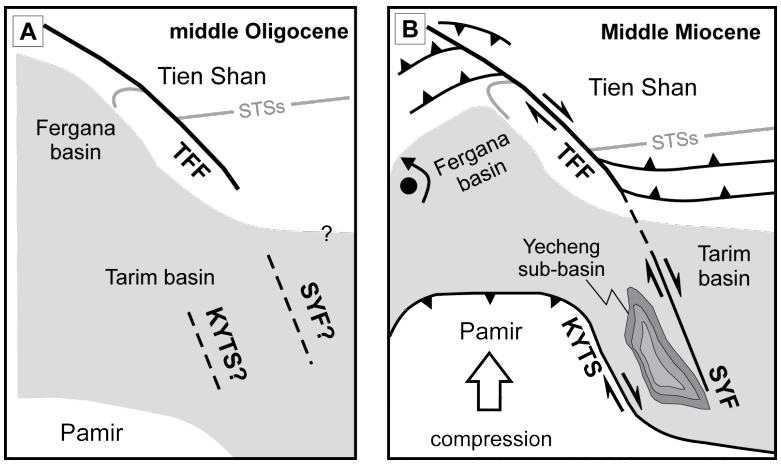

Figure 5.7 – Schematic cartoon showing the tectonic evolution of the region. In grey, areas of active sedimentation; in white uplifted areas; dark grey line South Tien Shan suture (STSs). A: Early Cenozoic location of the TFF, displaced STSs and speculative location of the KYTS and SYF. B: Commencing ~25 Ma, Pamir indentation driven shortening provoked compression and strike-slip displacement along the KYTS and SYF. Between these structures a pull-apart basin developed (Yecheng subbasin). Simultaneously, compression is absorbed by the TFF and transpressive horsetail splays develop in both ends of the fault and the Fergana basin experienced counter-clockwise rotation.

of exhumation. This situation could be explained if the localities are kinematically connected. We propose that both the north Western Tien Shan and STS east of the TFF are horsetail splays connected to the main strike-slip fault. We suggest that slip along the TFF was responsible for inducing exhumation at the proposed horsetail splays (Fig. 5.7). Moreover, the coincidence of pre-existing Paleozoic and Mesozoic structures with Cenozoic activity of the TFF implies that reactivation of favorably oriented structures must play a substantial role in how deformation was accommodated and how efficiently it was transmitted to the north.

Frequently, the initiation of horizontal strike-slip motion is hard to date because it does not produce substantial exhumation. However, in this case, the small size of the rotating block and the close proximity of the rotational pivot-axis (Fig. 5.1) mean that strike-slip movement and compression are expected to be synchronous with the onset of rotation. This local configuration allows us to date the initiation of strike slip displacement at ca. 25 Ma.

5.5.2 Connection to Pamir indentation

Indentation of the Pamir was underway by ~20 Ma based on AFT ages along the Kashgar Yecheng Transfer System (KYTS) (Sobel & Dumitru 1997). Recent stratigraphic work (Klocke et al. in press) in the northern Tajik basin suggests late Oligocene uplift of the northern Pamir. Those changes are a consequence of a south-dipping subduction zone at the northern margin of the Pamir, which is proposed to have initiated during the latest Oligocene- early Miocene (Burtman & Molnar 1993; Sobel et al. 2013). The northward indentation of the Pamir salient

was accommodated not only by the right-lateral KYTS (Cowgill 2010) but also by the Shache-Yangdaman Fault (SYF) (Wei et al. 2013). The latter structure lies in the subsurface of the Western Tarim basin and was recently highlighted in an international journal for the first time (Wei et al. 2013). Moreover, these authors propose that a right stepover between these two faults formed the Yecheng pull-apart basin. Based on the spatial distribution, the SYF can be connected to the TFF, representing the southernmost portion of a major right-lateral strike-slip system. Following this interpretation, this regional strike-slip system was able to transfer shortening driven by Pamir indentation as far north as the northern portion of the Western Tien Shan (Fig. 5.7). The connection between the TFF and the SYF worked efficiently during the Oligo-Miocene. However, Late Miocene deformation in the STS (Sobel et al. 2006a; Heermance et al. 2008) was responsible for shaping the actual Kokshal Range and Tarim basin foothills. Moreover, the active Miocene and Pliocene deformation of the STS and the Pamir triggered younger sedimentation in the NW Tarim basin keeping in the subsurface the SYF and the connection with the TFF.

We propose that the observed vertical-axis rotation of the Fergana basin which is coupled with the dextral slip TFF (Thomas et al. 1993) was driven by Pamir indentation. The transtensional Yecheng subbasin was filled with up to 6 km of Wuqia Group sediments (Wei et al. 2013). The basal age of this unit is apparently contemporaneous with the basal Massaget Formation, which we describe as a syn-rotational unit in the Fergana Basin (Fig. 5.2). Therefore, both units are syn-tectonic units genetically-related by the same tectonic driver. Magnetostratigraphy shows that shortening in the Kokshal range propagated rapidly southward into the Tarim basin between 16.3 and 13.5 Ma (Heermance et al. 2008). Therefore, relatively rapid slip along the TFF persisted from ca. 25 Ma until at least 13.5 Ma. This timing appears to agree well with the formation of the transtensional Yecheng depression in the SW Tarim basin (Wei et al. 2013), supporting our contention that the SYF and TFF are kinematically linked. Younger tectonic episodes affecting the STS and Pamir triggered the deposition of large volumes of sediment in the western Tarim basin, leaving the SYF covered in the subsurface.

In the Western Tien Shan the maximum amount of Oligo-Miocene shortening and exhumation is located close to the TFF. Our thermochronologic data shows that exhumation significantly decreases to the west in the Chatkal Ranges. Furthermore, the topography of the Chatkal Ranges also reflects the higher amount of shortening close to the TFF. Higher peaks (~4000 m) are located in close proximity to the strike-slip fault, while to the west, elevation decreases gradually until reaching elevations close to 400 m. Significant Oligo-Miocene deformation in the Alai range, between the Alai and Fergana basins, has not yet been documented. Although a relatively small Oligo-Miocene exhumational event is described in the Central (Kyrgyz) Tien Shan, the majority of the exhumation there occurred since Mid-Late Miocene times (Sobel et al. 2006b; Glorie et al. 2011; Macaulay et al. 2013; 2014). Therefore,

the TFF was able to efficiently transfer shortening driven by Pamir indentation far into the hinterland. This shortening occurred even when the Alai intracontinental subduction zone was active and accommodating most of the shortening in this sector of the orogen. This explains why more shortening and exhumation was located near the dextral strike-slip fault and decreased both to the east and west during the late Oligocene – early Miocene.

5.6 Conclusions

It is widely accepted that deformation in Central Asia is a far-field effect of the India-Asia collision (e.g., Molnar & Tapponnier 1975; Allen et al. 1991; Hendrix et al. 1994). During the late Miocene, a strong deformational event was responsible for shaping the current structure of many of the Central Asian Ranges (e.g., Bullen et al. 2003; Macaulay et al. 2014; Heermance et al. 2008). However, a growing body of evidence (Hendrix et al. 1994; Sobel & Dumitru 1997; Sobel et al. 2006a; Heermance et al. 2008; Amidon & Hynek 2010; Macaulay et al. 2013, 2014; Wei et al. 2013) points to a smaller, but important deformational event in the late Oligocene – early Miocene. By dating the onset of Cenozoic strike-slip movement along the TFF and in adjacent linked structures which distribute shortening within the NW Tien Shan, we are able to better document and areally extend the footprint of this Oligo-Miocene event. Furthermore, we present a kinematic mechanism that explains how contraction related to Pamir indentation was propagated hundreds of kilometers north into the Chatkal, Talas and Fergana Ranges. The proposed connection of the KYTS, SYF and TFF would have formed an efficient system to transfer this shortening to the north. Finally, we suggest that the presence of pre-existing crustal discontinuities such as the TFF played a significant role in establishing, localizing, and efficiently transferring shortening far into the hinterland.

Acknowledgements This study was supported by the Darius Programme, DFG-Graduate School 1364 and a fellowship from the German Academic Exchange Service (DAAD) to A. Bande. We thank Y. Rolland, J. Kley and corresponding editor M-F Brunet for constructive and conscious reviews that strengthened the paper. M.Wack and S.Gilder are acknowledged for detailed discussion and explanations about paleomagnetism. We also thank S. Sen, E. Macaulay, D. Melnick and M. Strecker for constructive discussion that improved earlier versions of the manuscript. We are grateful to the members of the Materials Research Department at the GSI Helmholtzzentrum (Darmstad, Germany) for heavy ions irradiations.

Table 5.1 – Summary of AFT data.

Sample	Latitude (N°)	Longitude (E°)	Elev. (m)	n[a]	P(χ^2)[b] %	**Age (Ma)**	**±1σ**	# lengths[c]	Length (µm)	SD[d] (µm)
				Talas Range						
10TR02	42.163	72.040	2571	20	100	**22**	**3.1**	104*	13.6	1.5
10TR03	42.138	72.041	2678	20	57	**23**	**2.3**	2	15.4	0.4
10TR04	42.109	72.043	3120	20	56	**25.4**	**2.9**	5*	10.6	2.1
10TR05	42.122	72.037	2921	20	97	**25.1**	**3.1**	71*	11.7	2.1
10TR17	42.459	71.534	1269	19	91	**25.2**	**2.8**	13*	13.6	1.7
				Ugam Range						
10UM12	42.233	71.407	3456	18	85	**51.5**	**2.8**	101	12.8	1.5
10UM14	42.240	71.410	2082	7	50	**27.5**	**3.2**	15	12.9	1.4
10UM15	42.242	71.413	2945	17	82	**37.6**	**3.8**	9	12.2	1.5
10CA26	41.887	70.852	3161	8	83	**40.9**	**4.4**	7	12.0	1.9
10CA27	41.881	70.854	2953	21	84	**43.6**	**3**	101*	11.8	1.9
10CA29	41.875	70.863	2535	19	40	**30.1**	**2.3**	106	11.5	1.8
				Shandalash Range						
10TR19	42.199	71.586	2978	19	68	**29.8**	**2.4**	19	11.6	2.3
10TR20	42.186	71.574	2815	20	97	**27.4**	**3.5**	13*	11.8	2.0
10TR21	42.184	71.570	2778	20	97	**24.5**	**2.6**	49	12.2	2.4
10TR22	42.129	71.558	2458	19	8	**26.4**	**2.9**	28*	11.6	2.6
10TR23	42.120	71.547	2.713	17	96	**11**	**1.6**	4	13.0	2.4
				Chatkal Range						
10CK34	41.574	70.699	1763	20	5	**124.3**	**6.6**	101*	12.8	1.5
10CK37	41.497	71.024	1762	20	61	**53.6**	**3.8**	56	12.1	1.9
10CK41	41.438	71.227	1369	20	35	**119.7**	**6.7**	105*	11.7	1.9
10CK43	41.584	71.527	1874	16	100	**51**	**5.5**	14*	12.5	1.7
10CK44	41.566	71.529	1695	20	65	**64.7**	**5**	37*	12.2	2.1
				Fergana Range						
10SU67	41.531	72.332	922	7	100	**19.2**	**5.6**	ND	ND	ND
10SU65	41.613	72.364	2578	20	84	**20.8**	**1.9**	101*	13.2	1.4
10SU61	41.590	72.329	1985	20	7	**16.4**	**2**	100*	11.6	1.9
10SU62	41.609	72.356	2386	20	91	**23.9**	**2.1**	101*	13.2	1.7
10SU64	41.623	72.368	2767	19	50	**43**	**2.7**	105*	12.4	1.9

Note: All samples counted by AB (zeta=369.5 ± 7.9, unpub. 2012)

[a] number of individual crystals dated.

[b] P(χ^2) (%) is the chi-squred probability (Galbraith (1981); Green (1981)).

All ages pass the P(χ^2) test and are reported as pooled ages.

[c] Asterisk (*) indicates track lengths measured from heavy ions irradiation slide.

[d] Standard deviation of measured lengths.

Chapter 6

Discussion

In this chapter, I synthesize my contributions toward a better understanding of the thermochronological evolution of the Kenya Rift and the quantification of denudation rates in different climatic and geomorphic sectors of rift-shoulder areas in Kenya. I will focus on chapters 2, 3 and 4 of this thesis, as chapter 5 concerns the results of a study that I co-authored on tectonic deformation processes in the Pamir mountains of Central Asia.

In chapters 2 to 4, I presented the timing of the tectonic evolution of the Kenya Rift as well as past and present-day denudation rates, following the initial questions that motivated my study: ***When did extensional processes begin in the eastern branch of the East African Rift?*** How do pulses of thermo-tectonic events relate to extension, erosion and sedimentation during the Cenozoic? And, ***what are the principal factors modulating erosion in the rift landscape?*** This relates to the factors that control erosion processes over time and possible changes in form and rate, especially during wetter or climatic transition periods in the geological past.

As a result of the long-term tectonic processes affecting the overall configuration of the Kenya Rift, the study region is segmented into three different sectors, the northern, central and southern Kenya Rift. I studied these different regions with the aim to gain a better understanding of climatic, tectonic and environmental conditions that influence erosion processes in the most relevant drainage-basin areas and to finally compare them with respect to shaping the landscape over time.

6.1 Erosion and exhumation in the Kenya Rift through time

In this study, I have used the term "erosion" as the process in the context of mass transport through various transport agents (e.g., fluvial regime, landsliding). Processes of erosion have different timescales and here I address these processes on a timescale range of 1-10^5 yrs. Additionally, the term "denudation" is used as the combined effect of chemical and physical processes that cause the removal of mass on the surface of the Earth (von Blanckenburg, 2005). Here, I refer to basin-wide denudation that encapsulates process rates that reflect how fast

a catchment is physically and chemically eroding, assuming a uniform denudation over time (von Blancklenburg, 2005). For much longer timescales, exhumation defines the integration of erosional processes over 10^5-10^6 yrs. It is therefore the removal of rocks with respect to the surface of the Earth (i.e., England and Molnar, 1990). Consequently, exhumation rates are the rates of physical erosion caused by tectonic processes. While erosion processes on short timescales are primarily driven by climate-related parameters, exhumation as used in this discussion is influenced by crustal dynamics and lithospheric processes.

As shown in chapters 3 and 4, the rate at which the surface of the Earth is eroded depends on many different factors, including the tectonic setting, lithology, relief, slope, vegetation cover, and precipitation (Willet, 1999; Molnar, 2007; Whipple et al., 1999). Climatically controlled factors (principally precipitation and vegetation cover) can be highly variable, particularly in light of variations in orbitally-controlled parameters over the past 2 million years that are known to have caused changes in African moisture regimes (deMenocal, 1995; Tierney et al. 2011; Feakins et al. 2013, Bonnefille, 2010); such variability may be exacerbated by anthropogenic impacts on shorter timescales during the ultimate millennia. Indeed, in tropical East Africa, land cover and vegetation distribution are fundamentally impacted by pastoralism and other land use, beginning at least ten thousand years ago (McGregor and Nieuwolt 1998) and forcing erosion processes (e.g., Fleitmann et al., 2007).

In general, erosion can be quantified in different ways, among others through the measurement of sediment volumes transported in rivers (e.g., Fuller et al. 2003), the analysis of the chemical composition of bedload, suspended load or dissolved load in rivers (e.g., Galy and France-Lanord, 2001) or through basin-wide cosmogenic radionuclide analysis of river sediments (e.g., von Blanckenburg, 2005 and references therein). As erosion is a function of the combined effects of relief, lithology, tectonic activity and climate (Summerfield and Hulton, 1994; Montgomery and Brandon, 2002), abrupt changes in erosion rates in the past can be detected when present-day erosion rates are compared to paleo-erosion rates over different timescales. As long as present-day and paleo-erosion rate estimates are determined with the same method that roughly integrate processes over the same timescale, the comparison is relatively straightforward, as in the case of ^{10}Be analysis of detrital quartz in basin-wide erosion measurements. However, when short-term erosion rates are compared to long-term erosion rates inferred from exhumation rates that were derived from thermochronologic data or that are based on other techniques, a comparison becomes more complicated.

6.1.1 Present-day to millennial scale basin-wide denudation rates using ^{10}Be cosmogenic radionuclide analysis

Over the last several million years tectonically driven surface uplift, normal faulting, and volcanism have been responsible for the major features of topography and relief development in the EARS (e.g., Ebinger and Sleep, 1998; Moucha and Forte, 2011; Ebinger and Scholz, 2012;

Wichura et al., 2015). The present-day precipitation distribution and drainage systems follow this topographic pattern, while millennial-scale or longer lake-level fluctuations follow the combined control of topography and the effects of climate variability superposed on this system (Pickford, 1994; Trauth et al., 2005; Bergner et al., 2009; Garcin et al., 2009; Ebinger and Scholz, 2012).

Rivers transfer sediments from the catchments of the source areas to the sink in topographically low-lying regions. Typically, in most sedimentary systems the sink region corresponds to ocean basins, but in the case of most sectors of the EARS, the individual rift basins or transiently linked basins constitute important terrestrial sinks over million-year timescales (Lezzar and Tiercelin, 1996; Garcin et al., 2009; Ebinger and Scholz, 2012; Frostick and Reid, 1986).

Basin-wide denudation rates in this study were estimated based on in-situ ^{10}Be in fluvial river sands (Brown et al., 1995; Bierman and Steig, 1996; Granger et al., 1996). The method measures the timescales of transport that associated with quartz-rich materials (von Blanckenburg, 2005). I determined basin-wide mean denudation rates from quartz-rich river sands and linked these with climatic, topographic and the dynamics of tectonic processes impacting the rift landscape, as shown in chapters 3 and 4. Due to the fact that these measurements are limited to quartz-bearing lithologies, not all catchments have denudation-rate estimates based on cosmogenic radionuclides. Nonetheless, this approach is useful for obtaining at least first-order estimates on erosion in many catchments that determine the production of sediments, which will be ultimately stored in the adjacent rift basins, where they influence hydrocarbon generation and storage.

In chapter 3, I showed that drainage basin-wide mean denudation rates of individual catchments in different compartments of the Kenya Rift range over at least one order of magnitude between 0.01$\pm$ 0.001 and 0.13 $\pm$ 0.01 mm/yr. Importantly, my studies reveal that vegetation cover plays a fundamental role in influencing the voracity of erosion processes and dictates the spatial efficacy of erosion patterns. Drainages with a thin vegetation cover and Enhanced Vegetation Index (EVI) values <0.35 record faster denudation rates than drainage basins with more densely covered vegetation and EVI values >0.35, even if their median slopes are much steeper. Interestingly, in the denser vegetated areas an increase in median slope values from to 10° to 20° does not cause an increase in denudation rates. Therefore, I suggest that vegetation cover has a strong influence on denudation rates, causing a threshold effect, similar to predictions originally suggested by Langbein and Schumm, (1958) and Bull and Kirkby, (2002). Accordingly, EVI values larger and smaller than 0.35, respectively, separate faster from slower eroding areas in regions with the same median slope values. In light of these observations denudation rates will most likely change when vegetation density changes as a function of precipitation and overall climatic conditions. A humid climate should result in a denser vegetation cover, and therefore slower overall denudation rates and vice versa.

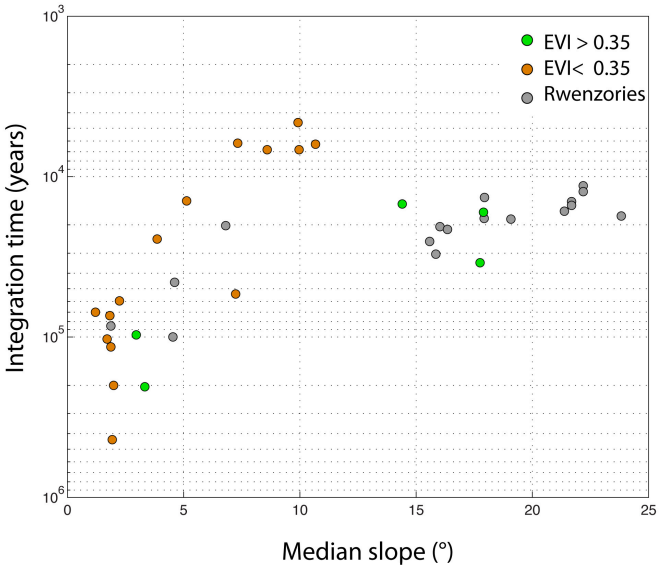

Figure 6.1 – Integration time versus median slope for samples collected in catchments from the Kenya Rift and published data from the Rwezori Mountains in Uganda (Roller et al., 2012). Samples separate into two different trends according to vegetation cover. EVI>0.35, densely vegetated areas; <0.35 sparsely vegetated areas. Note that cosmogenic-nuclide integration time on the y axis is reversed to follow catchment-mean denudation rates.

This is also reflected by the relationships between median slope and integration time for all samples from the different drainage-basin areas that were analyzed in this study (Figure 6.1). Slower denudation rates are integrated over longer time periods, therefore averaging the erosional processes in the drainage basin, even if the region may have been affected by changes in environmental conditions (e.g., wetter to drier climate transitions, and denser or sparse vegetation covers) during these time periods. This also means that for those drainages that are subjected to fast denudation rates, the integration time is short, and only the most recent erosion processes and environmental conditions are represented. Therefore, when considering the integration time, the median slope of the drainage basin exerts a certain control resulting in faster denudation rates that are generally correlated with steeper slopes.

Viewing these results in the context of paleoclimate and paleovegetation particularly in East Africa, reveals that catchments with integration times of thousands to hundreds of thousands of years, involving a range between 4.6 and 437 kyr, average erosion processes over episodes when the climate was significantly wetter and the vegetation cover was different than today (DeMenocal, 1995; Hessler et al., 2010).

However, the strong relationship between erosion rate and vegetation cover is not as straightforward as it appears, because often crucial information on the amount, frequency and distribution of precipitation is not available for the drainage areas under consideration, and these issues become even more complex if one considers changing frequencies of extreme events in

the recent past. These aspects are important as they determine the efficacy of erosion events and sediment transport in the catchment (Korup and Clague, 2009; Wulf et al., 2010; Andermann et al., 2012). The importance of extreme events in accounting for geomorphic rate changes over time has been emphasized in several recent studies (Bookhagen, 2010; Wulf et al., 2010; Andermann et al., 2012, Castino et al., 2015).

To assess the relationships between erosion rate, rainfall and vegetation cover in the past, I compared paleo-erosion rate estimates derived from ^{10}Be analyses of detrital quartz deposited in fluvio-deltaic sediments at the eastern margin of paleo-lake Suguta with denudation rates determined from present-day river sediments of the Baragoi River drainage in the same location. The paleo-erosion rate determination in the fluvio-deltaic units focussed on the episode of the African Humid Period, which affected the study region between 11.5 and approximately 5 ky B.P. at about 11 ky B.P. the paleo-highstand of Lake Suguta was associated with a much wetter climate than today as documented by paleo-lake shorelines more than 300 m above the present-day basin floor. At that time existed an outlet of the paleo-lake toward Lake Turkana in the north, which was connected to the White Nile and the Mediterranean (Butzer et al., 1972; Butzer, 1980; Harvey and Grove, 1982; Garcin et al., 2012). Interestingly, the basin-wide paleo-denudation rates are about four times greater than present-day basin-wide denudation rates for the same catchment areas. This suggests that at the time when the fluvio-deltaic sediments were deposited, sediment-transport processes in a more humid environment were very efficient in transferring mass from the catchments of the Baragoi River to the Suguta Basin.

In light of my results concerning present-day erosion rates and their relationships with rainfall amount and vegetation cover this suggests a lag time between the onset of a more humid climate and ensuing stabilizing effects of the development of a vegetative cover in the catchment. The higher paleo-denudation rates indicate that higher precipitation - as shown by the onset of deltaic and lacustrine deposition in the Suguta Basin - must have had a strong impact on denudation rates in earlier stages of the African Humid Period. These conditions were probably superseded by more stable conditions of the landscape, when an inferred denser vegetative cover retarded erosive processes. By analogy, these areas may have been similar to conditions that characterize the present-day threshold regions between dry and humid areas that co-vary with vegetation density. Future studies of paleo-vegetation using palynology may reveal the finer details of these relationships, but general trends can already be observed in East African pollen records and related proxies of paleo-climate conditions (Vincens, 1991; Vincens et al., 1993; 2005; Cohen et al., 2007; Vincens et al., 2007; Mumbi et al., 2008; Hessler et al., 2010).

6.1.2 Long-term exhumation history and implications for the onset of rifting

Exhumation of crustal rocks may be driven either by extension (normal faulting by crustal thinning) or uplift in the course of crustal shortening and stacking (England and Molnar, 1990; Willet, 1999; Braun and Beaumont, 1989). In both cases exhumation by these tectonic processes is aided or may be even accelerated by erosion, as an increase in topography and relief will lead to changes in precipitation gradients, runoff, vegetation, and the efficiency of surface processes in removing material advected to the surface. Long-term exhumation rates can be deciphered with thermo-chronological methods (e.g., Fitzgerald et al., 1995) using fission-track or (U-Th)/He analyses, as I have shown in chapter 2. By analyzing samples collected from vertical elevation profiles with the apatite fission-track and zircon (U-Th)/He methods I obtained data needed for modeling time-temperature histories of basement rocks exposed along three sections of the Kenya Rift flanks. The thermal history models presented in chapter 2 reflect the cooling history of these rocks while they were exhumed during their advection toward the surface. It is evident from the Cenozoic thermal histories that occurred between 65 and 50 Ma and in the interval between about 15 Ma and the present rapid cooling affected the EARS in the region that now constitutes the Kenya Rift. In turn, the time between 45 and 15 Ma, the episode between the end of the first cooling and the onset of the second cooling event, was characterized by a quasi-isothermal or slow reheating phase. I relate the phases of cooling to times of pronounced extension during which rocks of the rift shoulders were rapidly exhumed by extensional faulting. This inferred onset of early Cenozoic extension processes in the equatorial sectors of Kenya followed by Neogene extension fits very well with the notion of coeval erosion and sedimentation processes in the region east of the Elgeyo escarpment during the Paleogene, which were subsequently affected by a second phase of extensional faulting, erosion and sedimentation (Mugisha et al., 1997; Chapman et al., 1978) (Figure 6.2).

Sedimentary deposits in the adjacent Kerio Basin are mainly known from pronounced negative gravity anomalies and strata imaged on seismic reflection profiles that define a tectonic phase of subsidence followed by a regional thermal subsidence with onlaps onto the Elgeyo basement rocks (Morley et al., 1992; Mugisha et al., 1997; Hautot et al., 2000). Taken together, the early onset of extensional processes during the Tertiary inferred from my new data, evidence for sedimentation in the pre-Kerio Basin, and regional thermo-chronological information from areas farther north and west (i.e., Foster and Gleadow, 1996; Spiegel et al., 2007) help to reconcile sedimentary records related to a period of protracted erosion, areally extensive sedimentation and basin subsidence prior to the onset of rifting processes that are responsible for the present-day configuration of the Kenya Rift. These early extensional processes are furthermore compatible with an increasing body of geological and thermochronological evidence that suggests a regionally widespread, partly overlapping early Cenozoic onset of rifting in East Africa. As such, my new data constitute a missing link between

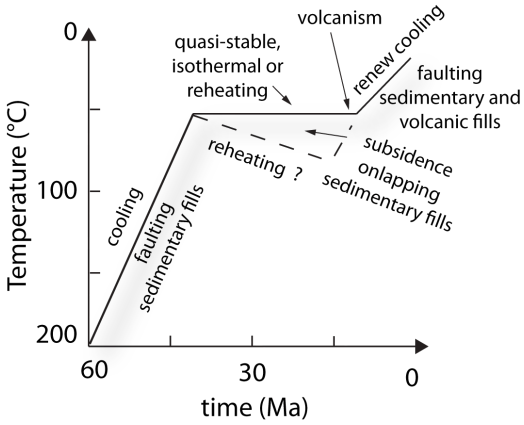

Figure 6.2 – Cartoon of the thermal evolution of the Kenya Rift in the equatorial region. Pronounced cooling begins in the Paleogene, followed by extensive sedimentation until about 15 Ma, when renewed cooling and extensional faulting initiated processes that were responsible for the present-day topography.

observations of early Cenozoic extensional processes documented in Tanzania and in the Lake Rukwa and Malawi regions in the south (van der Beek et al., 1998), and broadly compatible indicators of early extension in northern Kenya and the Rwenzori Mountains in the western rift (Foster and Gleadow, 1996; Bauer et al., 2013).

As Africa has been surrounded by divergent plate boundaries in the east and west and a convergent, collisional plate boundary in the north, it is unlikely that these early extensional processes were related to compressional far-field stresses. Rather, the underlying rifting mechanism must have been associated with mantle-driven convection processes that uplifted the lithosphere of the East African Plateau, including the Tanzania Craton and its peripheral Proterozoic orogenic belts. It can be envisaged that this process resulted in the generation of differential stresses that caused extensional faulting in areas characterized by inherited zones of weakness. These areas correspond to shear zones or pronounced metamorphic fabrics as observed along the Elgeyo escarpment of the Kenya Rift and other sectors of the EARS where lithospheric and crustal-scale anisotropies have been invoked to focus extensional processes (Hetzel and Strecker, 1994;Smith, 1994; Smith and Mosley, 1993). Due to compositional differences of the lithosphere in these different regions, volcanism may not have been always associated with these processes from the beginning, as the lithospheric mantle did not have a composition conducive to melting. These inferences are supported by predictions on the nature of extensional processes based on three-dimensional thermo-mechanical modeling of the EARS (i.e., Koptev et al., 2015). These authors suggested an asymmetric distribution of volcanism in East Africa, and the evolution of broadly coeval, partly overlapping extensional processes in the different sectors of the EARS due to the asymmetric impingement of convecting mantle. Taken together, geological, thermochronological, and modeling results

support earlier models of the evolution of topography, rift-basin formation, and loci of volcanism in light of combined lithospheric characteristics and underlying convective mantle patterns (i.e., Ashwal and Burke, 1989). Importantly, my own results and the compilation of geological and thermo-chronological data on the onset of extensional processes in East Africa contradict models that claim a north-south migration of volcanic activity and rifting as a result of spatially changing plume activity (Ebinger and Sleep, 1998; Brazier and Nyblade, 2000).

References

Abdrakhmatov, K.Y., Aldazhanov, S.A., Hager, B.H., Hamburger, M.W., Herring, T.A., Kalabaev, K.B., Makarov, V.I., Molnar, P., Panasyuk, S.V., Prilepin, M.T., Reilinger, R.E., Sadybakasov, I.S., Souter, B.J., Trapeznikov, Y.A., Tsurkov, V.Y., Zubovich, A.V., 1996. Relatively recent construction of the Tien Shan inferred from GPS measurements of present-day crustal deformation rates. Nature 384, 450–453.

Abrahams, A.D., Parsons, A.J., Wainwright, J., 1995. Effects of vegetation change on interrill runoff and erosion, Walnut Gulch, southern Arizona. Geomorphology 13, 37–48.

Achauer, U., Glahn, A., Ritter, J.R.R., Maguire, P.K.H., Meyer, R.P., Davis, P., Slack, P., Green, W.V., 1994. New ideas on the Kenya rift based on the inversion of the combined dataset of the 1985 and 1989/90 seismic tomography experiments. Tectonophysics 236, 305–329.

Achauer, U., Masson, F., 2002. Seismic tomography of continental rifts revisited: from relative to absolute heterogeneities. Tectonophysics 358, 17 – 37.

Ackermann, E., Heinrichs, T. (Eds.), 2001. Geological map of East Africa. Scale 1:1,000,000. Borntraeger and Deutsche Forschungsgemeinschaft.

Afonichev, N.A., Vlasov, N.G. (Eds.), 1984. Geological map of Kazakhstan and Central Asia. Scale 1:1,500,000. Ministry of Geology of the USSR, Leningrad.

Ahnert, F., 1970. Funtional relationships between denudation, relief and uplift in large mid-latitude drainage basins. American Journal of Sciences 268, 1–21.

Alexeiev, D.V., Cook, H.E., Buvtyshkin, V.M., Golub, L.Y., 2009. Structural evolution of the Ural–Tian Shan junction: A view from Karatau ridge, South Kazakhstan. Comptes Rendus Geoscience 341, 287–297.

Aljabri, S.S., 1990. Geology, Mineralogy and Geochemistry of fluorite mineralization in the Kerio valley and Tugen Escarpment of Kenya. Master's thesis. Univeristy of Nairobi, Kenya.

Allen, M.B., Vincent, S.J., 1997. Fault reactivation in the Junggar region, northwest China: the role of basement structures during Mesozoic-Cenozoic compression. Journal of the Geological Society 154, 151–155.

Allen, M.B., Windley, B.F., Chi, Z., Zhong-Yan, Z., Guang-Rei, W., 1991. Basin evolution within and adjacent to the Tien Shan Range, NW China. Journal of the Geological Society 148, 369–378.

Amidon, W., Hynek, S., 2010. Exhumational history of the north central Pamir. Tectonics 29, TC5017.

Artyomova, Z.P., Brodskiy, I.L., Vnuchkov, V.I., 1971. Geological map of the USSR. Ministry of Geology of the USSR.

Ashley, G.M., 2007. Orbital rhythms, monsoons, and playa lake response, Olduvai Basin, equatorial East Africa (ca. 1.85–1.74 Ma). Geology 35, 1091–1094.

Ashwal, L.D., Burke, K., 1989. African lithospheric structure, volcanism, and topography. Earth and Planetary Science Letters 96, 8–14.

Avouac, J.P., Tapponnier, P., Bai, M., You, H., Wang, G., 1993. Active thrusting and folding along the northern Tien Shan and Late Cenozoic rotation of the Tarim relative to Dzungaria and Kazakhstan. Journal of Geophysical Research: Solid Earth 98, 6755–6804.

Bailey, G.N., King, G.C.P., 2011. Dynamic landscapes and human dispersal patterns: tectonics, coastlines, and the reconstruction of human habitats. Quaternary Science Reviews 30, 1533–1553.

Bailey, G.N., Reynolds, S.C., King, G.C.P., 2011. Landscapes of human evolution: models and methods of tectonic geomorphology and the reconstruction of hominin landscapes, journal = Journal of Human Evolution 60, 257–280.

Baker, B.H., 1963. Geology of the Baragoi area. Geological Survey of Kenya, Nairobi, Kenya.

Baker, B.H., Mitchell, J.G., Williams, L.A.J., 1988. Stratigraphy, geochronology and volcano-tectonic evolution of the Kedong–Naivasha-Kinangop region, Gregory Rift Valley, Kenya. Journal of the Geological Society 145, 107–116.

Baker, B.H., Wohlenberg, J., 1971. Structure and Evolution of the Kenya Rift Valley. Nature 229, 538–542.

Bakirov, A.B., Ghes, M., Maksumova, R.A., Gusak, L., 2001. Geodynamic map of Kyrgyzstan. Scale 1:500,000. Geological Survey of Kyrgystan, Bishkek, Kyrgystan.

Balco, G., Stone, J.O., Lifton, N.A., Dunai, T.J., 2008. A complete and easily accessible means of calculating surface exposure ages or erosion rates from ^{10}Be and 26Al measurements. Quaternary Geochronology 3, 174–195.

Barber, D.A., 2014. Africa's Rift Valley Geothermal Energy Investment Boom Heats Up. URL: `http://afkinsider.com/40369/africas-rift-valley-geothermal-energy- boom-heats/`.

Bauer, F.U., Glasmacher, U.A., Ring, U., Karl, M., Schumann, A., Nagudi, B., 2013. Tracing the exhumation history of the Rwenzori Mountains, Albertine Rift, Uganda, using low-temperature thermochronology. Tectonophysics 599, 8–28.

Bauer, F.U., Glasmacher, U.A., Ring, U., Schumann, A., Nagudi, B., 2010. Thermal and exhumation history of the central Rwenzori Mountains, Western Rift of the East African Rift System, Uganda. International Journal of Earth Sciences 99, 1575–1597.

Bauer, F.U., Karl, M., Glasmacher, U.A., Nagudi, B., Schumann, A., Mroszewski, L., 2012. The Rwenzori Mountains of western Uganda - Aspects on the evolution of their remarkable morphology within the Albertine Rift. Journal of African Earth Sciences 73-74, 44–56.

Bazhenov, M.L., 1993. Cretaceous paleomagnetism of the Fergana Basin and adjacent ranges, central Asia: tectonic implications. Tectonophysics 221, 251–267.

Bazhenov, M.L., Mikolaichuk, A.V., 2004. Structural Evolution of Central Asia to the North of Tibet: A Synthesis of Paleomagnetic and Geological Data. Geotectonics 38, 3–393.

van der Beek, P.A., MBede, E., Andriessen, P., Delvaux, D., 1998. Denudation history of the Malawi and Rukwa Rift flanks (East African Rift System) from apatite fission track thermochronology. Journal of African Earth Sciences 26, 363–385.

van der Beek, P.A., Valla, P.G., Herman, F., Braun, J., Persano, C., Dobson, K.J., Labrin, E., 2010. Inversion of thermochronological age–elevation profiles to extract independent estimates of denudation and relief history — II: Application to the French Western Alps. Earth and Planetary Science Letters 296, 9–22.

Behrensmeyer, A.K., 2006. Climate Change and Human Evolution. Science 311, 476–478.

BEICIP, 1987. Geological Map of Kenya. Scale 1:1,000,000. Ministry of Energy and Regional Development of Kenya, Nairobi, Kenya.

Berger, A., Loutre, M.F., 1997. Intertropical latitudes and precessional and half-precessional cycles. Science 278, 1476–1478.

Bergner, A.G.N., Strecker, M.R., Trauth, M.H., Deino, A.L., Gasse, F., Blisniuk, P.M., Dühnforth, M., 2009. Tectonic and climatic control on evolution of rift lakes in the Central Kenya Rift, East Africa. Quaternary Science Reviews 28, 2804–2816.

Bergner, A.G.N., Trauth, M.H., Bookhagen, B., 2003. Paleoprecipitation estimates for the Lake Naivasha basin (Kenya) during the last 175 k.y. using a lake-balance model. Global and Planetary Change 36, 117–136.

Bierman, P., Steig, E.J., 1996. Estimating rates of denudation using cosmogenic isotope abundances in sediment. Earth Surface Processes and Landforms 21, 125–139.

Binnie, S.A., Phillips, W.M., Summerfield, M.A., Fifield, L.K., 2007. Tectonic uplift, threshold hillslopes, and denudation rates in a developing mountain range. Geology 35, 743–746.

Binnie, S.A., Phillips, W.M., Summerfield, M.A., Fifield, L.K., Spotila, J.A., 2010. Tectonic and climatic controls of denudation rates in active orogens: The San Bernardino Mountains, California. Geomorphology 118, 249–261.

von Blanckenburg, F., 2005. The control mechanisms of erosion and weathering at basin scale from cosmogenic nuclides in river sediment. Earth and Planetary Science Letters 237, 462–479.

Bobe, R., Behrensmeyer, A.K., 2004. The expansion of grassland ecosystems in Africa in relation to mammalian evolution and the origin of the genus Homo. Palaeogeography, Palaeoclimatology, Palaeoecology 207, 399–420.

Bonnefille, R., 2010. Cenozoic vegetation, climate changes and hominid evolution in tropical Africa. Global and Planetary Change 72, 390–411.

Bookhagen, B., 2010. Appearance of extreme monsoonal rainfall events and their impact on erosion in the Himalaya. Geomatics, Natural Hazards, and Risk , 37–50.

Bookhagen, B., Burbank, D.W., 2006. Topography, relief, and TRMM–derived rainfall variations along the Himalaya. Geophysical Research Letters 33.

Bookhagen, B., Strecker, M.R., 2008. Orographic barriers, high–resolution TRMM rainfall, and relief variations along the eastern Andes. Geophysical Research Letters 35.

Bookhagen, B., Strecker, M.R., 2012. Spatiotemporal trends in erosion rates across a pronounced rainfall gradient: Examples from the southern Central Andes. Earth and Planetary Science Letters 327, 97–110.

Bosboom, R., Mandic, O., Dupont-Nivet, G., Proust, J.N., Ormukov, C., Aminov, J., in press. Late Eocene paleogeography of the Proto-Paratethys Sea in Central Asia (NW China, S Kyrgyzstan and SW Tajikistan). The Geological Society .

Bosboom, R.E., 2013. Paleogeography of the Central Asian proto-Paratethys Sea in the Eocene: controlling mechanisms and paleoenvironmental impacts. Ph.D. thesis. Utrecht University.

Bosworth, W., Maurin, A., 1993. Structure, geochronology and tectonic significance of the northern Suguta Valley (Gregory Rift), Kenya. Journal of the Geological Society 150, 751–762.

Bosworth, W., Morley, C.K., 1994. Structural and stratigraphic evolution of the Anza rift, Kenya. Tectonophysics 236, 93–115.

Braun, J., Beaumont, C., 1989. A physical explanation of the relation between flank uplifts and the breakup unconformity at rifted continental margins. Geology 17, 760–764.

Brazier, R.A., Nyblade, A.A., Langston, C.A., Owens, T.J., 2000. Pn wave velocities beneath the Tanzania Craton and adjacent rifted mobile belts, east Africa. Geophysical Research Letters 27, 2365–2368.

Brown, E.T., Stallard, R.F., Larsen, M.C., Bourlès, D.L., Raisbeck, G.M., Yiou, F., 1998. Determination of predevelopment denudation rates of an agricultural watershed (Cayaguás River, Puerto Rico) using in-situ-produced ^{10}Be in river-borne quartz. Earth and Planetary Science Letters 160, 723–728.

Buck, W.R., 1988. Flexural rotation of normal faults. Tectonics 7, 959–973.

Buck, W.R., Martinez, F., Steckler, M.S., Cochran, J.R., 1988. Thermal consequences of lithospheric extension - pure and simple. Tectonics 7, 213–234.

Bull, L.J., Kirkby, M.J., 2002. Dryland rivers; hydrology and geomorphology of semi-arid channels. John Wiley and Sons. chapter Dryland river characteristics and concepts. pp. 3–15.

Bullen, M.E., Burbank, D.W., Garver, J.I., 2003. Building the Northern Tien Shan: Integrated Thermal, Structural, and Topographic Constraints. The Journal of Geology 111, 149–165.

Burke, K., 1996. The African plate. South African Journal of Geology 99, 341–409.

Burke, K., Whiteman, A.J., 1972. Uplift, rifting and break-up of Africa, in: Tarling, D., Runcorn, S. (Eds.), Implications of continental drift to the earth sciences. Academic Press, London, pp. 735–755.

Burtman, V.S., 1975. Structural geology of variscan Tien Shan, USSR. American Journal of Sciences 275-A, 157–186.

Burtman, V.S., 1980. Faults of Middle Asia. American Journal of Sciences 280, 25–744.

Burtman, V.S., 2010. Tien Shan, Pamir, and Tibet: History and Geodynamics of Phanerozoic Oceanic Basins. Geotectonics 44, 388–404.

Burtman, V.S., Molnar, P., 1993. Geological and Geophysical Evidence for Deep Subduction of Continental Crust Beneath the Pamir. Geological Society of America Special Papers 281, 1–76.

Burtman, V.S., Skobelev, S.F., Molnar, P., 1996. Late Cenozoic slip on the Talas-Ferghana fault, the Tien Shan, central Asia. Geological Society of America Special Papers 108, 1004–1021.

Butzer, K.W., 1980. The Holocene Lake Plain of North Rudolph, East Africa. Physical Geography 1, 42–58.

Butzer, K.W., Isaac, G.L., Richardson, J.L., Washbourn-Kamau, C., 1972. Radiocarbon Dating of East African Lake Levels. Science 175, 1069–1076.

Camberlin, P., Philippon, N., 2002. The East African March-May Rainy Season: Associated Atmospheric Dynamics and Predictability over the 1968-97 Period.

Carlson, W.D., Donelick, R.A., Ketcham, R.A., 1999. Variability of apatite fission-track annealing kinetics: I. Experimental results. American Mineralogist 84, 1213–1223.

Carretier, S., Regard, V., Vassallo, R., Aguilar, G., Martinod, J., Riquelme, R., Pepin, E., Charrier, R., Herail, G., Farias, M., Guyot, J.L., Vargas, G., Lagane, C., 2013. Slope and climate variability control of erosion in the Andes of central Chile. Geology 41, 195–198.

Castino, F., Bookhagen, B., Strecker., M., 2015. Climate variability, precipitation trends, and impacts on surface processes in humid to arid climate transition zones of the NW Argentine Andes (24ř S, 65ř W), in: EGU General Assembly.

Cerling, T.E., 2014. Stable Isotope Evidence for Hominin Environments in Africa, in: Turekian, H.D., Holland, K.K. (Eds.), Treatise on Geochemistry (Second Edition). Elsevier, Oxford, pp. 157–167.

Cerling, T.E., Wynn, J.G., Andanje, S.A., Bird, M.I., Korir, D.K., Levin, N.E., Mace, W., Macharia, A.N., Quade, J., Remien, C.H., 2011. Woody cover and hominin environments in the past 6 million years. Nature 476, 51–56.

Champagnac, J.D., Molnar, P., Sue, C., Herman, F., 2012. Tectonics, climate, and mountain topography. Journal of Geophysical Research 117, B02403.

Chang, J., Qiu, N., Li, J., 2012. Tectono-thermal evolution of the northwestern edge of the Tarim Basin in China: Constraints from apatite (U–Th)/He thermochronology. Journal of Asian Earth Sciences 61, 187–198.

Chapman, G.R., Brook, M., 1978. Chronostratigraphy of the Baringo Basin, Kenya. Geological Society, London, Special Publications 6, 207–223.

Chapman, G.R., Lippard, S.J., Martyn, J.E., 1978. The stratigraphy and structure of the Kamasia Range, Kenya Rift Valley. Journal of the Geological Society 135, 265–281.

Chen, J., Heermance, R., Burbank, D.W., Scharer, K.M., Miao, J., Wang, C., 2007. Quantification of growth and lateral propagation of the Kashi anticline, southwest Chinese Tian Shan. Journal of Geophysical Research 112, B03S16.

Chmeleff, J.R.M., von Blanckenburg, F., Kossert, K., Jakob, D., 2010. Determination of the ^{10}Be half-life by multicollector ICP-MS and liquid scintillation counting. Nuclear Instruments and Methods in Physics Research Section B: Beam Interactions with Materials and Atoms 268, 192–199.

Chorowicz, J., 2005. The East African rift system. Journal of African Earth Sciences 43, 379–410.

Clarke, J.W., 1984. Geology and possible uranium deposits of the Fergana region of Soviet Central Asia, in: Open-File Report. U.S. Geological Survey, pp. 1–41.

Cobbold, P., Sadybakasov, E., Thomas, J., 1996. Cenozoic transpression and basin development, Kyrgyz Tien Shan, central Asia, in: Roure, F., Ellouz, N., V.S., S., Skvortsov, I. (Eds.), Geodynamic Evolution of Sedimentary Basins. Technip, Paris, pp. 181–202.

Cobbold, P.R., Sadybakasov, E., Thomas, J.C., 1988. Indentation tectonics in nature and experiment. 2. Central Asia. Bulletin of the Geological Institute of Uppsala, 14, 143–162.

Cohen, A.S., 2003. Paleolimnology: The History and Evolution of Lake Systems. Oxford University Press, New York.

Cohen, A.S., Soreghan, M.J., Scholz, C.A., 1993. Estimating the age of formation of lakes: An example from Lake Tanganyika, East African Rift system. Geology 21, 511–514.

Cohen, A.S., Stone, J.R., Beuning, K.R.M., Park, L.E., Reinthal, P.N., Dettman, D., Scholz, C.A., Johnson, T.C., King, J.W., Talbot, M.R., Brown, E.T., Ivory, S.J., 2007. Ecological consequences of early Late Pleistocene megadroughts in tropical Africa. Proceedings of the National Academy of Sciences 104, 16422–16427.

Collins, D.B.G., Bras, R.L., Tucker, G.E., 2004. Modeling the effects of vegetation-erosion coupling on landscape evolution. Journal of Geophysical Research 109, F03004.

Cowgill, E., 2010. Cenozoic right-slip faulting along the eastern margin of the Pamir salient, northwestern China. Geological Society of America Special Papers 122, 145–161.

Crossley, R., 1979. The Cenozoic stratigraphy and structure of the western part of the Rift Valley in southern Kenya. Journal of the Geological Society 136, 393–405.

Crough, S.T., 1983. Rifts and swells: Geophysical constraints on causality. Tectonophysics 94, 23–37.

Cunningham, W.D., Mann, P., 2007. Tectonics of strike-slip restraining and releasing bends. Geological Society, London, Special Publications 290, 1–12.

Cyr, A.J., Granger, D.E., Olivetti, V., Molin, P., 2010. Quantifying rock uplift rates using channel steepness and cosmogenic nuclide–determined erosion rates: Examples from northern and southern Italy. Lithosphere 2, 188–198.

De Grave, J., Glorie, S., Buslov, M.M., Izmer, A., Fournier-Carrie, A., Batalev, V.Y., Vanhaecke, F., Elburg, M.A., Van den haute, P., 2011. The thermo-tectonic history of the Song-Kul plateau, Kyrgyz Tien Shan: Constraints by apatite and titanite thermochronometry and zircon U/Pb dating. Gondwana Research 20, 745–763.

De Grave, J., Glorie, S., Ryabinin, A., Zhimulev, F., Buslov, M.M., Izmer, A., Elburg, M.A., Vanhaecke, F., Van den haute, P., 2012. Late Palaeozoic and Meso-Cenozoic tectonic evolution of the southern Kyrgyz Tien Shan: Constraints from multi-method thermochronology in the Trans-Alai, Turkestan-Alai segment and the southeastern Ferghana Basin. Journal of Asian Earth Sciences 44, 149–168.

Deino, A.L., Kingston, J.D., Glen, J.M., Edgar, R.K., Hill, A., 2006. Precessional forcing of lacustrine sedimentation in the late Cenozoic Chemeron Basin, Central Kenya Rift, and calibration of the Gauss/Matuyama boundary. Earth and Planetary Science Letters 247, 41–60.

deMenocal, P., 1995. Plio-Pleistocene African climate. Science 270.

deMenocal, P., Ortiz, J., Guilderson, T., Adkins, J., Sarnthein, M., Baker, L., Yarusinsky, M., 2000. Abrupt onset and termination of the African Humid Period: rapid climate responses to gradual insolation forcing. Quaternary Science Reviews 19, 347–361.

DiBiase, R.A., Whipple, K.X., 2011. The influence of erosion thresholds and runoff variability on the relationships among topography, climate, and erosion rate. Journal of Geophysical Research 116, F04036.

DiBiase, R.A., Whipple, K.X., Heimsath, A.M., Ouimet, W.B., 2010. Landscape form and millennial erosion rates in the San Gabriel Mountains, CA. Earth and Planetary Science Letters 289, 134–144.

Dixon, J.L., Heimsath, A.M., Amundson, R., 2009a. The critical role of climate and saprolite weathering in landscape evolution. Earth Surface Processes and Landforms 34, 1507–1521.

Dixon, J.L., Heimsath, A.M., Kaste, J., Amundson, R., 2009b. Climate-driven processes of hillslope weathering. Geology 37, 975–978.

Dobson, K.J., 2006. The zircon (U–Th)/He thermochronometer: development and application of thermochronometers in igneous provinces. Ph.D. thesis. University of Glasgow.

Dobson, K.J., Persano, C., Stuart, F.M., 2009. Quantitative constraints on mid- to shallow-crustal processes using the zircon (U–Th)/He thermochronometer. Geological Society, London, Special Publications 324, 47–56.

Dodson, M.H., 1973. Closure temperature in cooling geochronological and petrological systems. Contributions to Mineralogy and Petrology 40, 259–274.

Dodson, R., 1963. Geology of the South Horr area: degree sheet 19, south-east quarter. Geological Survey of Kenya, Nairobi, Kenya.

Donelick, R.A., Ketcham, R.A., Carlson, W.D., 1999. Variability of apatite fission-track annealing kinetics: II. Crystallographic orientation effects. American Mineralogist 84, 1224–1234.

Donelick, R.A., O'Sullivan, P.B., Ketcham, R.A., 2005. Apatite Fission-Track Analysis. Reviews in Mineralogy and Geochemistry 58, 49–94.

Dumitru, T.A., 1993. A new computer automated microscope stage system for fission track analysis. Nuc.Tracks 21, 575–580.

Dumitru, T.A., Zhou, D., Chang, E.Z., Graham, S.A., Hendrix, M.S., Sobel, E.R., Carroll, A.R., 2001. Uplift, exhumation, and deformation in the Chinese Tian Shan, in: Hendrix, M.S., Davis, G.A. (Eds.), Paleozoic and Mesozoic Tectonic Evolution of Central and Eastern Asia: From Continental Assembly to Intracontinental Deformation, Mem 194. Geological Society of America, USA, pp. 71–99.

Dunkley, P.N., Smith, M., Allen, D.J., Darling, W.G., 1993. The Geothermal Activity and Geology of the Northern Sector of the Kenya Rift Valley. British Geological Survey Research Report SC/93/1.

Dunne, T., 1979. Sediment yield and land use in tropical catchments. Journal of Hydrology 42, 281–300.

Dunne, T., Malmon, D.V., Mudd, S.M., 2010. A rain splash transport equation assimilating field and laboratory measurements. Journal of Geophysical Research 115, F01001.

Dunne, W., Dietrich, W.E., Brunengo, M.J., 1978. Recent and past erosion rates in semi-arid Kenya. Zeitschrift für Geomorphologie 29, 130–140.

Durán Zuazo, V.H., Pleguezuelo, C.R.R., Francia Martinez, José Ramón Martínez Raya, A., Arroyo Panadero, L., Cárceles Rodríguez, B., Navarro Moll, M.C., 2008. Benefits of plant strips for sustainable mountain agriculture. Agronomy for Sustainable Development 28, 497–505.

Ebinger, C.J., 2005. Continental break-up: The East African perspective. Astronomy and Geophysics 46, 16–21.

Ebinger, C.J., Bechtel, T.D., Forsyth, D.W., Bowin, C.O., 1989. Effective elastic plate thickness beneath the East African and Afar plateaus and dynamic compensation of the uplifts. Journal of Geophysical Research 94, 2883–2901.

Ebinger, C.J., Petit, C., Burov, E., 2002. Causes and consequences of lithospheric extension: The ups and downs of continental rifts, in: Renault, R.W., Ashley, G.M. (Eds.), Sedimentation in Continental Rifts. SEPM, Special Publications, pp. 11–23.

Ebinger, C.J., Scholz, C.A., 2012. Continental Rift Basins: The East African Perspective, in: Busby, C., Azor, A. (Eds.), Tectonics of Sedimentary Basins: Recent Advances. John Wiley and Sons, Ltd, Chichester, UK, pp. 185–208.

Ebinger, C.J., Sleep, N.H., 1998. Cenozoic magmatism throughout east Africa resulting from impact of a single plume. Nature 395, 788–791.

Ebinger, C.J., Yemane, T., Harding, D.J., Tesfaye, S., Kelley, S., Rex, D.C., 2000. Rift deflection, migration, and propagation: Linkage of the Ethiopian and Eastern rifts, Africa. Geological Society of America Special Papers 112, 163–176.

Ego, J.K., 1994. Sedimentology and diagenesis of neogene sediments in the Central Kenya Rift Valley. Master's thesis. University of Saskatchewan.

Ehlers, T.A., Farley, K.A., 2003. Apatite (U–Th)/He thermochronometry: methods and applications to problems in tectonic and surface processes. Earth and Planetary Science Letters 206, 1–14.

England, P., Molnar, P., 1990. Surface uplift, uplift of rocks, and exhumation of rocks. Geology 18, 1173–1177.

Farley, K.A., Stockli, D.F., 2002. (U–Th)/He Dating of Phosphates: Apatite, Monazite, and Xenotime. Reviews in Mineralogy and Geochemistry 48, 559–577.

Farley, K.A., Wolf, R.A., Silver, L.T., 1996. The effects of long alpha-stopping distances on (UîŮÿTh)/He ages. Geochimica et Cosmochimica Acta 60, 4223–4229.

Feakins, S.J., Demenocal, P.B., Eglinton, T.I., 2005. Biomarker records of late Neogene changes in northeast African vegetation. Geology 33, 977.

Feakins, S.J., Levin, N.E., Liddy, H.M., Sieracki, A., Eglinton, T.I., Bonnefille, R., 2013. Northeast African vegetation change over 12 m.y. Geology , 1–5.

Feibel, C.S., 2011. A Geological History of the Turkana Basin. Evol. Anthropol. 20, 206–216. doi:10.1002/evan.20331.

Fitzgerald, P.G., 1992. The Transantarctic Mountains of southern Victoria Land: The application of apatite fission track analysis to a rift shoulder uplift. Tectonics 11, 634–662.

Fitzgerald, P.G., Sorkhabi, R.B., Redfield, T.F., Stump, E., 1995. Uplift and denudation of the central Alaska Range; a case study in the use of apatite fission track thermochronology to determine absolute uplift parameters. Journal of Geophysical Research 20, 175–191.

Flannery, J.W., Rosendahl, B.R., 1990. The seismic stratigraphy of Lake Malawi, Africa: implications for interpreting geological processes in lacustrine rifts. Journal of African Earth Sciences 10, 519–548.

Fleitmann, D., Dunbar, R.B., Mcculloch, M., Mudelsee, M., Vuille, M., Mcclanahan, T.R., Cole, J.E., Eggins, S., 2007. East African soil erosion recorded in a 300 year old coral colony from Kenya. Geophysical Research Letters 34, L04401.

Flowers, R.M., 2009. Exploiting radiation damage control on apatite (U–Th)/He dates in cratonic regions. Earth and Planetary Science Letters 277, 148–155.

Flowers, R.M., Shuster, D.L., Wernicke, B.P., Farley, K.A., 2007. Radiation damage control on apatite (U–Th)/He dates from the Grand Canyon region, Colorado Plateau. Geology 35, 447–450.

Foeken, J.P.T., Stuart, F.M., Dobson, K.J., Persano, C., Vilbert, D., 2006. A diode laser system for heating minerals for (U–Th)/He chronometry. Geochemistry, Geophysics, Geosystems 7, Q04015.

Foster, A., Ebinger, C.J., MBede, E., Rex, D., 1997. Tectonic development of the northern Tanzanian sector of the East African Rift System. Journal of the Geological Society 154, 689–700.

Foster, D.A., Gleadow, A.J.W., 1992. The morphotectonic evolution of rift-margin mountains in central Kenya: Constraints from apatite fission-track thermochronology. Earth and Planetary Science Letters 113, 157–171.

Foster, D.A., Gleadow, A.J.W., 1996. Structural framework and denudation history of the flanks of the Kenya and Anza Rifts, East Africa. Tectonics 15, 258–271.

Frostick, L.E., Reid, I., 1990. Structural control of sedimentation patterns and implication for the economic potential of the East African Rift basins. Journal of African Earth Sciences 10, 307–318.

Fuller, I.C., Large, A.R.G., Charlton, M.E., Heritage, G.L., Milan, D.J., 2003. Reach-scale sediment transfers: an evaluation of two morphological budgeting approaches. Earth Surface Processes and Landforms 28, 889–903.

Gabet, E.J., Reichman, O.J., Seabloom, E.W., 2003. The effects of bioturbation on soil processes and sediment transport. Annual Review of Earth and Planetary Sciences 31, 249–273.

Galbraith, R.F., 1981. On statistical models for fission track counts. Journal of the International Association for Mathematical Geology 13, 471–478.

Gallagher, K., 2012. Transdimensional inverse thermal history modeling for quantitative thermochronology. Journal of Geophysical Research 117, B02408.

Gallagher, K., Brown, R., Johnson, C., 1998. Fission track analysis and its applications to geological problems. Annual Review of Earth and Planetary Sciences 26, 519–572.

Gallagher, K., Charvin, K., Nielsen, S., Sambridge, M., Stephenson, J., 2009. Markov chain Monte Carlo (MCMC) sampling methods to determine optimal models, model resolution and model choice for Earth Science problems. Marine and Petroleum Geology 26, 525–535.

Gallagher, K., Stephenson, J., Brown, R., Holmes, C., Ballester, P., 2005. Exploiting 3D Spatial Sampling in Inverse Modeling of Thermochronological Data. Reviews in Mineralogy and Geochemistry 58, 375–387.

Galy, A., France-Lanord, C., 2001. Higher erosion rates in the Himalaya: Geochemical constraints on riverine fluxes. Geology 29, 23–26.

Garcin, Y., Junginger, A., Melnick, D., Olago, D.O., Strecker, M.R., Trauth, M.H., 2009. Late Pleistocene-Holocene rise and collapse of Lake Suguta, northern Kenya Rift. Quaternary Science Reviews 28, 911–925.

Garcin, Y., Melnick, D., Strecker, M.R., Olago, D., Tiercelin, J.J., 2012. East African mid-Holocene wet-dry transition recorded in palaeo-shorelines of Lake Turkana, northern Kenya Rift. Earth and Planetary Science Letters 331, 322–334.

Gautheron, C., Tassan-Got, L., Barbarand, J., Pagel, M., 2009. Effect of alpha-damage annealing on apatite (U–Th)/He thermochronology. Chemical Geology 266, 157–170.

George, R., Rogers, N., Kelley, S., 1998. Earliest magmatism in Ethiopia: Evidence for two mantle plumes in one flood basalt province. Geology 26, 923–926.

Gilbert, G.K., 1877. Geology of the Henry Mountains: Washington, D.C., U.S. Geological and Geographical Survey of the Rocky Mountain Region, Government Printing Office.

Gilder, S.A., Leloup, P.H., Courtillot, V., Y, C., Coe, R.S., Zhao, X., Xiao, W., Halim, N., Cogné, J.P., Zhu, R., 1999. Tectonic evolution of the Tancheng-Lujiang (Tan-Lu) fault via Middle Triassic to Early Cenozoic paleomagnetic data. Journal of Geophysical Research 104, 15365–15390.

Glorie, S., De Grave, J., Buslov, M.M., Zhimulev, F.I., Stockli, D.F., Batalev, V.Y., Izmer, A., Van den haute, P., Vanhaecke, F., Elburg, M.A., 2011. Tectonic history of the Kyrgyz South Tien Shan (Atbashi-Inylchek) suture zone: The role of inherited structures during deformation-propagation. Tectonics 30, TC6016.

Granger, D.E., Kirchner, J.W., Finkel, R., 1996. Spatially Averaged Long-Term Erosion Rates Measured from in Situ-Produced Cosmogenic Nuclides in Alluvial Sediment. The Journal of Geology 104, 249–257.

Green, P.F., 1981. A new look at statistics in fission-track dating. Nuclear Tracks 5, 77–86.

Green, P.F., Crowhurst, P.V., Duddy, I.R., Japsen, P., Holford, S.P., 2006. Conflicting (U–Th)/He and fission track ages in apatite: Enhanced He retention, not anomalous annealing behaviour. Earth and Planetary Science Letters 250, 407–427.

Green, P.F., Duddy, I.R., Laslett, G.M., Hegarty, K.A., Gleadow, A.J.W., Lovering, J.F., 1989. Thermal annealing of fission tracks in apatite 4. Quantitative modelling techniques and extension to geological timescales. Chemical Geology 79, 155–182.

Griffiths, J.F., 1972. Climate of Africa. World Survey of Climatology. volume 10. Elsevier, Amsterdam.

Gyssels, G., Poesen, J., 2003. The importance of plant root characteristics in controlling concentrated flow erosion rates. Earth Surface Processes and Landforms 28, 371–384.

Hackman, B.D., Charsley, T.J., Key, R.M., Wilkinson, A.F., 1990. The development of the East African Rift system in north-central Kenya. Tectonophysics 184, 189–211.

Hahm, W.J., Riebe, C.S., Lukens, C.E., Araki, S., 2014. Bedrock composition regulates mountain ecosystems and landscape evolution. Proceedings of the National Academy of Sciences .

Hansen, K., Reiners, P.W., 2006. Low temperature thermochronology of the southern East Greenland continental margin: Evidence from apatite (U–Th)/He and fission track analysis and implications for intermethod calibration. Lithos 92, 117–136.

Hao, Y., Guan, S., Ye, L., Huang, Y., Zhou, Y., 2002. Neogene stratigraphy and paleogeography in the western Tarim basin. Acta Geological Sinica 76, 289–298.

Harkins, N., Kirby, E., Heimsath, A.M., Robinson, R., Reiser, U., 2007. Transient fluvial incision in the headwaters of the Yellow River, northeastern Tibet, China. Journal of Geophysical Research 112, F03S04.

Harvey, C.P.D., Grove, A.T., 1982. A Prehistoric Source of the Nile. The Geographical Journal 148, pp. 327–336.

Hastenrath, S., 1984. Interannual Variability and Annual Cycle: Mechanisms of Circulation and Climate in the Tropical Atlantic Sector. Monthly Weather Review 112, 1097–1107.

Hastenrath, S., 2009. Past glaciation in the tropics. Quaternary Science Reviews 28, 790–798.

Hautot, S., Tarits, P., Whaler, K., Le Gall, B., Tiercelin, J.J., Le Turdu, C., 2000. Deep structure of the Baringo Rift Basin (central Kenya) from three-dimensional magnetotelluric imaging: Implications for rift evolution. Journal of Geophysical Research 105, 23493–23518.

Hays, J.D., Imbrie, J.Z., Shackleton, N.J., 1976. Variations in the Earth's Orbit: Pacemaker of the Ice Ages. Science 194, 1121–1132.

Heermance, R.V., Chen, J., Burbank, D.W., Miao, J., 2008. Temporal constraints and pulsed Late Cenozoic deformation during the structural disruption of the active Kashi foreland, northwest China. Tectonics 27.

Hegner, E., Klemd, R., Kröner, A., Corsini, M., Alexeiev, D.V., Iaccheri, L.M., Zack, T., Dulski, P., Xia, X., Windley, B.F., 2010. Mineral ages and P-T conditions of Late Paleozoic high-pressure eclogite and provenance of mélange sediments from Atbashi in the south Tianshan orogen of Kyrgyzstan. American Journal of Sciences 310, 916–950.

Heimsath, A.M., Chappell, J., Fifield, L.K., 2010. Eroding Australia: rates and processes from Bega Valley to Arnhem Land. Geological Society, London, Special Publications 346, 225–241.

Hendrix, M.S., Dumitru, T.A., Graham, S.A., 1994. Late Oligocene-early Miocene unroofing in the Chinese Tian Shan: An early effect of the India-Asia collision. Geology 22, 487–490.

Hendrix, M.S., Graham, S.A., Carroll, A.R., Sobel, E.R., McKnight, C.L., Schulein, B.J., Wang, Z., 1992. Sedimentary record and climatic implications of recurrent deformation in the Tian Shan: Evidence from Mesozoic strata of the north Tarim, south Junggar, and Turpan basins, northwest China. Geological Society of America Special Papers 104, 53–79.

Hendrix, M.S., Sobel, E.R., Carrol, A.R., 2001. Uplift, Exhumation, and deformation in the chinese Tian Shan, in: Hendrix, M.S., Davis, G.A. (Eds.), Paleozoic and Mesozoic tectonic evolution of Central and Eastern Asia: from continental assembly to intracontinental deformation, pp. 71–99.

Hessler, I., Dupont, L., Bonnefille, R., Behling, H., González, C., Helmens, K.F., Hooghiemstra, H., Lebamba, J., Ledru, M.P., Lézine, A.M., Maley, J., Marret, F., Vincens, A., 2010. Millennial-scale changes in vegetation records from tropical Africa and South America during the last glacial. Quaternary Science Reviews 29, 2882–2899.

Hetzel, R., Strecker, M.R., 1994. Late Mozambique Belt structures in western Kenya and their influence on the evolution of the Cenozoic Kenya Rift. Journal of Structural Geology 16, 189–201.

Horton, R.E., 1933. The Rôle of infiltration in the hydrologic cycle. Eos, Transactions American Geophysical Union 14, 446–460.

Horton, R.E., 1945. Erosional development of streams and their drainage basins; hidrophysical approach to quantitative morphology. Geological Society of America Special Papers 56, 275–370.

Howard, A.D., 1994. A Detachment-Limited Model of Drainage-Basin Evolution. Water Resources Research 30, 2261–2285.

Huete, A., Didan, K., Miura, T., Rodriguez, E.P., Gao, X., Ferreira, L.G., 2002. Overview of the radiometric and biophysical performance of the MODIS vegetation indices. Remote Sensing of Environment 83, 195–213.

Hurford, A.J., Green, P.F., 1983. The zeta age calibration of fission-track dating. Chemical Geology 41, 285–317.

Huybers, P., Wunsch, C., 2005. Obliquity pacing of the late Pleistocene glacial terminations. Nature 434, 491–494.

Imbrie, J.Z., 1980. Modeling the Climatic Response to Orbital Variations. Science 207, 943–953.

Insel, N., Ehlers, T.A., Schaller, M., Barnes, J.B., Tawackoli, S., Poulsen, C.J., 2010. Spatial and temporal variability in denudation across the Bolivian Andes from multiple geochronometers. Geomorphology 122, 65–77.

IRI-LDEO, 2015. Climate Data Library URL: `http://iridl.ldeo.columbia.edu/`.

Istanbulluoglu, E., Bras, R.L., 2005. Vegetation-modulated landscape evolution: Effects of vegetation on landscape processes, drainage density, and topography. Journal of Geophysical Research 110.

Jenny, H., 1941. Factors of Soil Formation. McGraw-Hill, New York.

Jolivet, M., Dominguez, S., Charreau, J., Chen, Y., Li, Y., Wang, Q., 2010. Mesozoic and Cenozoic tectonic history of the central Chinese Tian Shan: Reactivated tectonic structures and active deformation. Tectonics 29.

Jonckheere, R., Enkelmann, E., Min, M., Trautmann, C., Ratschbacher, L., 2007. Confined fission tracks in ion-irradiated and step-etched prismatic sections of Durango apatite. Chemical Geology 242, 202–217.

Jones, W.B., Lippard, S.J., 1979. New age determinations and the geology of the Kenya Rift-Kavirondo Rift junction,W Kenya. Journal of the Geological Society 136, 693–704.

Junginger, A., 2011. East African Climate Variability on Different Time Scales: The Suguta Valley in the African–Asian Monsoon Domain. Ph.D. thesis. University of Potsdam.

Junginger, A., Roller, S., Olaka, L.A., Trauth, M.H., 2014. The effects of solar irradiation changes on the migration of the Congo Air Boundary and water levels of paleo-Lake Suguta, Northern Kenya Rift, during the African Humid Period (15–5 ka BP). Palaeogeography, Palaeoclimatology, Palaeoecology 396, 1–16.

Junginger, A., Trauth, M.H., 2013. Hydrological constraints of paleo-Lake Suguta in the Northern Kenya Rift during the African Humid Period (15–5 ka BP). Global and Planetary Change 111, 174–188.

Kalmetieva, Z.A., Mikolaichuk, A.V., Moldobekov, B.D., Meleshko, A.V., Jantaev, M.M., Zubovich, A.V., 2009. Atlas of earthquakes in Kyrgyzstan. Central-Asian Institute for Applied Geosciences (CAIAG), Bishkek.

Ketcham, R.A., 2005. Forward and Inverse Modeling of Low-Temperature Thermochronometry Data. Reviews in Mineralogy and Geochemistry 58, 275–314.

Ketcham, R.A., Donelick, R.A., Carlson, W.D., 1999. Variability of apatite fission-track annealing kinetics: III. Extrapolation to geological time scales. American Mineralogist 84, 1235–1255.

King, B.C., 1978. Structural and volcanic evolution of the Gregory Rift Valley. Journal of the Geological Society 6, 29–54.

Kirby, E., Whipple, K.X., 2012. Expression of active tectonics in erosional landscapes. Journal of Structural Geology 44, 54–75.

Kirkby, M.J., 1969. Infiltration, through flow and overland flow, in: Water, Earth and Man. London, Methuen, pp. 215–228.

Klocke, A., Voigt, T., Kley, J., Pfeifer, S., Rocktäschel, T., Gaupp, R., in press. Cenozoic evolution of the Pamir and Tien Shan Mountains reflected in syntectonic deposits of the Tajik Basin. The Geological Society .

Knox, J.C., 1972. Valley alluviation in southwestern Wisconsin. Annals of the Association of American Geographers 62, 401–410.

Kober, F., Ivy-Ochs, S., Schlunegger, F., Baur, H., Kubik, P.W., Wieler, R., 2007. Denudation rates and a topography-driven rainfall threshold in northern Chile: Multiple cosmogenic nuclide data and sediment yield budgets. Geomorphology 83, 97–120.

Koehn, D., Aanyu, K., Haines, S., Sachau, T., 2008. Rift nucleation, rift propagation and the creation of basement micro-plates within active rifts. Tectonophysics 458, 105–116.

Kohl, C.P., Nishiizumi, K., 1992. Chemical isolation of quartz for measurement of in-situ -produced cosmogenic nuclides. Geochimica et Cosmochimica Acta 56, 3583–3587.

Konopelko, D., Seltmann, R., Apayarov, F., Belousova, E., Izokh, A., Lepekhina, E., 2013. U–Pb–Hf zircon study of two mylonitic granite complexes in the Talas-Fergana fault zone, Kyrgyzstan, and Ar–Ar age of deformations along the fault. Journal of Asian Earth Sciences 73, 334–346.

Koppen, W., 1936. Das geographische System der Klimate, in: Köppen, W., Geiger, R. (Eds.), Handbuch der Klimatologie. Gebrüder Borntraeger, Berlin.

Koptev, A., Calais, E., Burov, E., Leroy, S., Gerya, T., 2015. Dual continental rift systems generated by plume-lithosphere interaction. Nature Geoscience 8, 388–392.

Korschinek, G., Bergmaier, A., Faestermann, T., Gerstmann, U.C., Knie, K., Rugel, G., Wallner, A., Dillmann, I., Dollinger, G., von Gostomski, C.L., Kossert, K., Maiti, M., Poutivtsev, M., Remmert, A., 2010. A new value for the half-life of ^{10}Be by Heavy-Ion Elastic Recoil Detection and liquid scintillation counting. Nuclear Instruments and Methods in Physics Research Section B: Beam Interactions with Materials and Atoms 268, 187–191.

Lague, D., Hovius, N., Davy, P., 2005. Discharge, discharge variability, and the bedrock channel profile. Journal of Geophysical Research 110, F04006.

Lal, D., 1991. Cosmic ray labeling of erosion surfaces: in situ nuclide production rates and erosion models. Earth and Planetary Science Letters 104, 424–439.

Lamb, H., Darbyshire, I., Verschuren, D., 2003. Vegetation response to rainfall variation and human impact in central Kenya during the past 1100 years. The Holocene 13, 285–292.

Langbein, W.B., Schumm, S.A., 1958. Yield of Sediment in Relation to Mean Annual Precipitation. Transsactions, AGU 39, 1–9.

Latin, D., Norry, M.J., Tarzey, R.J.E., 1993. Magmatism in the Gregory Rift, East Africa: Evidence for Melt Generation by a Plume. Journal of Petrology 34, 1007–1027.

Lesik, O.M., Mikolaichuk, A.V., 2001. Deep structure of the Turkestan paleo-ocean suture. Russian Geology and Geophysics 42, 1386–1392.

Levin, N.E., Zipser, E.J., Cerling, T.E., 2009. Isotopic composition of waters from Ethiopia and Kenya: Insights into moisture sources for eastern Africa. Journal of Geophysical Research 114, D23306.

Lezzar, K.E., Tiercelin, J.J., Batist, M.D., Cohen, A.S., Bandora, T., Rensbergen, P.V., Turdu, C.L., Mifundu, W., Klerkx, J., 1996. New seismic stratigraphy and Late Tertiary history of the North Tanganyika Basin, East African Rift system, deduced from multichannel and high-resolution reflection seismic data and piston core evidence. Basin Research 8, 1–28.

Lippard, S.J., 1973. The petrology of phonolites from the Kenya Rift. Lithos 6, 217–234.

Lithgow-Bertelloni, C., Silver, P.G., 1998. Dynamic topography, plate driving forces and the African superswell. Nature 395, 269–272.

Loury, C., Rolland, Y., Guillot, S., Mikolaichuk, A.V., Lanari, P., Bruguier, O., Bosch, D., in press. Crustal-scale structure of South Tianshan: implications for subduction polarity and Cenozoic reactivation. The Geological Society .

Maboko, M.A.H., Boelrijk, N.A.I.M., Priem, H.N.A., Verdurmen, E.A.T., 1985. Zircon U-Pb and biotite Rb-Sr dating of the wami river granulites, Eastern Granulites, Tanzania: Evidence for approximately 715 Ma old granulite-facies metamorphism and final Pan-African cooling approximately 475 Ma ago. Precambrian Research 30, 361–378.

Macaulay, E.A., Sobel, E.R., Mikolaichuk, A.V., Kohn, B., Stuart, F.M., 2014. Cenozoic deformation and exhumation history of the Central Kyrgyz Tien Shan. Tectonics 33, 135–165.

Macaulay, E.A., Sobel, E.R., Mikolaichuk, A.V., Landgraf, A., Kohn, B., Stuart, F.M., 2013. Thermochronologic insight into late Cenozoic deformation in the basement-cored Terskey Range, Kyrgyz Tien Shan. Tectonics 32, 487–500.

Marty, B., Pik, R., Gezahegn, Y., 1996. Helium isotopic variations in Ethiopian plume lavas: nature of magmatic sources and limit on lower mantle contribution. Earth and Planetary Science Letters 144, 223–237.

Maslin, M.A., Shultz, S., Trauth, M.H., 2015. A synthesis of the theories and concepts of early human evolution. Philosophical Transactions B 370, 1–12.

MBede, E., 2001. Tectonic setting and uplift analyiss of the Pangani Rift Basin in Northern Tanzania using apatite fission track thermochronology. Tanzanian Journal of Sciences 27, 1–16.

McClay, K., Bonora, M., 2001. Analog Models of Restraining Stepovers in Strike-Slip Fault Systems. Bulletin of the American Association of Petroleum Geologists 85, 233–260.

McDougall, I., Brown, F.H., 2009. Timing of volcanism and evolution of the northern Kenya Rift. Geological Magazine 146, 34–47.

McGregor, G.R., Nieuwolt, S., 1998. Tropical Climatology: An Introduction to the Climates of the Low Latitudes. 2 ed., Wiley, Chichester, U.K.

Melnick, D., Garcin, Y., Quinteros, J., Strecker, M.R., Olago, D., Tiercelin, J.J., 2012. Steady rifting in northern Kenya inferred from deformed Holocene lake shorelines of the Suguta and Turkana basins. Earth and Planetary Science Letters 331, 335–346.

Michon, L., 2015. What the volcanism of the East African Rift tells us on its evolution and dynamics: a reappraisal, in: EGU General Assembly, Vienna, Austria.

Milankovitch, M., 1941. Canon of Insolation and the Ice-Age Problem (in German). Special Publications of the Royal Serbian Academy 132, 484.

Miller, S.R., Sak, P.B., Kirby, E., Bierman, P.R., 2013. Neogene rejuvenation of central Appalachian topography: Evidence for differential rock uplift from stream profiles and erosion rates. Earth and Planetary Science Letters 369–370, 1–12.

Milliman, J.D., Meade, R.H., 1983. World-Wide Delivery of River Sediment to the Oceans. The Journal of Geology 91, 1–21.

Mills, K., Ryves, D.B., Anderson, N.J., Bryant, C.L., Tyler, J.J., 2014. Expressions of climate perturbations in western Ugandan crater lake sediment records during the last 1000 years. Climate of the Past 10, 1581–1601.

Molina, A., Govers, G., Poesen, J., Van Hemelryck, H., De Bièvre, B., Vanacker, V., 2008. Environmental factors controlling spatial variation in sediment yield in a central Andean mountain area. Geomorphology 98, 176–186.

Molnar, P., 2004. Late Cenozoic increase in accumulation rates of terrestrial sediment: How Might Climate Change Have Affected Erosion Rates? Annual Review of Earth and Planetary Sciences 32, 67–89.

Molnar, P., Anderson, R.S., Anderson, S.P., 2007. Tectonics, fracturing of rock, and erosion. Journal of Geophysical Research 112, F03014.

Molnar, P., Anderson, R.S., Kier, G., Rose, J., 2006. Relationships among probability distributions of stream discharges in floods, climate, bed load transport, and river incision. Journal of Geophysical Research 111.

Molnar, P., England, P., 1990. Late Cenozoic uplift of mountain ranges and global climate change: chicken or egg? Nature 346, 29–34.

Molnar, P., Tapponnier, P., 1975. Cenozoic Tectonics of Asia: Effects of a Continental Collision: Features of recent continental tectonics in Asia can be interpreted as results of the India-Eurasia collision. Science 189, 419–426.

Montgomery, D., Balco, G., Willett, S.D., 2001. Climate, tectonics, and the morphology of the Andes. Geology 29, 579–582.

Montgomery, D.R., Brandon, M.T., 2002. Topographic controls on erosion rates in tectonically active mountain ranges. Earth and Planetary Science Letters 201, 481–489.

Moon, S., Chamberlain, C.P., Blisniuk, P.M., Levine, N., Rood, D.H., Hilley, G.E., 2011. Climatic control of denudation in the deglaciated landscape of the Washington Cascades. Nature Geoscience 4, 469–473.

Morgan, W.T.W., 1971. The South Turkana Expedition scientific papers IV. Land units of the Lokori area. Geography Journal 137, 14–28.

Morley, C.K., Wescott, W.A., Stone, D.M., Harper, R.M., Karanja, F.M., 1992. Tectonic evolution of the northern kenyan rift. Journal of the Geological Society 149, 333–348.

Moucha, R., Forte, A.M., 2011. Changes in African topography driven by mantle convection. Nature Geoscience 4, 707–712.

Mudelsee, M., Bickert, T., Lear, C.H., Lohmann, G., 2014. Cenozoic climate changes: A review based on time series analysis of marine benthic δ18O records. Review of Geophyisics 52, 333–374.

Mugisha, F., Ebinger, C.J., Strecker, M.R., Pope, D., 1997. Two-stage rifting in the Kenya rift: implications for half-graben models. Tectonophysics 278, 63–81.

Mumbi, C.T., Marchant, R., Hooghiemstra, H., Wooller, M.J., 2008. Late Quaternary vegetation reconstruction from the Eastern Arc Mountains, Tanzania. Quaternary Research 69, 326–341.

Nearing, M.A., Jetten, V., Baffaut, C., Cerdan, O., Couturier, A., Hernandez, M., Le Bissonnais, Y., Nichols, M.H., Nunes, J.P., Renschler, C.S., Souchère, V., van Oost, K., 2005. Modeling response of soil erosion and runoff to changes in precipitation and cover. Catena 61, 131–154.

Nicholson, S.E., 1988. Land surface atmosphere interaction. Progress in Physical Geography .

Nicholson, S.E., 1996. A review of climate dynamics and climate variability in eastern Africa, in: Johnson, T.C., Odada, E.O. (Eds.), The Limnology, Climatology and Paleoclimatology of the East African Lakes. Gordon and Breach Publishers, Amsterdam, pp. 25–56.

Nicholson, S.E., 2001. Climatic and environmental change in Africa during the last two centuries. Climate Research , 1–22.

Niemi, N.A., Buscher, J., Spotila, J.A., House, M., Kelley, S.A., 2013. Insights from low-temperature thermochronometry into transpressional deformation and crustal exhumation along the San Andreas fault in the western Transverse Ranges, California. Tectonics 32, 1602–1622.

Nyblade, A.A., Brazier, R.A., 2002. Precambrian lithospheric controls on the development of the East African rift system. Geology 30, 755–758.

Nyblade, A.A., Owens, T.J., Gurrola, H., Ritsema, J., Langston, C.A., 2000. Seismic evidence for a deep upper mantle thermal anomaly beneath east Africa. Geology 28, 599–602.

Odada, E., 2013. Our Freshwater Under Threat–Vulnerability of Water Resources to Environmental Change in Africa. Technical Report.

Ogola, J.S., Behr, H.J., van den Kerkhof, A.M., 1994. Fluid inclusion and cathodoluminescence studies on fluorite from the Kerio valley, Kenya. Journal of African Earth Sciences 18, 309–323.

Ojany, F.F., Ogenoo, R.B., Longman, 1973. Kenya: A Study in Physical and Human Geography. Longman, Nairobi.

Olago, D., 2001. Vegetation changes over palaeo-time scales in Africa. Climate Research 17, 105–121.

ORNL-DAAC, 2012. Oak Ridge National Laboratory Distributed Active Archive Center – MODIS Subsetted Land Products, Collection 5. Oak Ridge, Tennessee, ORNL DAAC (http://daac.ornl.gov/MODIS/modis.html, last accessed 19 July 2013).

Osmaston, H.A., Harrison, S.P., 2005. The Late Quaternary glaciation of Africa: A regional synthesis. Quaternary International 138–139, 32–54.

Ouimet, W.B., Whipple, K.X., Granger, D.E., 2009. Beyond threshold hillslopes: Channel adjustment to base-level fall in tectonically active mountain ranges. Geology 37, 579–582.

Ovuka, M., 2000. More people, more erosion? Land use, soil erosion and soil productivity in Murang'a district, Kenya. Land Degradation and Development 11, 111–124.

Owen, R.B., Barthelme, J.W., Renaut, R.W., Vincens, A., archaeology of Holocene deposits north-east of Lake Turkana, K., 1982. Palaeolimnology and archaeology of Holocene deposits north-east of Lake Turkana, Kenya. Nature 298, 523–529.

Owen, R.B., Renaut, R.W., Behrensmeyer, A.K., Potts, R., 2014. Quaternary geochemical stratigraphy of the Kedong?ÄìOlorgesailie section of the southern Kenya Rift valley. Palaeogeography, Palaeoclimatology, Palaeoecology 396, 194–212.

Pelletier, J.D., Brad Murray, A., Pierce, J.L., Bierman, P.R., Breshears, D.D., Crosby, B.T., Ellis, M., Foufoula-Georgiou, E., Heimsath, A.M., Houser, C., Lancaster, N., Marani, M., Merritts, D.J., Moore, L.J., Pederson, J.L., Poulos, M.J., Rittenour, T.M., Rowland, J.C., Ruggiero, P., Ward, D.J., Wickert, A.D., Yager, E.M., 2015. Forecasting the response of Earth's surface to future climatic and land-use changes: A review of methods and research needs. Earth's Future .

Pelletier, J.D., McGuire, L.A., Ash, J.L., Engelder, T.M., Hill, L.E., Leroy, K.W., Orem, C.A., Rosenthal, W.S., Trees, M.A., Rasmussen, C., Chorover, J., 2011. Calibration and testing of upland hillslope evolution models in a dated landscape: Banco Bonito, New Mexico. Journal of Geophysical Research 116, F04004.

Perry, F.V., Baldridge, W.S., DePaolo, D.J., 1987. Role of asthenosphere and lithosphere in the genesis of Late Cenozoic basaltic rocks from the Rio Grande Rift and adjacent regions of the southwestern United States. Journal of Geophysical Research 92, 9193–9213.

Persano, C., Stuart, F.M., Bishop, P., Barfod, D.N., 2002. Apatite (U–Th)/He age constraints on the development of the Great Escarpment on the southeastern Australian passive margin. Earth and Planetary Science Letters 200, 79–90.

Pickford, M., 1994. Patterns of sedimentation and fossil distribution in the Kenya Rift Valleys. Journal of African Earth Sciences 18, 51–60.

Pik, R., Marty, B., Carignan, J., Yirgu, G., Ayalew, T., 2008. Timing of East African Rift development in southern Ethiopia: Implication for mantle plume activity and evolution of topography. Geology 36, 167–170.

Popov, S., Rögl, F., Rozanov, A.Y., Steininger, F.F., Scherba, I.G., Kovac, M., 2004. Lithological-Paleogeographic maps of Paratethys. volume 250 of *10 maps Late Eocene to Pliocene*. Schweizerbart Science Publishers.

Portenga, E.W., Bierman, P.R., 2011. Understanding Earth's eroding surface with ^{10}Be. GSA Today 21, 4–10.

Potts, R., 1998. Environmental hypothesis of hominin evolution. American Journal of Physical Anthropology 41, 93–136.

Potts, R., 2013. Hominin evolution in settings of strong environmental variability. Quaternary Science Reviews 73, 1–13.

Prenzel, J., Lisker, F., Balestrieri, M.L., Läufer, A., Spiegel, C., 2013. The Eisenhower Range, Transantarctic Mountains: Evaluation of qualitative interpretation concepts of thermochronological data. Chemical Geology 352, 176–187.

Prosser, I.P., Dietrich, W.E., 1995. Field Experiments on Erosion by Overland Flow and Their Implication for a Digital Terrain Model of Channel Initiation. Water Resources Research 31, 2867–2876.

Quinn, R.L., Lepre, C.J., Wright, J.D., Feibel, C.S., 2007. Paleogeographic variations of pedogenic carbonate delta(13)C values from Koobi Fora, Kenya: implications for floral compositions of Plio-Pleistocene hominin environments. Journal of Human Evolution .

Ravi, S., Breshears, D.D., Huxman, T.E., D'Odorico, P., 2010. Land degradation in drylands: Interactions among hydrologic–aeolian erosion and vegetation dynamics. Geomorphology 116, 236–245.

Reimer, P., Baillie, M., Bard, E., Bayliss, A., Beck, J., Bertrand, C., Blackwell, P., Buck, C., Burr, G., Cutler, K., Damon, P., Edwards, R., Fairbanks, R., Friedrich, M., Guilderson, T., Hogg, A., Hughen, K., Kromer, B., McCormac, G., Manning, S., Ramsey, C., Reimer, R., Remmele, S., Southon, J., Stuiver, M., Reimer, P., Talamo, S., Taylor, F., van der Plicht, J., Weyhenmeyer, C., 2004. IntCal04 terrestrial radiocarbon age calibration, 0?26 cal kyr BP. Radiocarbon 46 , 1029–1058.

Reiners, P.W., 2005. Zircon (U–Th)/He thermochronometry. Low-Temperature Thermochronology: Techniques, Interpretations, and Applications 58, 151–179.

Reiners, P.W., Brandon, M.T., 2006. Using thermochronology to understand orogenic erosion. Annual Review of Earth and Planetary Sciences 34, 419–466.

Reiners, P.W., Ehlers, T.A., Mitchell, S.G., Montgomery, D.R., 2003. Coupled spatial variations in precipitation and long-term erosion rates across the Washington Cascades. Nature 426, 645–647.

Renaut, R.W., Ego, J.K., Tiercelin, J.J., Le Turdu, C., Owen, R.B., 1999. Saline, alkaline palaeolakes of the Tugen Hills–Kerio Valley region, Kenya Rift Valley, in: Andrews, P., Banham, P. (Eds.), Late Cenozoic Environments and Hominoid Evolution: A Tribute to Bill Bishop. The Geological Society, London, pp. 41–58.

Richardson, C.K., Holland, H.D., 1979. Fluorite deposition in hydrothermal systems. Geochimica et Cosmochimica Acta 43, 1327–1335.

Riebe, C.S., Granger, D.E., 2013. Quantifying effects of deep and near-surface chemical erosion on cosmogenic nuclides in soils, saprolite, and sediment. Earth Surface Processes and Landforms 38, 523–533.

Riebe, C.S., Kirchner, J.W., Granger, D.E., Finkel, R., 2001. Strong tectonic and weak climatic control of long-term chemical weathering rates. Geology 29, 511–514.

Roberts, E.M., Stevens, N.J., O'connor, P.M., Dirks, P.H.G.M., Gottfried, M.D., Clyde, W.C., Armstrong, R.A., Kemp, A.I.S., Heming, S., 2012. Initiation of the western branch of the East African Rift coeval with the eastern branch. Nature Geoscience 5, 289–294.

Roering, J.J., Kirchner, J.W., Dietrich, W.E., 1999. Evidence for nonlinear, diffusive sediment transport on hillslopes and implications for landscape morphology. Water Resources Research 35, 853–870.

Roering, J.J., Marshall, J., Booth, A.M., Mort, M., Jin, Q., 2010. Evidence for biotic controls on topography and soil production. Earth and Planetary Science Letters 298, 183–190.

Rolland, Y., Alexeiev, D.V., Kröner, A., Corsini, M., Loury, C., P, M., 2013. Late Palaeozoic to Mesozoic kinematic history of Talas-Ferghana strike-slip Fault (Kyrgyz West Tianshan) as revealed by ^{40}Ar/^{39}Ar dating of syn-kinematic phengite. Journal of Asian Earth Sciences 67-68, 76–92.

Roller, S., Wittmann, H., Kastowski, M., Hinderer, M., 2012. Erosion of the Rwenzori Mountains, East African Rift, from in situ-produced cosmogenic Be-10. Journal of Geophysical Research 117.

Russell, J.M., Johnson, T.C., 2005. A high-resolution geochemical record from Lake Edward, Uganda Congo and the timing and causes of tropical African drought during the late Holocene. Quaternary Science Reviews 24, 1375–1389.

Safran, E.B., Bierman, P.R., Aalto, R., Dunne, T., Whipple, K.X., Caffee, M., 2005. Erosion rates driven by channel network incision in the Bolivian Andes. Earth Surface Processes and Landforms 30, 1007–1024.

Saji, N.H., Goswami, B.N., Vinayachandran, P.N., Yamagata, T., 1999. A dipole mode in the tropical Indian Ocean. Nature 401, 360–363.

Saneyoshi, M., Nakayama, K., Sakai, T., Sawada, Y., Ishida, H., 2006. Half graben filling processes in the early phase of continental rifting: The Miocene Namurungule Formation of the Kenya Rift. Sedimentary Geology 186, 111–131.

Schaller, M., von Blanckenburg, F., Veldkamp, A., Tebbens, L.A., Hovius, N., Kubik, P.W., 2002. A 30000 yr record of erosion rates from cosmogenic ^{10}Be in Middle European river terraces. Earth and Planetary Science Letters 204, 307–320.

Scherler, D., Bookhagen, B., Strecker, M.R., 2014. Tectonic control on ^{10}Be-derived erosion rates in the Garhwal Himalaya, India. Journal of Geophysical Research 119, 2013JF002955.

Schmalholz, M., 2004. The amalgamation of the Pamirs and their subsequent evolution in the far field of the India–Asia collision. Ph.D. thesis. Universität Tübingen.

Schmidt, J., Hacker, B.R., Ratschbacher, L., Stübner, K., Stearns, M., Kylander-Clark, A., Cottle, J.M., Alexander, A., Webb, G., Gehrels, G., Minaev, V., 2011. Cenozoic deep crust in the Pamir. Earth and Planetary Science Letters 312, 411–421.

Scholz, C.A., Finney, B.P., 1994. Late Quaternary sequence stratigraphy of Lake Malawi (Nyasa), Africa. Sedimentology 41, 163–179.

Schull, T.J., 1988. Rift Basins of Interior Sudan: Petroleum Exploration and Discovery. Bulletin of the American Association of Petroleum Geologists 72, 1128–1142.

Schumm, S.A., 1993. River response to baselevel change: Implications for sequence stratigraphy. Journal of Geology 101, 279–294.

Selander, J., Oskin, M., Ormukov, C., K, A., 2012. Inherited strike-slip faults as an origin for basement-cored uplifts: Example of the Kungey and Zailiskey ranges, northern Tian Shan. Tectonics 31, TC4026.

Seliverstov, K.V., Ghes, M.D., 2001. Petrochemical features of magmatites and major kinematic parameters of middle Carboniferous–early Permian subduction of the Turkestan paleo-ocean (Tien Shan, Northern Ferghana). Russian Geology and Geophysics 42, 1393–1397.

Seltmann, R., Konopelko, D., Biske, G., Divaev, F., Sergeev, S., 2011. Hercynian post-collisional magmatism in the context of Paleozoic magmatic evolution of the Tien Shan orogenic belt. Journal of Asian Earth Sciences 42, 821–838.

Sengor, A.M.C., Natal'in, B.A., Burtman, V.S., 1993. Evolution of the Altaid tectonic collage and Palaeozoic crustal growth in Eurasia. Nature 364, 299–307.

Sepulchre, P., Ramstein, G., Fluteau, F., Schuster, M., Tiercelin, J.J., Brunet, M., 2006. Tectonic Uplift and Eastern Africa Aridification. Science 313, 1419–1423.

Shackleton, R.M., 1993. Tectonics of the Mozambique Belt in East Africa. The Geological Society 76, 345–362.

Shanahan, T., Overpeck, J., Anchukaitis, K., Beck, J., Cole, J., Dettman, D., Peck, J., Scholz, C., King, J., 2009. Atlantic forcing of persistent drought in West Africa. Science 324, 377?–380.

Simiyu, S.M., Keller, G.R., 1997. An integrated analysis of lithospheric structure across the East African plateau based on gravity anomalies and recent seismic studies. Tectonophysics 278, 291–313.

Sippl, C., Schurr, B., Yuan, X., Mechie, J., Schneider, F.M., Gadoev, M., Orunbaev, S., Oimahmadov, I., Haberland, C., Abdybachaev, U., Minaev, V., Negmatullaev, S., Radjabov, N., 2013. Geometry of the Pamir-Hindu Kush intermediate-depth earthquake zone from local seismic data. Journal of Geophysical Research 118, 1438–1457.

Smith, M., 1994. Stratigraphic and Structural Constraints on Mechanisms of Active Rifting in the Gregory Rift, Kenya. Tectonophysics 236, 3–22.

Smith, M., Mosley, P., 1993. Crustal heterogeneity and basement influence on the development of the Kenya Rift, East Africa. Tectonics 12, 591–606.

Sobel, E.R., 1999. Basin analysis of the Jurassic–Lower Cretaceous southwest Tarim basin, northwest China. Geological Society of America Special Papers 111, 709–724.

Sobel, E.R., Chen, J., Heermance, R.V., 2006a. Late Oligocene-Early Miocene initiation of shortening in the Southwestern Chinese Tian Shan: Implications for Neogene shortening rate variations. Earth and Planetary Science Letters 247, 70–81.

Sobel, E.R., Chen, J., Schoenbohm, L.M., Thiede, R., Stockli, D.F., Sudo, M., Strecker, M.R., 2013. Oceanic-style subduction controls late Cenozoic deformation of the Northern Pamir orogen. Earth and Planetary Science Letters 363, 204–218.

Sobel, E.R., Dumitru, T.A., 1997. Thrusting and exhumation around the margins of the western Tarim basin during the India-Asia collision. Journal of Geophysical Research 102, 5043–5063.

Sobel, E.R., Oskin, M., Burbank, D., Mikolaichuk, A.V., 2006b. Exhumation of basement-cored uplifts: Example of the Kyrgyz Range quantified with apatite fission track thermochronology. Tectonics 25, TC2008.

Sobel, E.R., Seward, D., 2010. Influence of etching conditions on apatite fission-track etch pit diameter. Chemical Geology 271, 59–69.

Spiegel, C., Kohn, B.P., Belton, D.X., Gleadow, A.J.W., 2007. Morphotectonic evolution of the central Kenya rift flanks: Implications for late Cenozoic environmental change in East Africa. Geology 35, 427–430.

Spotila, J.A., Niemi, N., Brady, R., House, M., Buscher, J., Oskin, M., 2007. Long-term continental deformation associated with transpressive plate motion: The San Andreas fault. Geology 35, 967–970.

Stamps, D.S., Calais, E., Saria, E., Hartnady, C., Nocquet, J.M., Ebinger, C.J., Fernandes, R.M., 2008. A kinematic model for the East African Rift. Geophysical Research Letters 35.

Stockli, D.F., 2005. Application of low-temperature thermochronometry to extensional eectonic settings. Reviews in Mineralogy and Geochemistry 58, 411–448.

Stone, J.O., 2000. Air pressure and cosmogenic isotope production. Journal of Geophysical Research 105, 23753–23759.

Strecker, M.R., Blisniuk, P.M., Eisbacher, G.H., 1990. Rotation of extension direction in the central Kenya Rift. Geology 18, 299–302.

Street-Perrott, F.A., Perrott, R.A., 1993. Holocene vegetation, lake levels and climate of Africa, in: Wright, H.E., Kutzbach, J.E., Webb, T.I., Ruddiman, W.F., Street-Perrott, F.A., Bartlein, P.J. (Eds.), Global climates since the last glacial maximum. University of Minnesota Press, Minneapolis, pp. 318–356.

Stuiver, M., Reimer, P., 1993. Extended 14C data base and revised 3.0 14C age calibration program. Radiocarbon 35. Radiocarbon 35 , 215–230.

Summerfield, M.A., Hulton, N.J., 1994. Natural controls of fluvial denudation rates in major world drainage basins. Journal of Geophysical Research 99, 13871–13883.

Sun, J., Li, Y., Zhang, Z., Fu, B., 2009. Magnetostratigraphic data on Neogene growth folding in the foreland basin of the southern Tianshan Mountains. Geology 37, 1051–1054.

Thomas, J.C., Perroud, H., Cobbold, P.R., Bazhenov, M.L., Burtman, V.S., Chauvin, A., Sadybakasov, E., 1993. A paleomagnetic study of tertiary formations from the Kyrgyz Tien-Shan and its tectonic implications. Journal of Geophysical Research 98, 9571–9589.

Tiercelin, J.J., Lezzar, K.E., 2002. A 300 million years history of rift lakes in Central and East Africa: an updated broad review, in: Odada, E., Olago, D. (Eds.), The East African Great Lakes: Limnology, Palaeolimnology and Biodiversity: Advances in Global Change Research.. Springer, pp. 3–60.

Tiercelin, J.J., Potdevin, J.L., Morley, C.K., Talbot, M.R., Bellon, H., Rio, A., Le Gall, B., Vétel, W., 2004. Hydrocarbon potential of the Meso-Cenozoic Turkana Depression, northern Kenya. I. Reservoirs: depositional environments, diagenetic characteristics, and source rock–reservoir relationships. Marine and Petroleum Geology 21, 41–62.

Tiercelin, J.J., Thuo, P., Potdevin, J.L., Nalpas, T., 2012. Hydrocarbon Prospectivity in Mesozoic and Early–Middle Cenozoic Rift Basins of Central and Northern Kenya, Eastern Africa, in: Gao, D. (Ed.), Tectonics and Sedimentation. American Association of Petroleum Geologists, Tulsa, Oklahoma, pp. 179–207.

Tiercelin, J.J., Vincens, A., 1987. Le Demi-Graben de Baringo-Bogoria, Rift Gregory, Kenya, 30,000 Ans d'Histoire Hydrologique et Sédimentaire. Bulletin des Centres de Recherches Exploration Production Elf-Aquitaine , 249–540.

Tierney, J.E., Russell, J.M., Huang, Y., Damsté, J.S.S., Hopmans, E.C., Cohen, A.S., 2008. Northern Hemisphere Controls on Tropical Southeast African Climate During the Past 60,000 Years. Science 322, 252–255.

Tierney, J.E., Russell, J.M., Sinninghe Damsté, J.S., Huang, Y., Verschuren, D., 2011. Late Quaternary behavior of the East African monsoon and the importance of the Congo Air Boundary. Quaternary Science Reviews 30, 798–807.

Torres Acosta, V., Schildgen, T.F., Clarke, B.A., Scherler, D., Bookhagen, B., Wittmann, H., von Blanckenburg, F., Strecker, M.R., 2015. Effect of vegetation cover on millennial-scale landscape denudation rates in East Africa. *In press* Lithosphere .

Trauth, M.H., Maslin, M.A., Deino, A.L., Strecker, M.R., 2005. Late Cenozoic Moisture History of East Africa. Science 309, 2051–2053.

Trauth, M.H., Maslin, M.A., Deino, A.L., Strecker, M.R., Bergner, A.G.N., Dühnforth, M., 2007. High- and low-latitude forcing of Plio-Pleistocene East African climate and human evolution. Journal of Human Evolution 53, 475–486.

Trenberth, K.E., 2011. Changes in precipitation with climate change. Climate Research 47, 123–138.

Trifonov, V.G., Makarov, V.I., Skobelev, S.F., 1992. The Talas-Ferghana active right-lateral fault. Annales Tectonicae VI, 224–237.

Truckle, P.H., 1976. Geology and late Cainozoic lake sediments of the Suguta Through, Kenya. Nature 263.

Tucker, G.E., 2004. Drainage basin sensitivity to tectonic and climatic forcing: implications of a stochastic model for the role of entrainment and erosion thresholds. Earth Surface Processes and Landforms 29, 185–205.

Turowski, J.M., Yager, E.M., Badoux, A., Rickenmann, D., Molnar, P., 2009. The impact of exceptional events on erosion, bedload transport and channel stability in a step-pool channel. Earth Surface Processes and Landforms 34, 1661–1673.

Valla, P.G., Herman, F., van der Beek, P.A., Braun, J., 2010. Inversion of thermochronological age-elevation profiles to extract independent estimates of denudation and relief history ? I: Theory and conceptual model. Earth and Planetary Science Letters 295, 511–522.

Van Schmus, W., Hinze, W., 1985. The midcontinent rift system. Annual Review of Earth and Planetary Sciences 13, 345–383.

Vanacker, V., von Blanckenburg, F., Govers, G., Molina, A., Poesen, J., Deckers, J., Kubik, P.W., 2007. Restoring dense vegetation can slow mountain erosion to near natural benchmark levels. Geology 35, 303–306.

Veldkamp, A., Buis, E., Wijbrans, J.R., Olago, D.O., Boshoven, E.H., Marée, M., van den Berg van Saparoea, R.M., 2007. Late Cenozoic fluvial dynamics of the River Tana, Kenya, an uplift dominated record. Quaternary Science Reviews 26, 2897–2912.

Verschuren, D., Laird, K.R., Cumming, B.F., 2000. Rainfall and drought in equatorial east Africa during the past 1,100 years. Nature 403, 410–414.

Verzilin, N.N., 1968. On the problem of the Talas-Ferghana strike-slip fault, in: Ognev, V.N. (Ed.), Problems of regional geology. Leningrad University, pp. 67–70.

Vincens, A., 1991. Late quaternary vegetation history of the South-Tanganyika basin. Climatic implications in South Central Africa. Palaeogeography, Palaeoclimatology, Palaeoecology 86, 207–226.

Vincens, A., Buchet, G., Williamson, D., Taieb, M., 2005. A 23,000 yr pollen record from Lake Rukwa (8°S, SW Tanzania): New data on vegetation dynamics and climate in Central Eastern Africa. Review of Palaeobotany and Palynology 137, 147–162.

Vincens, A., Chalié, F., Bonnefille, R., Guiot, J., Tiercelin, J.J., 1993. Pollen-Derived Rainfall and Temperature Estimates from Lake Tanganyika and Their Implication for Late Pleistocene Water Levels. Quaternary Research 40, 343–350.

Vincens, A., Garcin, Y., Buchet, G., 2007. Influence of rainfall seasonality on African lowland vegetation during the Late Quaternary: pollen evidence from Lake Masoko, Tanzania. Journal of Biogeography 34, 1274–1288.

Vlasov, N.G., Dyakov, Y.A., Cherev, E.S., 1991. Geological map of the Tajik SSR and adjacent territories: 1:500000.

Voytenko, V.N., Khudoley, A.K., 2012. Structural evolution of metamorphic rocks in the Talas Alatau, Tien Shan, Central Asia: Implication for early stages of the Talas-Ferghana Fault. Comptes Rendus Geoscience 344, 138–148.

Wack, M.R., Gilder, S.A., Macaulay, E.A., Sobel, E.R., Charreau, J., Mikolaichuk, A., 2014. Cenozoic magnetostratigraphy and magnetic properties of the southern Issyk-Kul basin, Kyrgyzstan. Tectonophysics 629, 14–26.

Wagner, M., Altherr, R., Van Den Haute, P., 1992. Apatite fission-track analysis of Kenyan basement rocks: constraints on the thermotectonic evolution of the Kenya dome. A reconnaissance study. Tectonophysics 204, 93–110.

Wainwright, J., Parsons, A.J., Abrahams, A.D., 2000. Plot-scale studies of vegetation, overland flow and erosion interactions: case studies from Arizona and New Mexico. Hydrological Processes 14, 2921–2943.

Wang, B., Faure, M., Cluzel, D., Shu, L., Charvet, J., Meffre, S., Ma, Q., 2006a. Late Paleozoic tectonic evolution of the northern West Chinese Tianshan Belt. Geodinamica Acta 19, 237–247.

Wang, B., Shu, L., Faure, M., Jahn, B.m., Cluzel, D., Charvet, J., Chung, S.l., Meffre, S., 2011. Paleozoic tectonics of the southern Chinese Tianshan: Insights from structural, chronological and geochemical studies of the Heiyingshan ophiolitic mélange (NW China). Tectonophysics 497, 85–104.

Wang, Y., Li, D., Xiao, X., Chi, Z., Min, L., Wang, J., Y, W., 2006b. Late Cenozoic tectonic movement in the front of the west Kunlun mountains and uplift of the northwestern margin of the Qinghai-Tibetan plateau. Geologica China 33, 41–47.

Webster, P.J., Moore, A.M., Loschnigg, J.P., Leben, R.R., 1999. Coupled ocean-atmosphere dynamics in the Indian Ocean during 1997-98. Nature 401, 356–360.

Wei, H.H., Meng, Q.R., Ding, L., Li, Z.Y., 2013. Tertiary evolution of the western Tarim basin, northwest China: A tectono-sedimentary response to northward indentation of the Pamir salient. Tectonics 32, 558–575.

Wheildon, J., Morgan, P., Williamson, K.H., Evans, T.R., Swanberg, C.A., 1994. Heat flow in the Kenya rift zone. Tectonophysics 236, 131–149.

Whipple, K., Kirby, E., Brocklehurst, S., 1999. Geomorphic limits to climate-induced increases in topographic relief. Nature 401, 39–43.

Whipple, K.X., Tucker, G.E., 2002. Implications of sediment-flux-dependent river incision models for landscape evolution. Journal of Geophysical Research 107, ETG 3–20.

White, F., 1983. The vegetation of Africa: a descriptive memoir to accompany the Unesco/AETFAT/UNSO vegetation map of Africa. Natural resources research, Unesco.

Wichura, H., Bousquet, R., Oberhansli, R., Strecker, M.R., Trauth, M.H., 2010. Evidence for middle Miocene uplift of the East African Plateau. Geology 38, 543–546.

Wichura, H., Jacobs, L.L., Lin, A., Polcyn, M.J., Manthi, F.K., Winkler, D.A., Strecker, M.R., Clemens, M., 2015. A 17-My-old whale constrains onset of uplift and climate change in east Africa. Proceedings of the National Academy of Sciences 112, 3910–3915.

Willett, S.D., 1999. Orogeny and orography: The effects of erosion on the structure of mountain belts. Journal of Geophysical Research 104, 28957–28981.

Williams, L.A.J., 1970. The volcanics of the gregory rift valley, east Africa. Bulletin Volcanologique 34, 439–465.

Wilson, J.T., 1966. Did the Atlantic close and then re-open? Nature 211, 676–681.

Wilson, L., 1973. Variations in mean annual sediment yield as a function of mean annual precipitation. American Journal of Sciences 273, 335–349.

Windley, B.F., Alexeiev, D.V., Xiao, W., Kröner, A., Badarch, G., 2007. Tectonic models for accretion of the Central Asian Orogenic Belt. Journal of the Geological Society 164, 31–47.

Wischmeier, W., Smith, D., 1965. Predicting rainfall-erosion losses from cropland east of the Rocky Mountains: guide for selection of practices for soil and water conservation. Agriculture handbook, Agricultural Research Service, U. S. Dept of Agriculture in cooperation with Purdue Agricultural Experiment Station.

Wittmann, H., von Blanckenburg, F., Kruesmann, T., Norton, K.P., Kubik, P.W., 2007. Relation between rock uplift and denudation from cosmogenic nuclides in river sediment in the Central Alps of Switzerland. Journal of Geophysical Research 112, F04010.

Wolf, R.A., Farley, K.A., Kass, D.M., 1998. Modeling of the temperature sensitivity of the apatite (U–Th)/He thermochronometer. Chemical Geology 148, 105–114.

Wolff, C., Haug, G.H., Timmermann, A., Damsté, J.S.S., Brauer, A., Sigman, D.M., Cane, M.A., Verschuren, D., 2011. Reduced Interannual Rainfall Variability in East Africa During the Last Ice Age. Science 333, 743–747.

Xiao, W., Han, C., Yuan, C., Sun, M., Lin, S., Chen, H., Li, Z., Li, J., Sun, S., 2008. Middle Cambrian to Permian subduction-related accretionary orogenesis of Northern Xinjiang, NW China: Implications for the tectonic evolution of central Asia. Journal of Asian Earth Sciences 32, 102–117.

Yin, A., Nie, S., Craig, P., Harrison, T.M., Ryerson, F.J., Qian, X.L., Yang, G., 1998. Late Cenozoic tectonic evolution of the southern Chinese Tian Shan. Tectonics 17, 1–27.

Yin, A., Rumelhart, P.E., Butler, R., Cowgill, E., Harrison, T.M., Foster, D.A., Ingersoll, R.V., Qing, Z., Xian-Qiang, Z., Xiao-Feng, W., Hanson, A., Raza, A., 2002. Tectonic history of the Altyn Tagh fault system in northern Tibet inferred from Cenozoic sedimentation. Geological Society of America Special Papers 114, 1257–1295.

Zhou, Y., Qiu, D., Wang, Y., 1984. The Petroleum potential of Miocene Series in the southwest part of Tarim basin. Oil Gas Geology 5, 261–270.

Zubovich, A.V., Wang, X.q., Scherba, Y.G., Schelochkov, G.G., Reilinger, R., Reigber, C., Mosienko, O.I., Molnar, P., Michajljow, W., Makarov, V.I., Li, J., Kuzikov, S.I., Herring, T.A., Hamburger, M.W., Hager, B.H., Dang, Y.m., Bragin, V.D., Beisenbaev, R.T., 2010. GPS velocity field for the Tien Shan and surrounding regions. Tectonics 29.

Appendix A

Additional data chapter 2

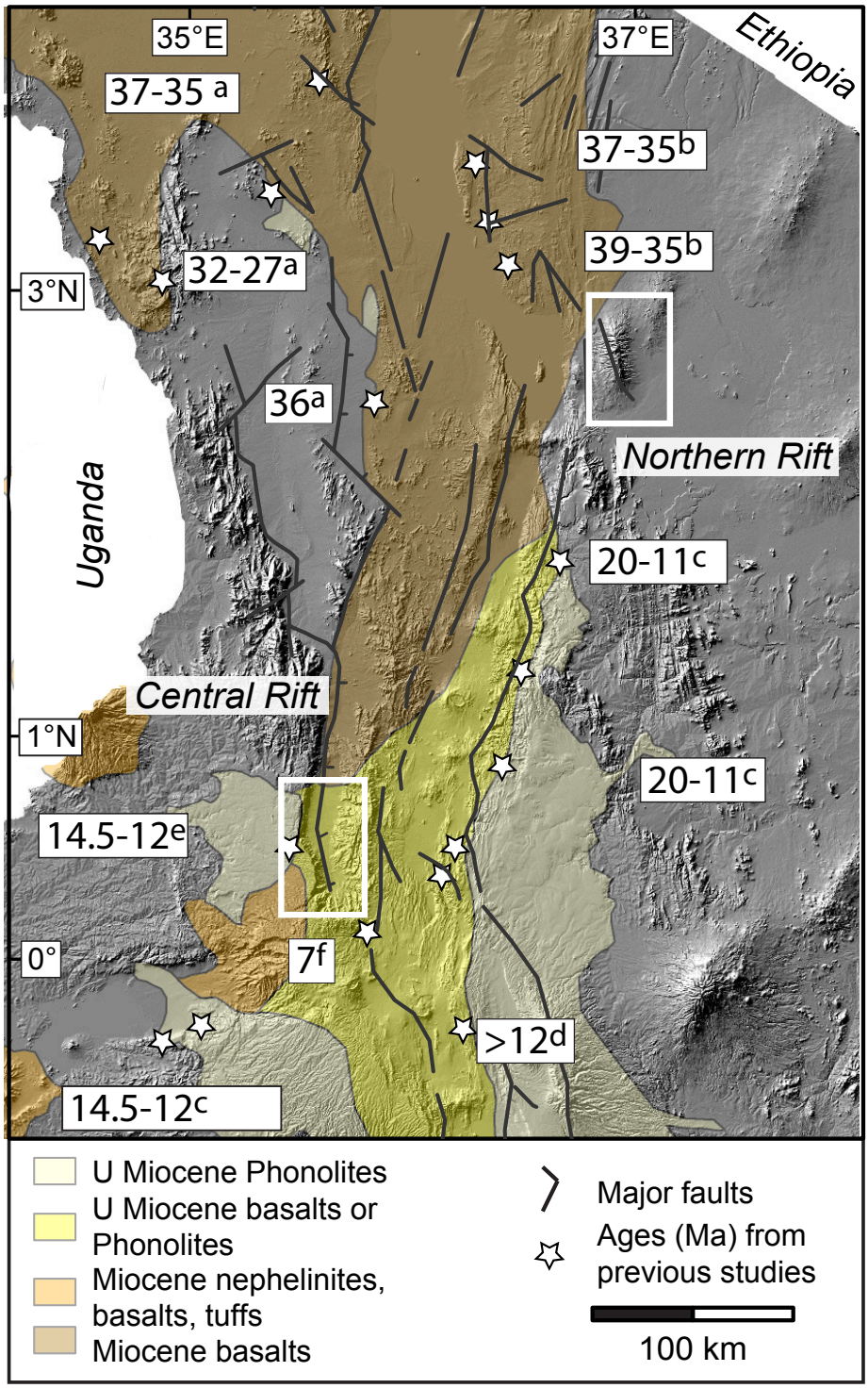

Figure A1. Distribution of the oldest volcanic rocks in the Kenya Rift. A: (Mcdougall and Brown, 2009;Thuo, 2009) using KAr dating. B: (Mcdougall, 2009) using Sr-Nd-Pb analysis. C: (Lippard, 1972; Caney, 1972), D: (Shackleton, 1945); Lippard, 1973, K-Ar. E: (Smith, 1994). F: (Lippard, 1973), K-Ar. White boxes denote the sampling area.

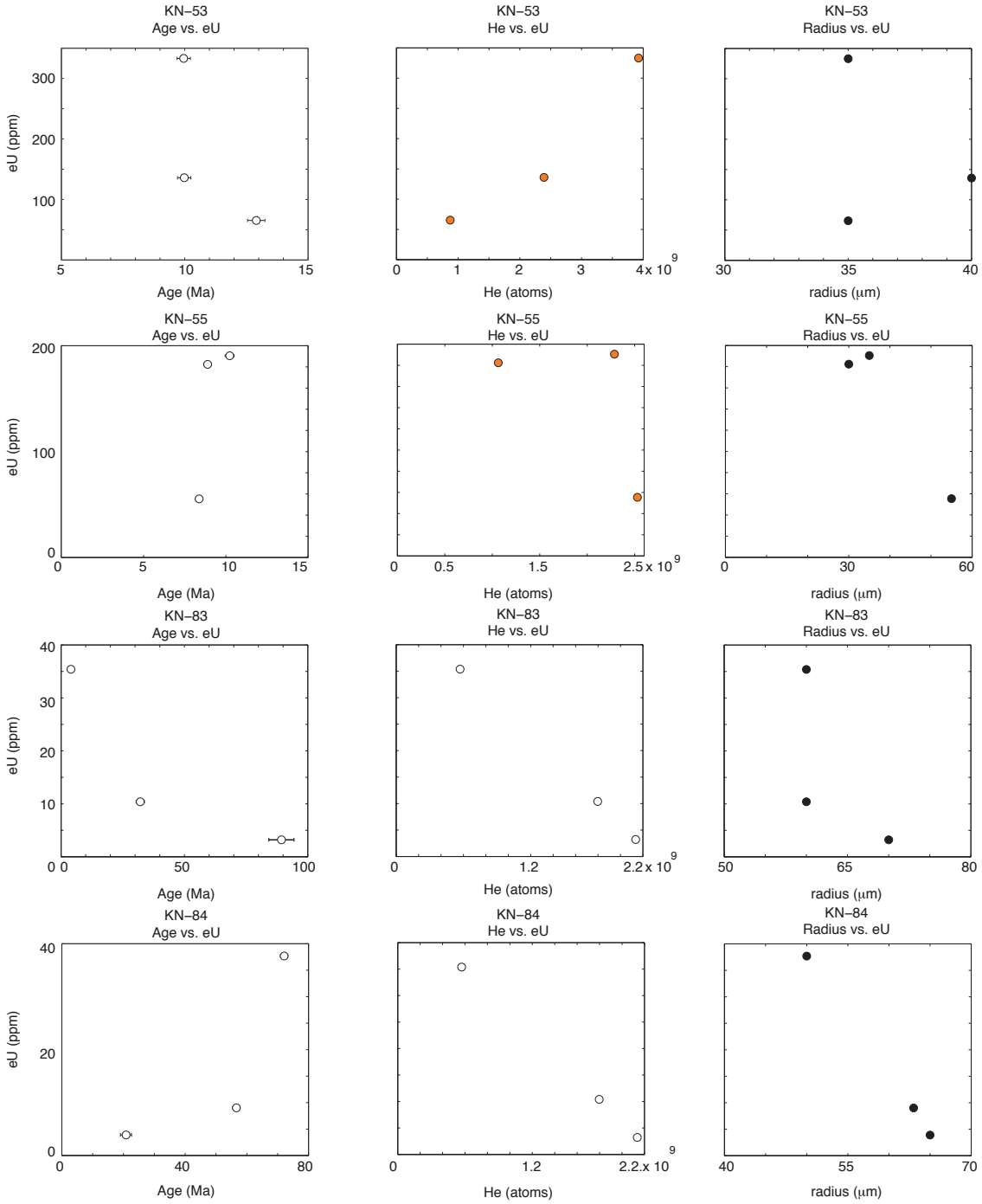

Figure A2. Effective Uranium (eU) in apatites. (eU) vs. AHe, eU vs. [He] and eU vs. radius. Samples KN53, KN55, KN83, KN84, KN85, KN86, KN87, KN89, KN91, KN92, KN94, KN97, KN98, KN99, KN100, KN101, KN102.

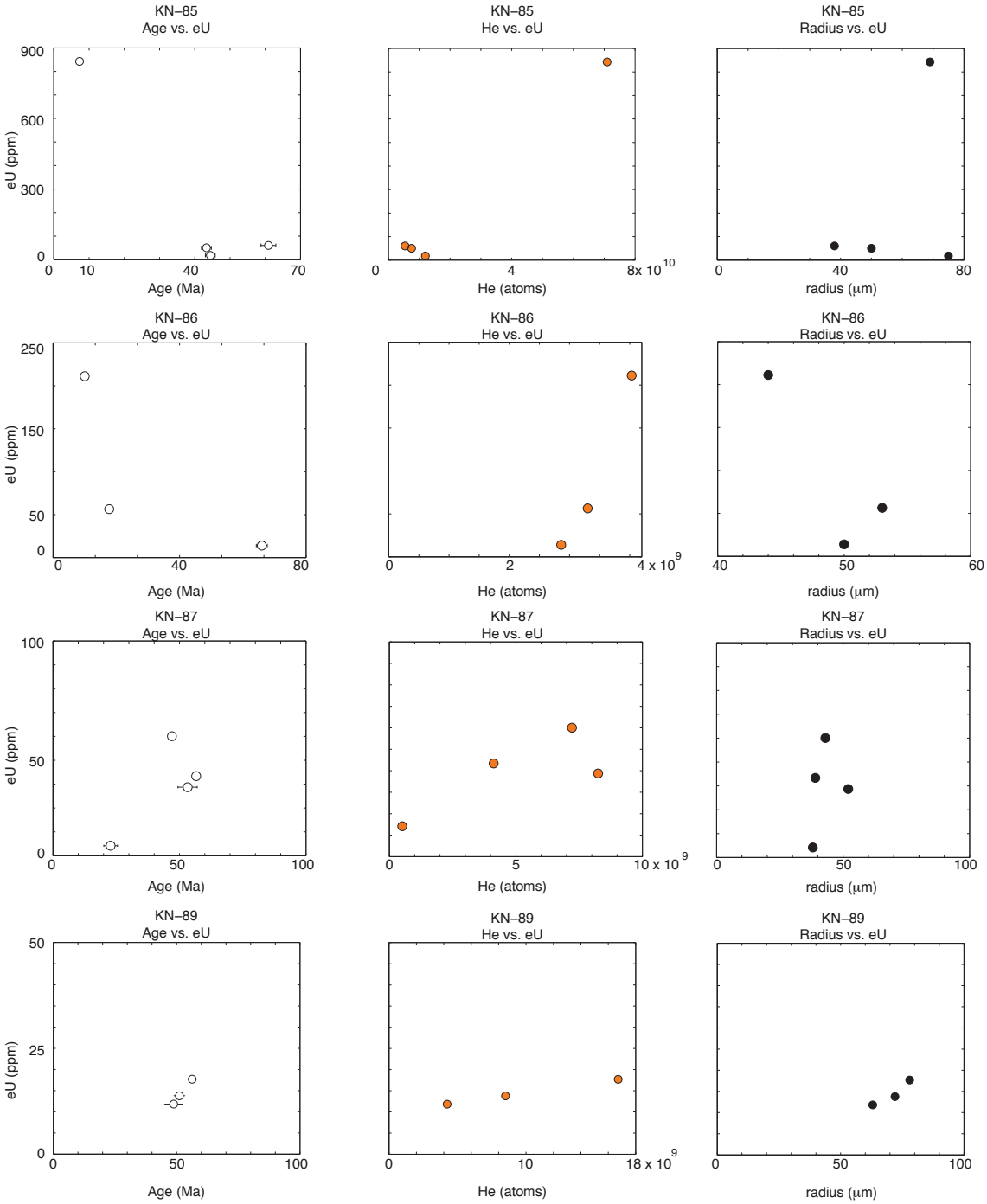
KN–85
Age vs. eU
eU (ppm)
900
600
300
0
0
10
40
70
Age (Ma)
KN–85
He vs. eU
0
4
8x 10^10
He (atoms)
KN–85
Radius vs. eU
0
40
80
radius (μm)
KN–86
Age vs. eU
eU (ppm)
250
150
50
0
0
40
80
Age (Ma)
KN–86
He vs. eU
0
2
4 x 10^9
He (atoms)
KN–86
Radius vs. eU
40
50
60
radius (μm)
KN–87
Age vs. eU
eU (ppm)
100
50
0
0
50
100
Age (Ma)
KN–87
He vs. eU
0
5
10 x 10^9
He (atoms)
KN–87
Radius vs. eU
0
50
100
radius (μm)
KN–89
Age vs. eU
eU (ppm)
50
25
0
0
50
100
Age (Ma)
KN–89
He vs. eU
0
10
18 x 10^9
He (atoms)
KN–89
Radius vs. eU
0
50
100
radius (μm)

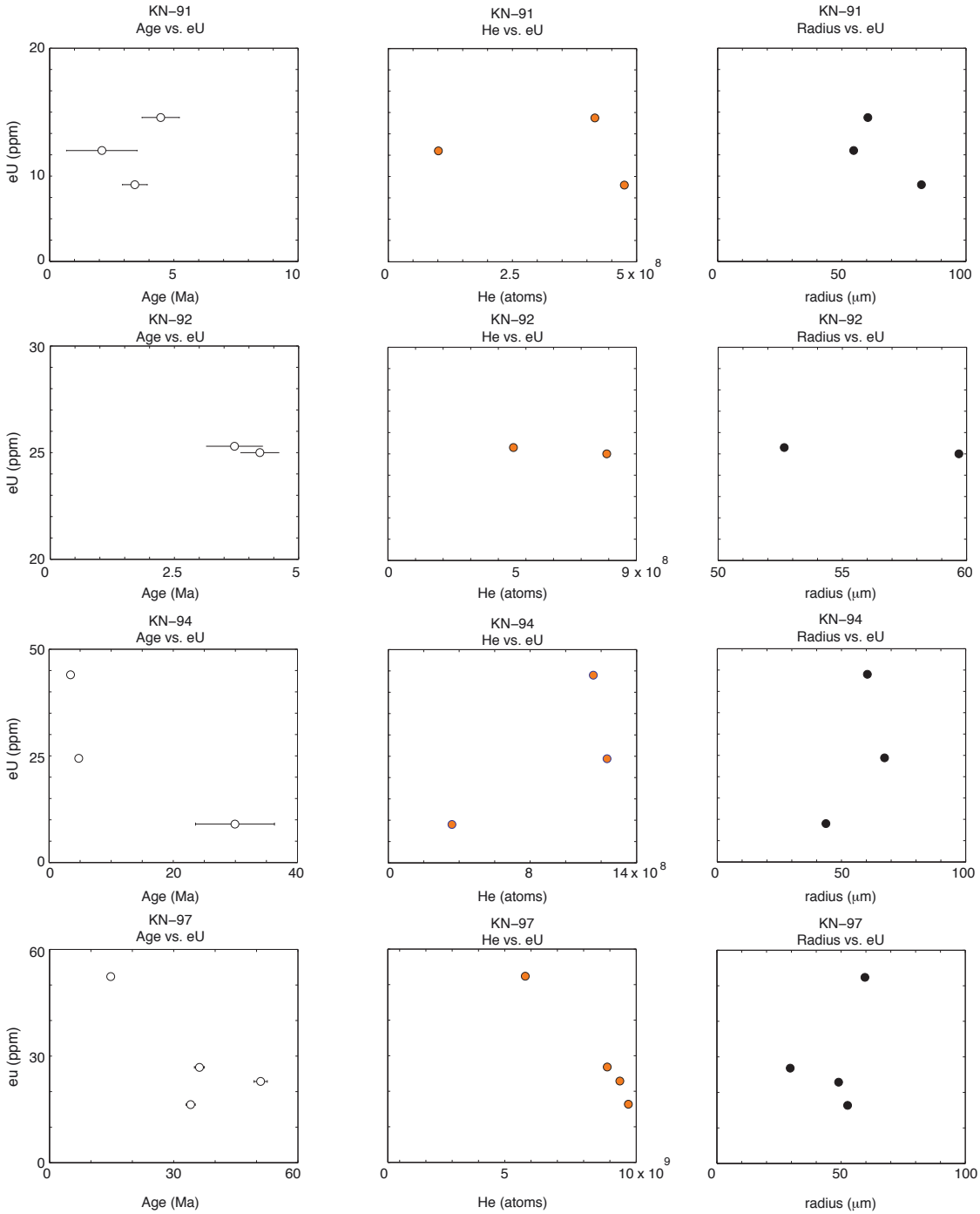
KN–91
Age vs. eU
eU (ppm)
Age (Ma)
KN–91
He vs. eU
He (atoms)
KN–91
Radius vs. eU
radius (μm)
KN–92
Age vs. eU
eU (ppm)
Age (Ma)
KN–92
He vs. eU
He (atoms)
KN–92
Radius vs. eU
radius (μm)
KN–94
Age vs. eU
eU (ppm)
Age (Ma)
KN–94
He vs. eU
He (atoms)
KN–94
Radius vs. eU
radius (μm)
KN–97
Age vs. eU
eu (ppm)
Age (Ma)
KN–97
He vs. eU
He (atoms)
KN–97
Radius vs. eU
radius (μm)

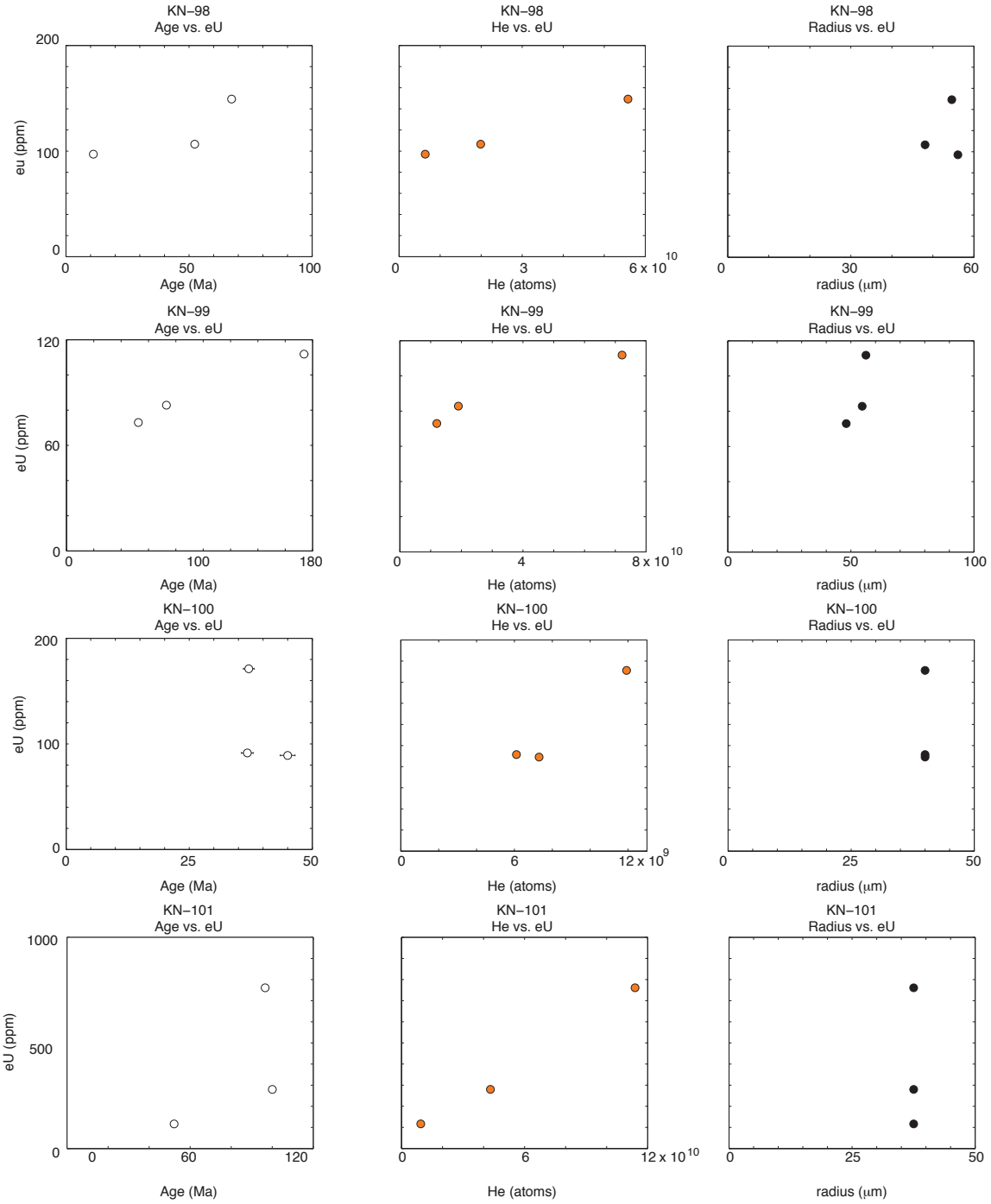
KN–98
Age vs. eU
eu (ppm)
200
100
0
0
50
100
Age (Ma)
KN–98
He vs. eU
0
3
6 x 10^10
He (atoms)
KN–98
Radius vs. eU
0
30
60
radius (μm)
KN–99
Age vs. eU
eU (ppm)
120
60
0
0
100
180
Age (Ma)
KN–99
He vs. eU
0
4
8 x 10^10
He (atoms)
KN–99
Radius vs. eU
0
50
100
radius (μm)
KN–100
Age vs. eU
eU (ppm)
200
100
0
0
25
50
Age (Ma)
KN–100
He vs. eU
0
6
12 x 10^9
He (atoms)
KN–100
Radius vs. eU
0
25
50
radius (μm)
KN–101
Age vs. eU
eU (ppm)
1000
500
0
0
60
120
Age (Ma)
KN–101
He vs. eU
0
6
12 x 10^10
He (atoms)
KN–101
Radius vs. eU
0
25
50
radius (μm)

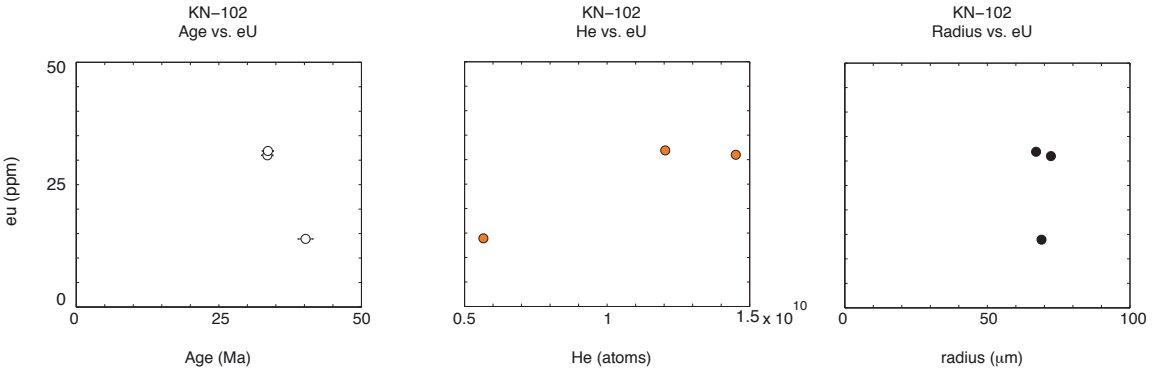
KN–102
Age vs. eU
eu (ppm)
50
25
0
0
25
50
Age (Ma)
KN–102
He vs. eU
0.5
1
1.5 x 10^10
He (atoms)
KN–102
Radius vs. eU
0
50
100
radius (μm)

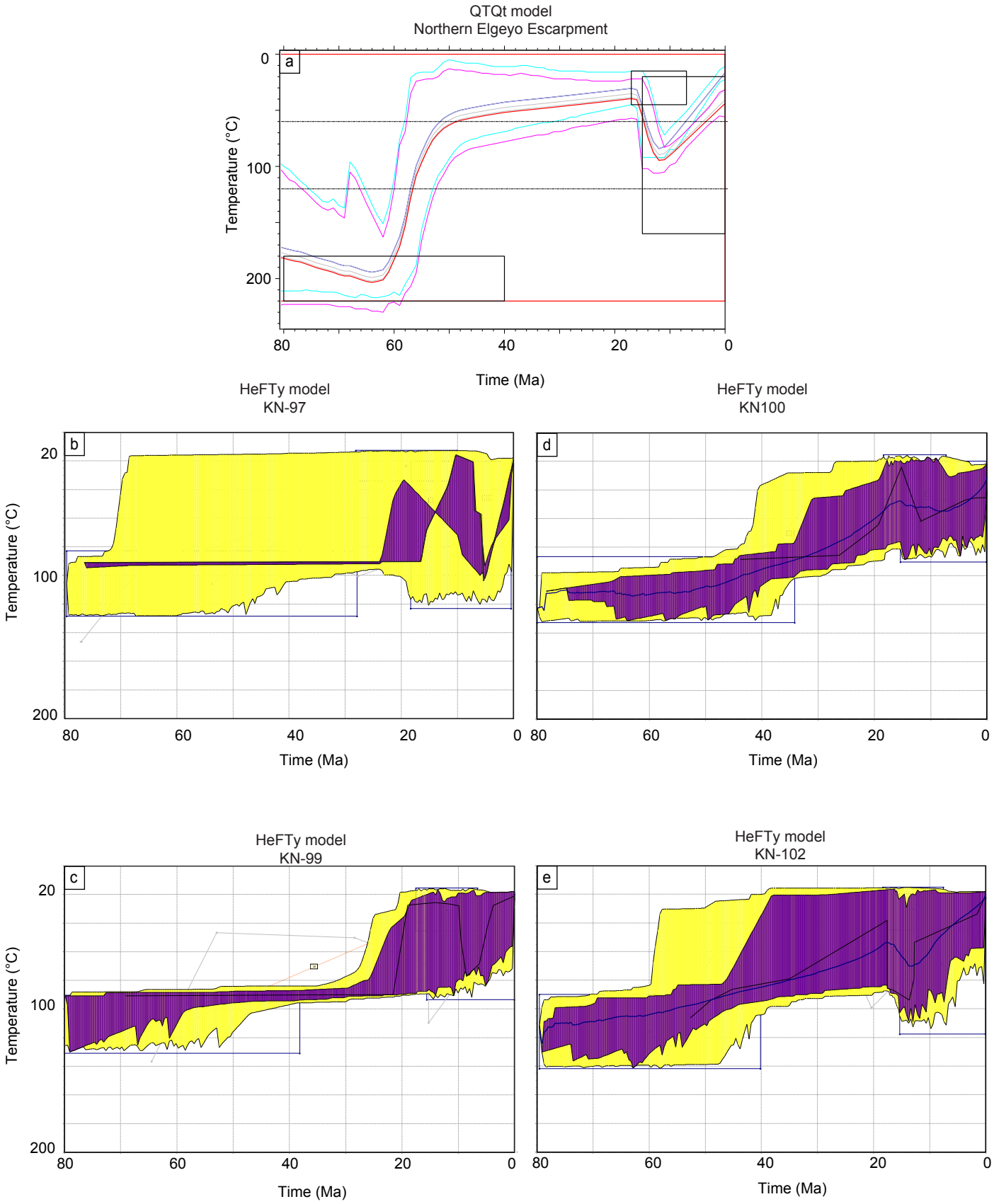

Figure A3. Thermal modeling results for the northern Elgeyo Escarpment (NEE) samples. Short duration pulse heating in the area of Elgeyo Escarpment. A. Time-temperature histories derived from QTQt (Gallagher et al 2009; Gallagher, 2012) modeling, with time-temperature constrain boxes were set to 160 to 20°C at 16 Ma to present day. Second constrain boxes were set to~50 to 18°C at ~17 to7.5 Ma. Third constrain boxes were set to ~240 – 180°C at ~80 -40 Ma. Dashed box denotes the temperature range of the apatite fission-track partial annealing zone (PAZ) and red box defines the limits of the modeling. B, C and D are single thermal modeling for samples KN97, KN99, KN100 and KN102 using HeFTy, with acceptable (yellow) and good (purple) time-temperature pathway envelopes and best-fit shown with black line. First constrain boxes were set to ~123 to 20°C at~18 to present day for samples KN97 and 102 and set to 93 – 22°C at ~ 15Ma to present day. Second constrain boxes were set to ~18 – 7°C at ~45 – 15 Ma for samples KN99, KN100 and KN102, and ~28 – 7 °C at ~30 – 10 Ma for sample KN97. Third constrain boxes were set to ~140 – 82°C at ~80-30 Ma for samples KN97, KN100 AND KN102, and were set to ~130 – 40°C at ~80 -40 Ma.

Table A1. (U-Th)/He ages of Apatite (AHe) in The Kenya Rift.

Sample	Latitude (°N)	Longitude (°E)	elev m asl	U (ppm)	Th (ppm)	Sm (ppm)	He (atoms)	Ft	eU	Terminations #	Corrected age (Ma)	error (1σ) (Ma)	mineral
Southern Elgeyo													
KN53	35.611	0.302	1616	99.97	152.97	N/A	2.39E+09	0.65	135.92	2	9.98	0.27	Apatite
KN53	35.611	0.302	1616	55.52	41.84	N/A	8.70E+08	0.61	65.35	2	12.90	0.35	Apatite
KN53	35.611	0.302	1616	293.52	168.54	N/A	3.93E+09	0.64	333.13	2	9.96	0.27	Apatite
KN55	35.611	0.302	1440	50.63	19.97	N/A	2.53E+09	0.77	55.33	2	8.38	0.22	Apatite
KN55	35.611	0.302	1440	159.94	95.59	N/A	1.06E+09	0.59	182.40	2	8.89	0.24	Apatite
KN55	35.611	0.302	1440	170.68	84.19	N/A	2.29E+09	0.65	190.46	2	10.23	0.27	Apatite
KN91	35.611	0.302	1776	6.18	4.33	49.77	4.75E+08	0.84	7.20	2	3.43	0.50	Apatite
KN91	35.611	0.302	1776	7.45	12.57	43.25	1.01E+08	0.77	10.41	1	2.10	1.42	Apatite
KN91	35.611	0.302	1776	10.26	13.75	60.17	4.16E+08	0.78	13.49	2	4.47	0.75	Apatite
KN92	35.611	0.302	1583	13.71	49.13	258.74	4.55E+08	0.75	25.25	2	3.71	0.57	Apatite
KN92	35.611	0.302	1583	13.37	49.35	154.85	7.93E+08	0.79	24.97	2	4.22	0.39	Apatite
KN94	35.631	0.312	1389	4.98	17.04	71.98	3.59E+08	0.70	8.98	2	29.94	6.35	Apatite
KN94	35.631	0.312	1389	32.71	48.12	107.45	1.16E+09	0.79	44.02	2	3.47	0.23	Apatite
KN94	35.631	0.312	1389	20.77	15.57	68.45	1.23E+09	0.81	24.43	2	4.79	0.30	Apatite
Northern Elgeyo													
KN97	35.552	0.660	1289	32.99	82.40	N/A	5.78E+09	0.80	52.35	2	14.80	0.28	Apatite
KN97	35.552	0.660	1289	12.00	63.15	507.14	8.89E+09	0.58	26.84	2	36.18	1.16	Apatite
KN97	35.552	0.660	1289	8.72	32.45	350.62	9.70E+09	0.78	16.34	2	34.11	1.09	Apatite
KN97	35.552	0.660	1289	11.37	48.86	337.71	9.38E+09	0.74	22.85	2	51.04	1.64	Apatite
KN98	35.548	0.661	1354	81.38	66.88	N/A	6.38E+09	0.77	97.09	2	11.09	0.21	Apatite
KN98	35.545	0.661	1354	75.89	130.19	N/A	1.99E+10	0.73	106.48	2	52.34	0.87	Apatite
KN98	35.539	0.660	1354	117.37	135.35	N/A	5.58E+10	0.78	149.18	2	67.28	1.10	Apatite
KN99	35.548	0.661	1480	100.70	47.47	N/A	7.22E+10	0.74	111.85	2	173.80	2.83	Apatite
KN99	35.548	0.661	1480	62.62	44.03	N/A	1.20E+10	0.66	72.96	2	52.56	0.90	Apatite
KN99	35.548	0.661	1480	70.28	53.49	N/A	1.90E+10	0.66	82.85	2	73.06	1.21	Apatite
KN100	35.548	0.661	1559	67.55	101.77	15.93	6.11E+09	0.69	91.47	2	36.75	1.21	Apatite
KN100	35.545	0.661	1559	64.25	105.87	40.31	7.30E+09	0.69	89.13	2	44.96	1.46	Apatite
KN100	35.539	0.660	1559	122.10	208.92	18.56	1.19E+10	0.69	171.20	2	37.13	1.15	Apatite
KN101	35.548	0.661	1700	58.41	246.46	N/A	9.38E+09	0.67	116.33	2	52.19	0.93	Apatite
KN101	35.545	0.661	1700	303.09	1948.53	N/A	1.14E+11	0.67	760.99	2	96.61	1.58	Apatite
KN101	35.539	0.660	1700	101.83	756.20	N/A	4.33E+10	0.67	279.54	2	100.09	1.63	Apatite
KN102	35.539	0.660	1852	21.50	40.44	140.40	1.45E+10	0.82	31.00	2	33.49	1.03	Apatite
KN102	35.539	0.660	1852	18.97	54.88	168.34	1.20E+10	0.81	31.87	2	33.65	1.05	Apatite
KN102	35.539	0.660	1852	11.43	10.50	185.83	5.66E+09	0.83	13.90	2	40.18	1.35	Apatite
Samburu Hills													
KN83	36.875	2.032	1487	2.71	2.20	13.20	2.14E+09	0.73	3.23	2	89.30	5.13	Apatite
KN83	36.875	2.032	1487	19.37	68.12	69.29	5.70E+08	0.77	35.38	2	4.00	0.51	Apatite
KN83	36.875	2.032	1487	6.75	15.72	96.95	1.80E+09	0.64	10.45	2	32.06	1.74	Apatite
KN84	36.875	2.032	1554	7.08	8.05	N/A	4.49E+09	0.82	8.97	2	56.59	1.20	Apatite
KN84	36.875	2.032	1554	27.14	44.79	N/A	1.20E+10	0.80	37.67	2	72.10	1.23	Apatite
KN84	36.875	2.032	1554	2.48	5.97	N/A	7.11E+08	0.73	3.88	2	20.79	1.76	Apatite
KN85	36.875	2.032	1600	40.95	38.42	N/A	7.53E+09	0.77	49.98	2	43.26	1.39	Apatite
KN85	36.875	2.032	1600	15.36	10.68	N/A	1.20E+10	0.83	17.87	2	44.37	1.39	Apatite
KN85	36.875	2.032	1600	50.74	40.82	N/A	5.42E+09	0.70	60.33	2	60.94	2.15	Apatite
KN85	36.875	2.032	1600	830.78	51.65	N/A	7.09E+10	0.82	842.91	2	7.34	0.17	Apatite
KN86	36.875	2.032	1631	10.88	13.12	N/A	2.86E+09	0.75	13.96	2	49.52	1.31	Apatite
KN86	36.875	2.032	1631	151.64	252.94	N/A	4.03E+09	0.73	211.08	2	7.50	0.20	Apatite
KN86	36.875	2.032	1631	37.58	80.64	N/A	3.30E+09	0.74	56.53	1	13.27	0.49	Apatite
KN87	36.875	2.032	1393	9.92	18.11	N/A	5.06E+08	0.67	14.17	2	22.75	2.69	Apatite
KN87	36.875	2.032	1393	54.23	24.66	N/A	7.21E+09	0.72	60.03	2	46.98	0.87	Apatite
KN87	36.875	2.032	1393	38.18	22.12	N/A	4.12E+09	0.67	43.38	2	56.56	1.26	Apatite
KN87	36.875	2.032	1393	31.21	31.96	N/A	8.25E+09	0.75	38.72	1	53.17	3.76	Apatite
KN88	36.875	2.032	1974	20.76	11.47	23.71	4.99E+09	0.81	23.45	2	42.32	0.55	Apatite
KN89	36.879	2.036	1852	8.09	24.26	N/A	8.51E+09	0.81	13.79	2	51.14	2.20	Apatite
KN89	36.879	2.036	1852	10.35	31.46	N/A	1.67E+10	0.83	17.75	2	56.33	1.58	Apatite
KN89	36.879	2.036	1852	6.23	23.91	N/A	4.24E+09	0.78	11.85	2	48.85	3.67	Apatite

Table A2. Apatite fission track data. Samples KN50 -KN102

Data from sample **UP111-7A.rtf**
Irradiation Number **UP111-7**, Counted by user#: **0**
The mineral is: **Apatite**
Elevation: NA , Location: NA
KN50

No.	Ns	Ni	Na	Ratio	U(ppm)	Rhoi	Rhos	Age (Ma)
1	9	36	56	0.25	6.7	1.648e5	0.659e6	56.2 ± 21.0
2	33	155	45	0.213	36.1	7.522e5	3.533e6	47.9 ± 9.3
3	15	120	56	0.125	22.5	2.747e5	2.198e6	28.2 ± 7.7
4	5	19	36	0.263	5.5	1.425e5	0.541e6	59.1 ± 29.8
5	28	160	42	0.175	40.0	6.838e5	3.907e6	39.4 ± 8.1
6	6	29	42	0.207	7.2	1.465e5	0.708e6	46.5 ± 20.9
7	9	41	42	0.22	10.2	2.198e5	1.001e6	49.4 ± 18.2
8	13	66	49	0.197	14.1	2.721e5	1.382e6	44.3 ± 13.5
9	9	101	54	0.089	19.6	1.71e5	1.918e6	20.1 ± 7.0
10	23	77	56	0.299	14.4	4.213e5	1.41e6	67.1 ± 16.0
11	3	65	56	0.046	12.2	0.549e5	1.191e6	10.4 ± 6.2
12	6	58	54	0.103	11.3	1.14e5	1.102e6	23.3 ± 10.0
13	32	101	40	0.317	26.5	8.206e5	2.59e6	71.1 ± 14.5
14	10	49	35	0.204	14.7	2.931e5	1.436e6	45.9 ± 16.0
15	10	47	50	0.213	9.9	2.051e5	0.964e6	47.9 ± 16.7
16	7	49	56	0.143	9.2	1.282e5	0.898e6	32.2 ± 13.0
17	22	100	72	0.22	14.6	3.134e5	1.425e6	49.5 ± 11.7
18	21	87	64	0.241	14.3	3.366e5	1.394e6	54.3 ± 13.3
19	7	41	56	0.171	7.7	1.282e5	0.751e6	38.4 ± 15.7
20	11	53	35	0.208	15.9	3.224e5	1.553e6	46.7 ± 15.5
	279	1454	996		15.3	2.873e5	1.497e6	

Area of basic unit 9.7493E-7cm-2 using Mic1: 9.7493E-7
Chi Square = 14.987 with 19 degrees of freedom.
P(chi square) = **2.56%**

Ns/Ni = 0.192 ± 0.013
Mean Ratio = 0.195 ± 0.015

Pooled Age = 43.2 ± 3.0 Ma
Mean Age = 43.9 ± 3.4 Ma
Central Age = **42.9 ± 3.7 Ma**
% Variation = **22.71%**

Ages calculated using a zeta of 369.55 ± 7.99 for CN5 with 12.5ppm.
RhoD = 1.222e6 cm-2; ND = 4978.

Data from sample **UP111-10A.rtf**
Irradiation Number **UP111-10**, Counted by user#: **0**
The mineral is: **Apatite**
Elevation: NA , Location: NA
KN53

No.	Ns	Ni	Na	Ratio	U(ppm)	Rhoi	Rhos	Age (Ma)
1	3	40	64	0.075	6.8	0.481e5	0.641e6	16.4 ± 9.8
2	5	88	64	0.057	14.9	0.801e5	1.41e6	12.4 ± 5.7
3	2	87	64	0.023	14.7	0.321e5	1.394e6	5.0 ± 3.6
4	4	78	49	0.051	17.2	0.837e5	1.633e6	11.2 ± 5.8
5	5	110	64	0.045	18.6	0.801e5	1.763e6	9.9 ± 4.6
6	3	130	36	0.023	39.1	0.855e5	3.704e6	5.1 ± 3.0
7	2	85	64	0.024	14.4	0.321e5	1.362e6	5.1 ± 3.7
8	3	128	64	0.023	21.6	0.481e5	2.051e6	5.1 ± 3.0
9	1	51	56	0.02	9.9	0.183e5	0.934e6	4.3 ± 4.3
10	3	147	90	0.02	17.7	0.342e5	1.675e6	4.5 ± 2.6
11	2	114	48	0.018	25.7	0.427e5	2.436e6	3.8 ± 2.7
12	5	211	81	0.024	28.2	0.633e5	2.672e6	5.2 ± 2.4
13	6	245	81	0.024	32.7	0.76e5	3.102e6	5.4 ± 2.2
14	2	83	36	0.024	24.9	0.57e5	2.365e6	5.3 ± 3.8
15	6	299	81	0.02	39.9	0.76e5	3.786e6	4.4 ± 1.8
16	5	157	56	0.032	30.3	0.916e5	2.876e6	7.0 ± 3.2
17	2	131	48	0.015	29.5	0.427e5	2.799e6	3.3 ± 2.4
18	1	118	81	0.0080	15.8	0.127e5	1.494e6	1.9 ± 1.9
19	5	165	64	0.03	27.9	0.801e5	2.644e6	6.6 ± 3.0
20	3	145	42	0.021	37.4	0.733e5	3.541e6	4.5 ± 2.6
	68	2612	1233		22.9	0.566e5	2.173e6	

Area of basic unit 9.7493E-7cm-2 using Mic1: 9.7493E-7
Chi Square = 6.696 with 19 degrees of freedom.
P(chi square) = **81.79%**

Ns/Ni = 0.026 ± 0.0030
Mean Ratio = 0.029 ± 0.0040

Pooled Age = 5.7 ± 0.7 Ma
Mean Age = 6.3 ± 0.8 Ma
Central Age = **5.7 ± 0.7 Ma**
% Variation = **0.0%**

Ages calculated using a zeta of 369.55 ± 7.99 for CN5 with 12.5ppm.
RhoD = 1.185e6 cm-2; ND = 4978.

Data from sample **UP111-14A.rtf**
Irradiation Number **UP111-14**, Counted by user#: **0**
The mineral is: **Apatite**
Elevation: NA , Location: NA
KN55

No.	Ns	Ni	Na	Ratio	U(ppm)	Rhoi	Rhos	Age (Ma)
1	7	248	48	0.028	58.3	1.496e5	5.3e6	5.9 ± 2.3
2	3	129	48	0.023	30.3	0.641e5	2.757e6	4.9 ± 2.9
3	4	201	64	0.02	35.5	0.641e5	3.221e6	4.2 ± 2.1
4	18	682	72	0.026	106.9	2.564e5	9.716e6	5.5 ± 1.3
5	4	174	30	0.023	65.5	1.368e5	5.949e6	4.8 ± 2.4
6	2	84	54	0.024	17.6	0.38e5	1.596e6	5.0 ± 3.6
7	1	31	36	0.032	9.7	0.285e5	0.883e6	6.8 ± 6.9
8	7	274	64	0.026	48.3	1.122e5	4.391e6	5.4 ± 2.1
9	2	60	48	0.033	14.1	0.427e5	1.282e6	7.0 ± 5.0
10	5	220	30	0.023	82.8	1.71e5	7.522e6	4.8 ± 2.2
11	5	201	72	0.025	31.5	0.712e5	2.863e6	5.2 ± 2.4
12	3	147	48	0.02	34.6	0.641e5	3.141e6	4.3 ± 2.5
13	9	332	48	0.027	78.1	1.923e5	7.095e6	5.7 ± 1.9
14	4	214	63	0.019	38.3	0.651e5	3.484e6	3.9 ± 2.0
15	2	62	42	0.032	16.7	0.488e5	1.514e6	6.8 ± 4.9
16	4	116	48	0.034	27.3	0.855e5	2.479e6	7.2 ± 3.7
17	6	171	56	0.035	34.5	1.099e5	3.132e6	7.4 ± 3.1
18	10	392	48	0.026	92.2	2.137e5	8.377e6	5.4 ± 1.7
19	3	111	42	0.027	29.8	0.733e5	2.711e6	5.7 ± 3.3
	99	3849	961		45.2	1.057e5	4.108e6	

Area of basic unit 9.7493E-7cm-2 using Mic1: 9.7493E-7
Chi Square = 1.137 with 18 degrees of freedom.
P(chi square) = **100.0%**

Ns/Ni = 0.026 ± 0.0030
Mean Ratio = 0.027 ± 0.0010

Pooled Age = 5.4 ± 0.6 Ma
Mean Age = 5.6 ± 0.2 Ma
Central Age = **5.4 ± 0.6 Ma**
% Variation = **0.0%**

Ages calculated using a zeta of 369.55 ± 7.99 for CN5 with 12.5ppm.
RhoD = 1.136e6 cm-2; ND = 4978.

Data from sample **UP112-13A.rtf**
Irradiation Number **UP112-13**, Counted by user#: **0**
The mineral is: **Apatite**
Elevation: NA , Location: NA
KN90

No.	Ns	Ni	Na	Ratio	U(ppm)	Rhoi	Rhos	Age (Ma)
1	2	152	54	0.013	26.4	0.38e5	2.887e6	3.3 ± 2.4
2	2	101	72	0.02	13.2	0.285e5	1.439e6	5.0 ± 3.6
3	2	102	32	0.02	29.9	0.641e5	3.269e6	4.9 ± 3.5
4	1	39	25	0.026	14.7	0.41e5	1.6e6	6.5 ± 6.5
5	1	42	42	0.024	9.4	0.244e5	1.026e6	6.0 ± 6.1
6	1	69	56	0.014	11.6	0.183e5	1.264e6	3.7 ± 3.7
7	1	69	49	0.014	13.2	0.209e5	1.444e6	3.7 ± 3.7
8	2	85	64	0.024	12.5	0.321e5	1.362e6	5.9 ± 4.2
9	1	34	32	0.029	10.0	0.321e5	1.09e6	7.4 ± 7.5
10	5	155	48	0.032	30.3	1.068e5	3.312e6	8.1 ± 3.7
11	2	86	35	0.023	23.1	0.586e5	2.52e6	5.9 ± 4.2
12	1	27	48	0.037	5.3	0.214e5	0.577e6	9.3 ± 9.5
13	1	52	49	0.019	10.0	0.209e5	1.089e6	4.8 ± 4.9
14	3	63	42	0.048	14.1	0.733e5	1.539e6	12.0 ± 7.1
15	2	39	49	0.051	7.5	0.419e5	0.816e6	12.9 ± 9.4
16	1	33	42	0.03	7.4	0.244e5	0.806e6	7.6 ± 7.8
17	2	54	48	0.037	10.6	0.427e5	1.154e6	9.3 ± 6.7
18	2	87	48	0.023	17.0	0.427e5	1.859e6	5.8 ± 4.1
	32	1289	835		14.5	0.393e5	1.583e6	

Area of basic unit 9.7493E-7cm-2 using Mic1: 9.7493E-7
Chi Square = 2.443 with 17 degrees of freedom.
P(chi square) = **99.81%**

Ns/Ni = 0.025 ± 0.0040
Mean Ratio = 0.027 ± 0.0030

Pooled Age = 6.3 ± 1.1 Ma
Mean Age = 6.8 ± 0.6 Ma
Central Age = **6.3 ± 1.1 Ma**
% Variation = **0.0%**

Ages calculated using a zeta of 369.55 ± 7.99 for CN5 with 12.5ppm.
RhoD = 1.365e6 cm-2; ND = 5713.

Data from sample **UP112-14A.rtf**
Irradiation Number **UP112-14**, Counted by user#: **0**
The mineral is: **Apatite**
Elevation: NA , Location: NA
KN91

No.	Ns	Ni	Na	Ratio	U(ppm)	Rhoi	Rhos	Age (Ma)
1	0	34	36	0.0	8.9	0.0e5	0.969e6	0.0 ± 0.0
2	3	57	64	0.053	8.4	0.481e5	0.914e6	13.2 ± 7.8
3	1	30	45	0.033	6.3	0.228e5	0.684e6	8.4 ± 8.5
4	4	142	64	0.028	20.9	0.641e5	2.276e6	7.1 ± 3.6
5	2	52	49	0.038	10.0	0.419e5	1.089e6	9.6 ± 7.0
6	1	26	54	0.038	4.5	0.19e5	0.494e6	9.6 ± 9.8
7	3	62	42	0.048	13.9	0.733e5	1.514e6	12.1 ± 7.2
8	2	65	64	0.031	9.6	0.321e5	1.042e6	7.7 ± 5.5
9	1	51	54	0.02	8.9	0.19e5	0.969e6	4.9 ± 5.0
10	2	54	49	0.037	10.4	0.419e5	1.13e6	9.3 ± 6.7
11	1	22	36	0.045	5.8	0.285e5	0.627e6	11.4 ± 11.7
12	2	47	49	0.043	9.1	0.419e5	0.984e6	10.7 ± 7.7
13	1	21	72	0.048	2.8	0.142e5	0.299e6	11.9 ± 12.2
14	3	50	64	0.06	7.4	0.481e5	0.801e6	15.0 ± 9.0
15	3	58	72	0.052	7.6	0.427e5	0.826e6	13.0 ± 7.7
16	3	103	99	0.029	9.8	0.311e5	1.067e6	7.3 ± 4.3
17	3	50	64	0.06	7.4	0.481e5	0.801e6	15.0 ± 9.0
18	1	33	49	0.03	6.4	0.209e5	0.691e6	7.6 ± 7.7
19	2	53	64	0.038	7.8	0.321e5	0.849e6	9.5 ± 6.8
20	2	76	64	0.026	11.2	0.321e5	1.218e6	6.6 ± 4.7
	40	1086	1154		8.9	0.356e5	0.965e6	

Area of basic unit 9.7493E-7cm-2 using Mic1: 9.7493E-7
Chi Square = 2.435 with 19 degrees of freedom.
P(chi square) = **99.95%**

Ns/Ni = 0.037 ± 0.0060
Mean Ratio = 0.038 ± 0.0030

Pooled Age = 9.2 ± 1.5 Ma
Mean Age = 9.5 ± 0.8 Ma
Central Age = **9.2 ± 1.5 Ma**
% Variation = **0.0%**

Ages calculated using a zeta of 369.55 ± 7.99 for CN5 with 12.5ppm.
RhoD = 1.359e6 cm-2; ND = 5713.

Data from sample **UP112-15A**.rtf
Irradiation Number **UP112-15**, Counted by user#: 0
The mineral is: **Apatite**
Elevation: NA , Location: NA
KN92

No.	Ns	Ni	Na	Ratio	U(ppm)	Rhoi	Rhos	Age (Ma)
1	2	215	49	0.0090	41.6	0.419e5	4.501e6	2.3 ± 1.7
2	1	107	64	0.0090	15.8	0.16e5	1.715e6	2.3 ± 2.3
3	2	98	64	0.02	14.5	0.321e5	1.571e6	5.1 ± 3.6
4	2	129	63	0.016	19.4	0.326e5	2.1e6	3.9 ± 2.8
5	1	76	56	0.013	12.9	0.183e5	1.392e6	3.3 ± 3.3
6	1	92	64	0.011	13.6	0.16e5	1.474e6	2.7 ± 2.7
7	2	63	64	0.032	9.3	0.321e5	1.01e6	7.9 ± 5.7
8	2	109	64	0.018	16.1	0.321e5	1.747e6	4.6 ± 3.3
9	3	58	63	0.052	8.7	0.488e5	0.944e6	12.9 ± 7.7
10	1	26	54	0.038	4.6	0.19e5	0.494e6	9.6 ± 9.8
11	2	110	64	0.018	16.3	0.321e5	1.763e6	4.5 ± 3.2
12	3	98	35	0.031	26.5	0.879e5	2.872e6	7.6 ± 4.5
13	2	180	49	0.011	34.8	0.419e5	3.768e6	2.8 ± 2.0
14	1	43	42	0.023	9.7	0.244e5	1.05e6	5.8 ± 5.9
15	2	135	64	0.015	20.0	0.321e5	2.164e6	3.7 ± 2.6
16	6	251	64	0.024	37.2	0.962e5	4.023e6	6.0 ± 2.5
17	2	38	40	0.053	9.0	0.513e5	0.974e6	13.1 ± 9.5
18	3	140	64	0.021	20.7	0.481e5	2.244e6	5.4 ± 3.1
19	1	74	40	0.014	17.5	0.256e5	1.898e6	3.4 ± 3.4
20	1	112	54	0.0090	19.7	0.19e5	2.127e6	2.2 ± 2.2
21	1	65	64	0.015	9.6	0.16e5	1.042e6	3.8 ± 3.9
22	2	103	64	0.019	15.3	0.321e5	1.651e6	4.9 ± 3.5
23	1	70	56	0.014	11.8	0.183e5	1.282e6	3.6 ± 3.6
	44	2392	1305		17.4	0.346e5	1.88e6	

Area of basic unit 9.7493E-7cm-2 using Mic1: 9.7493E-7
Chi Square = 5.656 with 22 degrees of freedom.
P(chi square) = **97.0%**

Ns/Ni = 0.018 ± 0.0030
Mean Ratio = 0.021 ± 0.0030

Pooled Age = 4.6 ± 0.7 Ma
Mean Age = 5.3 ± 0.6 Ma
Central Age = **4.6 ± 0.7 Ma**
% Variation = **0.0%**

Ages calculated using a zeta of 369.55 ± 7.99 for CN5 with 12.5ppm.
RhoD = 1.353e6 cm-2; ND = 5713.

Data from sample **UP112-16A.rtf**
Irradiation Number **UP112-16**, Counted by user#: **0**
The mineral is: **Apatite**
Elevation: NA , Location: NA
KN94

No.	Ns	Ni	Na	Ratio	U(ppm)	Rhoi	Rhos	Age (Ma)
1	2	49	30	0.041	15.6	0.684e5	1.675e6	10.1 ± 7.3
2	2	57	24	0.035	22.6	0.855e5	2.436e6	8.7 ± 6.3
3	2	120	48	0.017	23.8	0.427e5	2.564e6	4.1 ± 3.0
4	2	35	25	0.057	13.3	0.821e5	1.436e6	14.2 ± 10.3
5	2	73	40	0.027	17.4	0.513e5	1.872e6	6.8 ± 4.9
6	4	139	45	0.029	29.4	0.912e5	3.168e6	7.2 ± 3.6
7	1	64	36	0.016	16.9	0.285e5	1.823e6	3.9 ± 3.9
8	3	154	54	0.019	27.2	0.57e5	2.925e6	4.8 ± 2.8
9	3	167	48	0.018	33.1	0.641e5	3.569e6	4.5 ± 2.6
10	2	119	49	0.017	23.1	0.419e5	2.491e6	4.2 ± 3.0
11	2	100	40	0.02	23.8	0.513e5	2.564e6	5.0 ± 3.6
12	1	62	32	0.016	18.4	0.321e5	1.987e6	4.0 ± 4.0
13	2	63	35	0.032	17.1	0.586e5	1.846e6	7.9 ± 5.7
14	3	127	48	0.024	25.2	0.641e5	2.714e6	5.9 ± 3.4
15	2	69	36	0.029	18.2	0.57e5	1.966e6	7.2 ± 5.2
16	3	140	54	0.021	24.7	0.57e5	2.659e6	5.3 ± 3.1
17	2	70	48	0.029	13.9	0.427e5	1.496e6	7.1 ± 5.1
18	2	98	56	0.02	16.7	0.366e5	1.795e6	5.1 ± 3.6
19	2	60	36	0.033	15.9	0.57e5	1.71e6	8.3 ± 6.0
20	3	84	48	0.036	16.7	0.641e5	1.795e6	8.9 ± 5.2
	45	1850	832		21.2	0.555e5	2.281e6	

Area of basic unit 9.7493E-7cm-2 using Mic1: 9.7493E-7
Chi Square = 2.396 with 19 degrees of freedom.
P(chi square) = **99.96%**

Ns/Ni = 0.024 ± 0.0040
Mean Ratio = 0.027 ± 0.0020

Pooled Age = 6.0 ± 0.9 Ma
Mean Age = 6.7 ± 0.6 Ma
Central Age = **6.0 ± 0.9 Ma**
% Variation = **0.0%**

Ages calculated using a zeta of 369.55 ± 7.99 for CN5 with 12.5ppm.
RhoD = 1.347e6 cm-2; ND = 5713.

Data from sample **UP112-1A.rtf**
Irradiation Number **UP112-1**, Counted by user#: **0**
The mineral is: **Apatite**
Elevation: NA , Location: NA
KN97

No.	Ns	Ni	Na	Ratio	U(ppm)	Rhoi	Rhos	Age (Ma)
1	5	28	48	0.179	5.2	1.068e5	0.598e6	47.3 ± 23.0
2	4	48	40	0.083	10.7	1.026e5	1.231e6	22.1 ± 11.5
3	7	79	48	0.089	14.7	1.496e5	1.688e6	23.5 ± 9.3
4	4	49	32	0.082	13.7	1.282e5	1.571e6	21.6 ± 11.3
5	2	20	30	0.1	5.9	0.684e5	0.684e6	26.5 ± 19.7
6	2	22	18	0.091	10.9	1.14e5	1.254e6	24.1 ± 17.8
7	2	41	24	0.049	15.2	0.855e5	1.752e6	12.9 ± 9.4
8	11	47	40	0.234	10.5	2.821e5	1.205e6	61.9 ± 20.8
9	6	71	42	0.085	15.1	1.465e5	1.734e6	22.4 ± 9.5
10	4	43	48	0.093	8.0	0.855e5	0.919e6	24.7 ± 12.9
11	8	48	20	0.167	21.4	4.103e5	2.462e6	44.1 ± 16.9
12	6	39	24	0.154	14.5	2.564e5	1.667e6	40.7 ± 17.9
13	4	48	42	0.083	10.2	0.977e5	1.172e6	22.1 ± 11.5
14	2	32	24	0.063	11.9	0.855e5	1.368e6	16.6 ± 12.1
15	3	52	40	0.058	11.6	0.769e5	1.333e6	15.3 ± 9.1
16	2	14	32	0.143	3.9	0.641e5	0.449e6	37.8 ± 28.6
17	4	60	54	0.067	9.9	0.76e5	1.14e6	17.7 ± 9.1
18	5	70	36	0.071	17.3	1.425e5	1.994e6	18.9 ± 8.8
19	6	76	48	0.079	14.1	1.282e5	1.624e6	20.9 ± 8.9
20	8	73	45	0.11	14.5	1.823e5	1.664e6	29.0 ± 10.8
	95	960	735		11.6	1.326e5	1.34e6	

Area of basic unit 9.7493E-7cm-2 using Mic1: 9.7493E-7
Chi Square = 8.008 with 19 degrees of freedom.
P(chi square) = **65.61%**

Ns/Ni = 0.099 ± 0.011
Mean Ratio = 0.104 ± 0.011

Pooled Age = 26.2 ± 2.9 Ma
Mean Age = 27.5 ± 2.8 Ma
Central Age = **26.2 ± 2.8 Ma**
% Variation = **0.0%**

Ages calculated using a zeta of 369.55 ± 7.99 for CN5 with 12.5ppm.
RhoD = 1.438e6 cm-2; ND = 5713.

Data from sample **UP112-3A.rtf**
Irradiation Number **UP112-3**, Counted by user#: **0**
The mineral is: **Apatite**
Elevation: NA , Location: NA
KN99

No.	Ns	Ni	Na	Ratio	U(ppm)	Rhoi	Rhos	Age (Ma)
1	27	229	36	0.118	57.2	7.693e5	6.525e6	31.0 ± 6.4
2	12	94	18	0.128	47.0	6.838e5	5.357e6	33.5 ± 10.3
3	16	133	30	0.12	39.9	5.47e5	4.547e6	31.6 ± 8.4
4	23	248	42	0.093	53.1	5.617e5	6.057e6	24.4 ± 5.4
5	34	256	48	0.133	48.0	7.265e5	5.47e6	34.9 ± 6.4
6	22	138	25	0.159	49.6	9.026e5	5.662e6	41.9 ± 9.7
7	30	212	42	0.142	45.4	7.327e5	5.177e6	37.2 ± 7.3
8	11	94	21	0.117	40.3	5.373e5	4.591e6	30.8 ± 9.8
9	16	151	24	0.106	56.6	6.838e5	6.453e6	27.9 ± 7.4
10	22	200	35	0.11	51.4	6.447e5	5.861e6	28.9 ± 6.5
11	14	96	30	0.146	28.8	4.787e5	3.282e6	38.3 ± 11.0
12	19	152	21	0.125	65.1	9.28e5	7.424e6	32.8 ± 8.0
13	15	82	15	0.183	49.2	10.257e5	5.607e6	48.0 ± 13.5
14	23	155	25	0.148	55.8	9.437e5	6.359e6	39.0 ± 8.8
15	21	130	32	0.162	36.5	6.731e5	4.167e6	42.4 ± 10.0
	305	2370	444		48.0	7.046e5	5.475e6	

Area of basic unit 9.7493E-7cm-2 using Mic1: 9.7493E-7
Chi Square = 3.966 with 14 degrees of freedom.
P(chi square) = **89.28%**

Ns/Ni = 0.129 ± 0.0080
Mean Ratio = 0.133 ± 0.0060

Pooled Age = 33.8 ± 2.2 Ma
Mean Age = 34.8 ± 1.6 Ma
Central Age = **33.8 ± 2.1 Ma**
% Variation = **0.0%**

Ages calculated using a zeta of 369.55 ± 7.99 for CN5 with 12.5ppm.
RhoD = 1.426e6 cm-2; ND = 5713.

Data from sample **UP112-4A.rtf**
Irradiation Number **UP112-4**, Counted by user#: **0**
The mineral is: **Apatite**
Elevation: NA , Location: NA
KN100

No.	Ns	Ni	Na	Ratio	U(ppm)	Rhoi	Rhos	Age (Ma)
1	18	120	42	0.15	25.8	4.396e5	2.931e6	39.2 ± 10.0
2	30	210	54	0.143	35.1	5.698e5	3.989e6	37.4 ± 7.4
3	15	95	36	0.158	23.8	4.274e5	2.707e6	41.3 ± 11.5
4	18	148	42	0.122	31.8	4.396e5	3.614e6	31.8 ± 8.0
5	14	96	36	0.146	24.1	3.989e5	2.735e6	38.1 ± 11.0
6	12	86	30	0.14	25.9	4.103e5	2.94e6	36.5 ± 11.3
7	13	80	30	0.163	24.1	4.445e5	2.735e6	42.5 ± 12.7
8	7	52	24	0.135	19.6	2.992e5	2.222e6	35.2 ± 14.2
9	32	258	49	0.124	47.6	6.699e5	5.401e6	32.5 ± 6.1
10	12	110	32	0.109	31.0	3.846e5	3.526e6	28.5 ± 8.7
11	17	91	30	0.187	27.4	5.812e5	3.111e6	48.8 ± 13.0
12	20	124	49	0.161	22.9	4.187e5	2.596e6	42.2 ± 10.2
13	14	134	30	0.104	40.3	4.787e5	4.582e6	27.3 ± 7.7
14	18	126	56	0.143	20.3	3.297e5	2.308e6	37.4 ± 9.5
15	12	92	54	0.13	15.4	2.279e5	1.748e6	34.1 ± 10.5
16	17	135	52	0.126	23.4	3.353e5	2.663e6	32.9 ± 8.5
	269	1957	646		27.4	4.271e5	3.107e6	

Area of basic unit 9.7493E-7cm-2 using Mic1: 9.7493E-7
Chi Square = 2.41 with 15 degrees of freedom.
P(chi square) = **99.35%**

Ns/Ni = 0.137 ± 0.0090
Mean Ratio = 0.14 ± 0.0050

Pooled Age = 36.0 ± 2.5 Ma
Mean Age = 36.6 ± 1.4 Ma
Central Age = **36.0 ± 2.4 Ma**
% Variation = **0.0%**

Ages calculated using a zeta of 369.55 ± 7.99 for CN5 with 12.5ppm.
RhoD = 1.42e6 cm-2; ND = 5713.

Data from sample **UP112-6A.rtf**
Irradiation Number **UP112-6**, Counted by user#: **0**
The mineral is: **Apatite**
Elevation: NA , Location: NA
KN**102**

No.	Ns	Ni	Na	Ratio	U(ppm)	Rhoi	Rhos	Age (Ma)
1	18	61	48	0.295	11.6	3.846e5	1.304e6	76.3 ± 20.6
2	8	39	24	0.205	14.8	3.419e5	1.667e6	53.1 ± 20.7
3	4	32	49	0.125	5.9	0.837e5	0.67e6	32.4 ± 17.2
4	8	56	49	0.143	10.4	1.675e5	1.172e6	37.0 ± 14.0
5	8	85	48	0.094	16.1	1.71e5	1.816e6	24.4 ± 9.1
6	20	193	64	0.104	27.5	3.205e5	3.093e6	26.9 ± 6.4
7	4	37	54	0.108	6.2	0.76e5	0.703e6	28.1 ± 14.8
8	9	31	24	0.29	11.8	3.846e5	1.325e6	75.1 ± 28.5
9	9	67	48	0.134	12.7	1.923e5	1.432e6	34.8 ± 12.4
10	8	58	48	0.138	11.0	1.71e5	1.239e6	35.8 ± 13.5
11	8	76	64	0.105	10.8	1.282e5	1.218e6	27.3 ± 10.2
12	8	50	45	0.16	10.1	1.823e5	1.14e6	41.5 ± 15.8
13	8	50	54	0.16	8.4	1.52e5	0.95e6	41.5 ± 15.8
14	21	111	81	0.189	12.5	2.659e5	1.406e6	49.0 ± 11.7
15	9	69	42	0.13	15.0	2.198e5	1.685e6	33.8 ± 12.0
16	3	24	20	0.125	10.9	1.539e5	1.231e6	32.4 ± 19.9
17	9	69	36	0.13	17.5	2.564e5	1.966e6	33.8 ± 12.0
18	5	44	40	0.114	10.0	1.282e5	1.128e6	29.5 ± 13.9
19	19	79	64	0.241	11.2	3.045e5	1.266e6	62.2 ± 16.0
20	7	58	40	0.121	13.2	1.795e5	1.487e6	31.3 ± 12.6
	193	1289	942		12.5	2.102e5	1.404e6	

Area of basic unit 9.7493E-7cm-2 using Mic1: 9.7493E-7
Chi Square = 10.849 with 19 degrees of freedom.
P(chi square) = **10.29%**

Ns/Ni = 0.15 ± 0.012
Mean Ratio = 0.156 ± 0.013

Pooled Age = 38.8 ± 3.2 Ma
Mean Age = 40.3 ± 3.4 Ma
Central Age = **39.2 ± 3.4 Ma**
% Variation = **15.57%**

Ages calculated using a zeta of 369.55 ± 7.99 for CN5 with 12.5ppm.
RhoD = 1.407e6 cm-2; ND = 5713.

Data from sample **UP112-7A**.rtf
Irradiation Number **UP112-7**, Counted by user#: 0
The mineral is: **Apatite**
Elevation: NA , Location: NA
KN83

No.	Ns	Ni	Na	Ratio	U(ppm)	Rhoi	Rhos	Age (Ma)
1	4	18	48	0.222	3.4	0.855e5	0.385e6	57.3 ± 31.7
2	26	170	64	0.153	24.3	4.167e5	2.725e6	39.5 ± 8.4
3	6	35	32	0.171	10.0	1.923e5	1.122e6	44.2 ± 19.6
4	19	146	72	0.13	18.6	2.707e5	2.08e6	33.6 ± 8.2
5	28	225	72	0.124	28.6	3.989e5	3.205e6	32.1 ± 6.5
6	14	104	63	0.135	15.1	2.279e5	1.693e6	34.8 ± 9.9
7	19	174	45	0.109	35.4	4.331e5	3.966e6	28.2 ± 6.9
8	4	19	40	0.211	4.3	1.026e5	0.487e6	54.3 ± 29.9
9	9	72	49	0.125	13.4	1.884e5	1.507e6	32.3 ± 11.4
10	6	43	36	0.14	10.9	1.71e5	1.225e6	36.0 ± 15.7
11	24	190	64	0.126	27.2	3.846e5	3.045e6	32.6 ± 7.1
12	11	53	54	0.208	9.0	2.089e5	1.007e6	53.5 ± 17.8
13	16	49	36	0.327	12.5	4.559e5	1.396e6	84.0 ± 24.3
14	33	201	18	0.164	102.2	18.805e5	11.454e6	42.4 ± 8.0
15	18	101	64	0.178	14.4	2.885e5	1.619e6	46.0 ± 11.8
16	6	31	48	0.194	5.9	1.282e5	0.662e6	49.9 ± 22.3
17	4	28	64	0.143	4.0	0.641e5	0.449e6	36.9 ± 19.7
18	14	76	64	0.184	10.9	2.244e5	1.218e6	47.5 ± 13.9
19	33	241	64	0.137	34.5	5.289e5	3.862e6	35.4 ± 6.6
20	33	138	42	0.239	30.1	8.059e5	3.37e6	61.6 ± 12.0
	327	2114	1039		18.6	3.228e5	2.087e6	

Area of basic unit 9.7493E-7cm-2 using Mic1: 9.7493E-7
Chi Square = 10.293 with 19 degrees of freedom.
P(chi square) = **36.01%**

Ns/Ni = 0.155 ± 0.0090
Mean Ratio = 0.171 ± 0.012

Pooled Age = 39.9 ± 2.6 Ma
Mean Age = 44.1 ± 3.0 Ma
Central Age = **40.1 ± 2.6 Ma**
% Variation = **7.4%**

Ages calculated using a zeta of 369.55 ± 7.99 for CN5 with 12.5ppm.
RhoD = 1.401e6 cm-2; ND = 5713.

Data from sample **UP112-9A.rtf**
Irradiation Number **UP112-9**, Counted by user#: **0**
The mineral is: **Apatite**
Elevation: NA , Location: NA
KN85

No.	Ns	Ni	Na	Ratio	U(ppm)	Rhoi	Rhos	Age (Ma)
1	9	67	16	0.134	38.7	5.77e5	4.295e6	34.4 ± 12.2
2	9	70	30	0.129	21.5	3.077e5	2.393e6	32.9 ± 11.7
3	8	46	36	0.174	11.8	2.279e5	1.311e6	44.5 ± 17.1
4	5	26	28	0.192	8.6	1.832e5	0.952e6	49.2 ± 24.0
5	6	44	32	0.136	12.7	1.923e5	1.41e6	34.9 ± 15.2
6	8	66	30	0.121	20.3	2.735e5	2.257e6	31.0 ± 11.6
7	9	71	42	0.127	15.6	2.198e5	1.734e6	32.5 ± 11.5
8	15	79	27	0.19	27.0	5.698e5	3.001e6	48.6 ± 13.7
9	6	37	24	0.162	14.2	2.564e5	1.581e6	41.5 ± 18.3
10	17	128	54	0.133	21.9	3.229e5	2.431e6	34.0 ± 8.8
11	9	52	54	0.173	8.9	1.71e5	0.988e6	44.3 ± 16.0
12	9	56	24	0.161	21.5	3.846e5	2.393e6	41.1 ± 14.8
13	6	39	25	0.154	14.4	2.462e5	1.6e6	39.4 ± 17.3
14	9	94	40	0.096	21.7	2.308e5	2.41e6	24.5 ± 8.6
15	12	90	40	0.133	20.8	3.077e5	2.308e6	34.1 ± 10.5
16	13	81	48	0.16	15.6	2.778e5	1.731e6	41.1 ± 12.3
17	10	55	62	0.182	8.2	1.654e5	0.91e6	46.5 ± 16.0
18	21	124	48	0.169	23.8	4.488e5	2.65e6	43.3 ± 10.3
19	6	32	24	0.188	12.3	2.564e5	1.368e6	47.9 ± 21.4
20	8	32	36	0.25	8.2	2.279e5	0.912e6	63.9 ± 25.3
	195	1289	720		16.5	2.778e5	1.836e6	

Area of basic unit 9.7493E-7cm-2 using Mic1: 9.7493E-7
Chi Square = 3.408 with 19 degrees of freedom.
P(chi square) = **99.51%**

Ns/Ni = 0.151 ± 0.012
Mean Ratio = 0.158 ± 0.0080

Pooled Age = 38.7 ± 3.1 Ma
Mean Age = 40.5 ± 1.9 Ma
Central Age = **38.7 ± 3.0 Ma**
% Variation = **0.0%**

Ages calculated using a zeta of 369.55 ± 7.99 for CN5 with 12.5ppm.
RhoD = 1.389e6 cm-2; ND = 5713.

Data from sample **UP112-12A.rtf**
Irradiation Number **UP112-12**, Counted by user#: **0**
The mineral is: **Apatite**
Elevation: NA , Location: NA
KN89

No.	Ns	Ni	Na	Ratio	U(ppm)	Rhoi	Rhos	Age (Ma)
1	2	10	48	0.2	1.9	0.427e5	0.214e6	50.5 ± 39.1
2	8	25	49	0.32	4.8	1.675e5	0.523e6	80.6 ± 32.8
3	4	23	48	0.174	4.5	0.855e5	0.491e6	43.9 ± 23.8
4	2	13	24	0.154	5.1	0.855e5	0.556e6	38.9 ± 29.5
5	6	23	36	0.261	6.0	1.71e5	0.655e6	65.7 ± 30.2
6	5	32	64	0.156	4.7	0.801e5	0.513e6	39.5 ± 19.0
7	6	21	49	0.286	4.0	1.256e5	0.44e6	72.0 ± 33.4
8	9	54	64	0.167	7.9	1.442e5	0.865e6	42.1 ± 15.2
9	3	20	42	0.15	4.5	0.733e5	0.488e6	37.9 ± 23.5
10	7	44	48	0.159	8.6	1.496e5	0.94e6	40.2 ± 16.4
11	4	16	30	0.25	5.0	1.368e5	0.547e6	63.0 ± 35.3
	56	281	502		5.2	1.144e5	0.574e6	

Area of basic unit 9.7493E-7cm-2 using Mic1: 9.7493E-7
Chi Square = 1.857 with 10 degrees of freedom.
P(chi square) = **95.93%**

Ns/Ni = 0.199 ± 0.029
Mean Ratio = 0.207 ± 0.018

Pooled Age = 50.3 ± 7.5 Ma
Mean Age = 52.2 ± 4.6 Ma
Central Age = **50.3 ± 7.4 Ma**
% Variation = **0.0%**

Ages calculated using a zeta of 369.55 ± 7.99 for CN5 with 12.5ppm.
RhoD = 1.371e6 cm-2; ND = 5713.

Table A3. Track lengths data.

Data from sample UP112-1A.rtf
Irradiation Number UP112-1, Counted by user#: 0
The mineral is: Apatite

KN97

Length	angle	Dpar	Length	angle	Dpar
9.9	63.8	1.67	10.2	49.2	2.02
8.4	29.7	2.64	8.9	16.8	2.02
13.8	50.4	2.64	14.1	51.5	1.67
10.1	48.3	1.88	10.7	26.2	1.67
8.5	72.8	1.88	9.7	54.8	2.19
8.3	34	1.88	12.6	84.6	2.19
13.1	62.4	1.78	11.1	67.8	2.19
12.3	66.7	2.1	7.9	51.9	2.05
11.8	57.5	2.1	7.6	34.5	2.05
8.5	57.1	2.41	10.9	44.9	1.66
10.2	53	2.41	6.7	19.6	1.56
10.3	72.2	2.05	14.7	19.2	1.56
8.3	61.2	2.05	13.2	53.2	1.56
8.9	55.1	1.89	10.9	54.1	1.56
6.8	10	1.79	11.9	48	1.56
7.2	46.9	1.79	11.8	68.5	1.56
7	8.5	1.79	10.8	70.9	1.56
8.7	60.6	2.16	9.5	28.5	1.56
11.5	50.1	2.44	8.5	0.7	1.65
13.2	58.2	2.44	9.5	19.5	1.88
9.2	35.3	2.44	8.9	1.3	1.88
7.1	70	1.58	9	38.7	2.05
9.8	51.8	2.23	10.4	28.6	2.05
11	76.3	1.81	9.9	21.9	1.77
10.6	36.8	1.81	12.6	24.2	1.77
12.4	39.9	1.83	8.4	52.8	1.77
11.3	5.2	1.83	10.7	22.9	1.77
10.5	36.6	1.96	8.3	35.6	1.77
12.2	53.6	1.83	8.2	64.4	2.2
8.5	20.4	2.16	8.2	7.7	2.2
7.3	68.5	1.35	11.9	59.6	1.89
7.1	88.2	1.35	9.2	40.1	1.94
8.9	0.8	1.46	7.8	72.9	1.74
10.6	37	1.46	10.7	54.7	2.19
9.9	79.1	1.46	8.3	11.2	1.75
13.5	83.7	1.46	12.6	83.7	1.75
12.8	72.6	1.46	13	63.4	1.75
11.2	27.2	2.27	10.8	49.5	1.75
8.3	35.6	2.1	7.7	65.6	2.46
9.1	71.7	2.09	8.8	56.4	2.46
11	26.3	2.09	9.5	71.9	1.88
11.1	13.1	2.24	7.2	48.9	2.08
9	42	2.24	6.9	5.2	2.08
9.6	49.3	2.24	7.9	58.7	1.9
8.7	49.5	2.24	7.1	45.3	2.09
14.1	60.3	1.97	10.1	58.2	1.99
8.8	15.5	1.97	9.2	26.1	1.99
9.6	8.2	1.74	8.4	74.1	1.99
7.2	9.4	1.74			
9.3	8.8	1.74			
8.6	10	1.74			
11.8	64.8	2.26			
11.2	5.4	2.26			

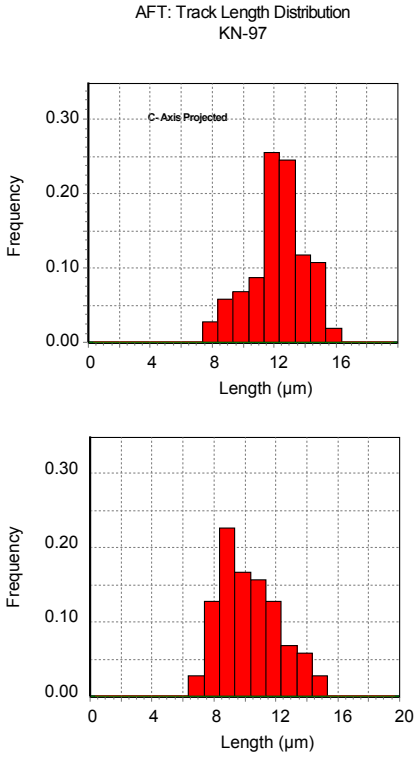

Data from sample UP112-3.rtf
Irradiation Number UPUP112-3, Counted by user#: 0
The mineral is: Apatite

KN99

Length	angle	Dpar	Length	angle	Dpar
10.5	18.7	2.61	10.3	75.3	1.7
12.4	53.4	2.04	12.1	52.1	2.2
9.3	57.3	2.04	8.2	39	2.2
9.7	21.8	1.82	12.1	51.1	2.2
12	67.2	1.56	10.3	5	2.2
14	54.3	1.48	12.4	68.8	2.2
14.4	11	1.38	10.5	78.4	2.2
13.3	29.8	1.96	14.5	68.3	2.49
12.4	19.2	1.96	9.6	33.6	2.49
11.6	27.5	2.68	8	42.5	2.49
12.8	45.5	2.68	9.2	86.6	2.49
13.6	84.7	1.56			
9.7	36.2	1.88			
9.7	31.4	1.88			
9.1	45.7	1.88			
13.3	48.8	2.63			
10.4	13.1	2.63			
12.6	72.4	2.39			
13.8	79.7	2.39			
9.5	34.5	2.39			
14.7	74.3	2.39			
9	68.2	2.3			
9.9	70.3	2.3			
13.8	52	2.3			
8.4	47.1	1.73			
13.9	57.9	1.76			
13.7	36.2	1.76			
13.9	57	1.76			
15.4	8.6	1.72			
11.1	31.4	1.72			
10.9	42.7	1.72			
12.2	66.8	1.72			
11.9	60	2.05			
8.3	38.7	2.74			
13.4	41.1	2.74			
9.5	67.2	2.74			
12.6	25.7	2.74			
9.8	32.9	2.74			
8.8	78	1.7			
7.6	3.2	1.7			
8.7	19.2	1.7			
9.2	52.7	1.86			
8.6	78.1	1.86			
13.1	13.7	1.86			
9.2	31	1.86			
8.9	0.2	1.61			
9.2	28.2	1.61			
9.3	5.2	1.61			
8.8	32.3	1.7			
12.4	75.9	1.7			
10.6	77.6	1.7			
14	56.9	1.7			
11.6	72.7	1.7			
11.9	57.5	1.7			

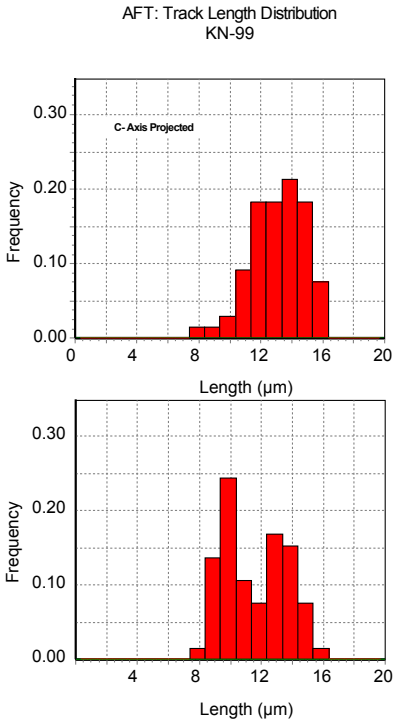

Data from sample UP112-4A.rtf
Irradiation Number UP112-4, Counted by user#: 0
The mineral is: Apatite

KN100

Length	angle	Dpar	Length	angle	Dpar
13.6	45.5	2.12	13.4	36	2.12
11	57.9	2.12	9.4	67.3	2.12
13.3	39.9	2.12	13	68.9	2.12
12.4	38.1	2.24	13	73.8	2.12
8.8	31.7	2.24	9.7	60.7	2.12
13.8	64.1	2.24	13.9	32.6	2.12
12.3	60.5	2.24	10.3	59.1	2.12
12.6	62.5	2.24	14.8	63.2	2.57
12.7	12.2	2.24	8.4	63.3	2.57
8.8	82.7	2.40	12.2	61.2	2.16
12.3	52.1	2.40	12.8	60.2	2.16
9.1	89.3	2.40	11.5	86.6	2.16
11	75.1	2.32			
8.7	34.1	2.32			
14.9	75.1	1.91			
11.2	62.9	1.91			
13.5	79.6	1.91			
12.6	71	1.91			
14.4	61.8	1.91			
8.1	57.5	1.91			
9.7	38.1	1.79			
12.5	87.7	2.20			
11	85.3	2.20			
10.8	82.3	2.35			
10.5	71	2.27			
13.8	55.8	2.45			
9.2	77.5	2.45			
12.7	60	2.45			
14.7	35.6	2.45			
14.1	79.6	2.45			
12	47.2	2.48			
12.9	36.5	2.48			
10.9	75.8	2.48			
12.4	62.6	1.96			
13.1	59.8	1.96			
9.5	79.7	2.24			
10.6	55.3	2.57			
12.1	57.7	2.27			
13.3	34.6	2.28			
9.3	88.9	2.28			
9.4	60.6	2.17			
14.2	82.8	2.07			
11.9	88.9	2.07			
13.6	81.8	2.12			

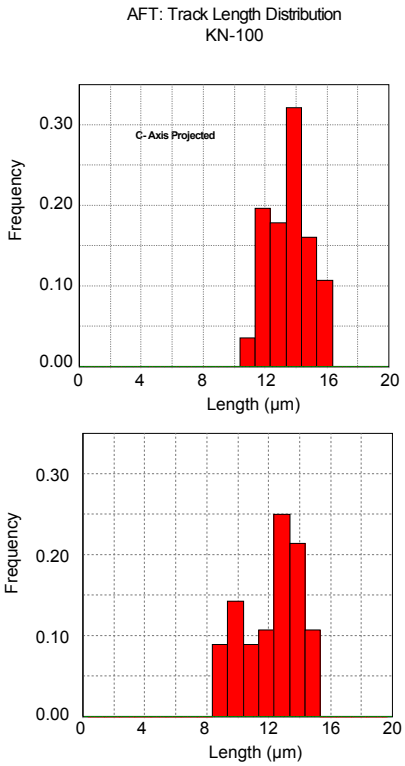

Data from sample UP112-6A.rtf
Irradiation Number UP112-6, Counted by user#: 0
The mineral is: Apatite

KN102

Length	angle	Dpar	Length	angle	Dpar	Length	angle	Dpar
9.4	51.6	1.91	13.2	61.9	2.01	9.3	34.1	2.17
11.1	83.4	1.3	13.7	74	1.52	11.4	64.6	2.08
9.9	31.9	2.14	11.9	26.8	2.29	15.3	53.6	2.16
8.3	42.3	1.67	8.4	29.4	1.8	14	62	1.74
8.4	54.1	1.67	11.6	68.4	1.68	8.2	20.7	1.99
10.1	33.6	1.45	10.7	74.4	1.91	12.7	58.7	2.01
12.7	43	2.05	8.9	67.8	1.3	11.1	44.5	1.52
10.6	75.6	1.52	15.3	34.8	2.14			
8.3	19.8	1.94	8.6	45.6	1.67			
10	51.7	2.17	14.1	84.9	1.67			
12.8	86.1	2.56	9.9	89.9	1.45			
9.8	40.8	2.12	10.7	88.5	2.05			
10	88.7	2.46	9.6	75.6	1.52			
11.4	30.8	2.72	14.8	83.7	1.94			
10	71.5	1.99	10	43.5	2.17			
12.8	84.1	1.66	11.3	27.8	2.56			
10.2	3.1	2.23	13.3	70	2.12			
9.9	78	1.58	11.2	11.1	2.46			
12.2	66	2.39	13.8	85.3	2.72			
12.2	58.7	1.8	13.7	43.9	1.99			
11.9	59.9	1.8	11.2	16.1	1.66			
10.8	47.1	2.21	8.4	79.4	2.23			
11.4	67.5	1.93	9.3	84.5	1.58			
12.7	44.5	1.81	7.4	5.8	2.39			
9.7	39.7	1.49	10.3	66.8	1.8			
10	66.2	2	14.1	86.3	1.8			
11.3	39.1	1.47	14.6	63	2.21			
10.2	65.3	2.17	10.3	67.2	1.93			
12.4	60.5	1.95	7.7	65.9	1.81			
7.5	49.6	2.47	8.2	31.5	1.49			
11.2	33.9	1.75	9.9	85.4	2			
11.8	59.8	2.21	10.8	62.9	1.47			
13.8	70.1	2.12	14.4	83.1	2.17			
12.9	50.9	1.65	13.7	66.1	1.95			
9.2	57	2.53	13.7	53.5	2.47			
13.1	75.7	1.5	13.4	60	1.75			
10.8	77.5	1.62	9.8	22.2	2.21			
14.6	62.4	2.27	10.5	63.3	2.12			
13.8	46.1	2.28	9.6	62.4	1.65			
9.7	65.9	1.66	13.5	80.5	2.53			
11	45.3	1.81	13.2	39.1	1.5			
9.4	78.7	2.06	10	56.8	1.62			
9.7	78.3	2.17	14	63.8	2.27			
10.6	46.4	2.08	13.9	53.4	2.28			
12	58.5	2.16	11.6	20.2	1.66			
9.1	66	1.74	9.5	61.2	1.81			
13.9	58.4	1.99	10.4	47.7	2.06			

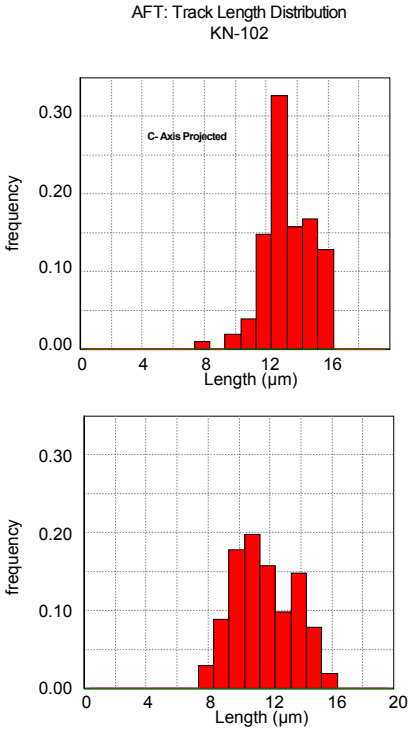

Data from sample UP112-7A.rtf
Irradiation Number UP112-7, Counted by user#: 0
The mineral is: Apatite

KN83

length	angle	Dpar
13.9	40.7	2.11
13.8	51.4	1.57
14.9	72.2	1.57
14.1	39.9	1.57
12.7	53.9	1.57
9.9	44.5	1.57
15.4	62.1	2.10
12.1	47.2	2.10
13.1	30.5	1.80
11.2	36.9	1.80
10.7	12.1	1.51
7.3	7.3	1.74
10.8	26.6	1.96
12.7	21.2	1.96
9.4	9	1.84
11.4	68.4	1.68
14.8	66.4	1.71
9	37.9	1.70
11	27.4	1.88
11.9	72.4	1.81
10.5	77.6	1.81
13.6	47.2	2.07
11.5	52	2.95
14.4	86.2	2.95
12.9	82.9	2.54
11	74.9	2.02
14	29.7	2.02
11.8	85.2	2.02
11.4	4.6	2.02
11.9	34.4	2.18
10.1	48.8	2.18
11.6	19.8	2.18
13.1	48.5	1.91
14.5	80.3	2.72
15.1	70.3	1.55
11.6	87	1.55
14.5	66.5	1.55
13.2	87.3	1.62
10.6	55.2	1.76

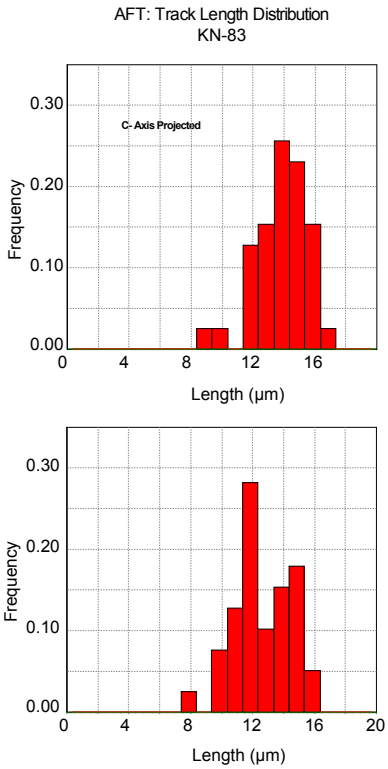

Data from sample UP112-9A.rtf
Irradiation Number UP112-9, Counted by user#: 0
The mineral is: Apatite

KN85

length	angle	Dpar	length	angle	Dpar
8.4	9.3	2.31	12.7	25.9	2.32
7.8	29.4	2.31	10.8	48.9	2.48
10.8	43.4	1.66	11.2	78	2.48
11.1	75.4	2.32	14.7	73.6	1.75
6.6	0.2	2.25	13.9	48.8	1.75
9.5	4.2	2.25	15.8	78	1.75
12.4	66.1	1.9	10.7	41.9	1.75
13.7	58.7	1.9	13.5	80.9	2.19
8.5	8.6	1.99	12.2	20.4	1.53
10.8	76.6	1.99	14	66.7	1.49
12	35.1	1.33	12.1	66.7	1.72
10.4	68.2	2.08	14.6	63.8	1.72
13.7	48	2.08	12.8	84.8	1.72
8.4	72.8	1.68	13	70.3	2.72
12.1	69.5	2.01	11.6	84.3	2.72
12.6	28.4	2.32	10.6	59	2.72
9.1	40.9	2.57	12.7	54.7	2.72
8.8	46	2.21	10.8	39.2	2.72
9.2	83.9	2.43	10.6	55.6	2.22
10.3	42	2.43	8	62.8	2.22
10	23.1	2.43	13.9	56.3	2.39
12.3	38	2.48	14	37.6	2.39
7.5	33.6	1.17	14.6	56.2	2.24
13.9	65.6	2.15	10.7	56.2	2.24
12.3	20.2	1.61	11.2	62.9	2.24
11	58.6	2.01	14.5	63.3	2.24
12.8	69.4	2.01	10.6	62.8	2.24
10.9	73.2	2.01	14	68.2	2.24
11.2	47.8	2.23	12.7	56.4	2.24
10.7	84.1	2.23	12.2	79.6	1.99
12.5	70	2.23	13.4	49.3	1.99
13.6	59.5	2.23	11.6	82.7	1.99
11.4	47.5	2.23	12	72.4	1.78
15.6	75.1	2.23	14.4	74.7	1.68
12.7	53	2.19	12.9	78.5	1.68
13.7	0.7	1.66	13.1	60.5	1.68
14.4	35.3	2.19	10.7	75.1	2.03
11.2	0.8	2.19	13	23.8	2.03
11.3	74.5	2.41	12.4	86.1	1.64
12.5	50	2.16	11.7	28.1	2.03
12.9	1.2	1.41	12.2	36.7	2.03
10.4	12.6	1.41	15.3	47.8	2.55
10.3	17.1	1.82	11.8	55.7	2.55
12.8	47.5	1.69	13.8	57.8	2.55
11.2	70.2	1.95	13.8	68.3	2.55
10.2	66.7	1.73	13.7	72.8	2.55
9.9	19.1	1.73	13.4	34.8	2.18
12.5	35.1	1.51	8.4	70.5	2.18
15	11.4	1.51	14.8	54.5	1.89
10.5	0.8	1.51			
12.9	58.1	2.32			

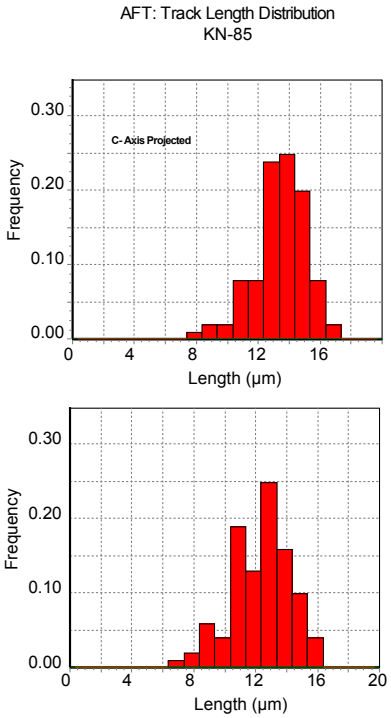

Appendix B

Additional data chapter 3

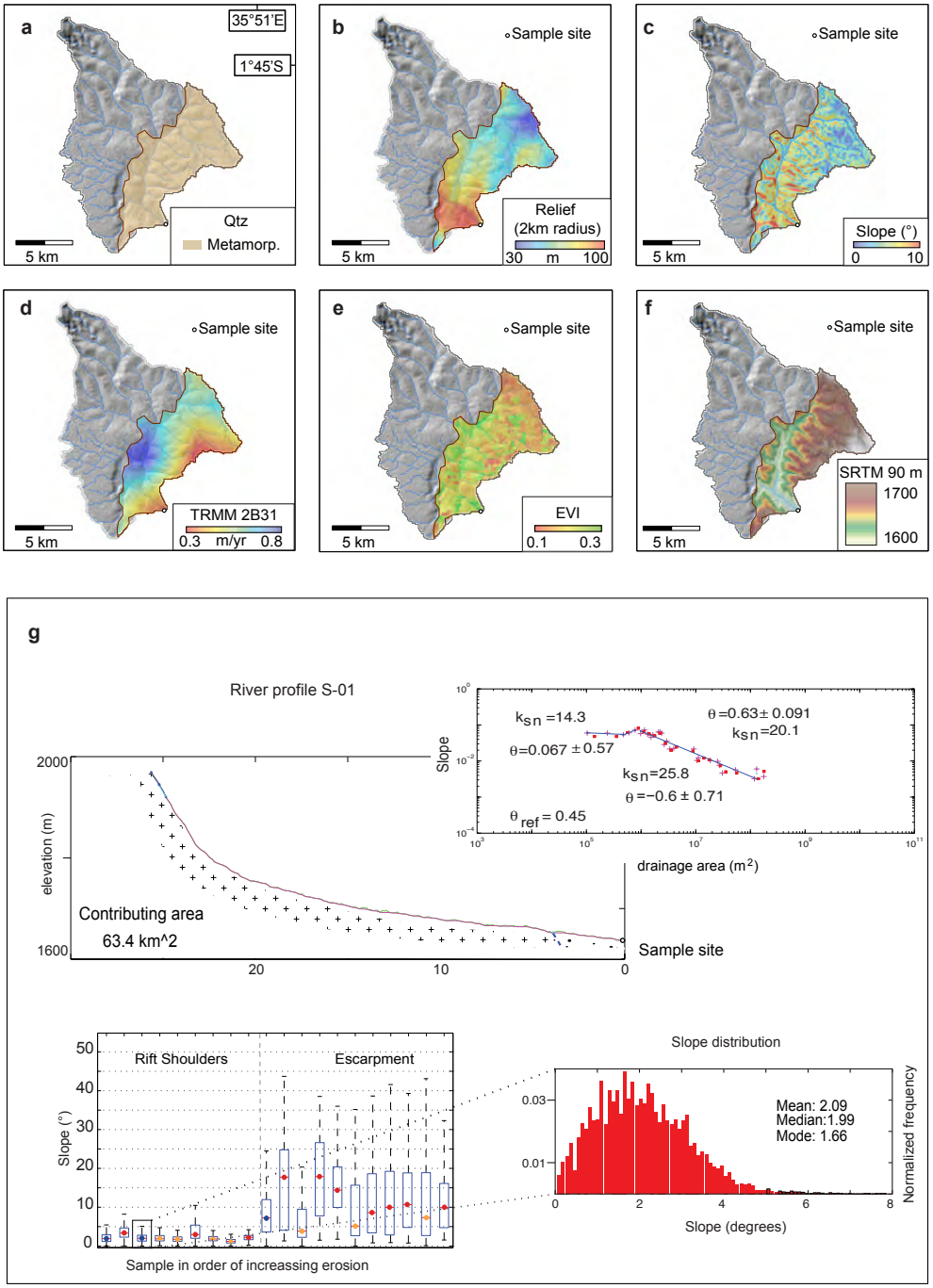

Figure B1. Catchment morphology for samples in the Northern, Central and Southern Kenya Rift. For each catchment (S01-S03, C01-C10, and N01-N07), we show (a) lithology, (b) relief, (c) median catchment slope, (d) mean annual precipitation, (e) vegetation cover based on Enhanced Vegetation Index (EVI), (f) elevation, based on 90-m resolution SRTM data, and (g) combination of the river longitudinal profile with schematic depiction of geology, slope-area plots, and the distribution of slope values for the catchment.

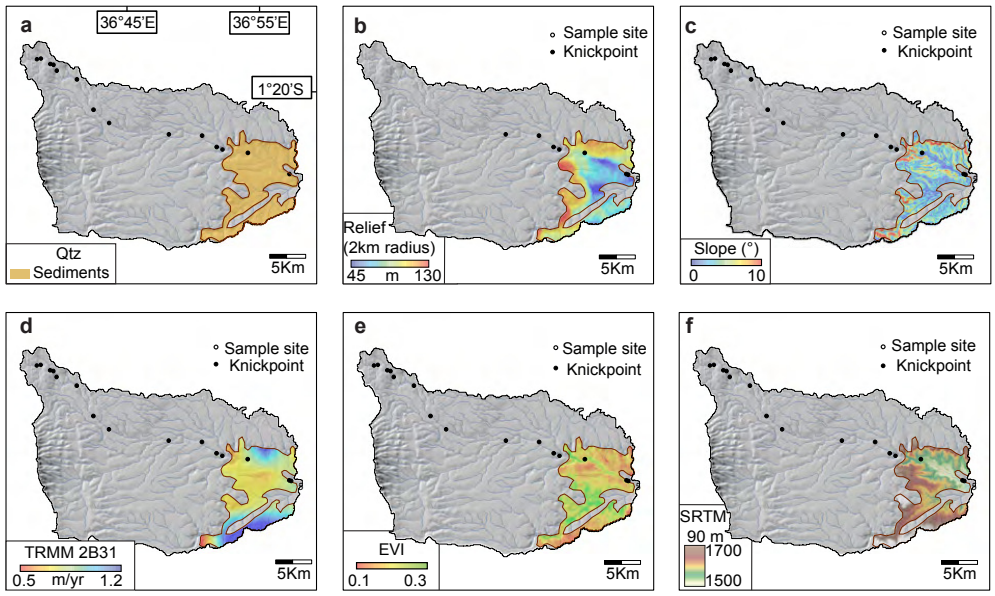
a
36°45'E
36°55'E
1°20'S
Qtz
Sediments
5Km
b
Sample site
Knickpoint
Relief
(2km radius)
45 m 130
5Km
c
Sample site
Knickpoint
Slope (°)
0 10
5Km
d
Sample site
Knickpoint
TRMM 2B31
0.5 m/yr 1.2
5Km
e
Sample site
Knickpoint
EVI
0.1 0.3
5Km
f
Sample site
Knickpoint
SRTM
90 m
1700
1500
5Km

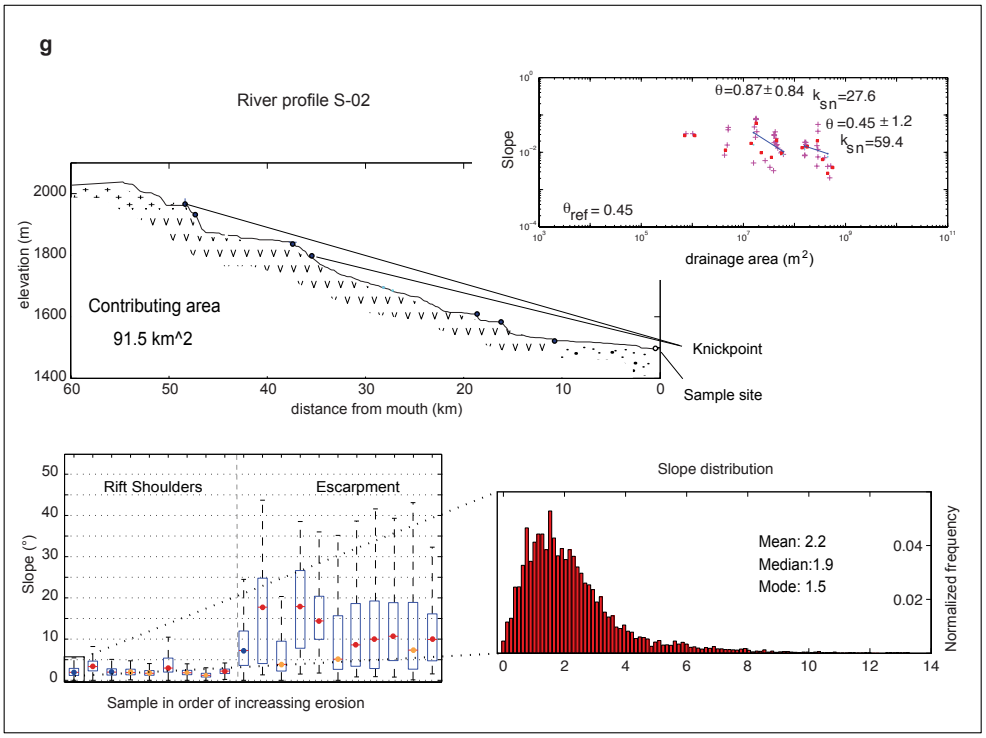
g
River profile S-02
elevation (m)
2000
1800
1600
1400
60
50
40
30
20
10
0
distance from mouth (km)
Contributing area
91.5 km^2
Knickpoint
Sample site
Slope
θ=0.87± 0.84 k_sn=27.6
θ =0.45 ± 1.2
k_sn=59.4
θ_ref = 0.45
drainage area (m^2)
Slope (°)
50
40
30
20
10
0
Rift Shoulders
Escarpment
Sample in order of increassing erosion
Slope distribution
Mean: 2.2
Median:1.9
Mode: 1.5
0.04
0.02
Normalized frequency
0
2
4
6
8
10
12
14

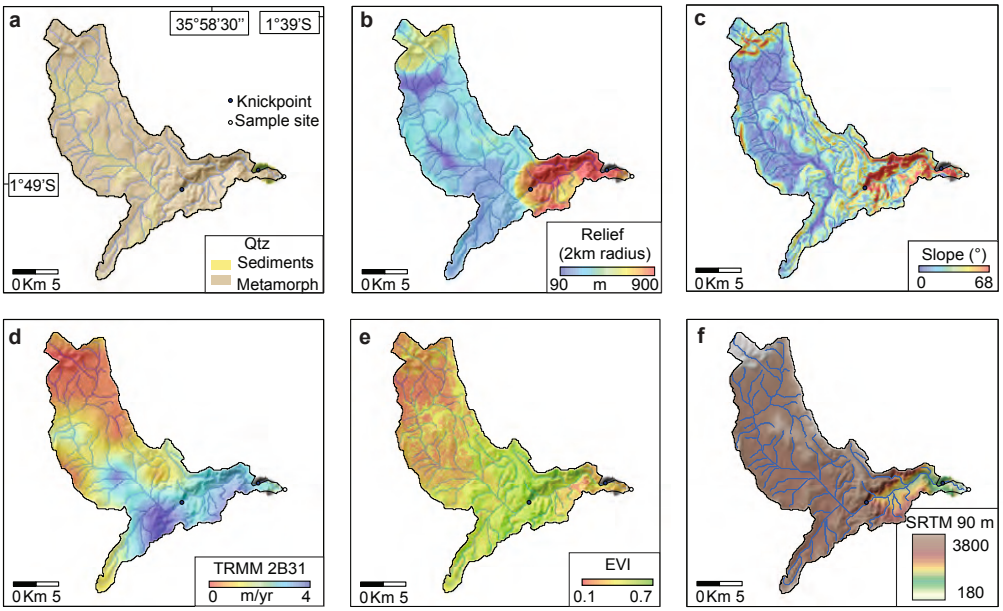
a
35°58'30"
1°39'S
Knickpoint
Sample site
1°49'S
Qtz
Sediments
Metamorph
0Km 5
b
Relief
(2km radius)
90 m 900
0Km 5
c
Slope (°)
0 68
0Km 5
d
TRMM 2B31
0 m/yr 4
0Km 5
e
EVI
0.1 0.7
0Km 5
f
SRTM 90 m
3800
180
0Km 5

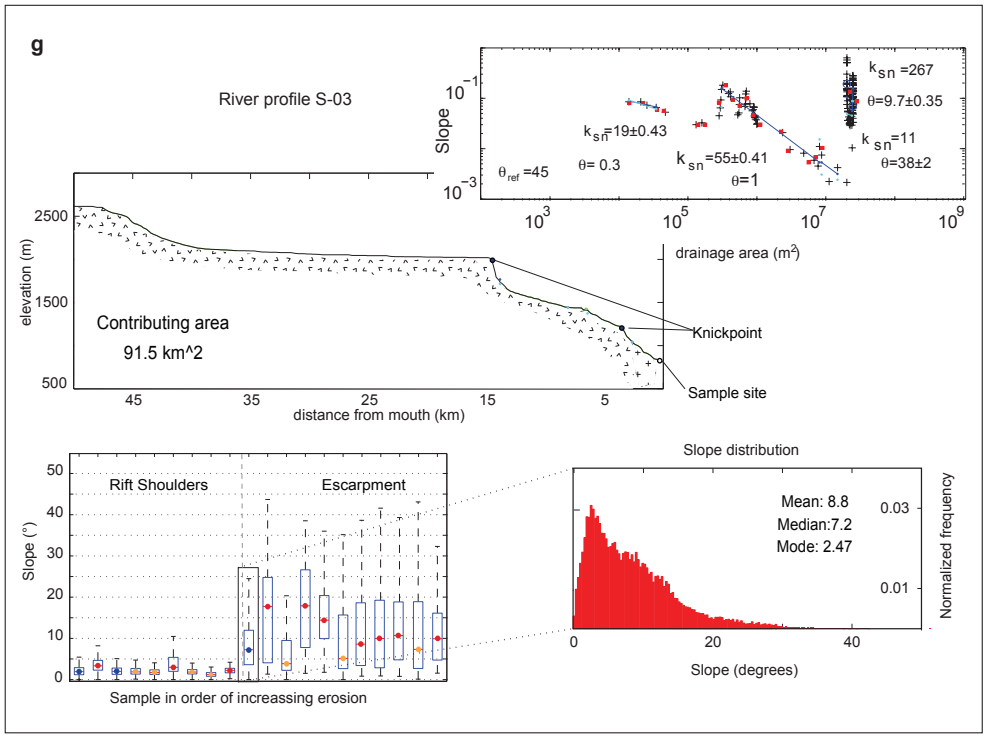
g
River profile S-03
Slope
10^{-1}
10^{-3}
k_{sn}=19±0.43
θ_{ref}=45
θ= 0.3
k_{sn}=55±0.41
θ=1
k_{sn}=267
θ=9.7±0.35
k_{sn}=11
θ=38±2
10^3 10^5 10^7 10^9
drainage area (m^2)
elevation (m)
2500
1500
500
Contributing area
91.5 km^2
Knickpoint
Sample site
45 35 25 15 5
distance from mouth (km)
Rift Shoulders
Escarpment
Slope (°)
50 40 30 20 10 0
Sample in order of increassing erosion
Slope distribution
Mean: 8.8
Median:7.2
Mode: 2.47
0.03
0.01
Normalized frequency
0 20 40
Slope (degrees)

C-01

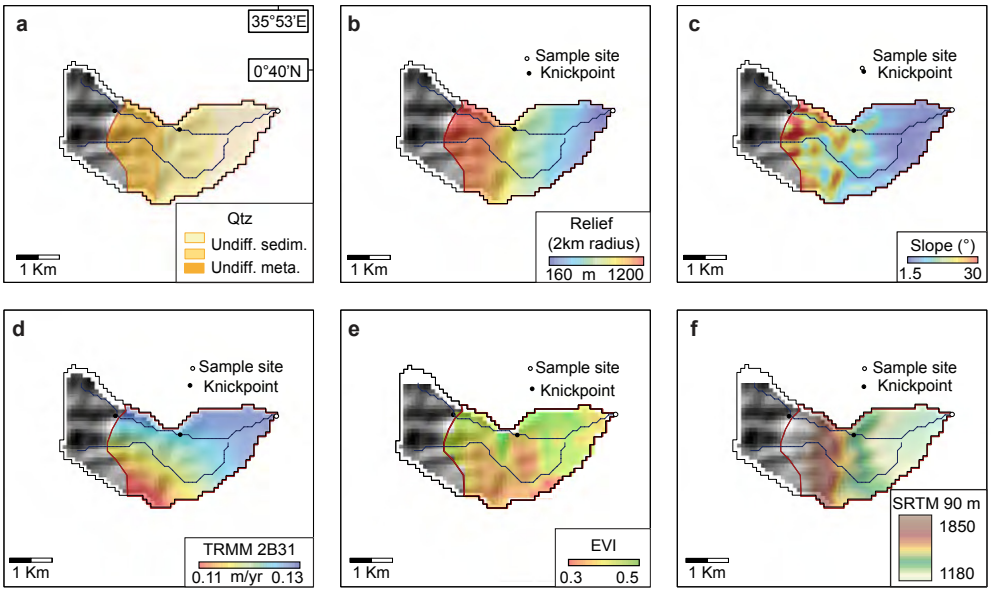
a
35°53'E
0°40'N
Qtz
Undiff. sedim.
Undiff. meta.
1 Km
b
Sample site
Knickpoint
Relief
(2km radius)
160 m 1200
1 Km
c
Sample site
Knickpoint
Slope (°)
1.5 30
1 Km
d
Sample site
Knickpoint
TRMM 2B31
0.11 m/yr 0.13
1 Km
e
Sample site
Knickpoint
EVI
0.3 0.5
1 Km
f
Sample site
Knickpoint
SRTM 90 m
1850
1180
1 Km

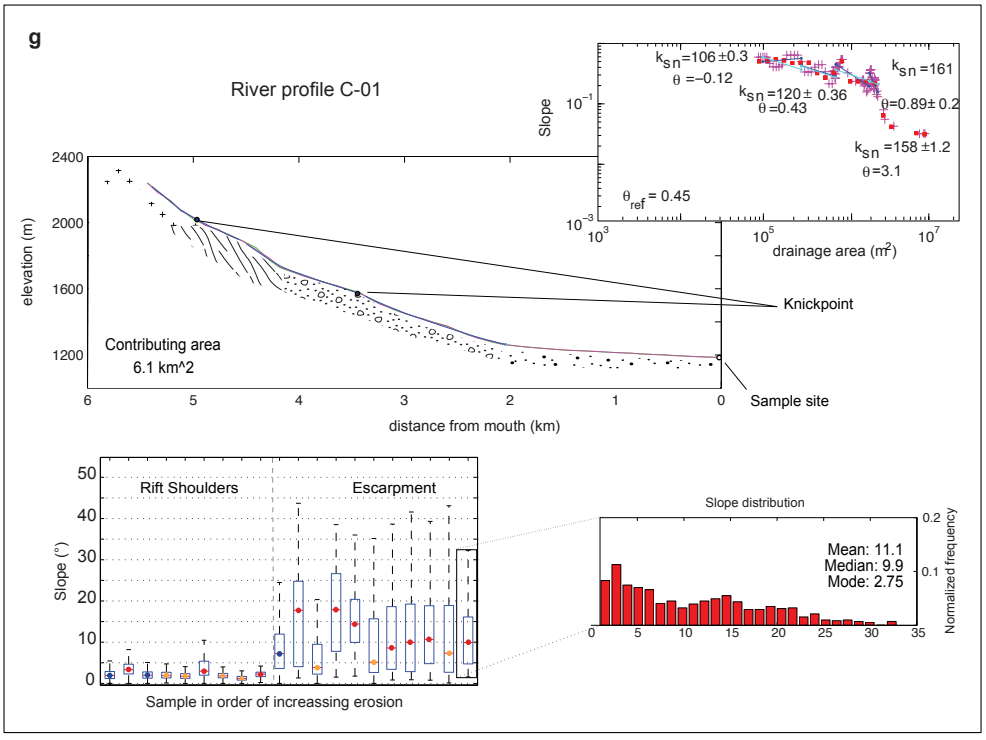
g
River profile C-01
Slope
k_{sn}=106±0.3
θ =–0.12
k_{sn}=120± 0.36
θ =0.43
k_{sn} =161
θ=0.89± 0.2
k_{sn} =158 ±1.2
θ=3.1
θ_{ref} = 0.45
drainage area (m^2)
elevation (m)
Knickpoint
Contributing area
6.1 km^2
Sample site
distance from mouth (km)
Rift Shoulders
Escarpment
Slope (°)
Sample in order of increasing erosion
Slope distribution
Mean: 11.1
Median: 9.9
Mode: 2.75
Normalized frequency

C-02

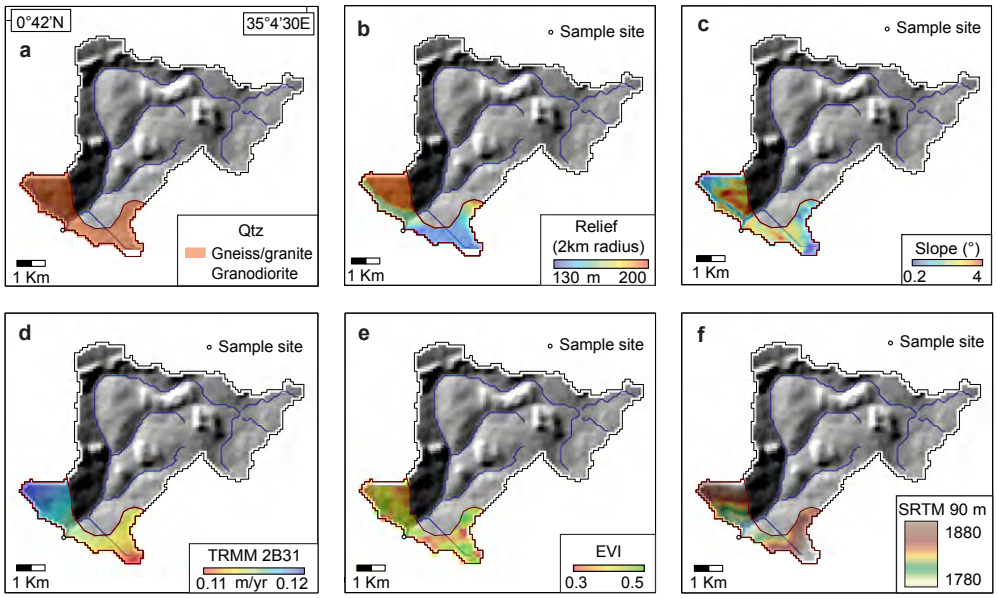
a
0°42'N
35°4'30E
Qtz
Gneiss/granite
Granodiorite
1 Km
b
Sample site
Relief
(2km radius)
130 m 200
1 Km
c
Sample site
Slope (°)
0.2 4
1 Km
d
Sample site
TRMM 2B31
0.11 m/yr 0.12
1 Km
e
Sample site
EVI
0.3 0.5
1 Km
f
Sample site
SRTM 90 m
1880
1780
1 Km

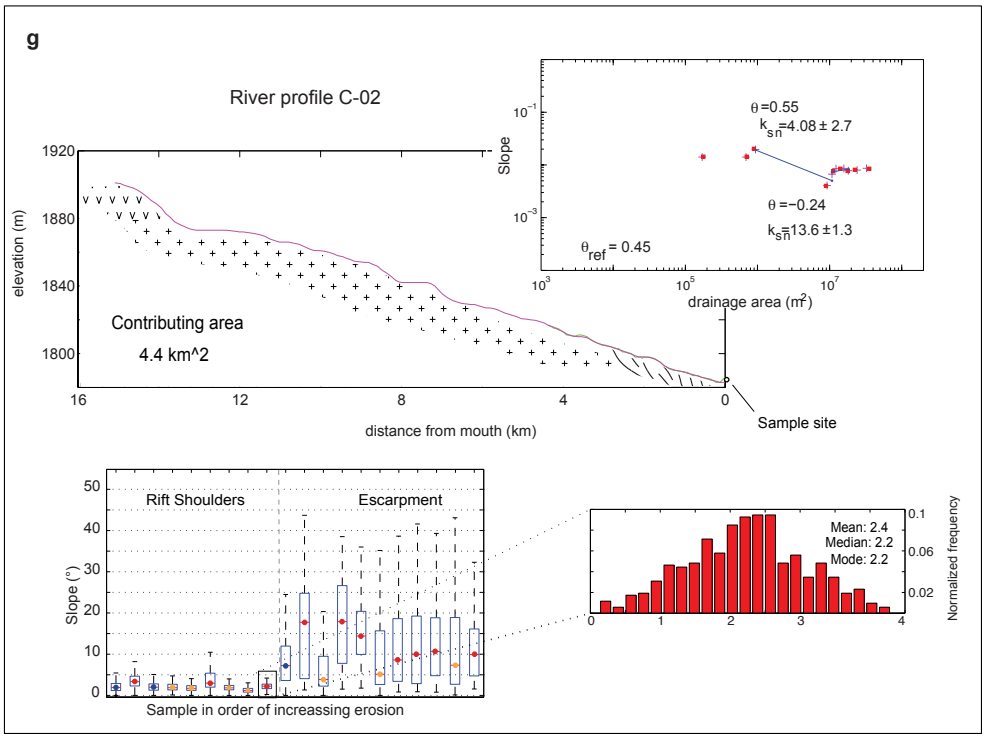
g
River profile C-02
elevation (m)
1920
1880
1840
1800
16
12
8
4
0
distance from mouth (km)
Contributing area
4.4 km^2
Sample site
Slope
θ=0.55
k_sn=4.08 ± 2.7
θ=−0.24
k_sn=13.6 ±1.3
θ_ref = 0.45
drainage area (m²)
Slope (°)
Rift Shoulders
Escarpment
Sample in order of increassing erosion
Mean: 2.4
Median: 2.2
Mode: 2.2
Normalized frequency

C-03

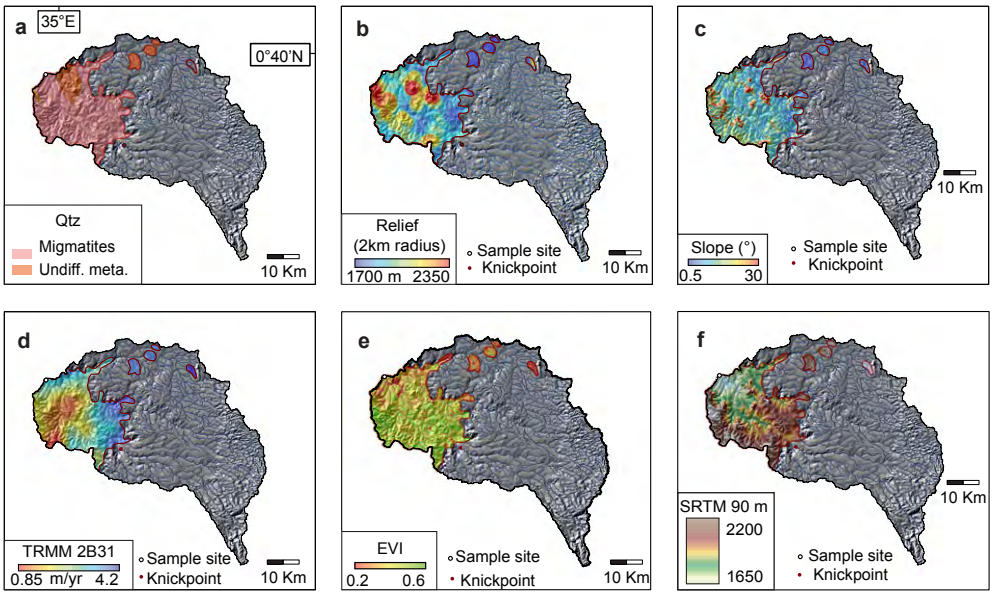
a
35°E
0°40'N
Qtz
Migmatites
Undiff. meta.
10 Km
b
Relief
(2km radius)
1700 m 2350
Sample site
Knickpoint
10 Km
c
Slope (°)
0.5 30
Sample site
Knickpoint
10 Km
d
TRMM 2B31
0.85 m/yr 4.2
Sample site
Knickpoint
10 Km
e
EVI
0.2 0.6
Sample site
Knickpoint
10 Km
f
SRTM 90 m
2200
1650
Sample site
Knickpoint
10 Km

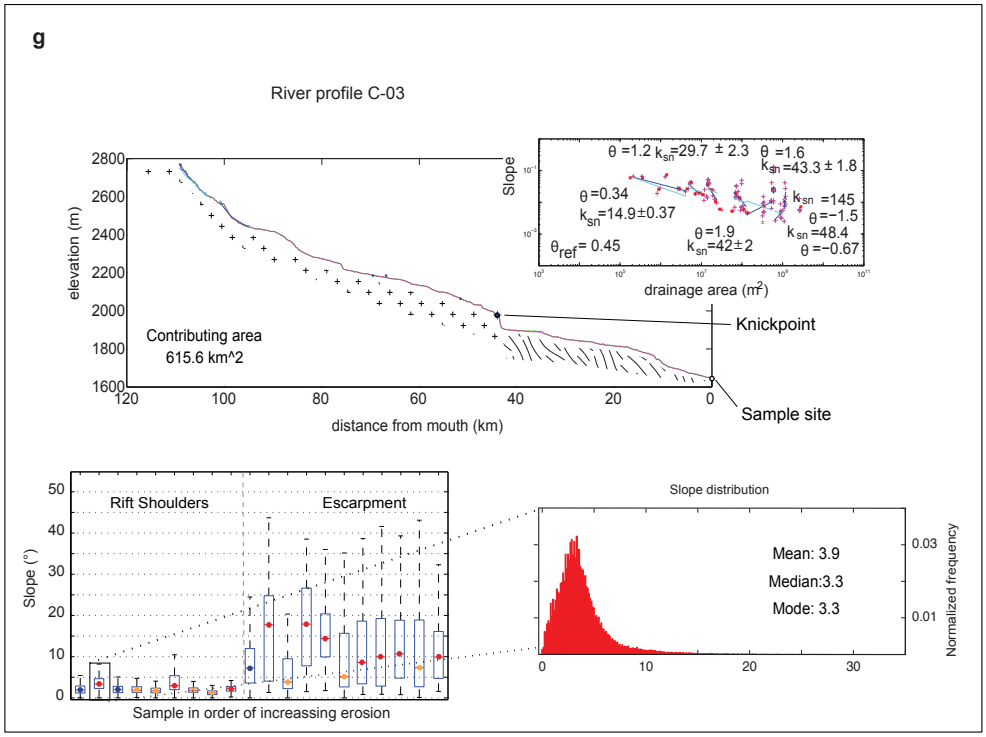
g
River profile C-03
elevation (m)
distance from mouth (km)
Contributing area
615.6 km^2
Knickpoint
Sample site
Slope
drainage area (m²)
θ =1.2 ksn=29.7 ± 2.3
θ =1.6
ksn=43.3 ± 1.8
θ=0.34
ksn=14.9±0.37
ksn =145
θ=−1.5
θref= 0.45
θ=1.9
ksn=42±2
ksn=48.4
θ=−0.67
Slope (°)
Rift Shoulders
Escarpment
Sample in order of increassing erosion
Slope distribution
Mean: 3.9
Median:3.3
Mode: 3.3
Normalized frequency

C-04

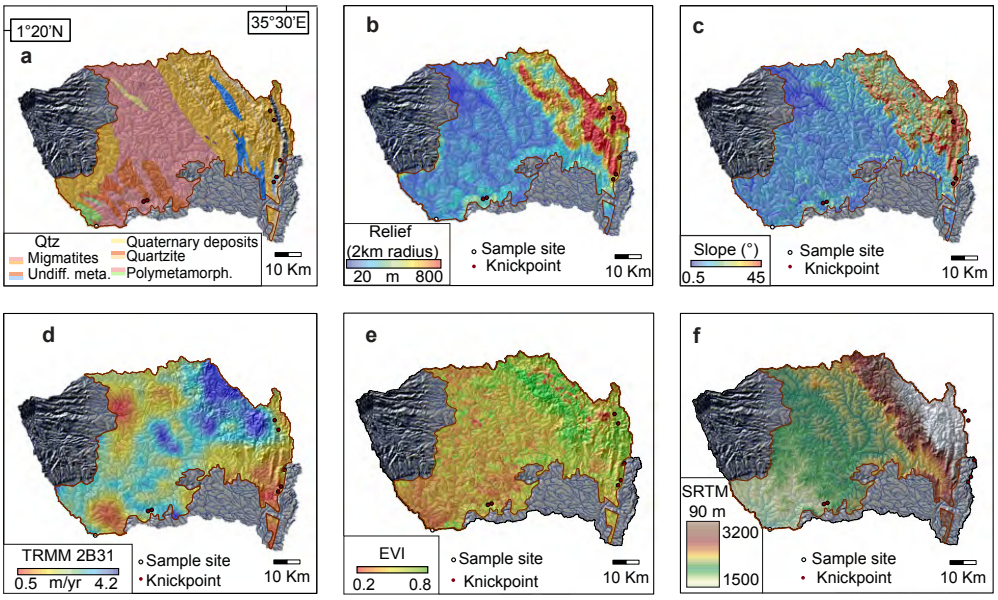
1°20'N
35°30'E
a
Qtz
Migmatites
Undiff. meta.
Quaternary deposits
Quartzite
Polymetamorph.
10 Km
b
Relief
(2km radius)
20 m 800
Sample site
Knickpoint
10 Km
c
Slope (°)
0.5 45
Sample site
Knickpoint
10 Km
d
TRMM 2B31
0.5 m/yr 4.2
Sample site
Knickpoint
10 Km
e
EVI
0.2 0.8
Sample site
Knickpoint
10 Km
f
SRTM
90 m
3200
1500
Sample site
Knickpoint
10 Km

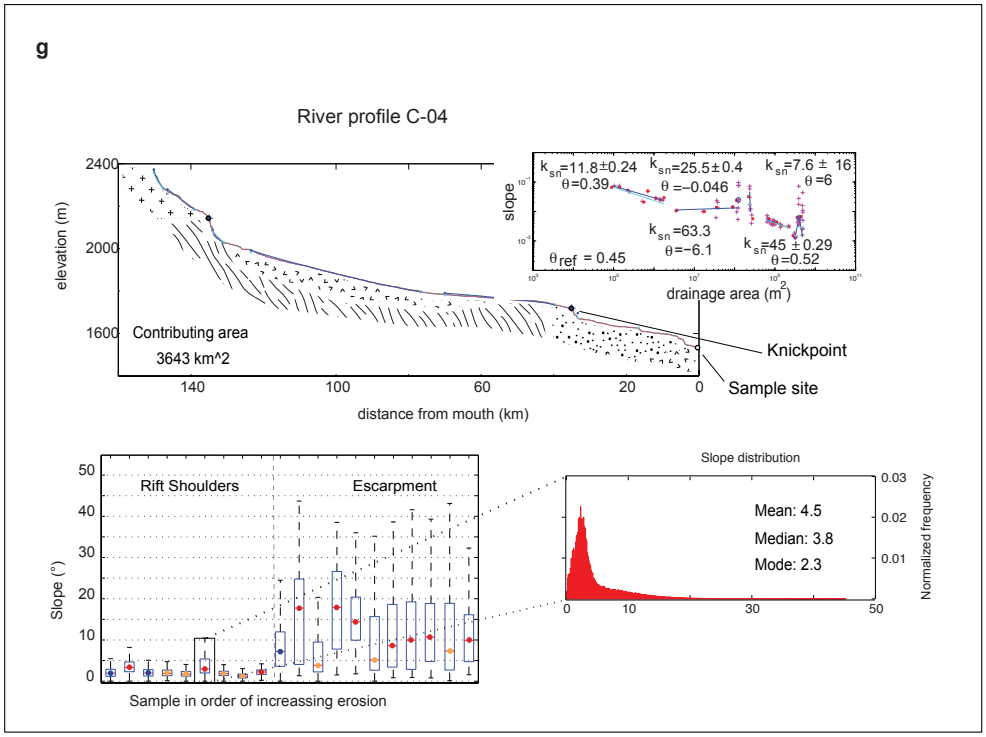
g
River profile C-04
elevation (m)
2400
2000
1600
Contributing area
3643 km^2
140
100
60
20
0
distance from mouth (km)
Knickpoint
Sample site
slope
drainage area (m^2)
θ ref = 0.45
Slope (°)
50
40
30
20
10
0
Rift Shoulders
Escarpment
Sample in order of increassing erosion
Slope distribution
Mean: 4.5
Median: 3.8
Mode: 2.3
Normalized frequency
0.03
0.02
0.01
0
10
30
50

C-05

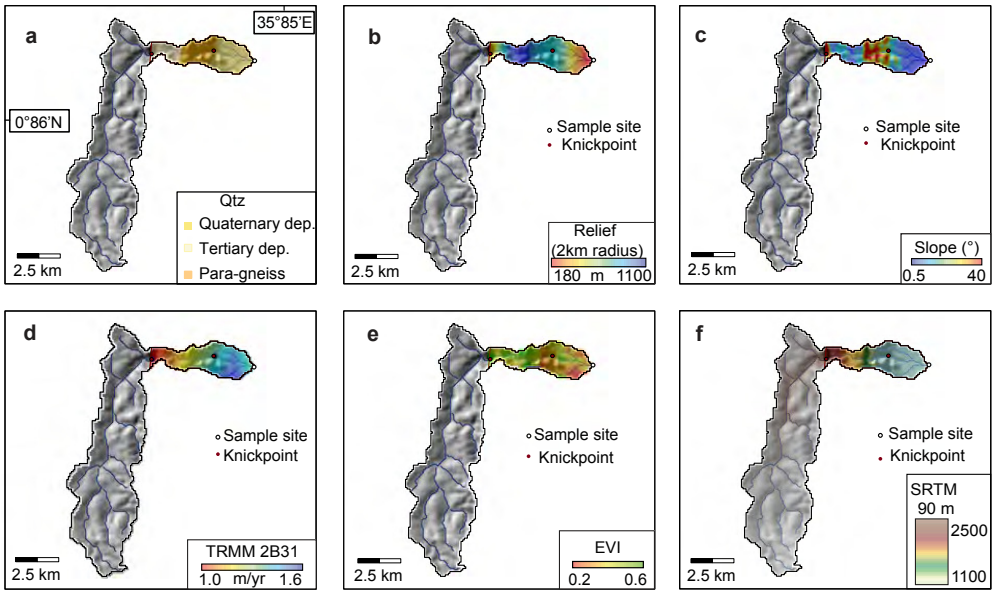
a
35°85'E
0°86'N
Qtz
Quaternary dep.
Tertiary dep.
Para-gneiss
2.5 km
b
Sample site
Knickpoint
Relief
(2km radius)
180 m 1100
2.5 km
c
Sample site
Knickpoint
Slope (°)
0.5 40
2.5 km
d
Sample site
Knickpoint
TRMM 2B31
1.0 m/yr 1.6
2.5 km
e
Sample site
Knickpoint
EVI
0.2 0.6
2.5 km
f
Sample site
Knickpoint
SRTM
90 m
2500
1100
2.5 km

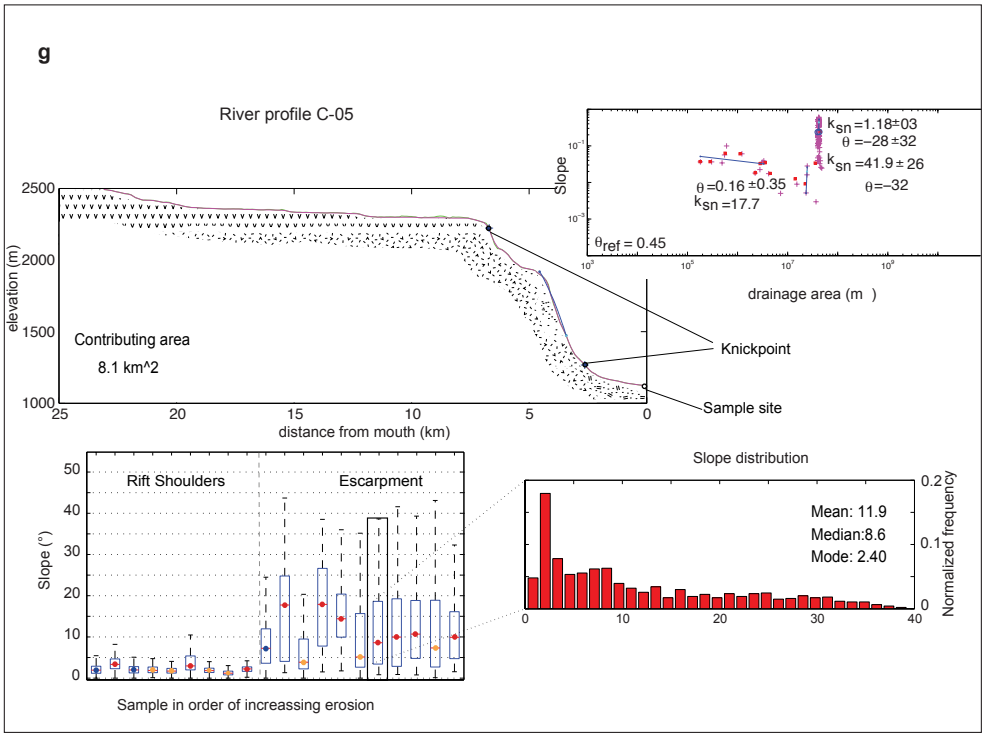
g
River profile C-05
elevation (m)
2500
2000
1500
1000
25
20
15
10
5
0
distance from mouth (km)
Contributing area
8.1 km^2
Knickpoint
Sample site
Slope
drainage area (m)
θ =0.16 ±0.35
k_sn =17.7
k_sn =1.18±03
θ =–28 ±32
k_sn =41.9 ± 26
θ=–32
θ_ref = 0.45
Rift Shoulders
Escarpment
Slope (°)
Sample in order of increassing erosion
Slope distribution
Mean: 11.9
Median:8.6
Mode: 2.40
Normalized frequency

C-06

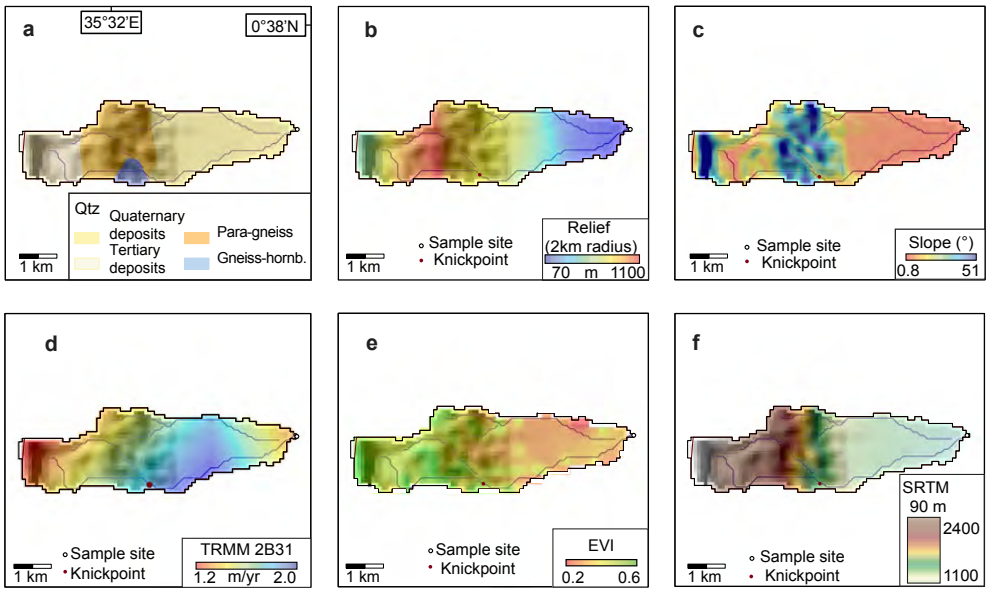
a
35°32'E
0°38'N
Qtz
Quaternary deposits
Tertiary deposits
Para-gneiss
Gneiss-hornb.
1 km
b
Sample site
Knickpoint
Relief (2km radius)
70 m 1100
c
Slope (°)
0.8 51
d
TRMM 2B31
1.2 m/yr 2.0
e
EVI
0.2 0.6
f
SRTM 90 m
2400
1100

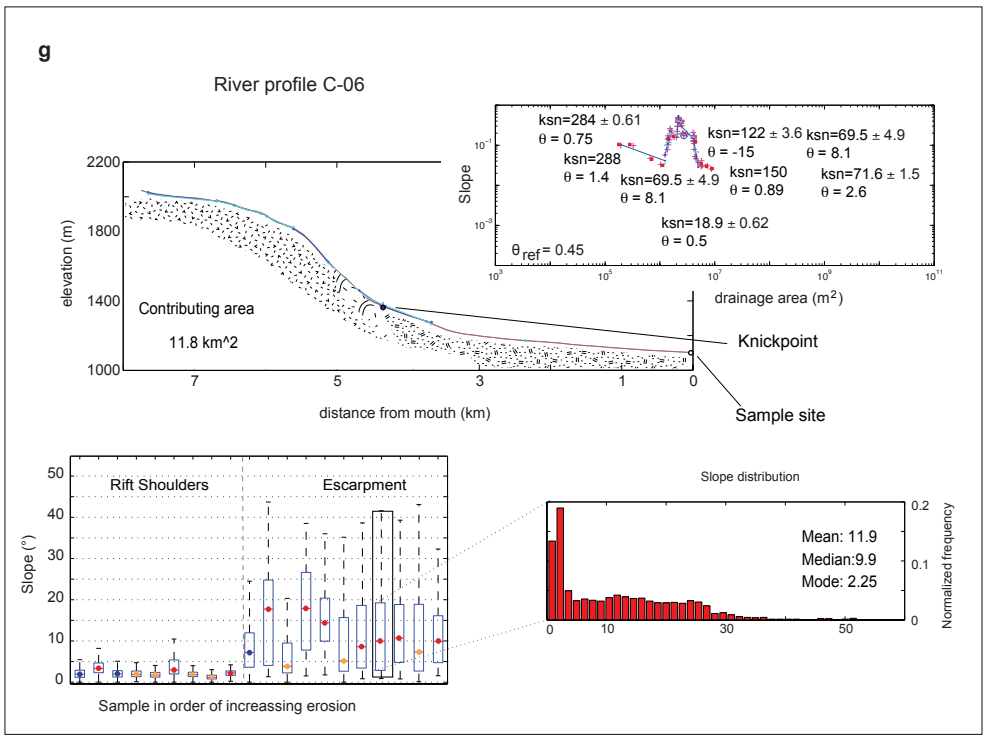
g
River profile C-06
elevation (m)
distance from mouth (km)
Contributing area
11.8 km^2
Knickpoint
Sample site
Slope
drainage area (m²)
ksn=284 ± 0.61
θ = 0.75
ksn=288
θ = 1.4
ksn=69.5 ± 4.9
θ = 8.1
ksn=122 ± 3.6
θ = -15
ksn=150
θ = 0.89
ksn=69.5 ± 4.9
θ = 8.1
ksn=71.6 ± 1.5
θ = 2.6
ksn=18.9 ± 0.62
θ = 0.5
θ ref = 0.45
Rift Shoulders
Escarpment
Slope (°)
Sample in order of increassing erosion
Slope distribution
Mean: 11.9
Median:9.9
Mode: 2.25
Normalized frequency

C-07

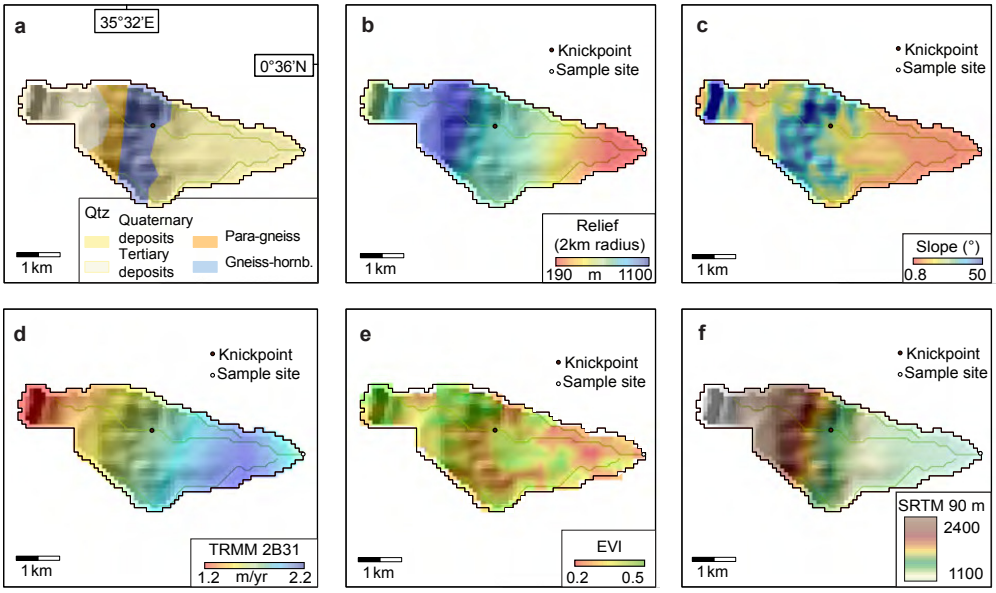
a
35°32'E
0°36'N
Qtz
Quaternary deposits
Tertiary deposits
Para-gneiss
Gneiss-hornb.
1 km
b
• Knickpoint
◦ Sample site
Relief (2km radius)
190 m 1100
1 km
c
• Knickpoint
◦ Sample site
Slope (°)
0.8 50
1 km
d
• Knickpoint
◦ Sample site
TRMM 2B31
1.2 m/yr 2.2
1 km
e
• Knickpoint
◦ Sample site
EVI
0.2 0.5
1 km
f
• Knickpoint
◦ Sample site
SRTM 90 m
2400
1100
1 km

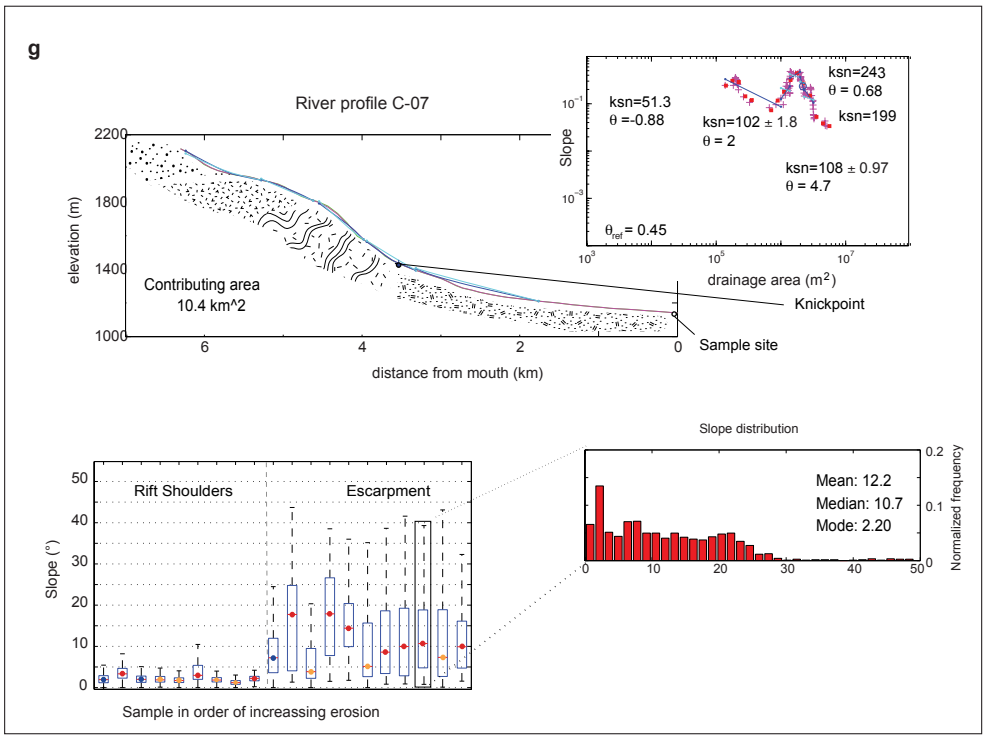
g
River profile C-07
elevation (m)
distance from mouth (km)
Contributing area
10.4 km^2
Knickpoint
Sample site
Slope
drainage area (m²)
ksn=51.3
θ =-0.88
ksn=102 ± 1.8
θ = 2
ksn=243
θ = 0.68
ksn=199
ksn=108 ± 0.97
θ = 4.7
θref = 0.45
Rift Shoulders
Escarpment
Slope (°)
Sample in order of increassing erosion
Slope distribution
Mean: 12.2
Median: 10.7
Mode: 2.20
Normalized frequency

C-08

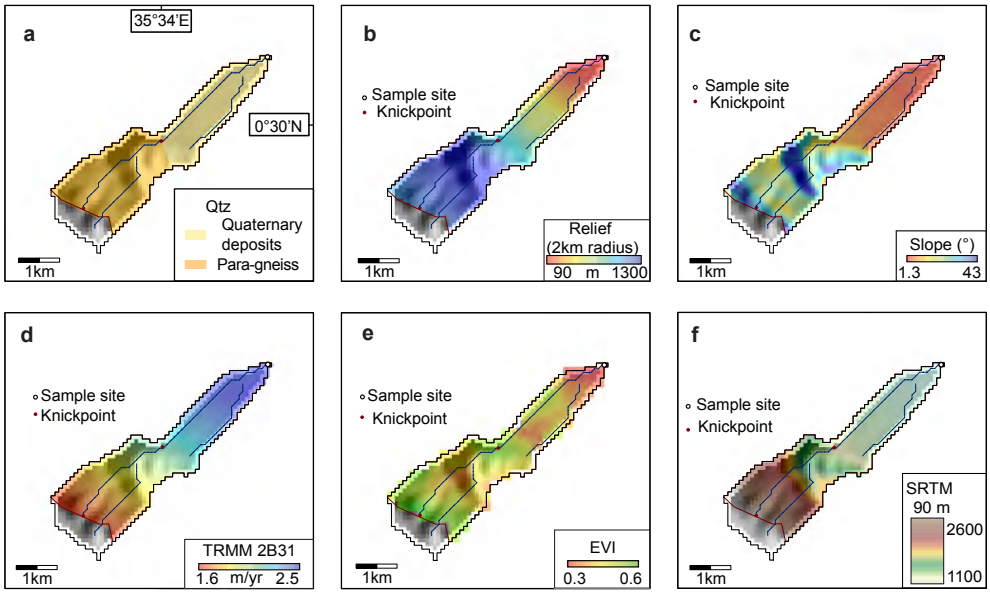
a
35°34'E
0°30'N
Qtz
Quaternary deposits
Para-gneiss
1km
b
Sample site
Knickpoint
Relief (2km radius)
90 m 1300
1km
c
Sample site
Knickpoint
Slope (°)
1.3 43
1km
d
Sample site
Knickpoint
TRMM 2B31
1.6 m/yr 2.5
1km
e
Sample site
Knickpoint
EVI
0.3 0.6
1km
f
Sample site
Knickpoint
SRTM 90 m
2600
1100
1km

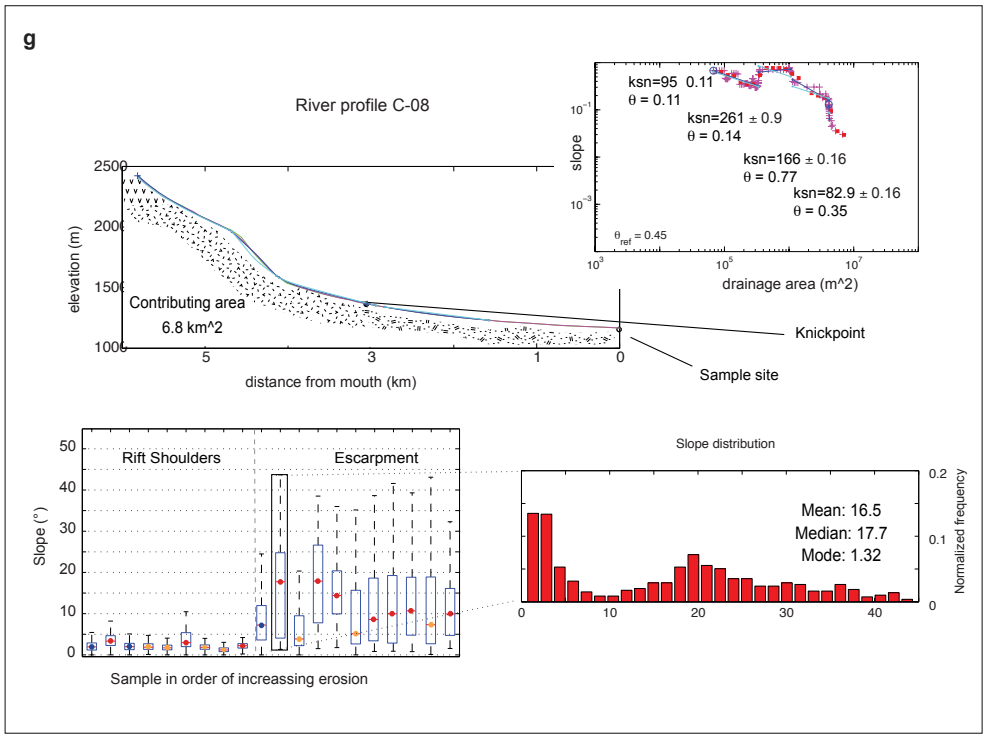
g
River profile C-08
elevation (m)
distance from mouth (km)
Contributing area
6.8 km^2
Knickpoint
Sample site
slope
drainage area (m^2)
ksn=95 0.11
θ = 0.11
ksn=261 ± 0.9
θ = 0.14
ksn=166 ± 0.16
θ = 0.77
ksn=82.9 ± 0.16
θ = 0.35
Rift Shoulders
Escarpment
Slope (°)
Sample in order of increassing erosion
Slope distribution
Mean: 16.5
Median: 17.7
Mode: 1.32
Normalized frequency

C-09

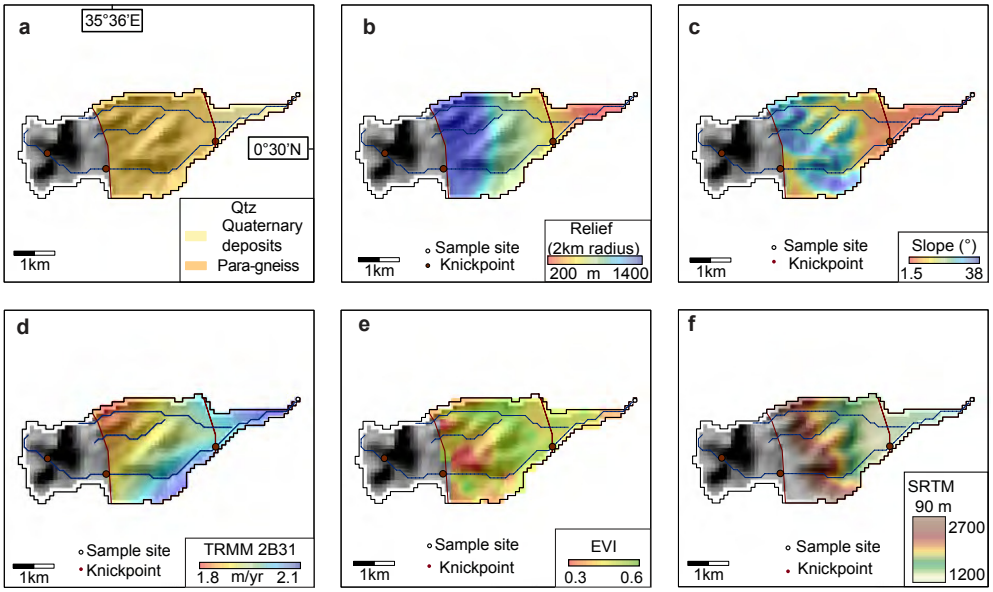
a
35°36'E
0°30'N
Qtz
Quaternary deposits
Para-gneiss
1km
b
Sample site
Knickpoint
Relief (2km radius)
200 m 1400
c
Slope (°)
1.5 38
d
TRMM 2B31
1.8 m/yr 2.1
e
EVI
0.3 0.6
f
SRTM 90 m
2700
1200

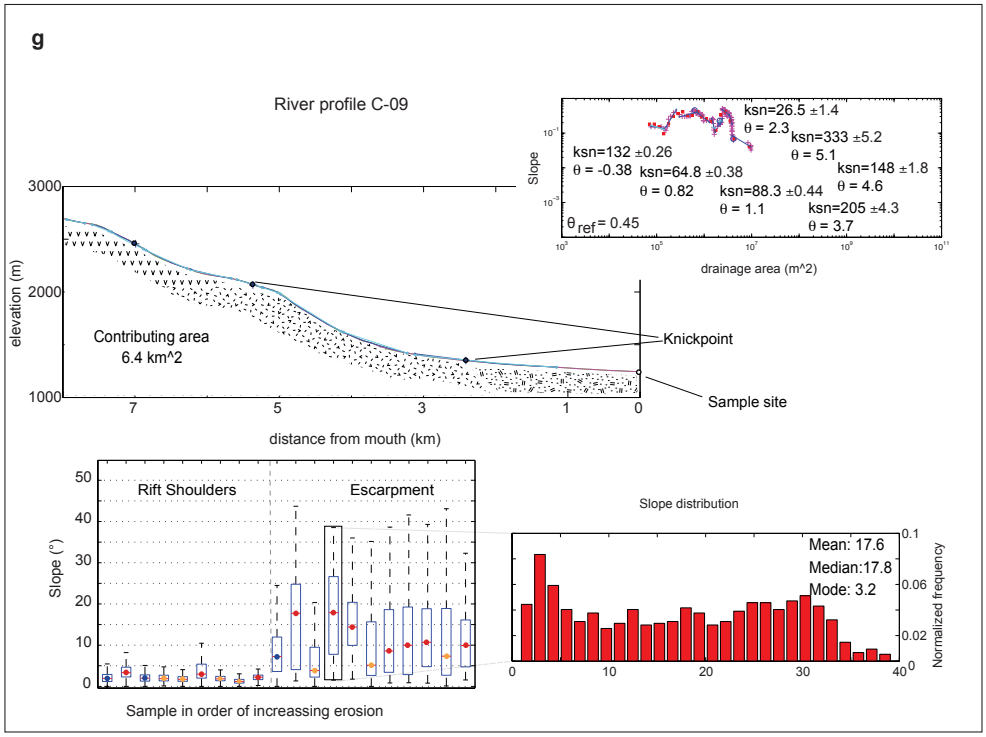
g
River profile C-09
ksn=26.5 ±1.4
θ = 2.3
ksn=333 ±5.2
θ = 5.1
ksn=148 ±1.8
θ = 4.6
ksn=205 ±4.3
θ = 3.7
ksn=132 ±0.26
θ = -0.38
ksn=64.8 ±0.38
θ = 0.82
ksn=88.3 ±0.44
θ = 1.1
θ ref = 0.45
Slope
drainage area (m^2)
elevation (m)
Contributing area
6.4 km^2
Knickpoint
Sample site
distance from mouth (km)
Rift Shoulders
Escarpment
Slope (°)
Sample in order of increasing erosion
Slope distribution
Mean: 17.6
Median:17.8
Mode: 3.2
Normalized frequency

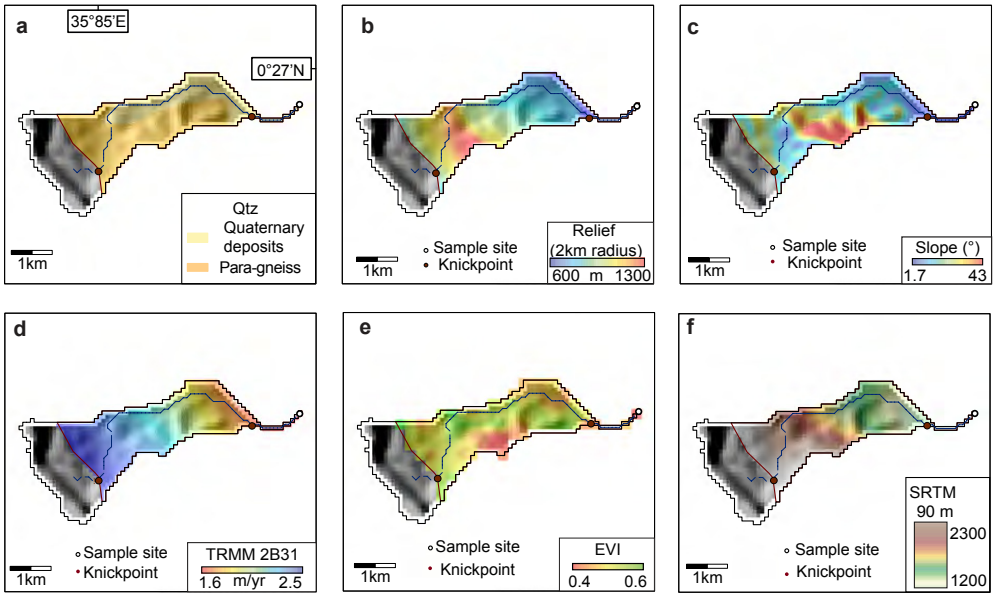
a
35°85'E
0°27'N
Qtz
Quaternary deposits
Para-gneiss
1km
b
Sample site
Knickpoint
Relief (2km radius)
600 m 1300
1km
c
Sample site
Knickpoint
Slope (°)
1.7 43
1km
d
Sample site
Knickpoint
TRMM 2B31
1.6 m/yr 2.5
1km
e
Sample site
Knickpoint
EVI
0.4 0.6
1km
f
Sample site
Knickpoint
SRTM 90 m
2300
1200
1km

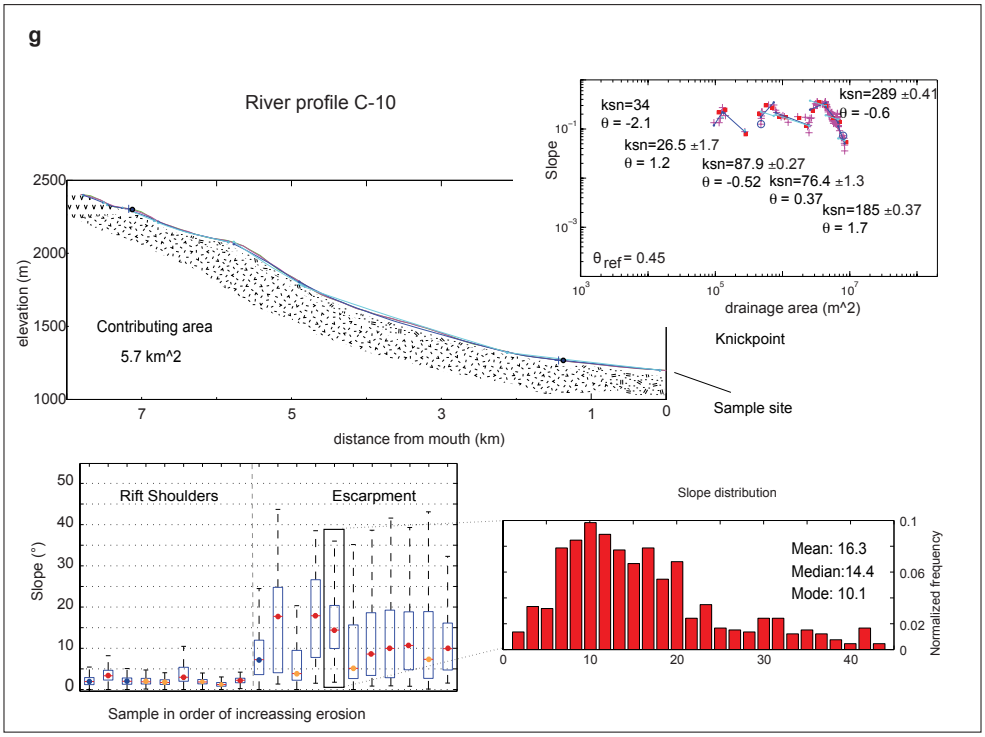
g
River profile C-10
elevation (m)
distance from mouth (km)
Contributing area
5.7 km^2
Knickpoint
Sample site
Slope
drainage area (m^2)
ksn=34
θ = -2.1
ksn=26.5 ±1.7
θ = 1.2
ksn=87.9 ±0.27
θ = -0.52
ksn=76.4 ±1.3
θ = 0.37
ksn=185 ±0.37
θ = 1.7
ksn=289 ±0.41
θ = -0.6
θ ref = 0.45
Rift Shoulders
Escarpment
Slope (°)
Sample in order of increassing erosion
Slope distribution
Mean: 16.3
Median:14.4
Mode: 10.1
Normalized frequency

N-01

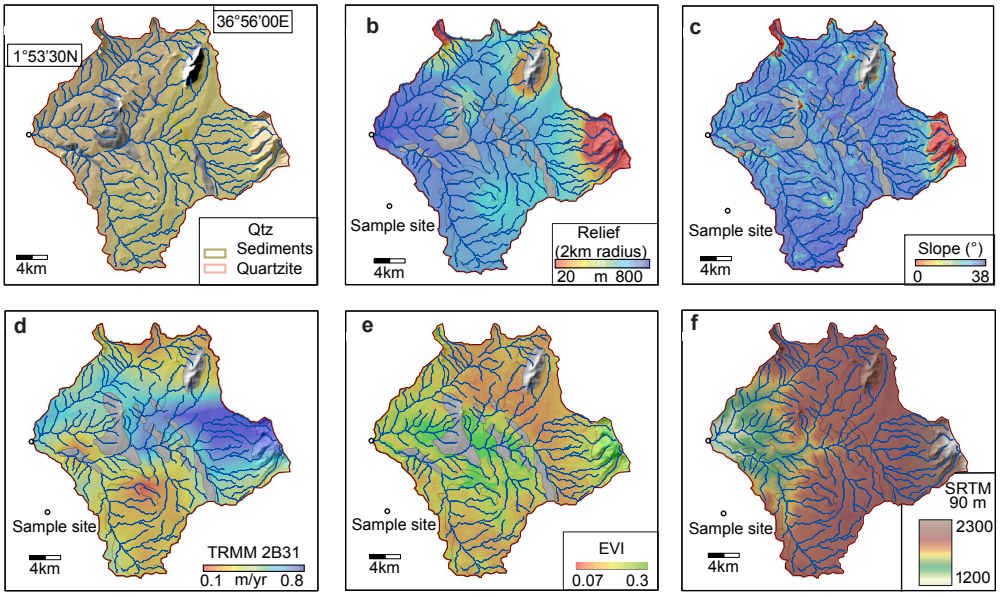
36°56'00E
1°53'30N
Qtz
Sediments
Quartzite
4km
b
Sample site
Relief
(2km radius)
20 m 800
c
Slope (°)
0 38
d
TRMM 2B31
0.1 m/yr 0.8
e
EVI
0.07 0.3
f
SRTM
90 m
2300
1200

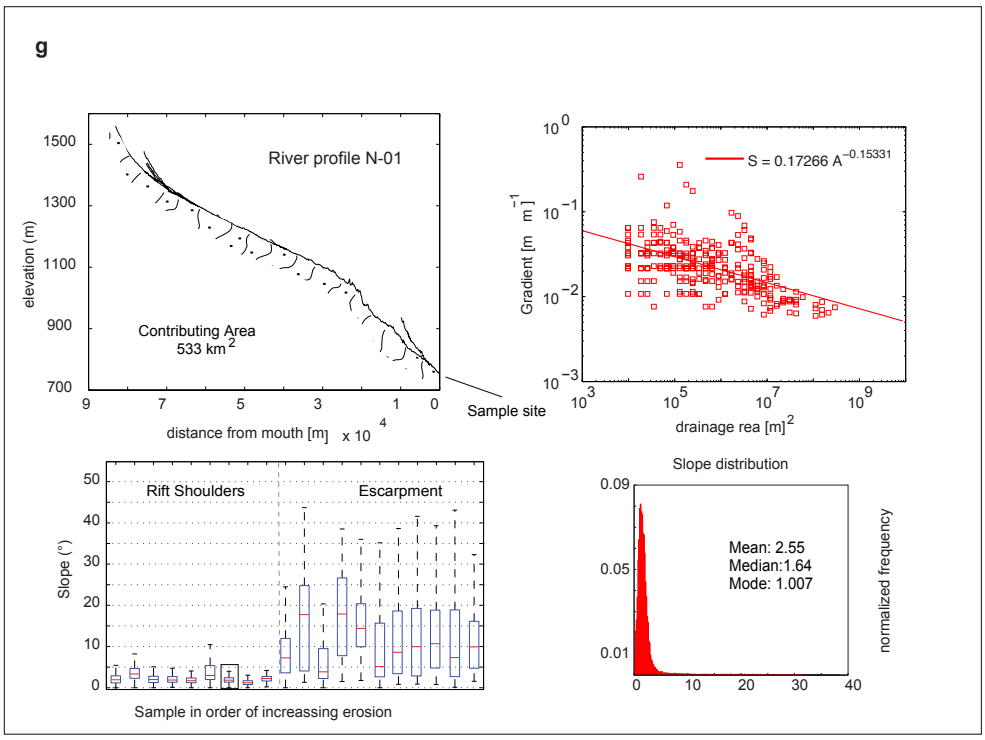
g
River profile N-01
elevation (m)
Contributing Area
533 km 2
distance from mouth [m] x 10 4
Sample site
S = 0.17266 A −0.15331
Gradient [m m −1]
drainage rea [m]2
Rift Shoulders
Escarpment
Slope (°)
Sample in order of increassing erosion
Slope distribution
Mean: 2.55
Median:1.64
Mode: 1.007
normalized frequency

N-02

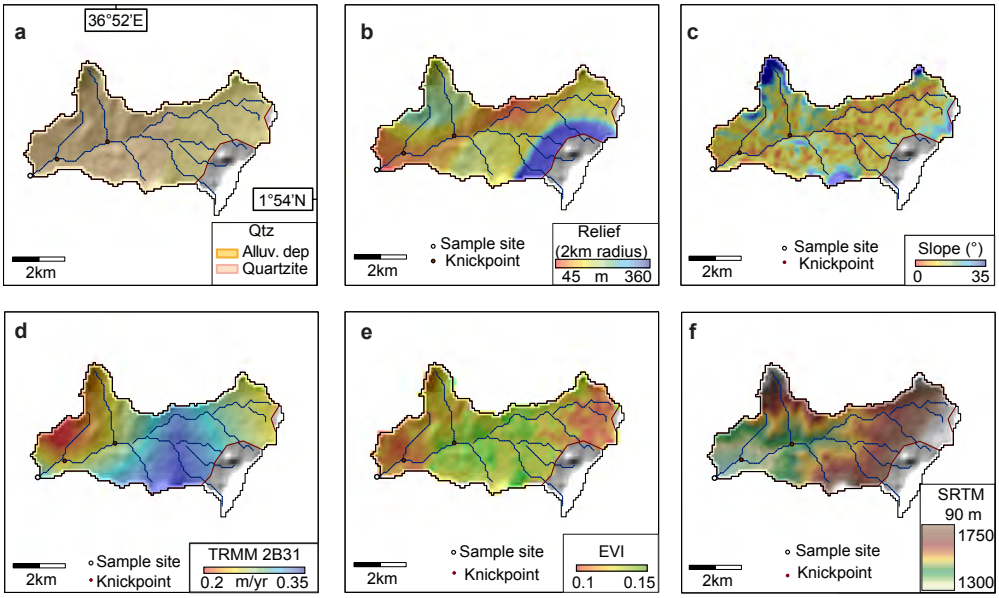
a
36°52'E
1°54'N
Qtz
Alluv. dep
Quartzite
2km
b
Sample site
Knickpoint
Relief
(2km radius)
45 m 360
2km
c
Sample site
Knickpoint
Slope (°)
0 35
2km
d
Sample site
Knickpoint
TRMM 2B31
0.2 m/yr 0.35
2km
e
Sample site
Knickpoint
EVI
0.1 0.15
2km
f
Sample site
Knickpoint
SRTM
90 m
1750
1300
2km

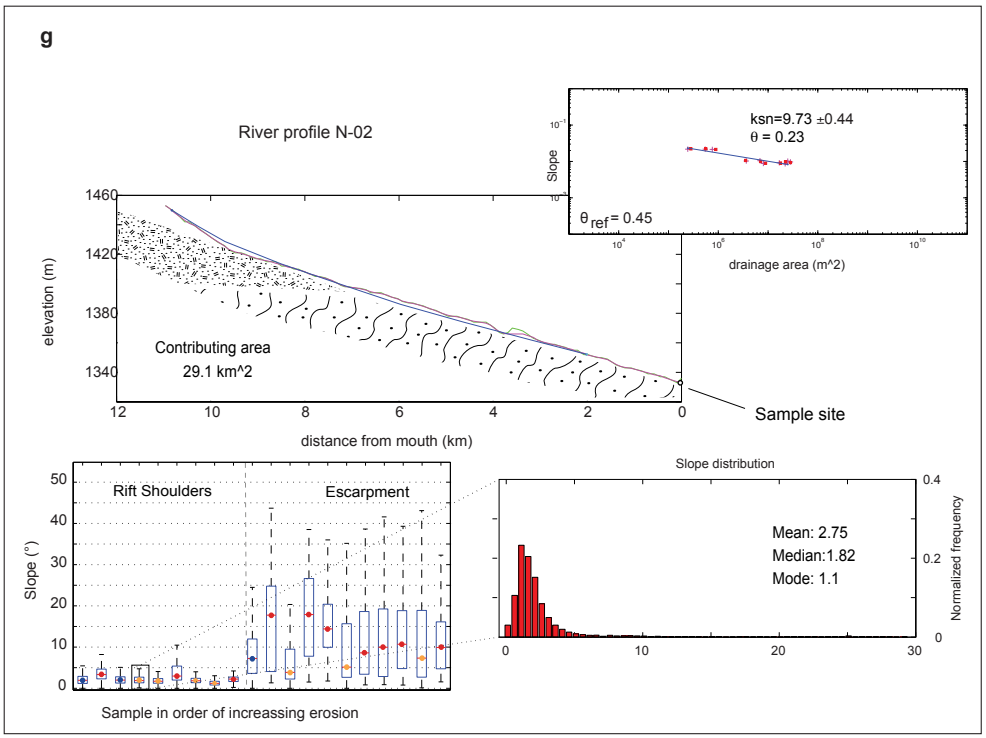
g
River profile N-02
ksn=9.73 ±0.44
θ = 0.23
θ ref = 0.45
Slope
drainage area (m^2)
elevation (m)
Contributing area
29.1 km^2
Sample site
distance from mouth (km)
Rift Shoulders
Escarpment
Slope (°)
Sample in order of increassing erosion
Slope distribution
Mean: 2.75
Median:1.82
Mode: 1.1
Normalized frequency

N-03

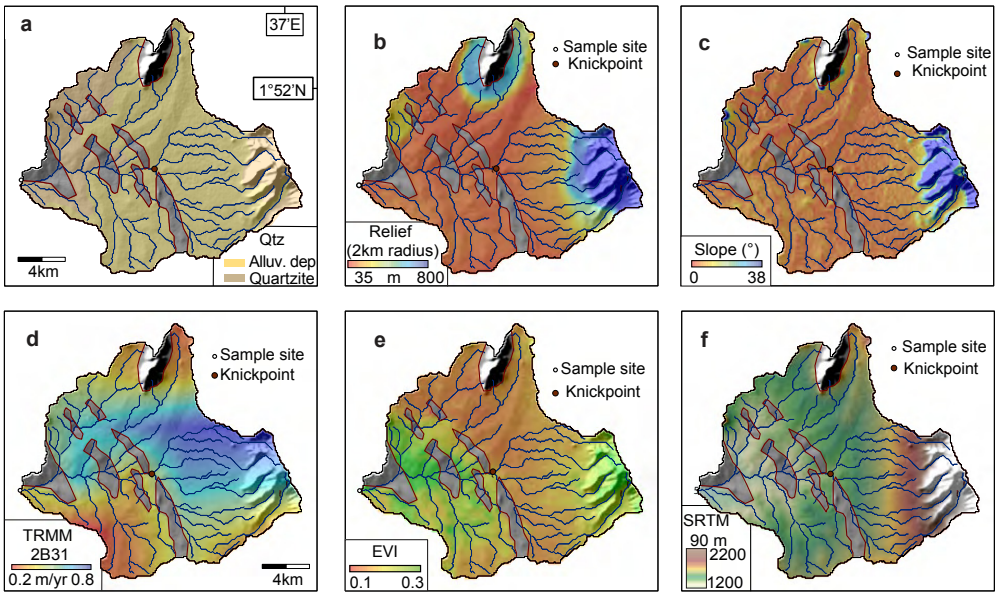
a
37°E
1°52'N
4km
Qtz
Alluv. dep
Quartzite
b
Sample site
Knickpoint
Relief
(2km radius)
35 m 800
c
Sample site
Knickpoint
Slope (°)
0 38
d
Sample site
Knickpoint
TRMM
2B31
0.2 m/yr 0.8
4km
e
Sample site
Knickpoint
EVI
0.1 0.3
f
Sample site
Knickpoint
SRTM
90 m
2200
1200

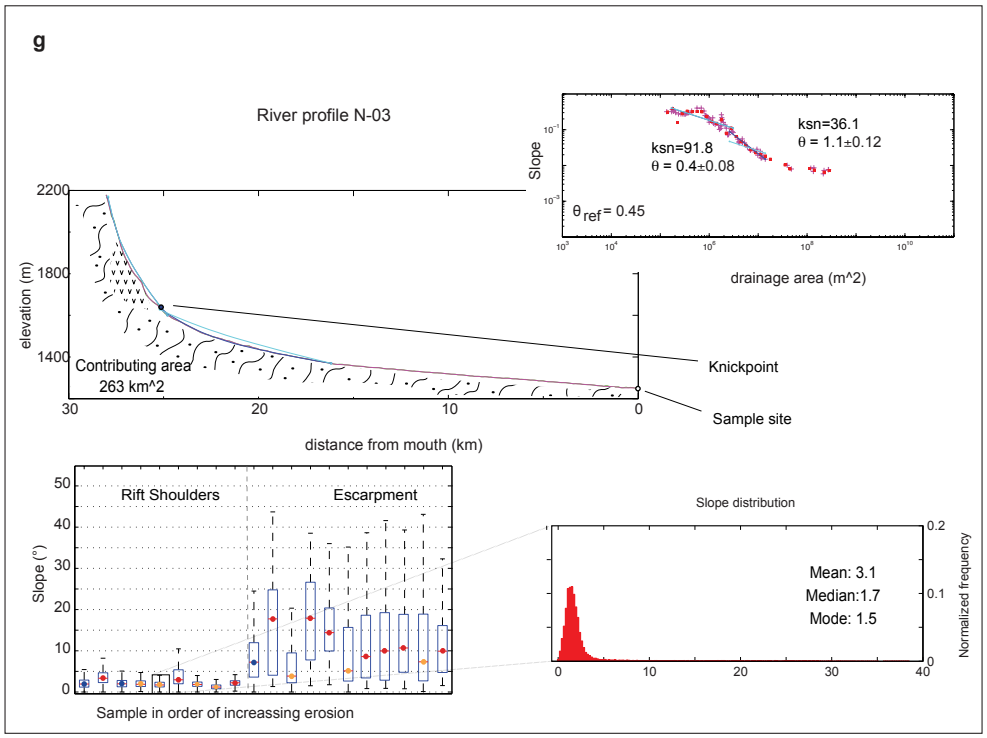
g
River profile N-03
ksn=91.8
θ = 0.4±0.08
ksn=36.1
θ = 1.1±0.12
θ ref = 0.45
Slope
drainage area (m^2)
elevation (m)
2200
1800
1400
Contributing area
263 km^2
Knickpoint
Sample site
30
20
10
0
distance from mouth (km)
Rift Shoulders
Escarpment
Slope (°)
50
40
30
20
10
0
Sample in order of increassing erosion
Slope distribution
Mean: 3.1
Median:1.7
Mode: 1.5
Normalized frequency
0.2
0.1
0
0
10
20
30
40

N-04

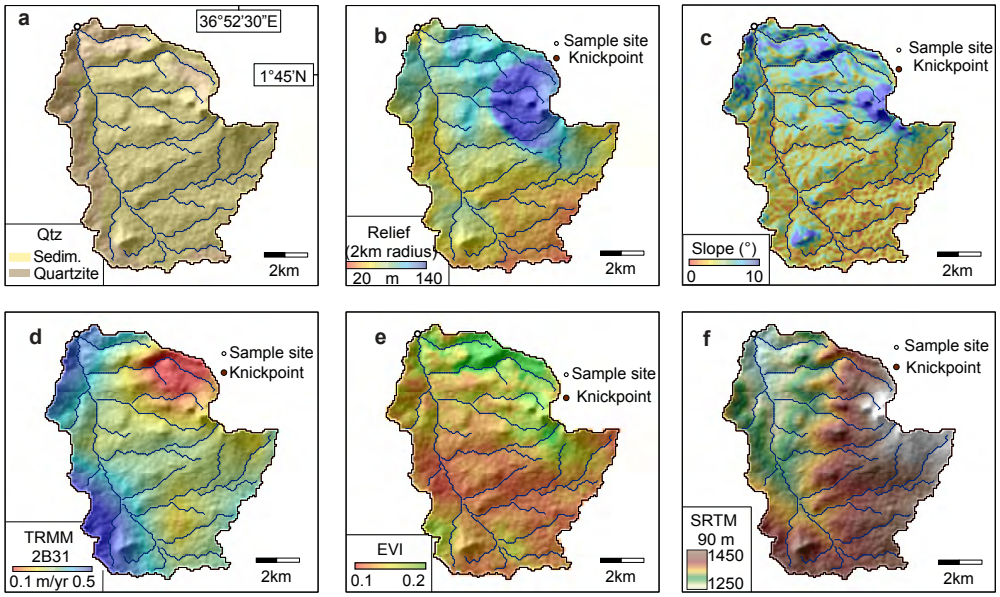
a
36°52'30"E
1°45'N
Qtz
Sedim.
Quartzite
2km
b
Sample site
Knickpoint
Relief
(2km radius)
20 m 140
2km
c
Sample site
Knickpoint
Slope (°)
0 10
2km
d
Sample site
Knickpoint
TRMM
2B31
0.1 m/yr 0.5
2km
e
Sample site
Knickpoint
EVI
0.1 0.2
2km
f
Sample site
Knickpoint
SRTM
90 m
1450
1250
2km

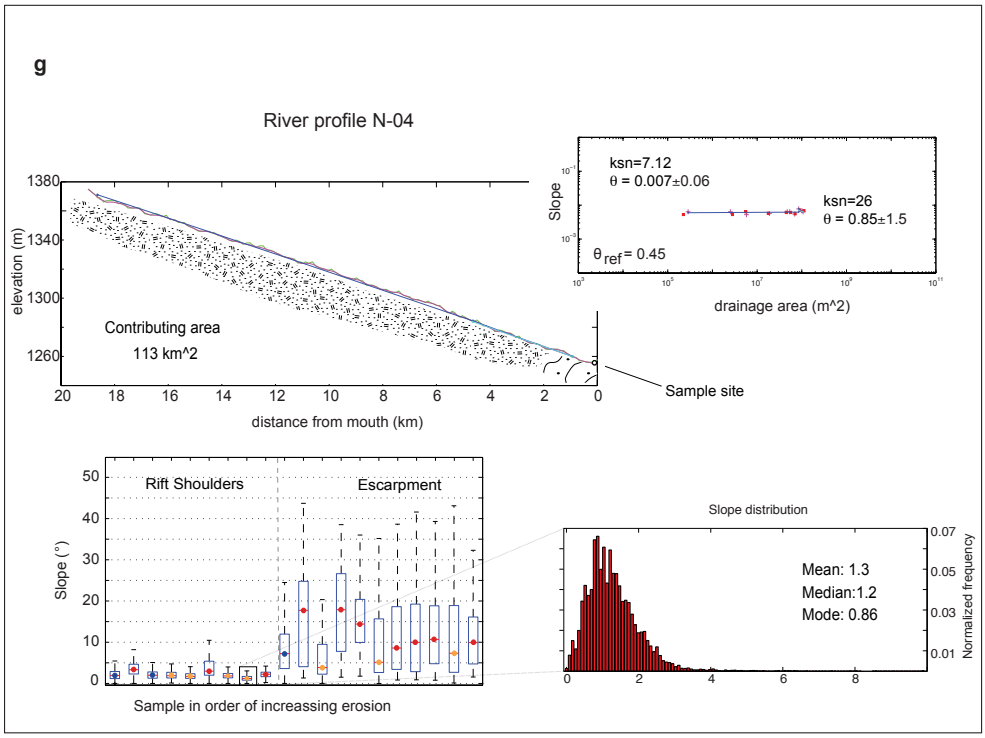
g
River profile N-04
elevation (m)
1380
1340
1300
1260
20 18 16 14 12 10 8 6 4 2 0
distance from mouth (km)
Contributing area
113 km^2
Sample site
Slope
ksn=7.12
θ = 0.007±0.06
ksn=26
θ = 0.85±1.5
θ ref = 0.45
drainage area (m^2)
Slope (°)
Rift Shoulders
Escarpment
Sample in order of increassing erosion
Slope distribution
Mean: 1.3
Median:1.2
Mode: 0.86
Normalized frequency

N-05

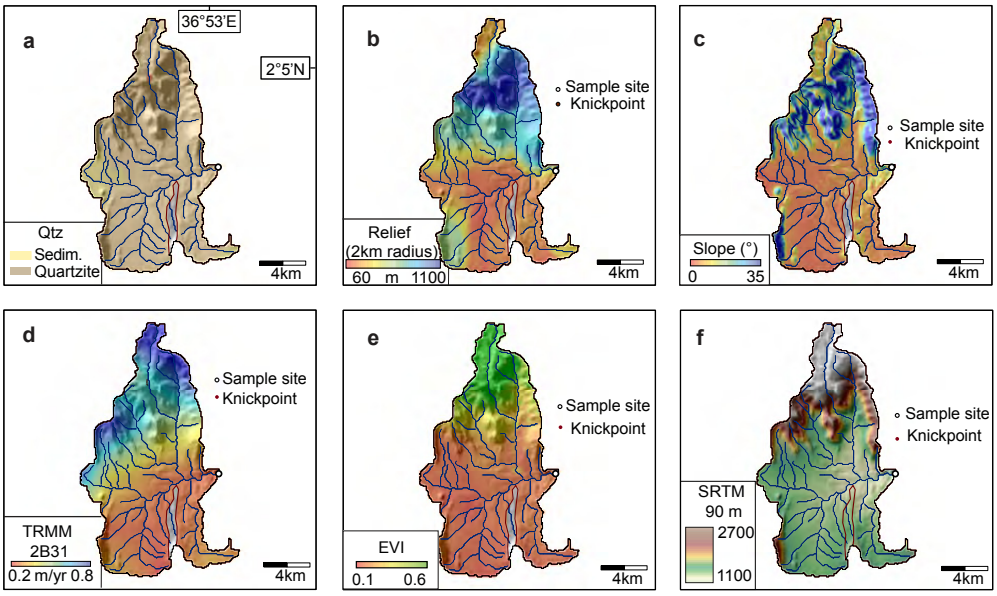
a
36°53'E
2°5'N
Qtz
Sedim.
Quartzite
4km
b
Sample site
Knickpoint
Relief
(2km radius)
60 m 1100
4km
c
Sample site
Knickpoint
Slope (°)
0 35
4km
d
Sample site
Knickpoint
TRMM
2B31
0.2 m/yr 0.8
4km
e
Sample site
Knickpoint
EVI
0.1 0.6
4km
f
Sample site
Knickpoint
SRTM
90 m
2700
1100
4km

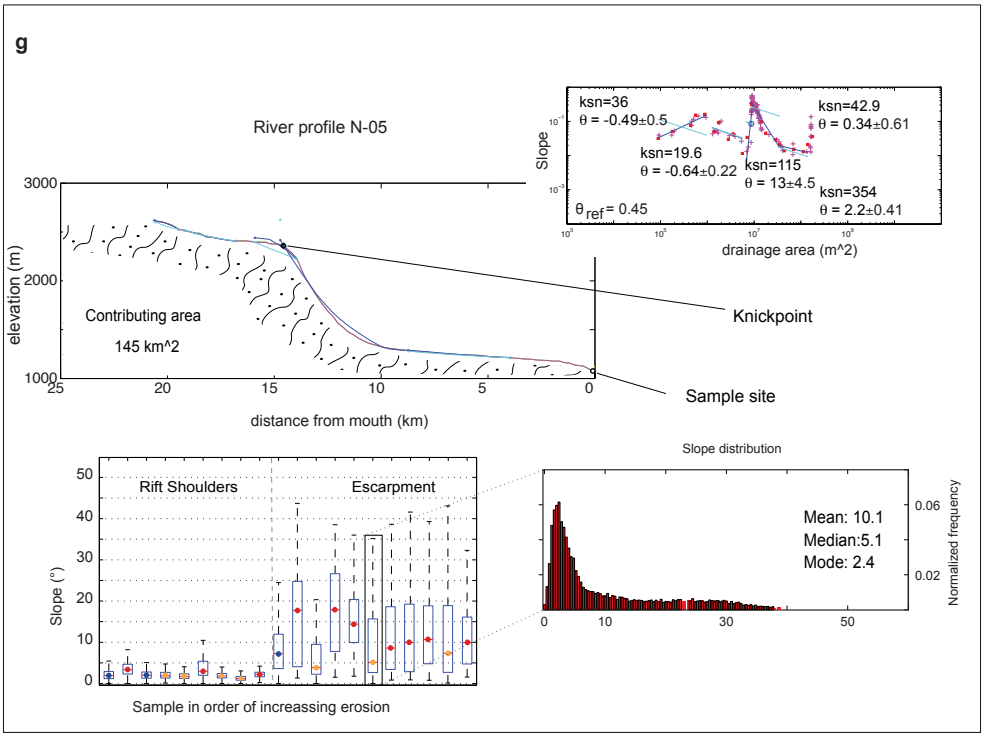
g
River profile N-05
ksn=36
θ = -0.49±0.5
ksn=19.6
θ = -0.64±0.22
ksn=115
θ = 13±4.5
ksn=42.9
θ = 0.34±0.61
ksn=354
θ = 2.2±0.41
θ ref = 0.45
Slope
drainage area (m^2)
elevation (m)
Contributing area
145 km^2
Knickpoint
Sample site
distance from mouth (km)
Rift Shoulders
Escarpment
Slope (°)
Sample in order of increassing erosion
Slope distribution
Mean: 10.1
Median:5.1
Mode: 2.4
Normalized frequency

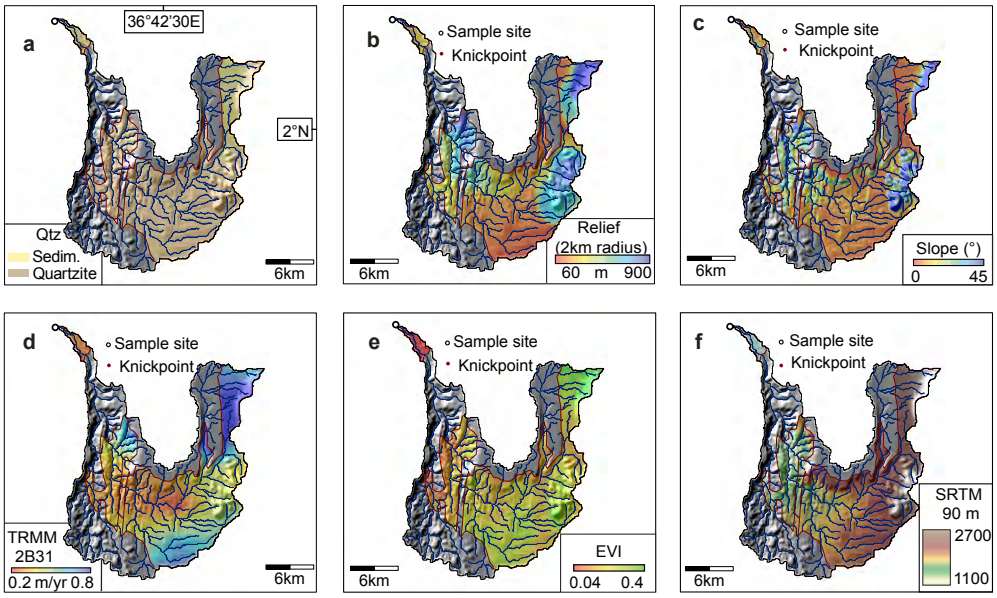
a
36°42'30E
2°N
Qtz
Sedim.
Quartzite
6km
b
Sample site
Knickpoint
Relief
(2km radius)
60 m 900
6km
c
Sample site
Knickpoint
Slope (°)
0 45
6km
d
Sample site
Knickpoint
TRMM
2B31
0.2 m/yr 0.8
6km
e
Sample site
Knickpoint
EVI
0.04 0.4
6km
f
Sample site
Knickpoint
SRTM
90 m
2700
1100
6km

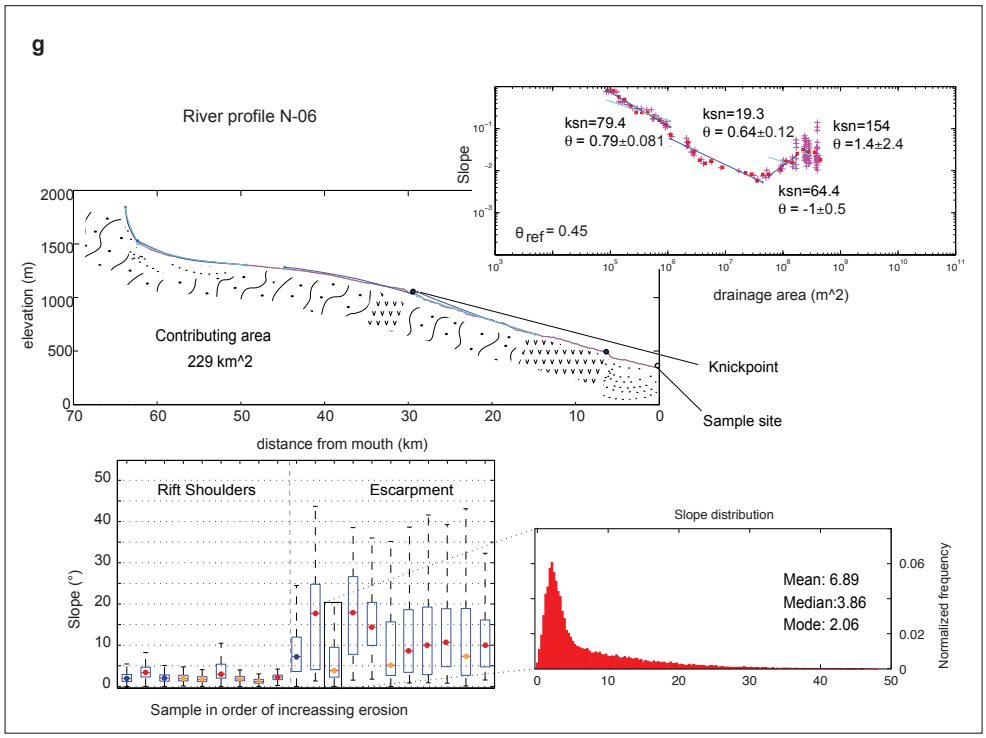
g
River profile N-06
elevation (m)
distance from mouth (km)
Contributing area
229 km^2
Knickpoint
Sample site
Slope
drainage area (m^2)
ksn=79.4
θ = 0.79±0.081
ksn=19.3
θ = 0.64±0.12
ksn=154
θ =1.4±2.4
ksn=64.4
θ = -1±0.5
θ ref = 0.45
Rift Shoulders
Escarpment
Slope (°)
Sample in order of increassing erosion
Slope distribution
Mean: 6.89
Median:3.86
Mode: 2.06
Normalized frequency

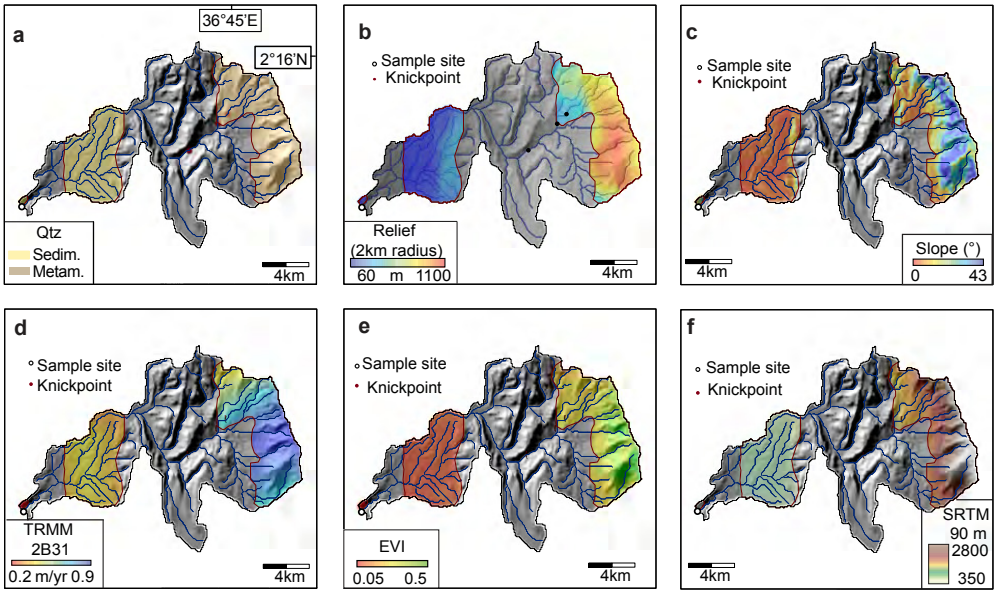
a
36°45'E
2°16'N
Qtz
Sedim.
Metam.
4km
b
Sample site
Knickpoint
Relief
(2km radius)
60 m 1100
4km
c
Sample site
Knickpoint
4km
Slope (°)
0 43
d
Sample site
Knickpoint
TRMM
2B31
0.2 m/yr 0.9
4km
e
Sample site
Knickpoint
EVI
0.05 0.5
4km
f
Sample site
Knickpoint
4km
SRTM
90 m
2800
350

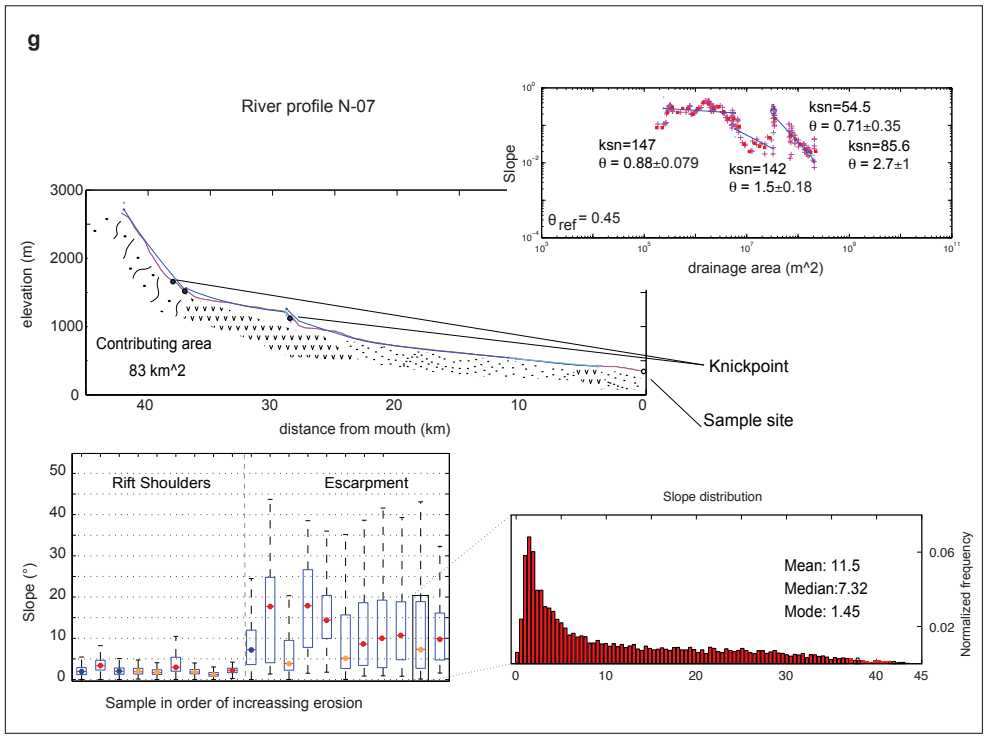
g
River profile N-07
elevation (m)
distance from mouth (km)
Contributing area
83 km^2
Knickpoint
Sample site
Slope
drainage area (m^2)
ksn=147
θ = 0.88±0.079
ksn=142
θ = 1.5±0.18
ksn=54.5
θ = 0.71±0.35
ksn=85.6
θ = 2.7±1
θ ref = 0.45
Rift Shoulders
Escarpment
Slope (°)
Sample in order of increassing erosion
Slope distribution
Mean: 11.5
Median:7.32
Mode: 1.45
Normalized frequency

294

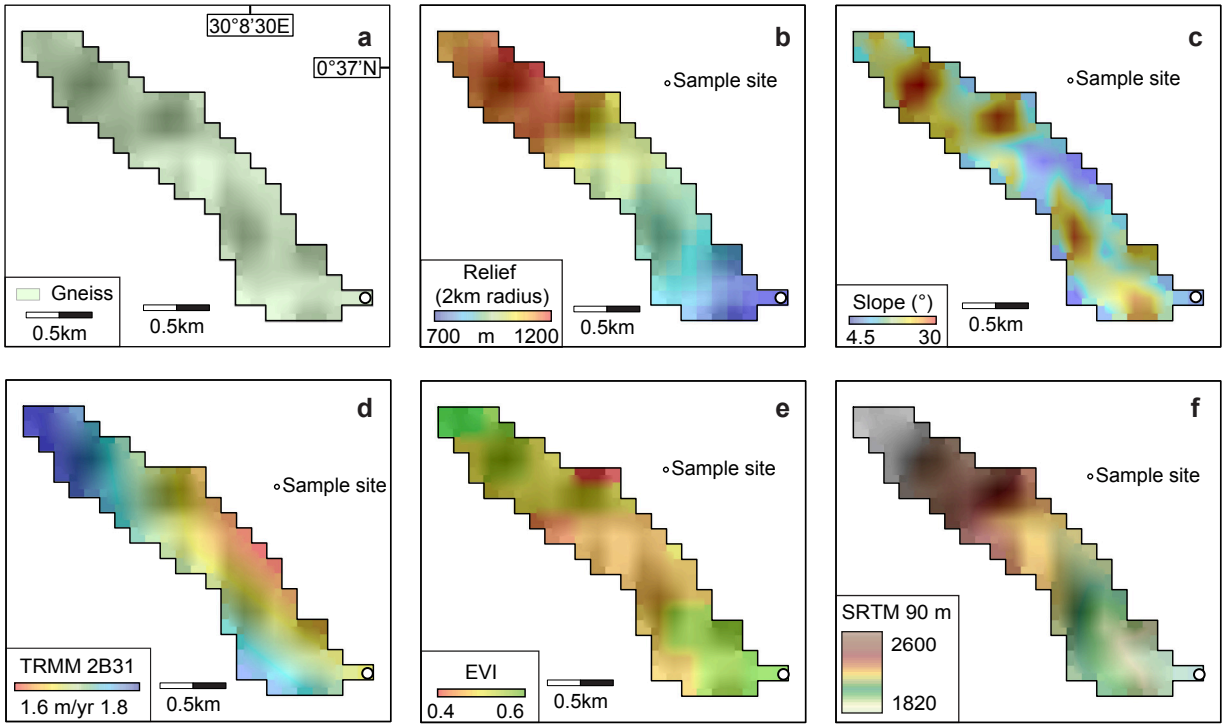

295

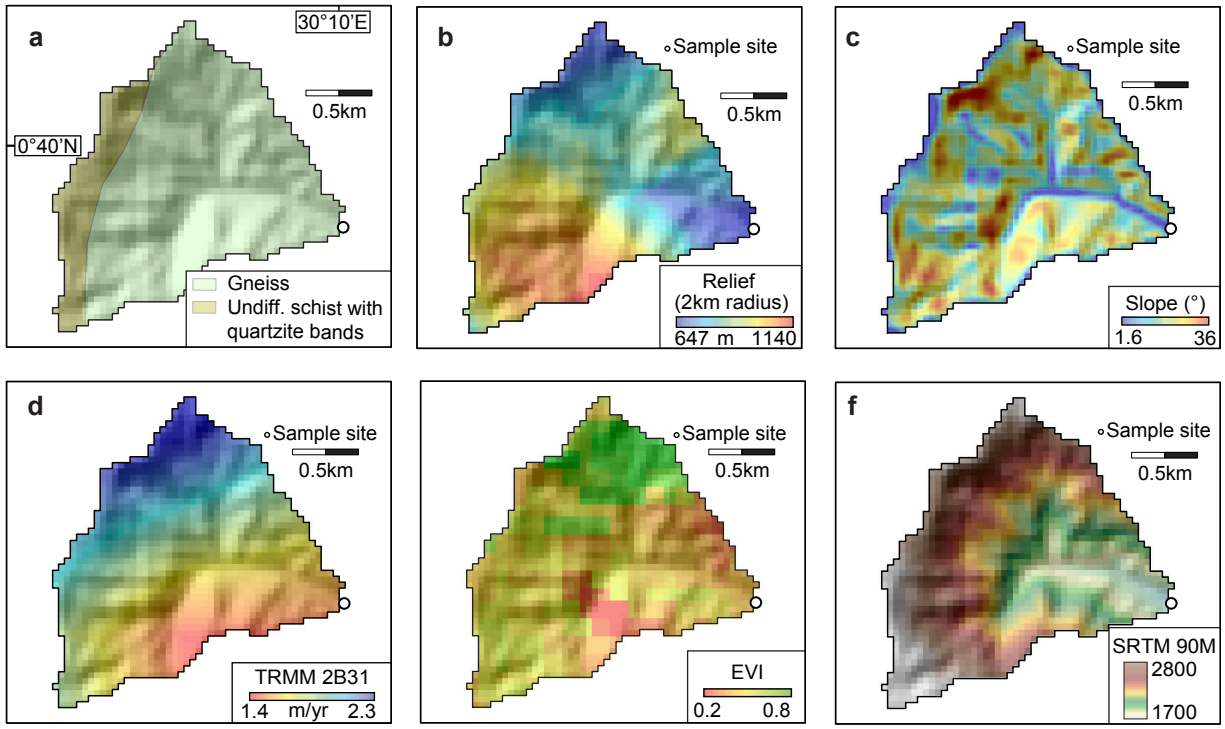

Figure B2. Catchment morphology for samples in the Rwenzori Mountains. For each catchment (294, 295, 300, 311, 316, 321, 337, 359, 375, 398, 399, 9, 28, 24, 538), we show (a) lithology, (b) relief, (c) median catchment slope, (d) mean annual precipitation, (e) vegetation cover based on Enhanced Vegetation Index (EVI), (f) elevation, based on 90-m resolution SRTM data.

300

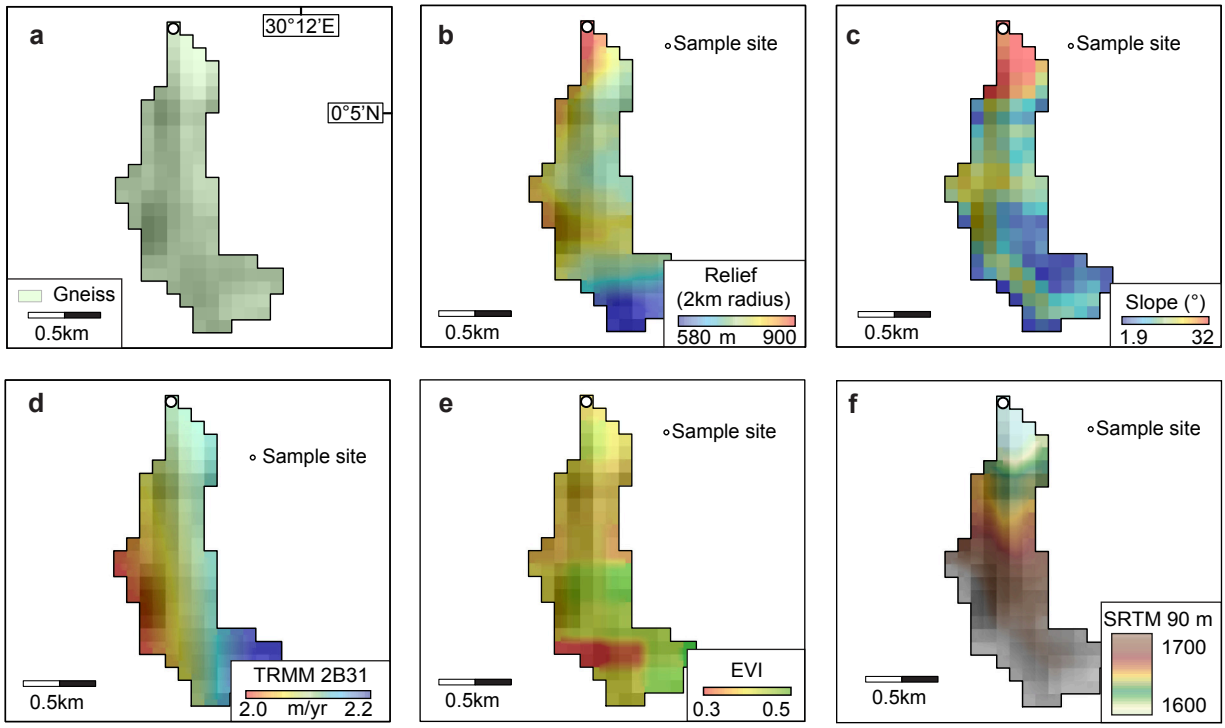
a
30°12'E
0°5'N
Gneiss
0.5km
b
Sample site
Relief
(2km radius)
580 m 900
0.5km
c
Sample site
Slope (°)
1.9 32
0.5km
d
Sample site
TRMM 2B31
2.0 m/yr 2.2
0.5km
e
Sample site
EVI
0.3 0.5
0.5km
f
Sample site
SRTM 90 m
1700
1600
0.5km

311

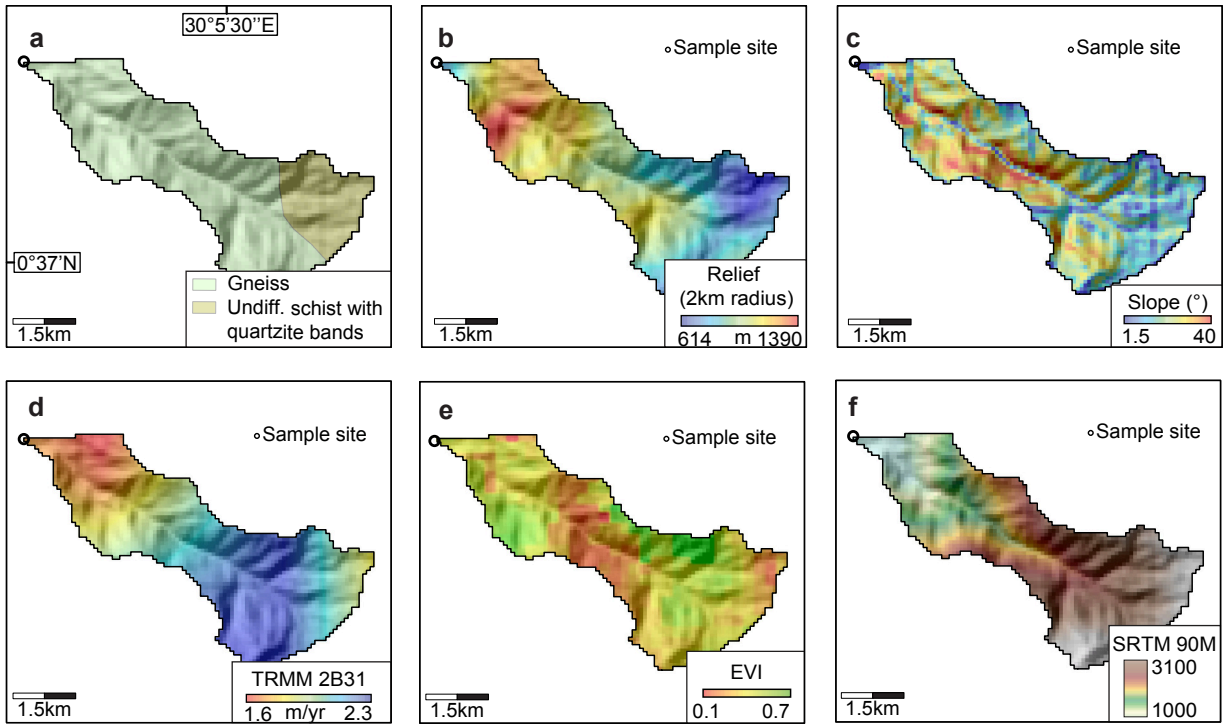
a
30°5'30"E
0°37'N
Gneiss
Undiff. schist with
quartzite bands
1.5km
b
Sample site
Relief
(2km radius)
614 m 1390
1.5km
c
Sample site
Slope (°)
1.5 40
1.5km
d
Sample site
TRMM 2B31
1.6 m/yr 2.3
1.5km
e
Sample site
EVI
0.1 0.7
1.5km
f
Sample site
SRTM 90M
3100
1000
1.5km

316

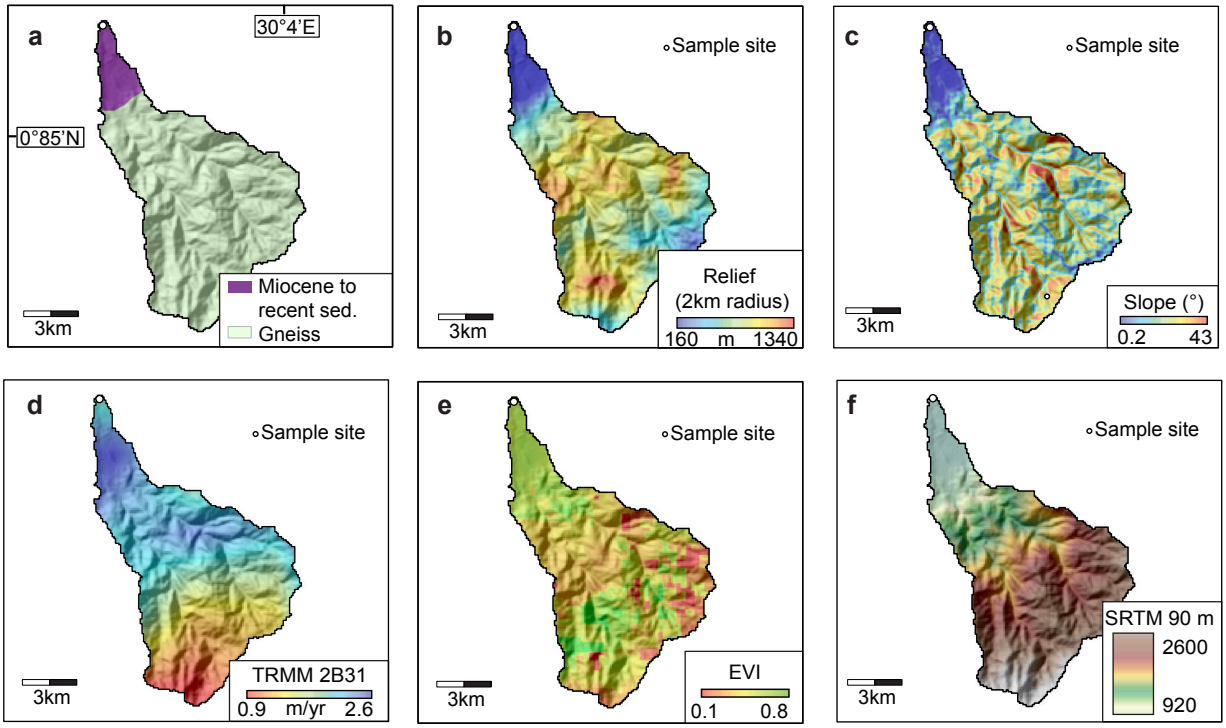
a
30°4'E
0°85'N
3km
Miocene to recent sed.
Gneiss
b
Sample site
3km
Relief (2km radius)
160 m 1340
c
Sample site
3km
Slope (°)
0.2 43
d
Sample site
3km
TRMM 2B31
0.9 m/yr 2.6
e
Sample site
3km
EVI
0.1 0.8
f
Sample site
3km
SRTM 90 m
2600
920

321

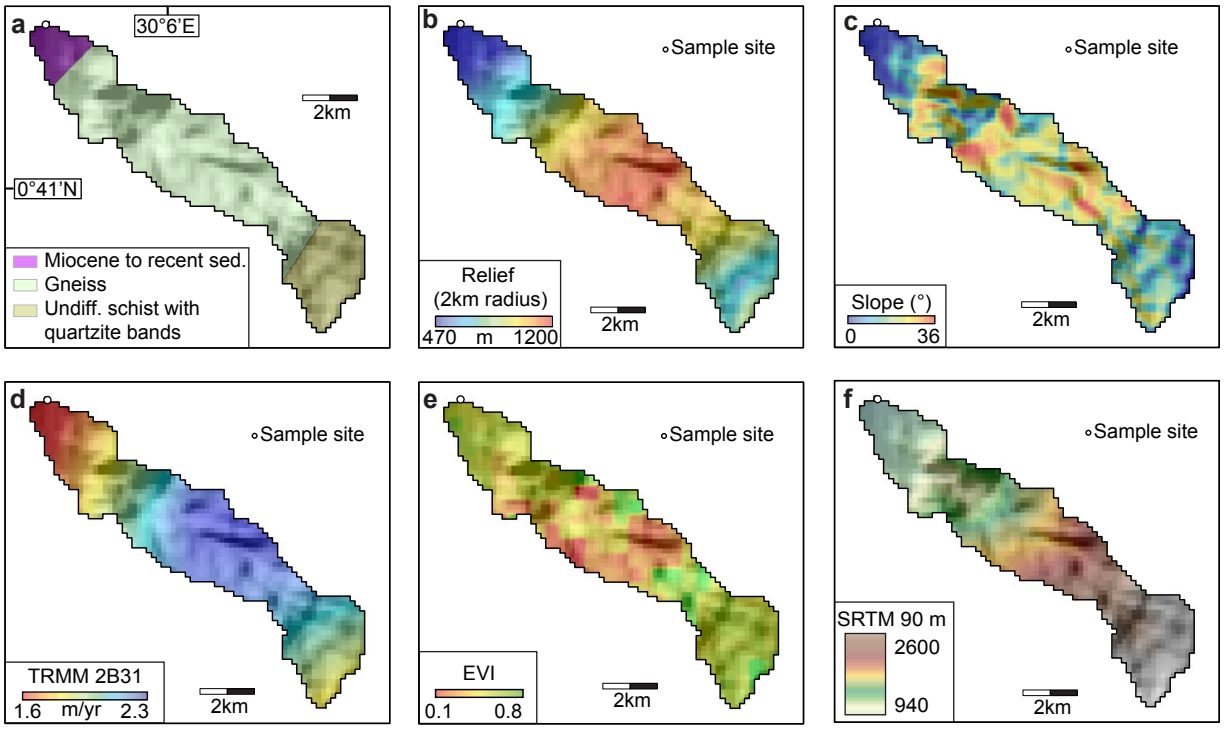
a
30°6'E
2km
0°41'N
Miocene to recent sed.
Gneiss
Undiff. schist with quartzite bands
b
Sample site
Relief (2km radius)
470 m 1200
2km
c
Sample site
Slope (°)
0 36
2km
d
Sample site
TRMM 2B31
1.6 m/yr 2.3
2km
e
Sample site
EVI
0.1 0.8
2km
f
Sample site
SRTM 90 m
2600
940
2km

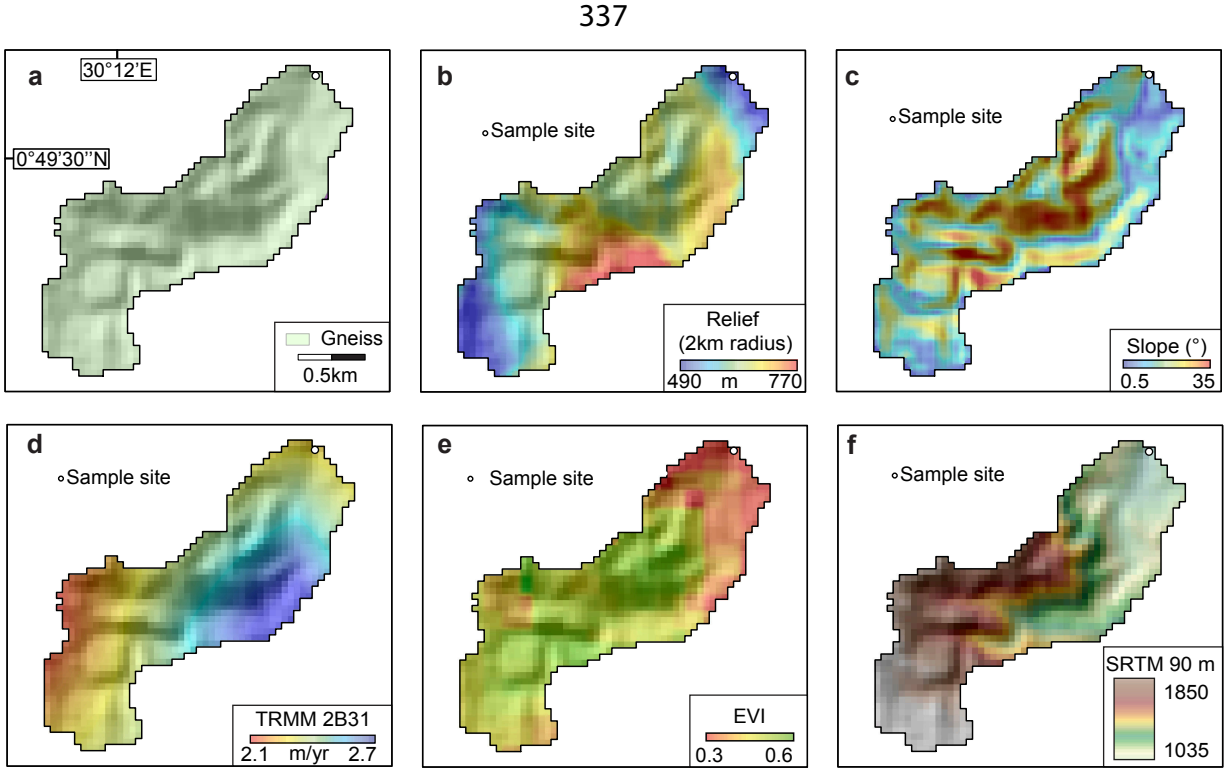
337
a
30°12'E
0°49'30"N
Gneiss
0.5km
b
Sample site
Relief
(2km radius)
490 m 770
c
Sample site
Slope (°)
0.5 35
d
Sample site
TRMM 2B31
2.1 m/yr 2.7
e
Sample site
EVI
0.3 0.6
f
Sample site
SRTM 90 m
1850
1035

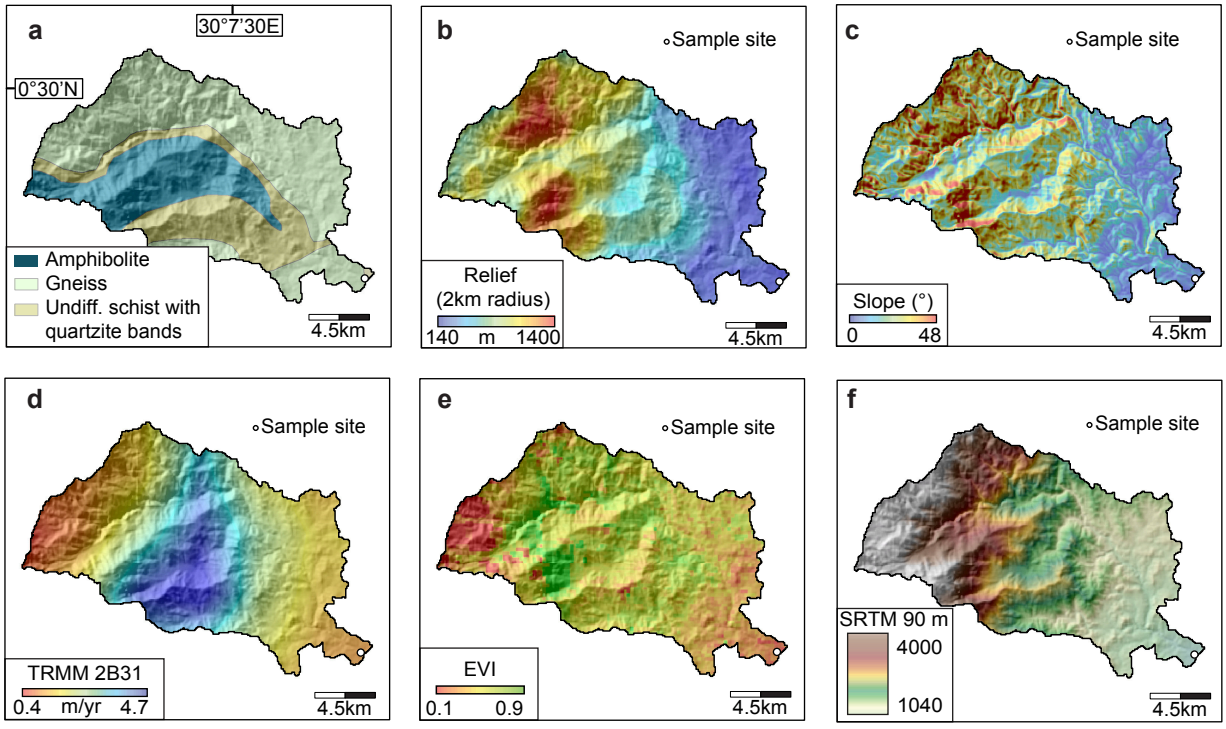
359
a
30°7'30E
0°30'N
Amphibolite
Gneiss
Undiff. schist with
quartzite bands
4.5km
b
Sample site
Relief
(2km radius)
140 m 1400
4.5km
c
Sample site
Slope (°)
0 48
4.5km
d
Sample site
TRMM 2B31
0.4 m/yr 4.7
4.5km
e
Sample site
EVI
0.1 0.9
4.5km
f
Sample site
SRTM 90 m
4000
1040
4.5km

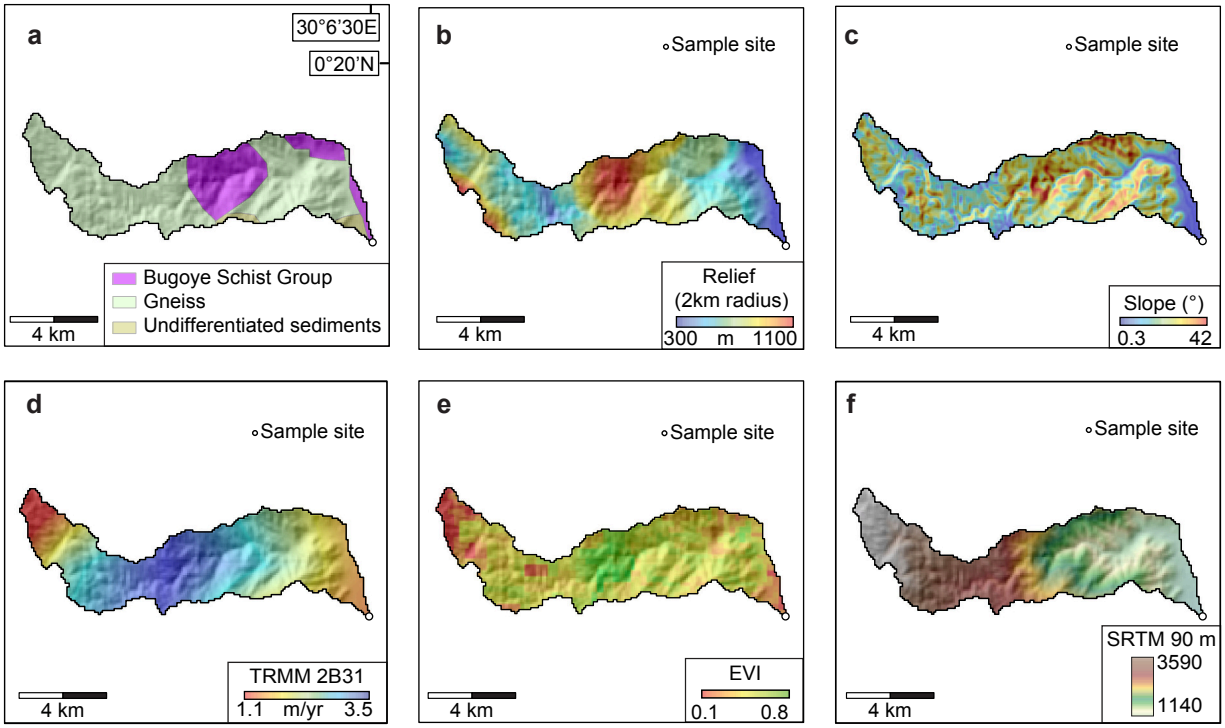
a
30°6'30E
0°20'N
Bugoye Schist Group
Gneiss
Undifferentiated sediments
4 km
b
Sample site
Relief
(2km radius)
300 m 1100
4 km
c
Sample site
Slope (°)
0.3 42
4 km
d
Sample site
TRMM 2B31
1.1 m/yr 3.5
4 km
e
Sample site
EVI
0.1 0.8
4 km
f
Sample site
SRTM 90 m
3590
1140
4 km

375

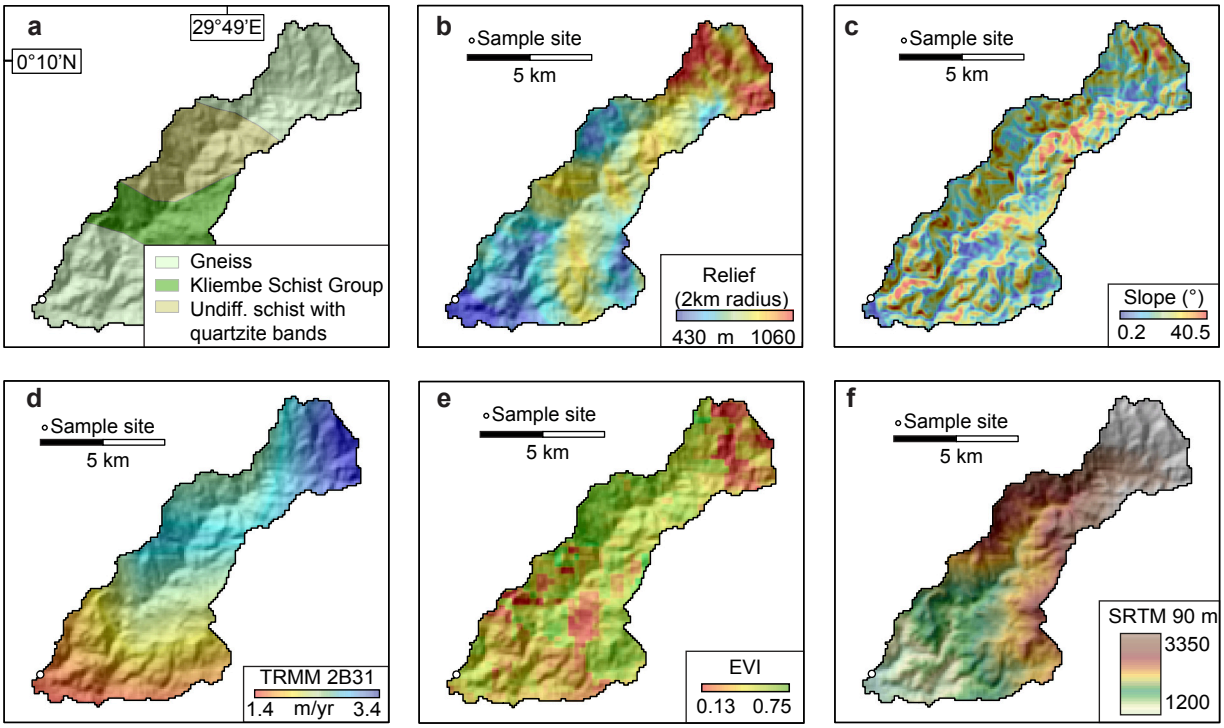
a
29°49'E
0°10'N
Gneiss
Kliembe Schist Group
Undiff. schist with
quartzite bands
b
Sample site
5 km
Relief
(2km radius)
430 m 1060
c
Sample site
5 km
Slope (°)
0.2 40.5
d
Sample site
5 km
TRMM 2B31
1.4 m/yr 3.4
e
Sample site
5 km
EVI
0.13 0.75
f
Sample site
5 km
SRTM 90 m
3350
1200

398

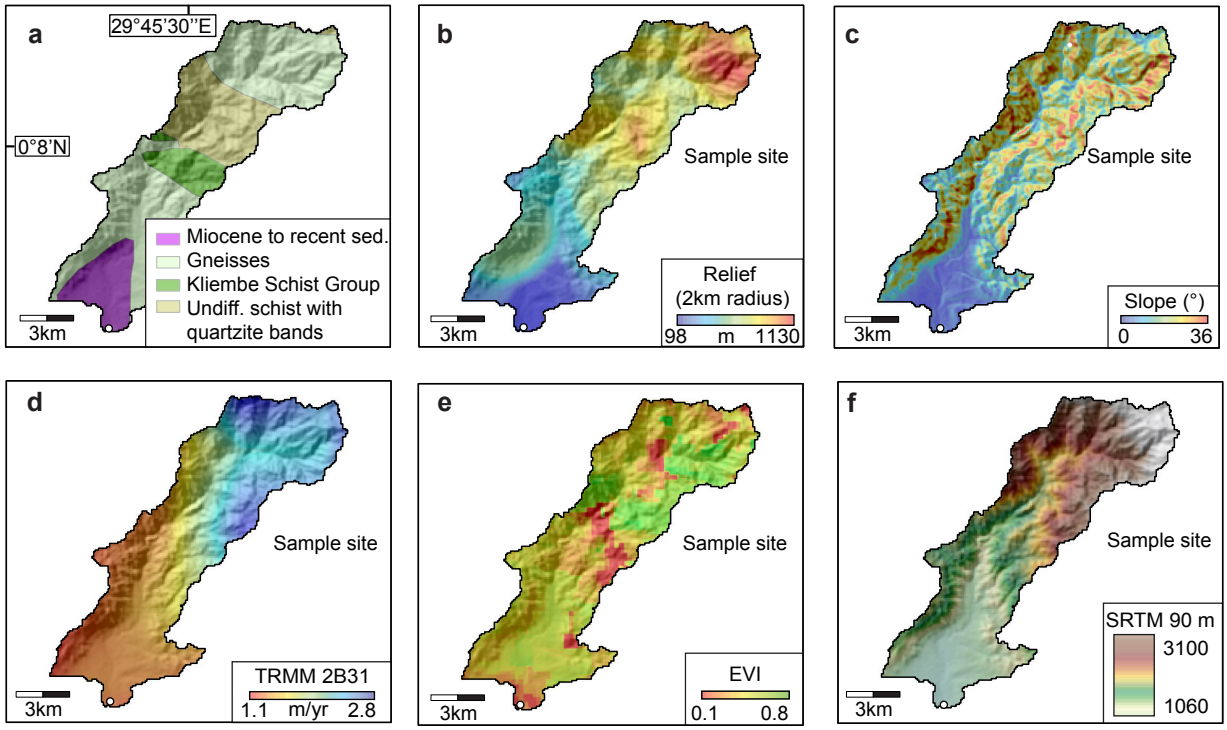
a
29°45'30''E
0°8'N
Miocene to recent sed.
Gneisses
Kliembe Schist Group
Undiff. schist with quartzite bands
3km
b
Sample site
Relief (2km radius)
98 m 1130
3km
c
Sample site
Slope (°)
0 36
3km
d
Sample site
TRMM 2B31
1.1 m/yr 2.8
3km
e
Sample site
EVI
0.1 0.8
3km
f
Sample site
SRTM 90 m
3100
1060
3km

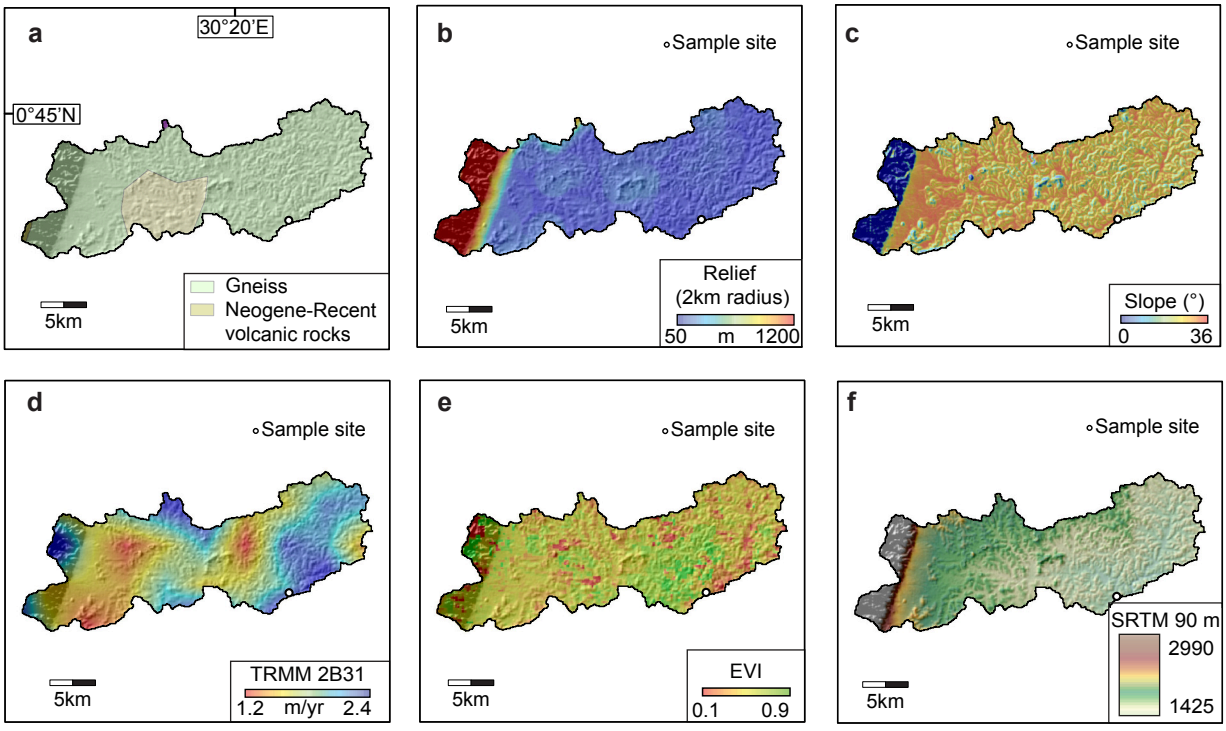
a
30°20'E
0°45'N
Gneiss
Neogene-Recent volcanic rocks
5km
b
Sample site
Relief (2km radius)
50 m 1200
5km
c
Sample site
Slope (°)
0 36
5km
d
Sample site
TRMM 2B31
1.2 m/yr 2.4
5km
e
Sample site
EVI
0.1 0.9
5km
f
Sample site
SRTM 90 m
2990
1425
5km

28

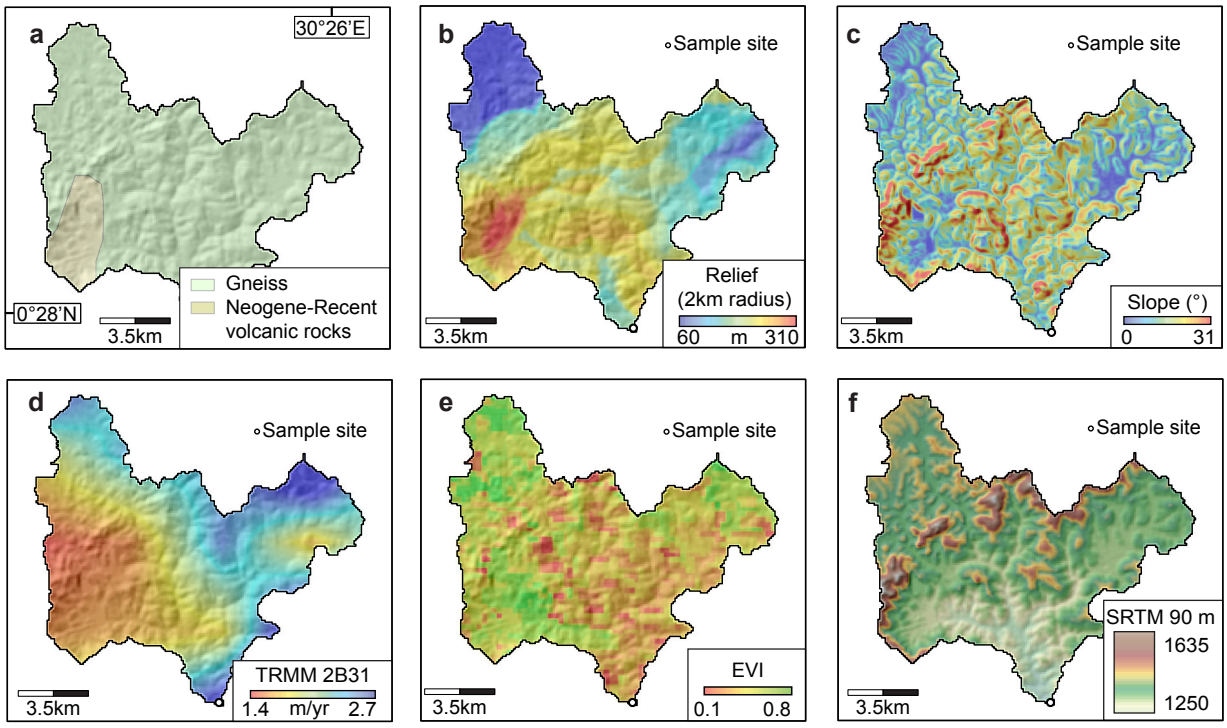
a
30°26'E
0°28'N
3.5km
Gneiss
Neogene-Recent volcanic rocks
b
Sample site
Relief (2km radius)
60 m 310
3.5km
c
Sample site
Slope (°)
0 31
3.5km
d
Sample site
TRMM 2B31
1.4 m/yr 2.7
3.5km
e
Sample site
EVI
0.1 0.8
3.5km
f
Sample site
SRTM 90 m
1635
1250
3.5km

24

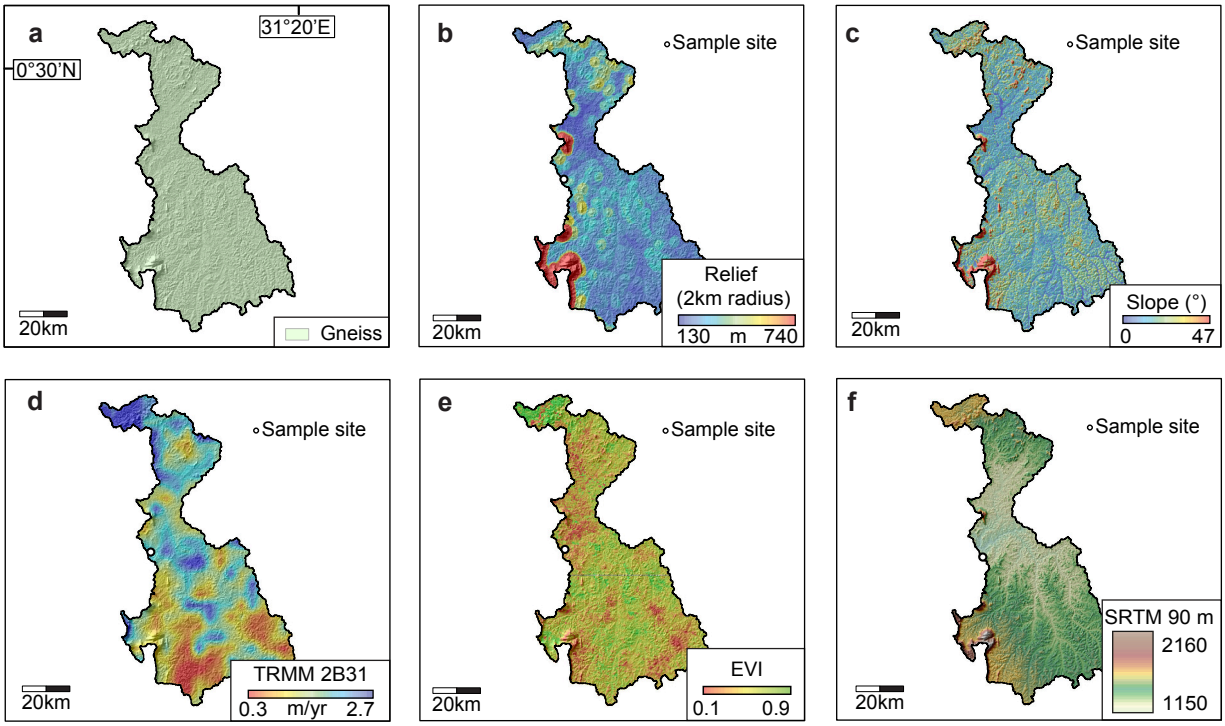
a
31°20'E
0°30'N
20km
Gneiss
b
Sample site
Relief (2km radius)
130 m 740
20km
c
Sample site
Slope (°)
0 47
20km
d
Sample site
TRMM 2B31
0.3 m/yr 2.7
20km
e
Sample site
EVI
0.1 0.9
20km
f
Sample site
SRTM 90 m
2160
1150
20km

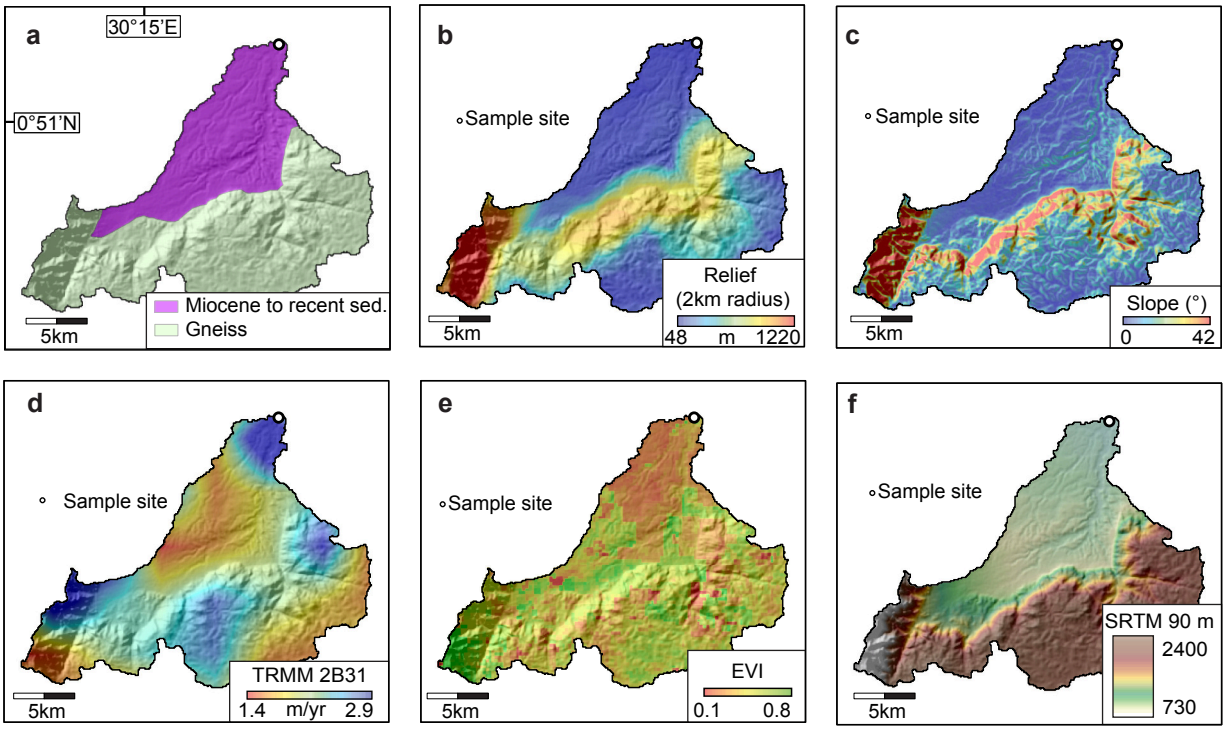
a
30°15'E
0°51'N
Miocene to recent sed.
Gneiss
5km
b
Sample site
Relief
(2km radius)
48 m 1220
5km
c
Sample site
Slope (°)
0 42
5km
d
Sample site
TRMM 2B31
1.4 m/yr 2.9
5km
e
Sample site
EVI
0.1 0.8
5km
f
Sample site
SRTM 90 m
2400
730
5km

Appendix C

Additional data chapter 4

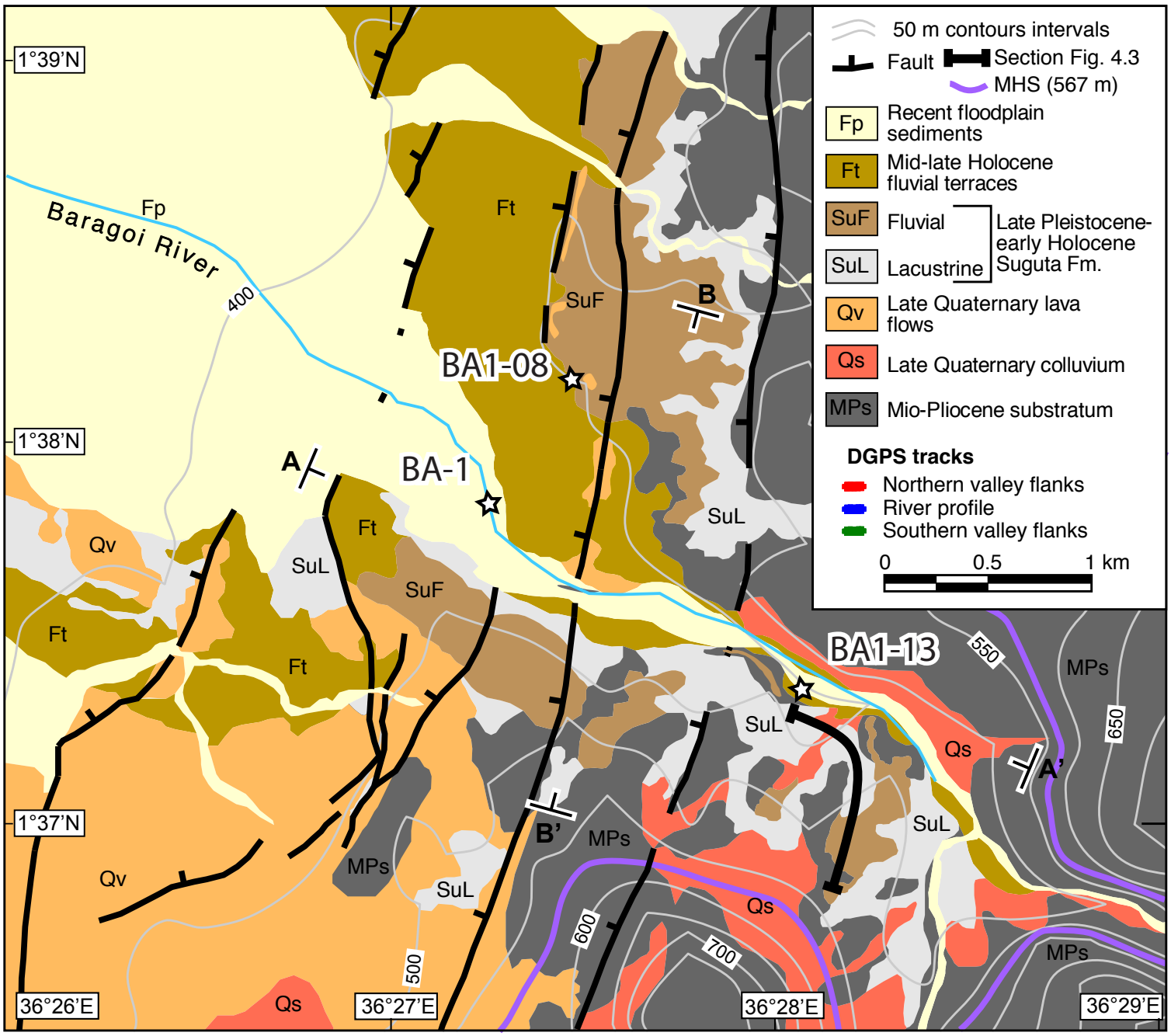
50 m contours intervals
Fault
Section Fig. 4.3
MHS (567 m)
Fp Recent floodplain sediments
Ft Mid-late Holocene fluvial terraces
SuF Fluvial
SuL Lacustrine
Late Pleistocene-early Holocene Suguta Fm.
Qv Late Quaternary lava flows
Qs Late Quaternary colluvium
MPs Mio-Pliocene substratum
DGPS tracks
Northern valley flanks
River profile
Southern valley flanks
0 0.5 1 km
1°39'N
1°38'N
1°37'N
36°26'E
36°27'E
36°28'E
36°29'E
Baragoi River
BA1-08
BA-1
BA1-13
A
A'
B
B'
400
500
550
600
650
700

Appendix D

Additional data chapter 5

Table D1. Apatite fission track full data

Sample	N Latitude (deg.)	E.Longitude (deg)	Elev. (m)	Age/Lith.	Xls[a]	Rho-S[b] x10^6	NS[c]	Rho-I[b] x10^5	NI[c]	P(χ^2)[d] %	RhoD[e] x10^6	ND[f]	Age (Ma)	±1σ	Dpar[g] mean	Dpar SD	# lengths[h]	Length (μm)	Length SD (μm)	Analyst[i]
Talas range																				
10TR02	42.163250	72.040472	2571	Pt/Ss	20	1.919	57	1.71	640	100	1.337	5231	22	3.1	2	0.15	104*	13.6	1.5	AB
10TR03	42.138222	72.040528	2678	Pt/Ss	20	1.37	122	1.291	1294	57	1.321	5231	23	2.3	2.05	0.18	2	15.4	0.4	AB
10TR04	42.108528	72.042611	3120	Pt/Ss	20	0.776	85	0.8	825	56	1.317	5231	25.4	2.9	1.98	0.18	5*	10.6	2.1	AB
10TR05	42.121972	72.037083	2921	Pt/Ss	20	1.242	72	1.345	665	97	1.258	5231	25.1	3.1	1.95	0.22	71*	11.7	2.1	AB
10TR17	42.458889	71.533806	1269	Pt/Ss	19	1.188	91	1.265	855	91	1.284	7234	25.2	2.80	1.92	0.26	13*	13.645	1.7	AB
Ugam Range																				
10UM12	42.233083	71.406694	3.456	C/Granite	18	3.275	438	7.042	2037	85	1.301	5674	51.5	2.8	2	0.16	101	12.8	1.5	AB
10UM14	42.240139	71.409833	2.082	C/Schist	7	3.127	87	3.598	756	50	1.286	5674	27.5	3.2	3	0.19	15	12.9	1.4	AB
10UM15	42.241528	71.413306	2.945	C/Granite	17	1.304	115	2.095	716	82	1.27	5674	37.6	3.8	2	0.26	9	12.2	1.5	AB
10CA26	41.886778	70.852194	3.161	C/Granite	8	1.406	103	2.546	569	83	1.228	5231	40.9	4.4	2	0.21	7	12.0	1.9	AB
10CA27	41.881278	70.853806	2.953	C/Granite	21	1.963	260	3.815	1338	84	1.218	5231	43.6	3	2	0.17	101*	11.8	1.9	AB
10CA29	41.874861	70.862750	2.535	C/Granite	19	2.433	197	3.286	1459	40	1.208	5231	30.1	2.3	2	0.15	106	11.5	1.8	AB
Shandalash Range																				
10TR19	42.199194	71.585583	2978	C/Granite	19	3.469	185	4.293	1495	68	1.307	5231	29.8	2.4	2	0.19	19	11.6	2.3	AB
10TR20	42.185528	71.574194	2815	C/Granite	20	0.599	70	0.686	611	97	1.297	5231	27.4	3.5	2.05	0.17	13*	11.8	2.0	AB
10TR21	42.183722	71.569722	2778	Є/Tillite	20	3.266	266	3.368	2579	97	1.287	5231	24.5	2.6	2.17	0.19	49	12.2	2.4	AB
10TR22	42.128722	71.557611	2458	Є/Tillite	19	1.27	135	1.389	1234	8	1.278	5231	26.4	2.9	2.82	0.47	28*	11.6	2.6	AB
10TR23	42.119528	71.546611	2.713	Dev/Ss	17	1.75	53	0.824	1126	96	1.268	5231	11	1.6	2	0.21	4	13.0	2.4	AB
Chatkal Range																				
10CK34	41.574028	70.699361	1.763	C/Granite	20	1.783	865	9.479	1627	5	1.298	7234	124.3	6.6	2.07	0.21	101*	12.8	1.5	AB
10CK37	41.496722	71.023611	1.762	C/Granite	20	1.288	249	2.932	1094	61	1.277	7234	53.6	3.8	2.11	0.19	56	12.1	1.9	AB
10CK41	41.437833	71.226806	1.369	Pz1/Gneiss	20	1.831	609	9.595	1162	35	1.248	5231	119.7	6.7	2.19	0.16	105*	11.7	1.9	AB
10CK43	41.584250	71.526972	1.874	Dev/Ss	16	1.081	108	2.372	492	100	1.264	7234	51	5.5	2.22	0.26	14*	12.5	1.7	AB
10CK44	41.565833	71.529167	1.695	Dev/Ss	20	1.326	241	3.751	852	65	1.238	5231	64.7	5	2.50	0.36	37*	12.2	2.1	AB
Fergana range																				
10SU67	41.530639	72.331833	0.922	Dev/Ss	7	0.667	13	0.667	130	100	1.041	7234	19.2	5.6	2.28	0.19	ND	ND	ND	AB
10SU65	41.612972	72.364083	2.578	Dev/Ss	20	0.922	137	0.931	1356	84	1.118	7234	20.8	1.9	2.30	0.17	101*	13.2	1.4	AB
10SU61	41.590000	72.328639	1.985	C/Granite	20	0.831	92	0.632	1209	7	1.131	7234	16.4	2	1.87	0.17	100*	11.6	1.9	AB
10SU62	41.609194	72.356056	2.386	C/Granite	20	1.082	157	1.144	1365	91	1.125	7234	23.9	2.1	2.31	0.02	101*	13.2	1.7	AB
10SU64	41.622861	72.367583	2.767	Dev/Granite	19	1.23	334	2.528	1625	50	1.136	4999	43	2.7	2.53	0.14	105*	12.4	1.9	AB